Università degli Studi di Torino

Ph.D. Thesis

Identified charged hadron production in Pb–Pb collisions at $\sqrt{s_{\mathrm{NN}}} = 2.76$ TeV with the ALICE experiment at the LHC

Author:
Leonardo Milano

Supervisor:
Prof. Massimo Masera

External reviewer:
Prof. Johannes P. Wessels

February 11, 2013

Abstract

Quark Gluon Plasma (QGP) is an unavoidable consequence of Quantum Chromodynamics (QCD). High-energy heavy-ion collisions offer the unique possibility to reproduce in the laboratory the conditions expected during the very first stages of the evolution of the universe. The ALICE (A Large Ion Collider Experiment) experiment at the Large Hadron Collider (LHC) allows the study of the dense nuclear environment created in nucleus-nucleus collisions. Particle Identification (PID) is one of the point of strength of the ALICE experiment. Identified particle spectra represent a crucial tool to understand the behaviour of the matter created in high-energy heavy-ion collisions. The transverse momentum p_{T} distributions of identified hadrons contain informations about the transverse expansion of the system and constrain the freeze-out properties of the system. The ALICE Inner Tracking System (ITS) can be used as a standalone tracker with a dedicated tracking algorithm. This allows the reconstruction of particles that decay before reaching the Time Projection Chamber (TPC) or that pass through the dead zones of the TPC. Hydrodynamic models have proved to be very successful reproducing a large number of features of heavy-ion collisions (e.g. particle p_{T} distributions, radial flow, elliptic flow, Hanbury Brown-Twiss correlations ...).

The measurement of the p_{T} distributions of identified π, K and p in Pb–Pb collisions at $\sqrt{s_{\mathrm{NN}}} = 2.76$ TeV is presented and discussed in terms of hydrodynamics. The VZERO detector allows the selection of events based on the eccentricity of the collision (related with the initial geometry). This makes possible the study the correlation between the p_{T} distribution of hadrons and elliptic flow on an events-by-event basis.

Hadron abundances can be obtained from the principle of maximum entropy using statistical concepts. This allows the extrapolation of the chemical freeze-out parameters from the data. Over the last years it has been proved that the chemical freeze-out temperature T_{ch} is connected with the phase transition temperature T_C. The measurements of the freeze-out parameters at the LHC energy is described in detail and the results obtained by different groups at lower energies are extended with the inclusion of the LHC measurement.

The LHC measurements cast a new light upon the hydrodynamic and thermal behaviour of the hadron production in heavy-ion collisions. The possible scenarios are described and commented.

Contents

1

Introduction: the Quark Gluon Plasma - QGP

"Before matter as we know emerged, the universe was filled with the primordial state of hadronic matter called Quark Gluon Plasma. This hot soup of quarks and gluons is effectively an inescapable consequence of our current knowledge about the fundamental hadronic interactions: Quantum Chromodynamics" [1].

The aim of this brief introduction is to give an overview of the subject of study of this work: the Quark Gluon Plasma (QGP). The main features of the theory behind it, the Quantum Chromodynamics (QCD), are described and the conditions under which the QGP is expected to be formed are reported.

1.1 Quantum Chromodynamics - QCD

Quantum Chromodynamics (QCD) is the gauge theory of strong interactions, one of the fundamental forces in physics. It is a Yang-Mills theory based on the $SU(3)_C$ group (C is the colour charge associated with this field). The associated gauge bosons are the gluons, which, together with colour-charged quarks make up hadrons. The key property of this theory is related with the coupling constant α_S, which depends on the energy transfer in the interaction. Its evolution is described with the DGLAP (Dokshitzer-Gribov-Lipatov-Altarelli-Parisi) equations. This is shown in Figure 1.1 [2] where it is

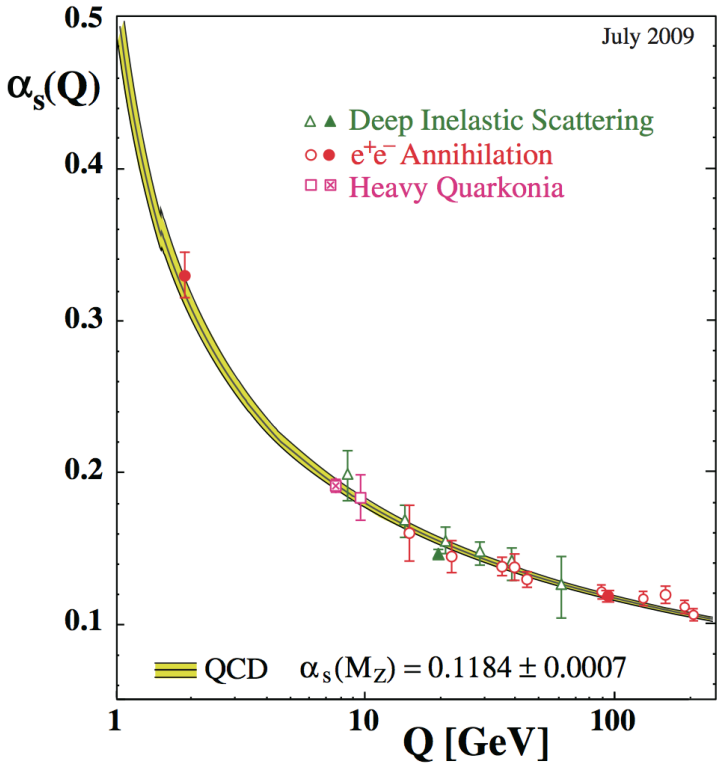

Figure 1.1: Summary of measurements of α_S as a function of the respective energy scale Q.

possible to distinguish, depending on the energy transfer Q in the interaction, two different regimes:

– **Confinement.** At small values of Q (i.e. large distance between quarks and gluons) the coupling constant is large and the associated force is strong enough to keep quarks and gluons bound into hadrons. The energy needed to separate partons increases with the distance between them, leading to confinement. This is the

energy regime were most of the known physics processes happen: it is our "hadron dominated" every day world. It is very important to mention that this is also the energy scale at which hadrons are measured in the experiments. From the theoretical point of view, given the large value of α_S at this energy scale it is not possible to adopt a perturbative approach. One way to circumvent this is by performing calculations on a lattice, in which the four dimensional space-time is treated not as a continuum but in a discrete way, just as in crystals [3]. In this way it is possible to solve QCD using numerical Monte Carlo simulations. The challenge for the calculations is to reduce the lattice space in order to approach the continuum.

– **Asymptotic freedom.** The coupling constant α_S becomes smaller with increasing energy (i.e. decreasing distance between quarks and gluons). This is a unique feature of non-Abelian gauge theories and it means that at high enough energies (i.e. small enough distances) quarks and gluons would be no longer confined into hadrons but should be themselves the degrees of freedom of the matter. This is the consequence of the anti-screening of the colour charge, given by the fact that gauge bosons (gluons) themselves carry colour charge. This state of deconfined matter is called Quark Gluon Plasma (QGP) and was firstly proposed in the seventies [4]. In this regime chiral symmetry is not broken. QGP is hence expected to be a chiral restored deconfined state of quarks and gluons.

1.2 The phase diagram of hadronic matter

Thermodynamical properties are usually expressed in terms of a phase diagram in the space of thermodynamic parameters. In the case of hadronic matter the thermodynamic state is defined by the temperature T and the baryochemical potential μ_B. A qualitative representation of the QCD phase diagram is reported in Figure 1.2 where μ_B is replaced by the net baryon density (directly proportional to μ_B). At high enough temperature $T \gg \Lambda_{QCD}$, due to asymptotic freedom, the approximation of gas of free quarks and gluons should become applicable. This is the region where the hadronic matter is in the QGP state. At lower T, due to confinement, quarks and gluons are bound into hadrons. The transition from hadrons to QGP can be evaluated from lattice calculations and is found to occur at $T \sim 170$ MeV for vanishing net baryon density. In the region of low μ_B it is expected that a smooth transition from hadrons to QGP, called "crossover", occurs. For larger values of μ_B the transition is expected to be of the first order. The point at

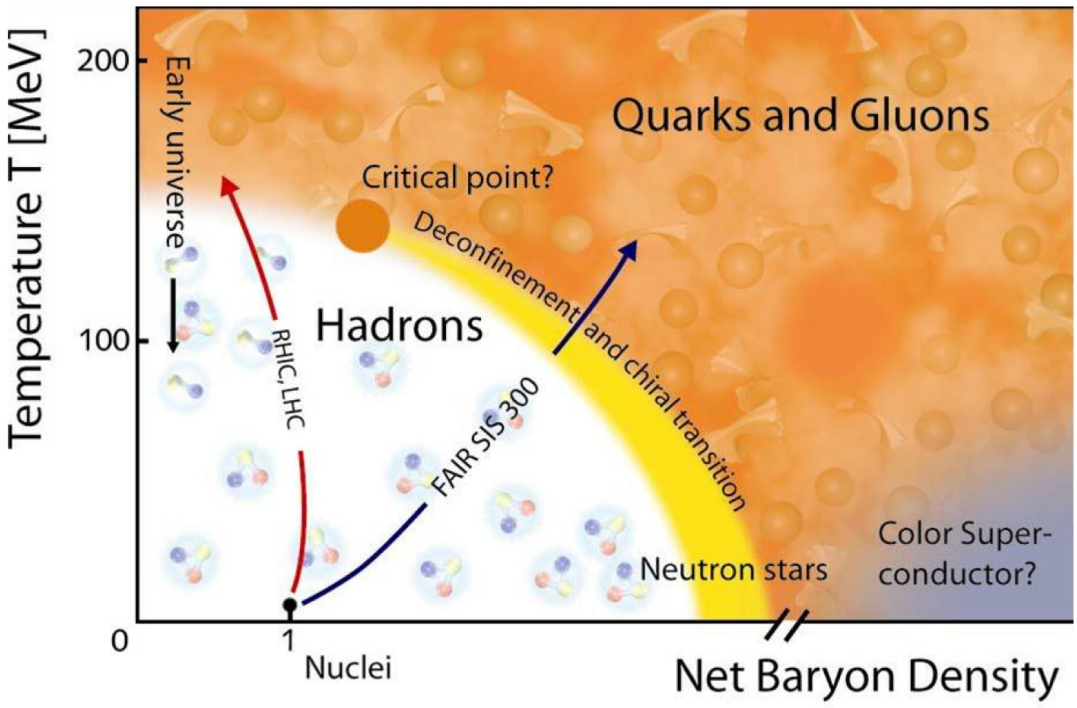

Figure 1.2: Qualitative representation of the QCD phase diagram.

which the first order phase transition becomes a crossover is called critical point. In the region of extremely high baryon density and low temperature, a colour superconductor state is expected [5].

It is important to stress that the different states of QCD matter are predicted by the QCD without any extra-assumptions: it is "natural" in the theory to have a deconfined state at high temperature.

1.2.1 QGP in the early universe

The time evolution of the universe is depicted in Figure 1.3. In the early stages of its evolution the thermodynamic conditions were such that the hadronic matter would be in the QGP region of the QCD phase diagram. During the first 10 μs the temperature was well above the critical temperature T_C and the baryon density was zero (the early universe was practically baryonless). Below T_C, this primordial QGP was transformed into a hot gas of hadrons which gradually cooled down. From this point onward the degrees of freedom of the universe were the hadrons instead of free quarks and gluons. Strong and electroweak interactions govern the evolution of the system.

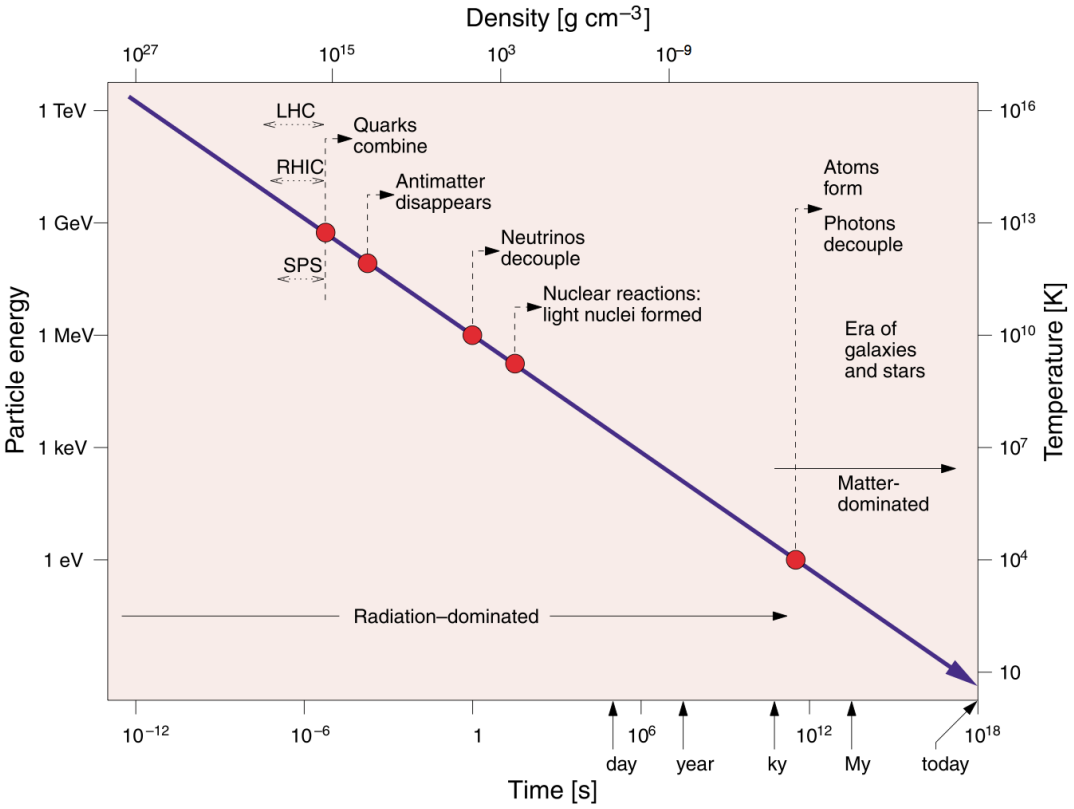

Figure 1.3: Time evolution of the universe.

1.2.2 QGP in the laboratory

In order to study the matter at its origin (i.e. in the first 10 μs of the universe) one needs:

- **High temperature.** The energy scale at which the QGP is expected to exist is $\gg \Lambda_{QCD}$.
- **Small (vanishing) baryon density.** The net baryon density of the early universe is practically zero.
- **Extended and long-lived system.** In order to study the behaviour of the QGP one needs a thermalised system which can be treated according to thermodynamics.

These conditions can be achieved at the particle accelerators using heavy-ion collisions. Nevertheless there are some differences between the "big-bang" of the universe and the "micro-bang" in the laboratory [1]:

- In the early universe the initial state was the QGP, which then was converted to hadrons. In the laboratory the initial state is given by hadrons and the QGP is expected to be formed after the collision. The QGP cools down until it reaches the critical temperature. At this time, the system crosses the phase transition line forming hadrons which are measured by the detectors.
- The baryonic content in high-energy heavy-ion collisions is not zero. Thus, unlike in the early universe, we expect in a laboratory micro-bang a significant matter-antimatter asymmetry. Only at the LHC energy the baryon transport at mid-rapidity is negligible, leading to a vanishing baryochemical potential in the central rapidity region.

The evolution of the system created in high-energy heavy-ion collisions is described in detail in Chapter 2 together with the observables related to the QGP formation.

2

Quark Gluon Plasma in the laboratory

As explained in Chapter 1 high-energy heavy-ion collisions offer the unique possibility to produce and study the Quark Gluon Plasma (QGP) in the laboratory. In this Chapter the experimental tools to probe the Quark Gluon Plasma are described in detail. It includes:

- **A description of the system evolution.** The hot and dense system created in such collisions rapidly expands and cools down. The different stages of the system evolution are reported, together with the models used to describe the system in such conditions (Sec. 2.1).
- **A review of the QGP creation observables.** The different observables related with the Quark Gluon Plasma formation are summarised and discussed. Both hard probes generated in the first stages of the system and collective observables emerging from the thermodynamic behaviour of the system (Sec. 2.2) are described.
- **A detailed description of the models used to reproduce the hadron yields and their momentum distributions.** Hadron yields can be interpreted using the Statistical Hadronisation Model - SHM (Sec. 2.3), assuming that hadrons evenly occupy all available phase space states. The collective behaviour of the particles produced in heavy-ion collisions can be described in terms of hydrodynamics (Sec. 2.4).

2.1 Evolution of the heavy-ion collision

The time evolution of an heavy-ion collision is depicted in Figure 2.1. The time of the collision between incoming nuclei is defined as $\tau = 0$.

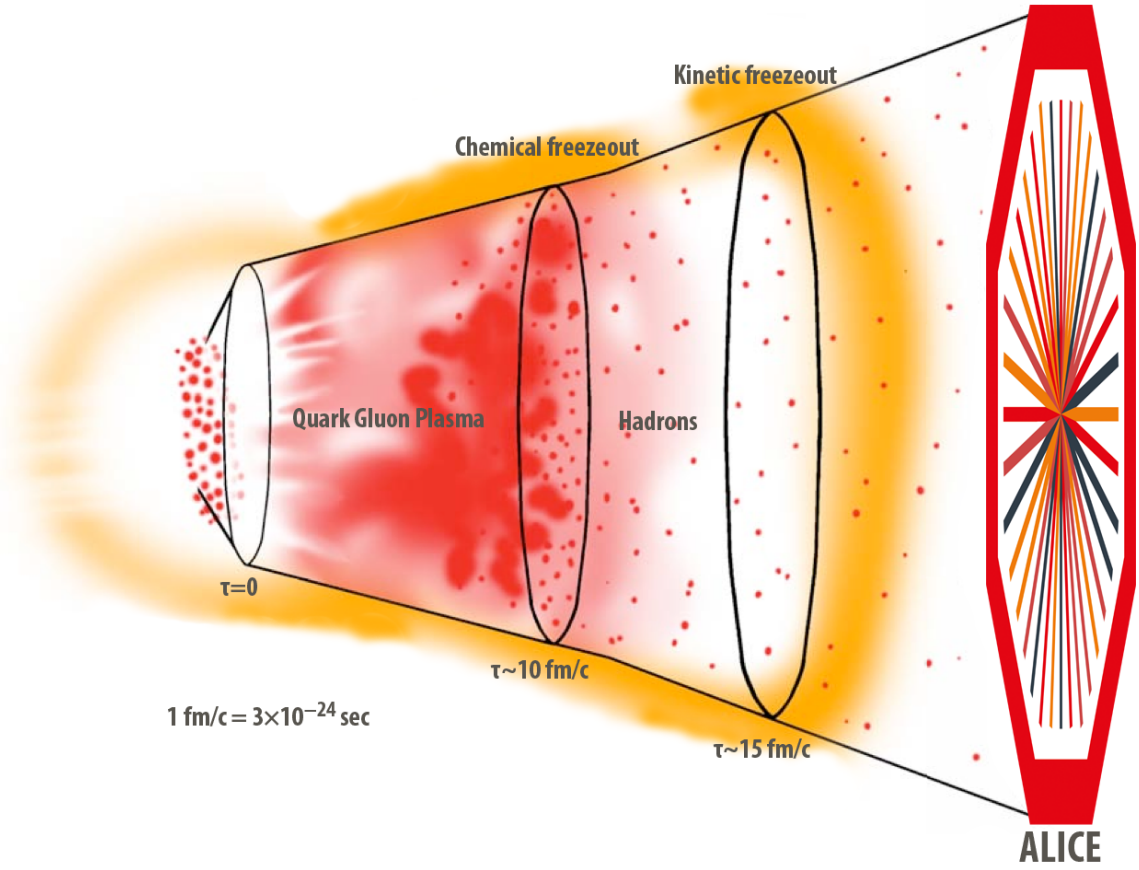

Figure 2.1: Sketch of an heavy-ion collision evolution. The values of τ are the indicative values expected at the LHC.

– $\tau < 10$ fm/c. **QGP phase.** The bulk of the quanta is created in the very first stages of the collision from the large energy deposit of the nuclei. The formation time is proportional to the parton energy ($\tau_{form} \sim 1/m_{\mathrm{T}}$) and corresponds to a fraction of fm/c). Before quarks and gluons have time to rescatter and thermalise hard partons with $p_{\mathrm{T}} \gg 1$ GeV/c are created. Once produced, these particles can be used to probe the soft bulk of partons in the system. Interactions between partons rapidly lead to thermalisation of the system ($\tau_{eq} \sim 0.5 - 1$ fm/c). From this point onward the temperature of the system can be defined and the thermodynamical

description of the QGP becomes applicable. The system expands and gradually cools down: this is the main difference between elementary particles and nucleus-nucleus collisions. In the latter case partons can't escape into the surrounding vacuum, but interact both elastically and inelastically leading to equipartitioning of the deposited energy (thermalisation). The temperature of the QGP decreases with the system expansion reaching the critical temperature T_C. The coupling constant α_S becomes large enough to confine quanta: below T_C quarks and gluons are no longer free (asymptotic freedom) but convert to hadrons (confinement). From this point onward the degrees of freedom of the system are hadrons instead of free quarks and gluons.

- 10 fm/c $\lesssim$ τ $\lesssim$ 15 fm/c. **Hadron gas.** The system below T_{ch} is composed of hadrons which have both elastic and inelastic interactions. The system keeps cooling down and expanding pushed by the internal pressure of the fireball: the density of the system decreases and the mean free path of hadrons increases.
  - When inelastic interaction rate becomes too small to keep up with the system expansion the hadron abundances freeze-out. This is the so-called "chemical freeze-out", the corresponding temperature is T_{ch}.
  - The system keeps expanding and the mean free path increasing. Hadrons still interact elastically without changing their relative abundances until the system reaches the temperature T_{kin} at which elastic interactions cease. This is the "kinetic freeze-out": p_{T} distributions are frozen.
- τ $\gtrsim$ 15 fm/c. **Free hadron stream.** Both elastic and inelastic interactions no longer play a role in the system evolution. Hadrons freely stream to the experiment where they are detected. The short-lived unstable particles decay, however, producing daughter particles with, on average, smaller transverse momenta which still modify the p_{T} shape of the longer-lived species (e.g. pion spectrum at low p_{T} is dominated by resonance decay contribution).

The centrality of the collision is determined by the impact parameter b, which is defined as the vector in the transverse plane connecting the centres of the two colliding nuclei. The collision centrality can also be expressed in terms of N_{part}, which is the number of nucleons that undergo at least one inelastic interaction, or N_{coll}, which is the total number of inelastic collisions between nucleons (Figure 2.2). Unfortunately the impact parameter b, N_{part} and N_{coll} cannot be observed directly. The centrality of the collisions can be

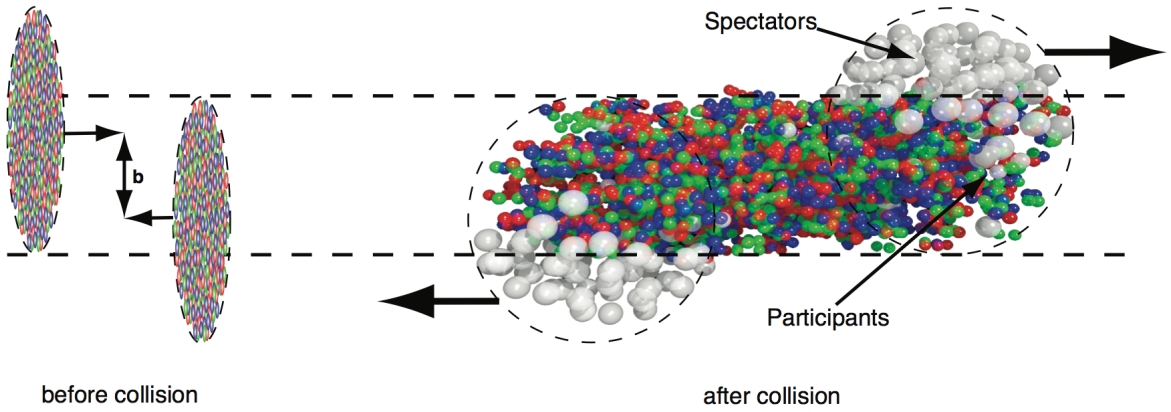

Figure 2.2: Left: two heavy-ions before collision with impact parameter b. Right: The spectator nucleons continue unaffected, while in the participant zone particle production takes place [6].

inferred by measuring the transverse energy, assuming that it is a monotonic function of b, or by measuring the energy in the detectors at forward rapidity, which is related to the number of spectator nucleons [7].

It is interesting to note that the time evolution of heavy-ion collisions and that of the early universe are strictly connected. The chemical freeze-out is the analogue of primordial nucleosynthesis in the Big Bang. The hydrodynamic expansion in heavy-ion collisions on the other hand is the analogue of the cosmic Hubble expansion of the universe. In this sense by studying heavy-ion collisions at the accelerators one gets important insights on the evolution of the early universe.

2.2 Observables related to QGP formation

To collect evidences of the formation of a QGP and to study its properties, the hadrons emerging from the heavy-ion collision are measured. From the study of these "late" hadronic observables one can get informations about the system created in the collision.

2.2.1 Hard probes of the QGP

Hard probes are characterised by processes with large energy transfer Q^2. In these processes the QCD coupling constant α_S is small enough that a perturbative approach to

QCD is possible. The experimental tools used to identify the effects induced by the QGP formation are mainly based on the comparison between:

– hadron-hadron and nucleus-nucleus collisions: in order to test that Pb–Pb is not a simple uncorrelated superposition of single p–p collisions. The number of particles produced in a nucleus-nucleus collision is expected to be proportional to the number of participants nucleons $N_{\rm part}$ at low $p_{\rm T}$ and to the number of binary nucleon-nucleon collisions $N_{\rm coll}$ at high $p_{\rm T}$. In order to estimate the modifications induced by the QGP presence the nuclear modification factor $R_{\rm AA}$ is defined as

$$R_{\rm AA} = \frac{1}{< N_{\rm coll} >} \frac{{\rm d}^2 N_{A-A}/{\rm d}\eta \ {\rm d}p_{\rm T}}{{\rm d}^2 N_{p-p}/{\rm d}\eta \ dp_{\rm T}} \tag{2.1}$$

From this definition, if nucleus-nucleus is an incoherent superposition of $N_{\rm coll}$ p–p collisions, one would expect $R_{\rm AA} = 1$ at high enough $p_{\rm T}$ (i.e. in the region where the hadron production is characterised by processes with large energy transfer). Initial state effects, such as the Cronin enhancement or nuclear modifications of the parton distribution functions (shadowing) [8] could modify this behaviour. The Cronin effect can be explained by the fact that before the inelastic collision nucleons could have elastic interactions which lead to a small extra $p_{\rm T}$ component of the parton in the case of nucleus-nucleus or hadron-nucleus. This would modify the $R_{\rm AA}$ to be larger than unity in the intermediate $p_{\rm T}$ region. Shadowing is a relative reduction of the PDF in a nucleus with respect to that of the proton for partons with $x < 10^{-2}$: it should modify significantly the measured values of $R_{\rm AA}$ only at low $p_{\rm T}$.

– Hadron-nucleus and nucleus-nucleus collisions: this is an important comparison because it allows to separate the initial state effects (given by the "cold" nuclear matter such as Cronin effect and shadowing) from the "hot" nuclear matter effects due to the QGP.

– Central and peripheral nucleus-nucleus collisions: in peripheral collisions the size of the QGP fireball is smaller with respect to central collisions. The modifications due to the QGP should become larger with increasing centrality.

High $p_{\rm T}$ hadron suppression

High $p_{\rm T}$ hadrons are mainly produced by the fragmentation of partons originated in the hard scatterings between partons occurring in the first stages of the collision. In heavy-ion collisions high $p_{\rm T}$ partons lose energy inside the coloured QGP medium, due to collisional

and radiative energy loss. This results in a suppression of the yield of high p_{T} hadrons with respect to hadron-hadron collisions. The nuclear modification factor measured in p–Pb collisions at $\sqrt{s_{\mathrm{NN}}} = 5.02$ TeV in $|\eta_{cms}| < 0.3$ [9], central (0-5% centrality) and peripheral (70-80%) Pb–Pb collisions at $\sqrt{s_{\mathrm{NN}}} = 2.76$ TeV [10] by the ALICE experiment is reported in Figure 2.3. It is a very interesting result because it compares different

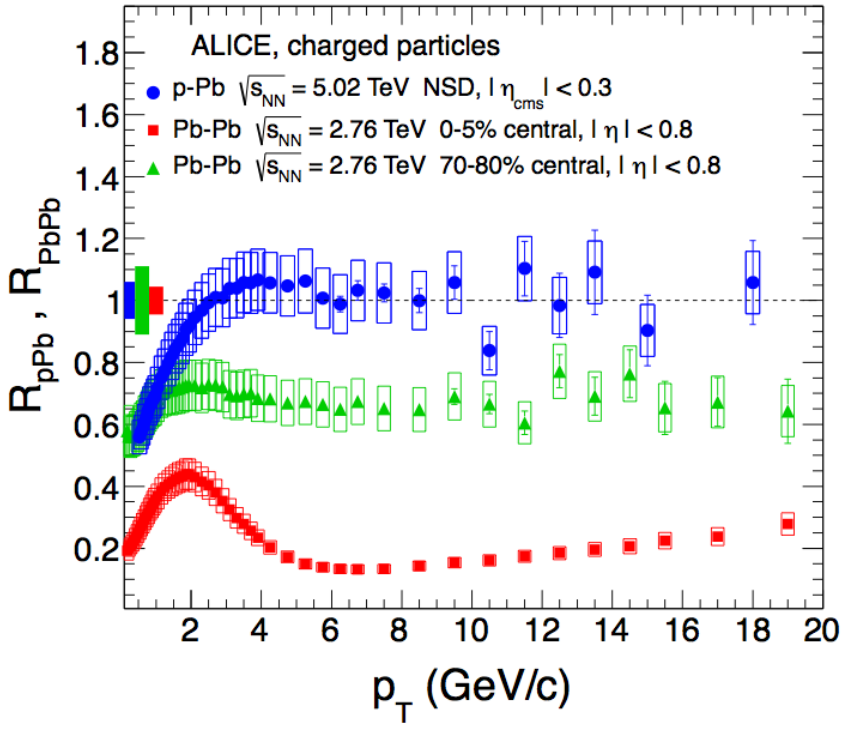

Figure 2.3: The nuclear modification factor of charged particles as a function of transverse momentum in non-single diffractive (NSD) p–Pb collisions at $\sqrt{s_{\mathrm{NN}}} = 5.02$ TeV in $|\eta_{cms}| < 0.3$ [9], central (0-5% centrality) and peripheral (70-80%) Pb–Pb collisions at $\sqrt{s_{\mathrm{NN}}} = 2.76$ TeV [10]. The statistical errors are represented by vertical bars, the systematic ones by (empty) boxes. The relative systematic uncertainties on the normalisation are shown as boxes around unity near $p_{\mathrm{T}} = 0$ for p–Pb (left box), peripheral Pb–Pb (middle box) and central Pb–Pb (right box).

systems:

– Central Pb–Pb. In the most central collisions (0-5%), the yield of hadrons is most suppressed, R_{AA} has a minimum of ≈ 0.13 at $p_{\mathrm{T}} = 6$-7 GeV/c and it rises at higher p_{T}. This suppression can be interpreted as a final state effect related to energy loss in the QGP.

– Peripheral Pb–Pb. The suppression is significantly smaller than in central Pb–Pb collisions. If the QGP is created in such collisions, the QGP phase is expected to be shorter and the system size to be smaller. For this reason, if the suppression is due to partonic energy loss in the QGP, one expects the suppression in peripheral collisions to be smaller.

– This is confirmed by the nuclear modification factor measurement in p–Pb where the spectrum is observed to scale with N_{coll} at high p_{T} ($R_{\mathrm{AA}} = 1$). p–Pb is a key measurement because in a proton-nucleus collision, quarks and gluons produced in the hard scattering are surrounded by cold (i.e. not deconfined, colour-neutral) nuclear matter. The absence of suppression in p–Pb collisions points to a "hot" nuclear matter effect in Pb–Pb. In the intermediate p_{T} region (between ~ 3 and 6 GeV/c) a hint of Cronin enhancement (not significative considering the error bars) can be observed.

Jet production

Parton energy loss may provide direct sensitivity to the colour charge density and to the transport properties of the QGP. High p_{T} partons are produced in the early stages of the collisions and travel through the QGP interacting with the colour charged medium. The hadronisation of these partons produces jets: a narrow cone of particles around the parton momentum direction. Highly asymmetric dijets in central Pb–Pb collisions have been observed at the LHC [12]. It can be interpreted as due to different path lengths of the partons in the matter, given by the fact that in a quark-antiquark pair the parton crossing the shortest path to the fireball surface loses significantly less energy than the other. A measurement of the "inclusive" jet quenching is reported in Figure 2.4 where the R_{CP} values as a function of the jet p_{T} in four different centrality bins in Pb–Pb collisions at $\sqrt{s_{\mathrm{NN}}} = 2.76$ TeV [11] are reported. R_{CP} is an analogous measurement to R_{AA}, in which central nucleus-nucleus collisions are compared to peripheral nucleus-nucleus (scaled to N_{coll}) instead of hadron-hadron collisions, assuming no QGP (or less extended in space-time) phase in peripheral nucleus-nucleus collisions. The inclusive jet yield is suppressed by a factor of about two in central collisions, relative to peripheral collisions. This is expected because energy loss increases with the density of the medium and with increasing path length of the parton in the medium. A weak p_{T} dependence of this suppression is observed.

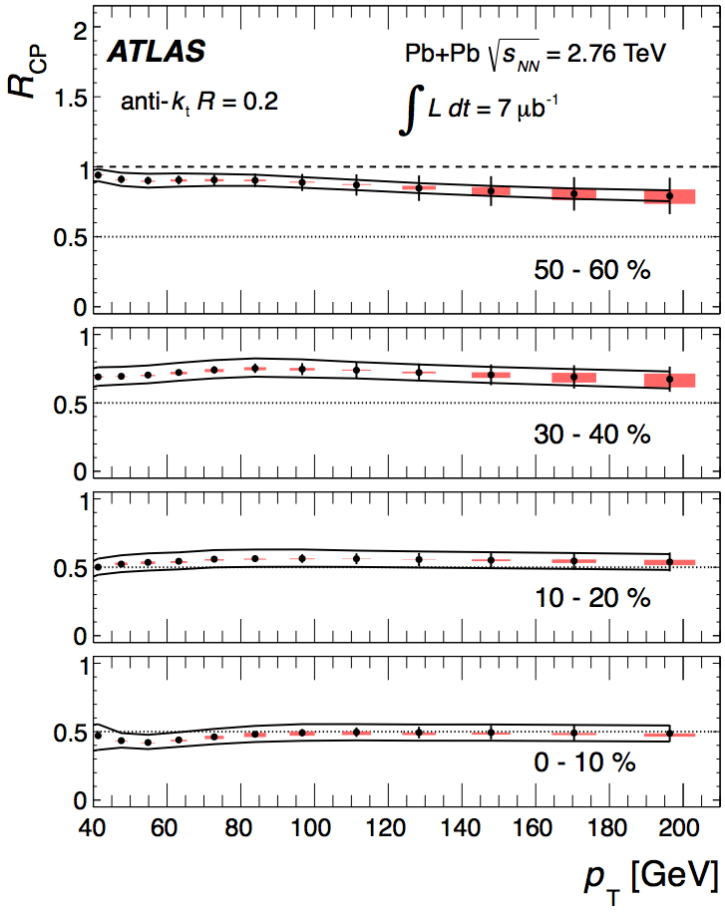

Figure 2.4: R_{CP} of reconstructed jets as a function of the jet p_{T} in four different centrality bins in Pb–Pb collisions at $\sqrt{s_{\mathrm{NN}}}$ = 2.76 TeV. Jets are reconstructed using an anti-k_t algorithm with cone radius R=0.2. The error bars indicate statistical errors, the shaded boxes indicate unfolding regularisation systematic errors that are partially correlated between points. The solid lines indicate systematic errors that are fully correlated between all points. The horizontal width of the systematic error band is chosen for presentation purposes only. Dotted lines indicate $R_{\mathrm{CP}} = 0.5$, and the dashed lines on the top panel indicate $R_{\mathrm{CP}} = 1$. The R_{CP} measurements presented here use the 60-80% centrality bin as a common peripheral reference [11].

Prompt photons

Photons are not sensitive to the colour charge of the QGP, they escape from the collision zone without interacting in the medium and carry pristine information about their parent quarks and gluons. Prompt photons are produced in the partonic collisions mainly

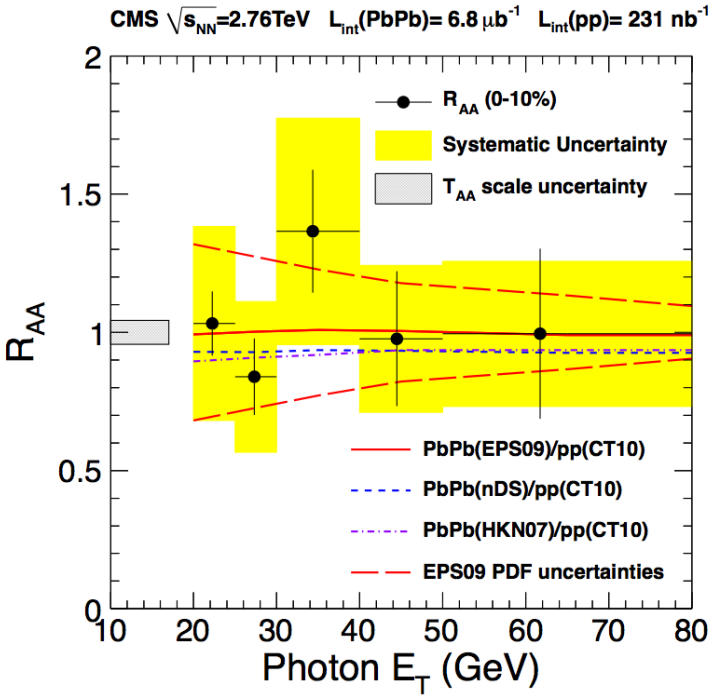

Figure 2.5: Nuclear modification factor R_{AA} of prompt photons as a function of the photon energy E_{T} in 0-10% most central Pb–Pb collisions at $\sqrt{s_{\mathrm{NN}}} = 2.76$ TeV. The vertical error bars indicate the statistical uncertainty. The total systematic uncertainties without the T_{AA} uncertainty are shown as yellow filled boxes. The T_{AA} uncertainty, common to all points, is indicated by the left box centred at unity. The curves show the theoretical predictions, obtained with JETPHOX for various nuclear PDFs. The uncertainty from the EPS09 PDF parameters is shown as the red dashed lines [13].

by quark-gluon Compton scattering $qg \to \gamma q$ and quark-antiquark annihilation $q\bar{q} \to \gamma g$.[1] The experimental challenge is to cope with the huge background from electromagnetic decays of neutral mesons. The nuclear modification factor R_{AA} of prompt photons as a function of the photon energy E_{T} in 0-10% most central Pb–Pb collisions at $\sqrt{s_{\mathrm{NN}}} = 2.76$ TeV is reported in Figure 2.5 [13]. The R_{AA} is close to unity (i.e. no modification

[1]These are not thermal photons produced by the electric charge of quarks and gluons in the very first stage of the collision [14]. Virtual and real photons are emitted throughout the expansion of the fireball.

given by the QGP) [15], as expected for an electromagnetic probe which escapes from the fireball without rescattering with the coloured medium.

Open Heavy Flavour

Given their large mass, heavy quarks (i.e. charm and beauty) can be produced in the first stages of the collision by the scattering of partons with high enough Q^2 to create a pair of them. Since the heavy flavour production is characterised by large energy transfer, the production rate can be computed with a perturbative approach to QCD. As these particles are produced at the beginning of the collision, they experience all the stages of the QGP evolution and finally hadronise forming heavy flavour hadrons. These hadrons carry a large fraction of the parton momentum, given by the fact that the fragmentation function is much harder for b and c quarks than for light flavours. Heavy flavour hadrons energy loss can be estimated by measuring the nuclear modification factor. This is reported in Figure 2.6 where the average R_{AA} of D mesons is compared to those of charged particles in 0-20% Pb–Pb collisions at $\sqrt{s_{\mathrm{NN}}} = 2.76$ TeV. The R_{AA} shows a suppression by a factor 3-4, for transverse momenta larger than 5 GeV/c in the 20% most central collisions. The suppression is almost as large as that observed for charged particles (mainly light-flavour hadrons). However data seems to suggest, but it is not fully significant with the present level of experimental uncertainties, that the suppression for D mesons is smaller that the one for charged hadrons. Energy loss models predict the R_{AA} value to be larger (i.e. a smaller suppression) when going from the mostly gluon-originated light-flavour hadrons (e.g. pions) to D and B mesons: $R^{\pi}_{AA} < R^{D}_{AA} < R^{B}_{AA}$.

Quarkonia

The interaction potential between quark and antiquark can be expressed as:

$$V(r) = -\frac{\alpha}{r} + kr \tag{2.2}$$

in which the first term is the "Coulomb" term given by gluon exchange between quark and antiquark and the second term represents the confinement term. When the quarkonium is immersed in the QGP, it is modified by the medium in the following ways:

- the confinement term vanishes,
- free colour charges in the plasma modify the Coulomb term to a Yukawa term $-\frac{\alpha}{r}e^{-r/\lambda_D}$ in which λ_D is called "Debye screening length". Long-range interaction is modified into a short-range Yukawa type interaction.

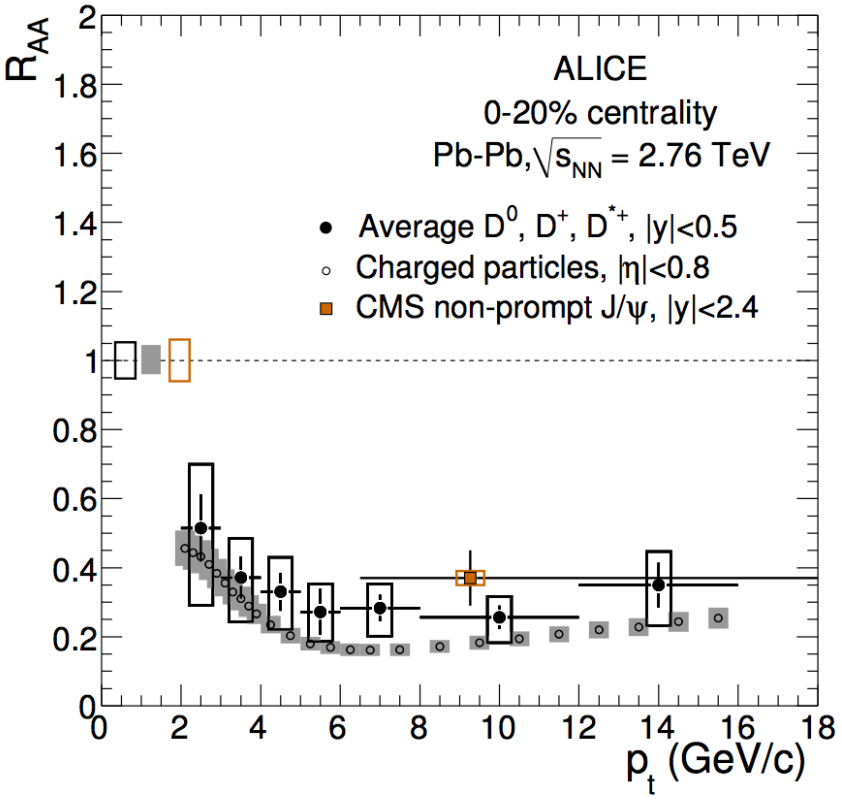

Figure 2.6: Average R_{AA} of D mesons, R_{AA} of charged particles and R_{AA} of non-prompt J/ψ from B decays in 0-20% Pb–Pb collisions at $\sqrt{s_{\mathrm{NN}}} = 2.76$ TeV [16]. The normalisation uncertainties are almost fully correlated.

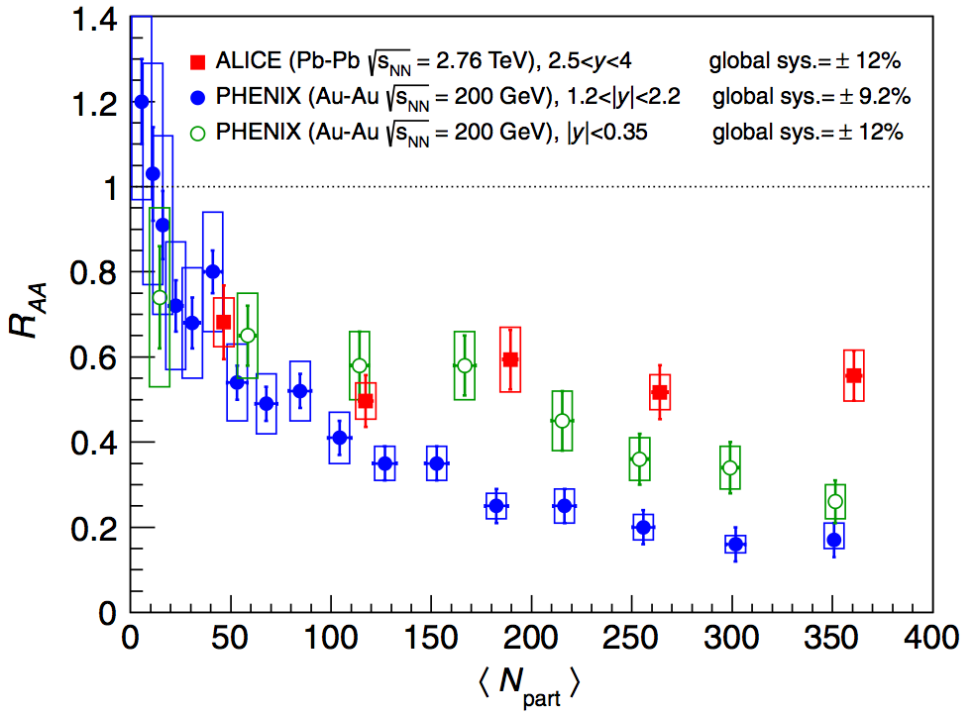

Figure 2.7: Inclusive J/ψ $R_{\rm AA}$ as a function of the number of participating nucleons measured in Pb–Pb collisions at $\sqrt{s_{\rm NN}}$= 2.76 TeV compared to results in Au–Au collisions at $\sqrt{s_{\rm NN}}$ = 200 GeV at midrapidity and forward rapidity [17].

The binding energy and the corresponding dimensions are different for different resonances: it is expected that the less tightly bound states melt at lower temperatures. Other effects can modify the quarkonium production in heavy-ion collisions: shadowing of the PDF, quarkonia suppression by hadronic matter (so called hadronic co-movers) and regeneration given by statistical recombination of quark-antiquark pairs in the medium. The inclusive J/ψ $R_{\rm AA}$ as a function of the number of participating nucleons $N_{\rm part}$ measured in Pb–Pb collisions at $\sqrt{s_{\rm NN}}$= 2.76 TeV compared to results in Au–Au collisions at $\sqrt{s_{\rm NN}}$ = 200 GeV at midrapidity and forward rapidity [17] is reported in Figure 2.7. The J/ψ $R_{\rm AA}$ is lower than unity, pointing to a suppression of the J/ψ production in Pb–Pb collisions. At the LHC the $R_{\rm AA}$ is larger than the one measured at RHIC for most central collisions and does not exhibit a significant centrality dependence. This can be interpreted as an increasing regeneration of J/ψ at the LHC with respect to RHIC. Models predict the J/ψ regeneration to be larger at forward rapidity with respect to mid-rapidity: this is in agreement with the CMS J/ψ $R_{\rm AA}$ measurement [18] which suggests a stronger suppression at mid-rapidity.

2.2.2 "We are the 99%!". Soft probes of the QGP

The bulk of the hadrons emerging from a heavy-ion collision consists of light hadrons with low momentum: they are more than the 99% of the hadrons produced in the collisions. These hadrons are originated by the hadronisation of soft partons in the QGP, which are in thermal equilibrium in the deconfined phase. These strongly interacting hadrons cannot decouple from the fireball before the system is so dilute that interactions cease. As mentioned before, first inelastic collisions cease at the instant of chemical freeze-out, at T_{ch}. When this occurs, the abundances of hadron species are frozen. Below T_{ch} hadrons still interact elastically until the system reaches the kinetic freeze-out temperature T_{kin}, at this point hadrons decouple from the fireball and are detected by the experiments. These hadrons are in equilibrium with the system (they are the system!): their measurement represents a "snapshot" of the fireball at the freeze-out time.

Relative hadron abundances

Relative hadron abundances can be interpreted in terms of statistical hadronisation from a thermal source. The chemical freeze-out temperature T_{ch} is connected with the phase transition temperature T_C. If one assumes that the hadronic matter is in equilibrium (both chemical and kinetic) at the moment of chemical freeze-out, hadron abundances

can be obtained using the principle of maximum entropy. This is described in detail in Sec. 2.3. The free parameters of this model are: the chemical freeze-out temperature T_{ch}, the baryochemical potential μ_B and the fireball volume V. These parameters can be extracted from a fit to particle yields. If one fits particle ratios instead of yields, the parameter V cancels out and only T_{ch} and μ_B are the free fit parameters (please read the remarks on thermal fit at the beginning of Sec. 6.2.4). Thermal fits to heavy-ion collisions at different $\sqrt{s_{\rm NN}}$ have been performed by different groups [19–21]. For each collision energy it is possible to extract T_{ch} and μ_B values. These values are reported in Figure 2.8 in which T_{ch} and μ_B are reported as a function of the center of mass energy of the collision $\sqrt{s_{\rm NN}}$ [19].

- T_{ch} is observed to be flat as a function of $\sqrt{s_{\rm NN}}$ above $\approx$ 10 GeV (SPS energy). This saturation of the chemical freeze-out occurs at the same temperature where the theoretical phase transition line (calculated from lattice QCD) is predicted. If this is the case T_{ch} would have a similar value at the LHC.

- μ_B keeps decreasing with increasing $\sqrt{s_{\rm NN}}$. This is due to the smaller baryon number transport at midrapidity with increasing energy, due to larger transparency. This argument suggests a vanishing baryochemical potential at the LHC.

The measurements of Fig. 2.8 can be presented in the (T_{ch},μ_B) plane: this is reported in Figure 2.9 [22]. This figure recalls the QGP phase diagram (Fig. 1.2). If one compares the T_{ch} and μ_B values extracted from thermal fits to hadron yields with the expected phase transition line (blue-dotted line) it is clear that the T_{ch} saturation is due to the fact that the freeze-out temperature lies close to the phase transition line above SPS energies. This implies that:

- above a given $\sqrt{s_{\rm NN}}$ ($\approx$ 10 GeV) the chemical freeze-out happens right after the hadronisation,

- below $\sqrt{s_{\rm NN}} \approx$ 10 GeV T_{ch} starts deviating from the predicted phase transition temperature. This can be due to a longer equilibrium phase after hadronisation or to the fact that the energy density in such collisions is not high enough to create the QGP.

It is clear how the measurement of T_{ch} and μ_B at the LHC is a key measurement in this picture : this is the main subject of Chapter 6.

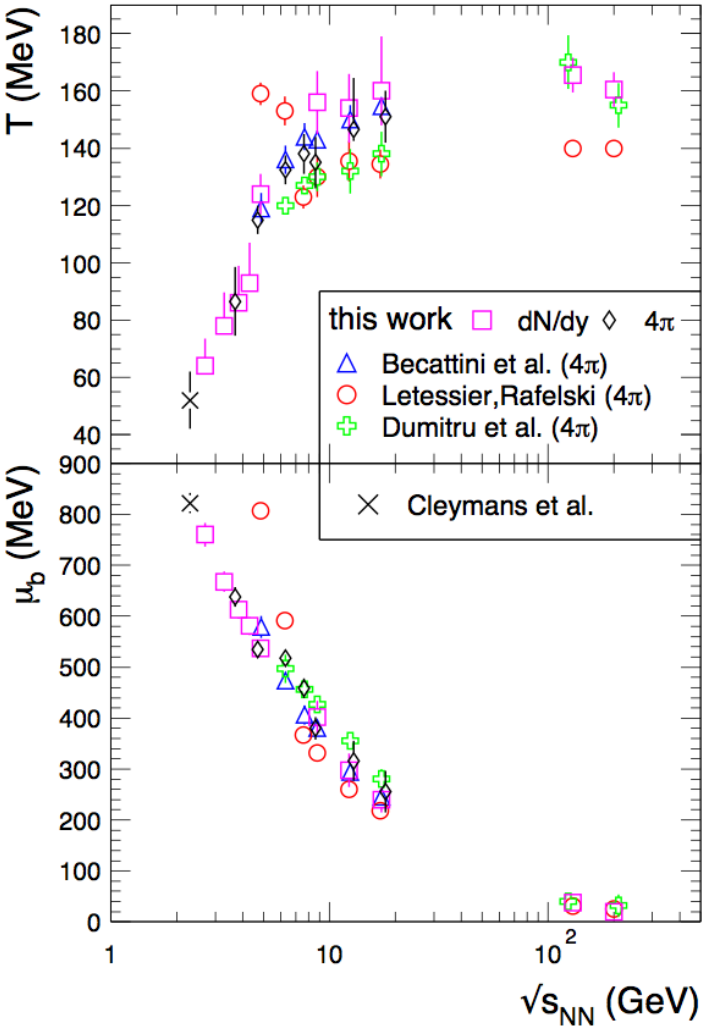

Figure 2.8: The energy $\sqrt{s_{\mathrm{NN}}}$ dependence of chemical freeze-out temperature T_{ch} and baryochemical potential μ_B. The results of [19] are compared to the values obtained in earlier studies.

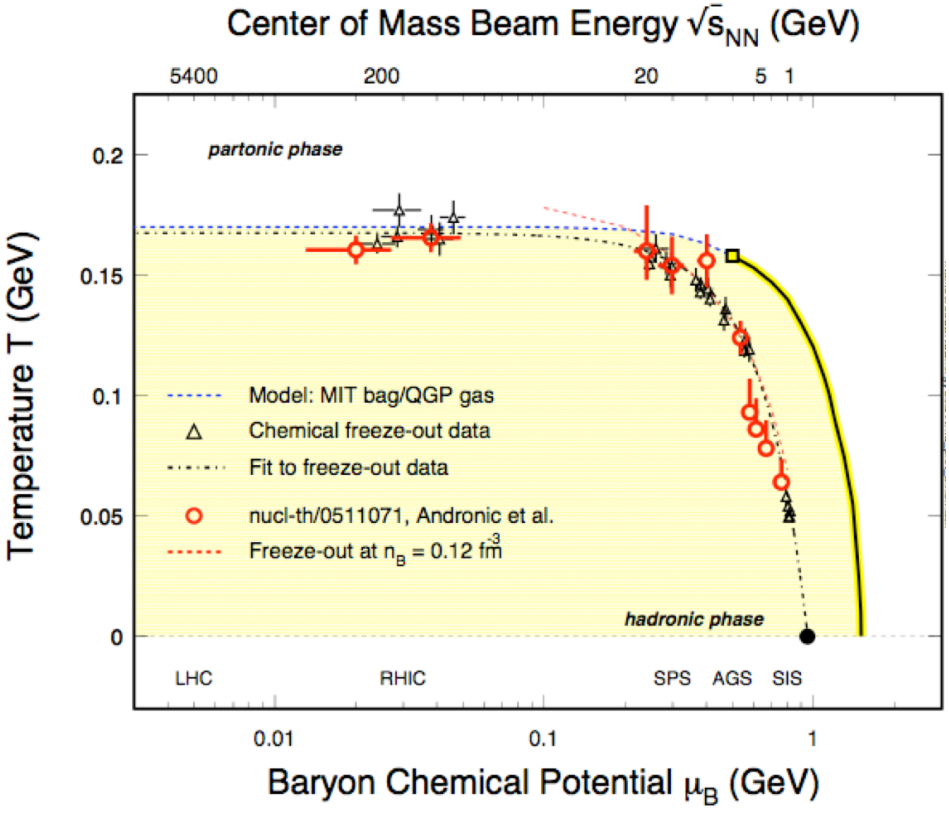

Figure 2.9: T_{ch} vs μ_B at different energies. The expected transition line (blue-dotted), a parameterisation of the chemical freeze-out curve (black-dotted) and the expected freeze-out curve (red-dotted) assuming $n_B = 0.12$ fm^{-3} are also reported [22].

The analogy with the early universe is clear. The universe is observed to be expanding and filled with radiation that is very cold today (2.725 K) but if we trace back its evolution it is found to be hotter and denser, such that during its first ≈ 1000 s it can be considered as a Primordial Nuclear Reactor. If one assumes that the universe is homogeneous and isotropic and that the Standard Model is the correct description of particle physics at temperatures of the order of few MeV, the relative abundances of protons and neutrons follow from simple thermodynamical arguments. The predictions of the standard Big Bang Nucleosynthesis (BBN) only depend on the baryon-to-photon ratio. The primordial yields of light elements are determined by a competition between the expansion rate of the universe and the rates of the nuclear reactions that build up the complex nuclei. This is based on the assumption that the system is in equilibrium until the freeze-out, which occurs when the interaction length for nuclear reaction becomes smaller than the mean free path of hadrons in the expending universe. This is analogous to what happens in heavy-ion collisions.

Strangeness enhancement

In the QGP a partial chiral symmetry restoration is expected. The effect is an increased production of s and $\bar{s}$ quarks with respect to hadronic collisions. As chiral symmetry is restored, the mass of the strange quark is expected to decrease from its constituent value to its current value of about 150 MeV: the production of $s\bar{s}$ pairs becomes competitive with that of $u\bar{u}$ and $d\bar{d}$ pairs. During the hadronisation the larger amount of strange quarks in the QGP turns into an increased production of strange hadrons with respect to p–p collisions. It is important to mention that inelastic scattering between hadrons like $\pi+\pi \rightarrow K+K$ or $\pi+N \rightarrow \Lambda+K$ could also enhance the measured amount of strangeness. Therefore it is important to look at the relative enhancement of strangeness for particles with different strange content [23]. The way to study the enhancement of a given specie X is by looking at the ratio $E(X) = \frac{(N_X/<N_{\rm part}>_{A-A})}{(N_{X_{p-p}})}$[2]. This is reported in Figure 2.10 as a function of $N_{\rm part}$ at the LHC and previous experiments. The enhancement is proportional to the strangeness content of the hadron, being $E(\Omega) > E(\Xi) > E(\Lambda)$ at all centralities. The centrality dependence shows that this effect is proportional to the space-time extension of the system (i.e. the centrality of the collision). A competitive process to the chiral symmetry restoration is the canonical suppression (expected to be smaller in

[2]Reminder for the reader: soft hadrons are expected to be proportional to the number of participants nucleons $N_{\rm part}$.

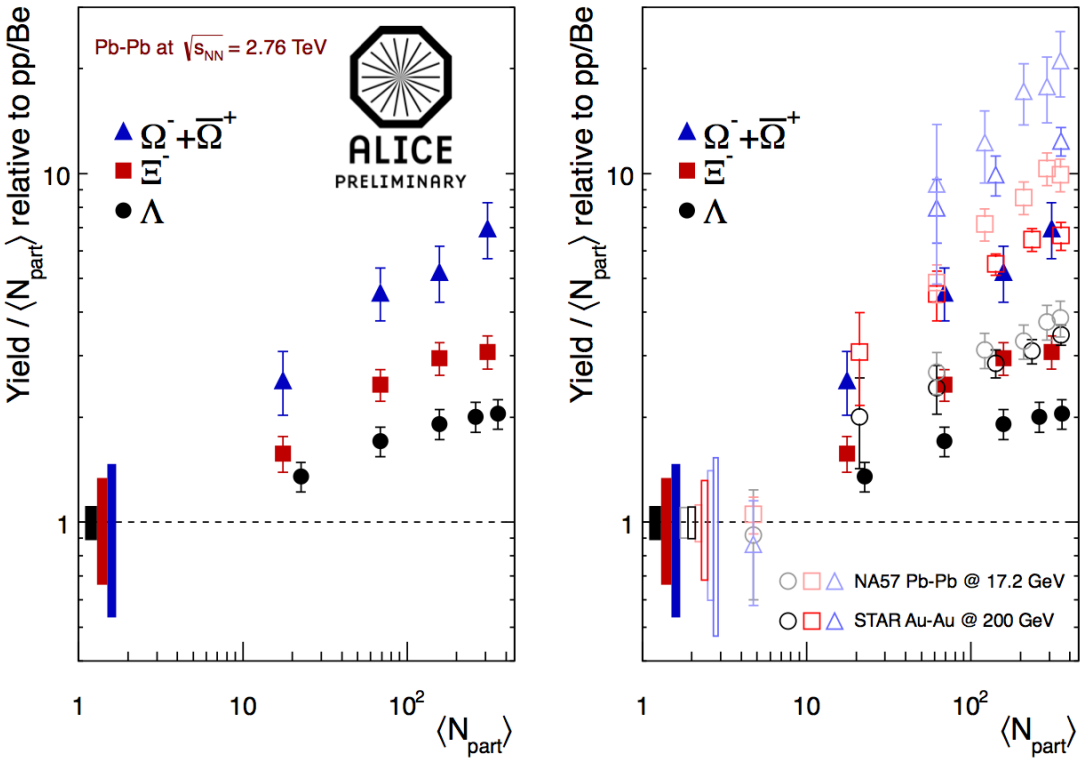

Figure 2.10: Strangeness enhancement observed at ALICE (full symbols) compared to NA57 and STAR measurements (open symbols).

nucleus-nucleus). In small systems (such as p–p collisions) the strangeness production is suppressed by the fact that the charge must be conserved locally. An extended system like nucleus-nucleus can be described using the the grand-canonical ensemble, which allows the charge conservation on average (see Sec. 2.3 for details).

Flow

Collective flow is an unavoidable consequence of the Quark Gluon Plasma formation. Since QGP is by definition a thermalised system of quark and gluons, it has an associated thermal pressure. The fireball is surrounded by the vacuum, this creates a pressure gradient which leads to a collective expansion of the system. The collective motion is interpreted by hydrodynamics (see Section 2.4 for details). Collective flow is an important tool to test the assumption of the equilibrium of the system.

– **Radial flow.** The collective expansion of the nuclear fireball results in a flattening of the p_{T} spectra with respect to hadron-hadron collisions. Particle spectra in central Au–Au and minimum bias p–p collisions at $\sqrt{s_{\mathrm{NN}}} = 200$ GeV are reported in Figure 2.11. In p–p collisions π, K and p have a common slope, indicating a ther-

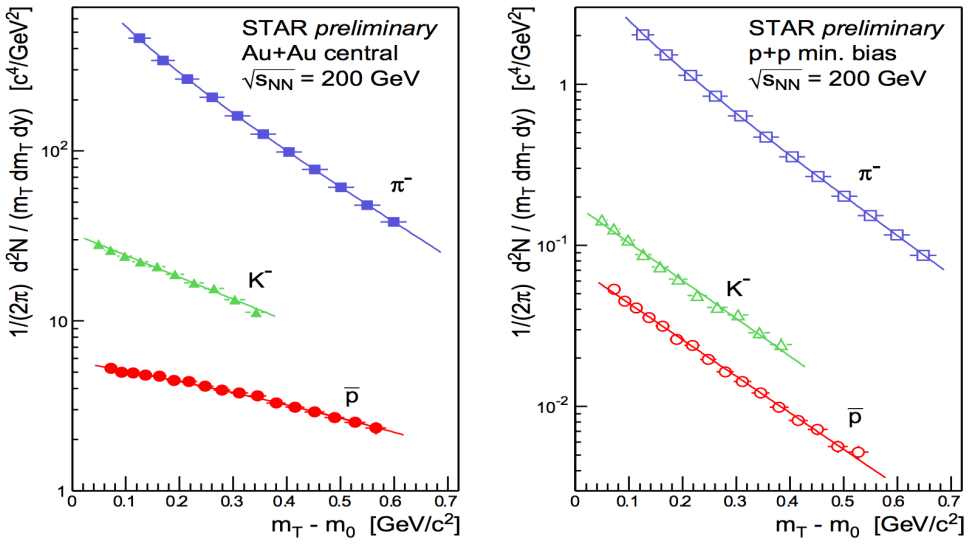

Figure 2.11: Pion, kaon and antiproton spectra from 200 A GeV central Au–Au (left) and minimum bias p–p collisions (right), measured by the STAR experiment. Note the similar slopes for kaons and antiprotons in p–p collisions and their dramatically different slopes at low transverse kinetic energy in central Au–Au collisions [8].

mal spectrum à la Boltzmann (m_{T} scaling). In central Pb–Pb the slope in no longer

the same for all the particle species (spectra become flatter with increasing mass). Collective flow breaks the m_{T} scaling. The inverse slope of these spectra reflects a blueshifted freeze-out temperature, given by the collective expansion of the system. The results at the LHC are reported and compared with RHIC in Section 5.1.2. The p_{T} shape of hadrons is frozen at the moment of the kinetic freeze-out: knowing the temperature T_{kin} at this instant it is possible to calculate the expected p_{T} distribution from the hydrodynamic evolution of the system.

The corresponding process in the early Universe is the Cosmic Microwave Background radiation (CMB) formation. When the universe was cold enough to allow protons and electrons to form neutral atoms, it became no longer able to absorb the thermal radiation. Photons decoupled form the surrounding hadrons and the universe became transparent. Knowing the surface of last scattering (i.e. the temperature at which photon decoupling occurred) it is possible to calculate the temperature (i.e. the p_{T} spectrum) of the CMB today.

– **Elliptic flow.** Heavy-ions are extended object and the system created in central nucleus-nucleus collisions is different from the one created in peripheral collisions. For non head-on collisions, the overlapping region is almond shaped: the pressure gradient is different along the two axes of the system in the transverse plane. These anisotropic pressure gradients give rise to azimuthal anisotropic patterns in the momentum distribution of particles in the final state. Anisotropic transverse flow is the momentum anisotropy with respect to the reaction plane given by this initial geometrical anisotropy. The reaction plane is defined by the impact parameter and the beam direction (Figure 2.12). It is important to stress that the observation of such anisotropy is a sign of multiple interactions between constituents, eventually leading to thermalisation. The invariant triple differential distribution can be expressed using a Fourier expansion as:

$$E\frac{\mathrm{d}^3N}{\mathrm{d}^3\mathbf{p}} = \frac{1}{2\pi}\frac{\mathrm{d}^2N}{p_{\mathrm{T}}\ \mathrm{d}p_{\mathrm{T}}\ \mathrm{d}y}(1 + 2\sum_{n=1}^{\infty} v_n \mathrm{cos}[n(\phi - \psi_{\mathrm{RP}})]) \tag{2.3}$$

were ψ_{RP} is the reaction plane angle. The Fourier coefficients:

$$v_n(p_{\mathrm{T}}, y) =< cos[n(\phi - \psi_{\mathrm{RP}})] > \tag{2.4}$$

are the flow coefficient. In particular v_2 is called elliptic flow and represents the momentum anisotropy between particles emitted along the two axes of the initial

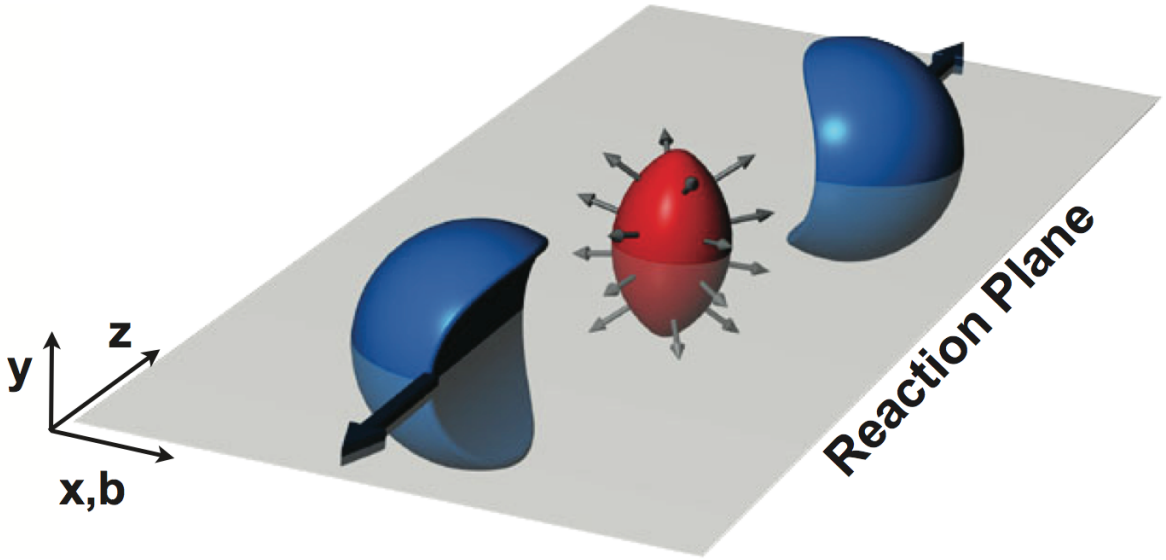

Figure 2.12: Almond shaped interaction volume after a non-central collision of two nuclei. The spatial anisotropy with respect to the x-z plane (reaction plane) translates into a momentum anisotropy of the produced particles (anisotropic flow) [6].

almond shaped system. Figure 2.13 shows the measured integrated elliptic flow as a function of $\sqrt{s_{\mathrm{NN}}}$. The results from the LHC in one centrality bin is compared to results from experiments at lower energies. The elliptic flow is measured to be significantly larger than zero at high enough energy (SPS, RHIC, LHC): this hints to the presence of important multiple interactions between the constituents of the system. Between $2 \lesssim \sqrt{s_{\mathrm{NN}}} \lesssim 4$ GeV, elliptic flow is measured to be < 0. In this energy range the passing time of nuclei and the expansion time of the fireball are comparable. Participant particles are deflected by spectators (spectator shadowing) leading to an out-of-plane preferential emission. Below $\sqrt{s_{\mathrm{NN}}} = 2$ GeV the v_2 value is found to be greater than zero. Collective rotational motion dominates the dynamic of the system, resulting to a in-plane preferential emission of particles.

There is a continuous increase in the elliptic flow from SPS to LHC energies. The v_2 increases by about 30% going from Au–Au collisions at $\sqrt{s_{\mathrm{NN}}} = 200$ GeV to Pb–Pb collisions at $\sqrt{s_{\mathrm{NN}}} = 2.76$ TeV. The elliptic flow is a key measurement to constrain the fundamental properties of the matter created in nucleus-nucleus collisions, in particular the sound velocity and the shear viscosity, but also the initial conditions, i.e. the spatial eccentricity.

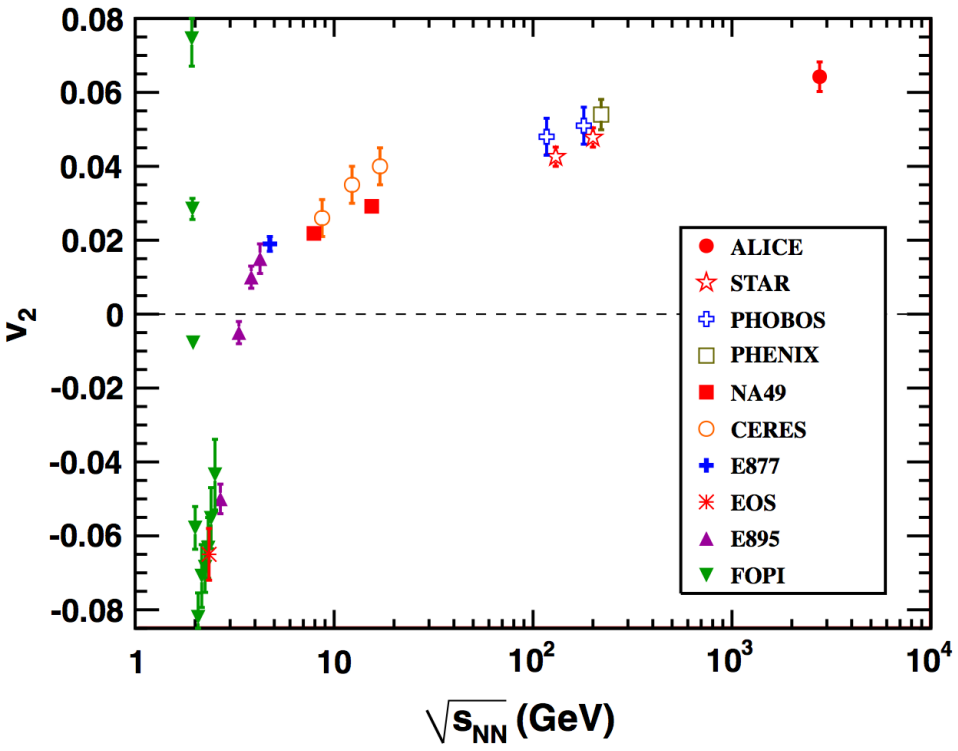

Figure 2.13: Integrated elliptic flow measurement as a function os $\sqrt{s_{\mathrm{NN}}}$. Data for ALICE in $\sqrt{s_{\mathrm{NN}}} = 2.76$ TeV Pb–Pb collisions 20-30% centrality class are compared with results from lower energies taken at similar centralities [24].

Hanbury Brown-Twiss (HBT)

Two particle correlations depend on the average separation of particles at decoupling and therefore provide valuable spatial and temporal information. Two particle momentum correlation between pairs of identical particles are caused by quantum statistical effects. In the case of two identical bosons, for instance pions, this technique is known as Hanbury Brown-Twiss (HBT) interferometry. It is based on the idea that the $\vec{q} = \vec{p_1} - \vec{p_2}$ measurement of identical bosons yields information on the average separation between emitters (HBT radius). The HBT radius $\vec{R}$ can be decomposed into (R_{out}, R_{side}, R_{long}), with the "out" axis pointing along the pair transverse momentum, the "side" axis perpendicular to it in the transverse plane, and the "long" axis along the beam [25]. The beam energy dependence of the HBT radii is reported in Figure 2.14. The HBT radii are measured to increase with the collision energy: this means that the fireball formed in nuclear collisions at higher energies is hotter, lives longer, and expands to a larger size at freeze-out as compared to lower energies. Available model predictions are compared to the experimental data: an hydrodynamic approach is used in AZHYDRO, KRAKOW, and HKM. HRM is an hadronic-kinematics-based model. The increase of the radii between RHIC and the LHC is roughly reproduced by all four calculations, only two of them (KRAKOW and HKM) are able to describe the experimental R_{out}/R_{side} ratio.

2.3 Statistical Hadronisation Model - SHM

The statistical hadronisation or thermal model is based on the idea that multi-particle production in high-energy collisions can be described using statistical concepts. The idea comes from a work of Fermi in 1950 [26], who assumed that particles originated from an excited region evenly occupy all the available phase space states. This was further developed by Hagedorn [27]. The model is based on the assumption that every multi-hadronic state in the system compatible with conservation laws is equally likely [28]. In this sense the phase space density is uniform over the accessible phase space, this is a necessary and sufficient condition for equilibrium. The key function to describe the hadron production is the partition function $Z(T, V)$. For heavy-ion collisions it can be calculated in the grand canonical ensemble, in which the system is in equilibrium with an external reservoir with which exchanges both particles and energy. The partition function for specie i is:

$$\ln Z_i = \frac{V g_i}{2\pi^2} \int_0^\infty \pm p^2 \, \mathrm{d}p \, \ln[1 \pm + e^{-\frac{E_i - \mu_i}{T}}] \tag{2.5}$$

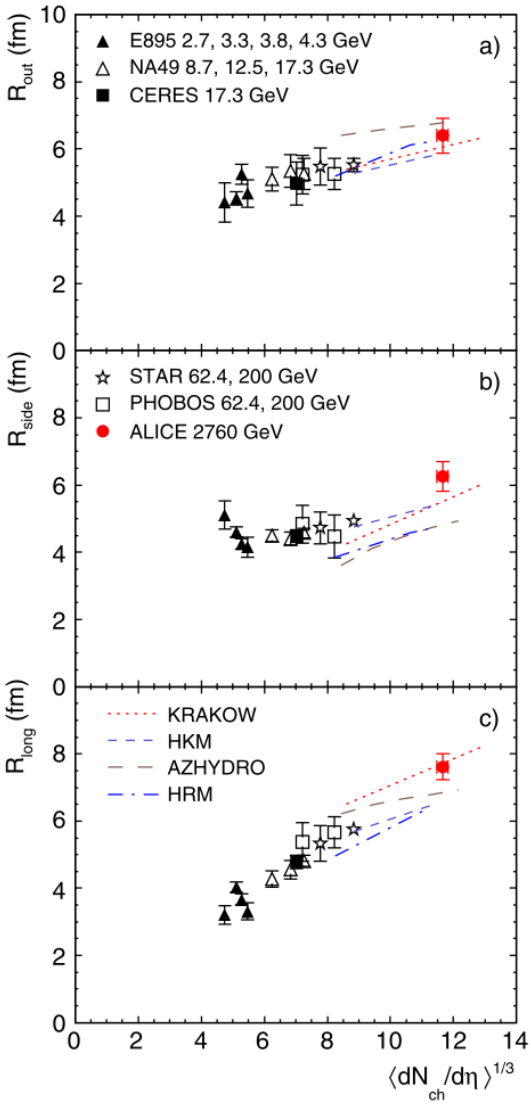

Figure 2.14: Pion HBT radii at $k_T = (|\vec{p}_{\mathrm{T},1} + \vec{p}_{\mathrm{T},2}|)/2 = 0.3$ GeV/c for the 5% most central Pb–Pb at $\sqrt{s_{\mathrm{NN}}} = 2.76$ TeV (red filled dot) and the radii obtained for central gold and lead collisions at lower energies at the AGS, SPS, and RHIC. Model predictions are shown as lines [25].

where $g_i = (2Ji + 1)$ is the spin degeneracy factor, T is the temperature and $E_i = \sqrt{p^2 + m_i^2}$ is the total energy. The + sign is for fermions and - is for bosons. For the hadron specie i the chemical potential μ_i is:

$$\mu_i = \mu_b B_i + \mu_{I_3} I_{3_i} + \mu_S S_i + \mu_C C_i \tag{2.6}$$

where B_i is the baryon number, I_{3_i} the third isospin component and S and C the strangeness and charmness of hadron i. The chemical potentials (μ_b, μ_{I_3}, μ_S and μ_C) ensure the conservation (on average) of the corresponding quantum numbers. Imposing the charge conservation (I_3) and strangeness and charmness conservation ($V \sum_i n_i S_i = 0$ and $V \sum_i n_i C_i = 0$ for heavy-ion collisions) the only remaining parameter is the baryochemical potential μ_B. The density of particle specie i can be calculated from Eq. 2.5 as

$$n_i = \frac{N_i}{V} = -\frac{T}{V}\frac{\partial \ln \mathrm{Z_i}}{\partial \mu} = \frac{g_i}{2\pi^2}\int_0^\infty \frac{p^2 dp}{e^{\frac{E_i - \mu_i}{T}} \pm 1} \tag{2.7}$$

There are only three free parameters: the temperature T, the baryochemical potential μ_B and the volume V.

For small systems (such as peripheral nucleus-nucleus or hadron-hadron collisions) a canonical treatment is mandatory. In these small particle multiplicity environments, conservation laws must be implemented locally on an event-by-event basis (canonical formulation). The canonical formulation is known to severely reduce the phase space available for strange particle production: this is known as canonical suppression. The canonical suppression factor is reported in Figure 2.15 as a function of $\sqrt{s_{\mathrm{NN}}}$ for a canonical volume $V_C = 1000$ fm^3. The ratio $F_S = I_0(x)/I_S(x)$, which corresponds to the ratio between the density calculated in the grand canonical ensemble and in the canonical ensemble $F_S = n_i^{GC}/n_i^C$ is reported for different $\sqrt{s_{\mathrm{NN}}}$. It depends on the strangeness contents of the hadron, being larger for hadrons with larger strangeness content. Above $\sqrt{s_{\mathrm{NN}}} \approx 5$ GeV the particle multiplicity is large enough to allow a grand canonical formulation ($F_S = 1$)

In some models a strangeness suppression factor, γ_S, is used to describe the data. This implies that the thermal density of any given hadron carrying strangeness has a suppression factor γ_S for every strange or antistrange quark. γ_S is meant to account for non-equilibration in the strangeness sector. The dependence of γ_S on $\sqrt{s_{\mathrm{NN}}}$ is reported in Figure 2.16 [29]. It is established that $\gamma_S \approx 1$ for central collisions at RHIC [19]. The strangeness suppression factor γ_S is not used in this work.

At the chemical freeze-out inelastic interactions cease and thermal densities are frozen. Particles are propagated to the final state assuming negligible inelastic interactions which

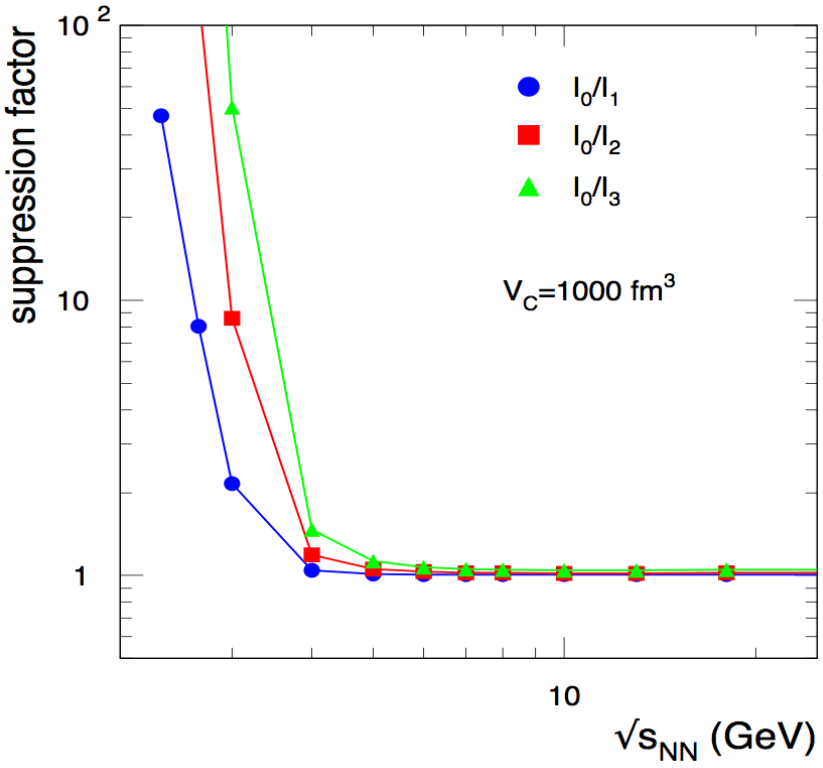

Figure 2.15: The energy dependence of the canonical suppression factor for strangeness, calculated for the canonical volume V_C=1000 fm^3 [19].

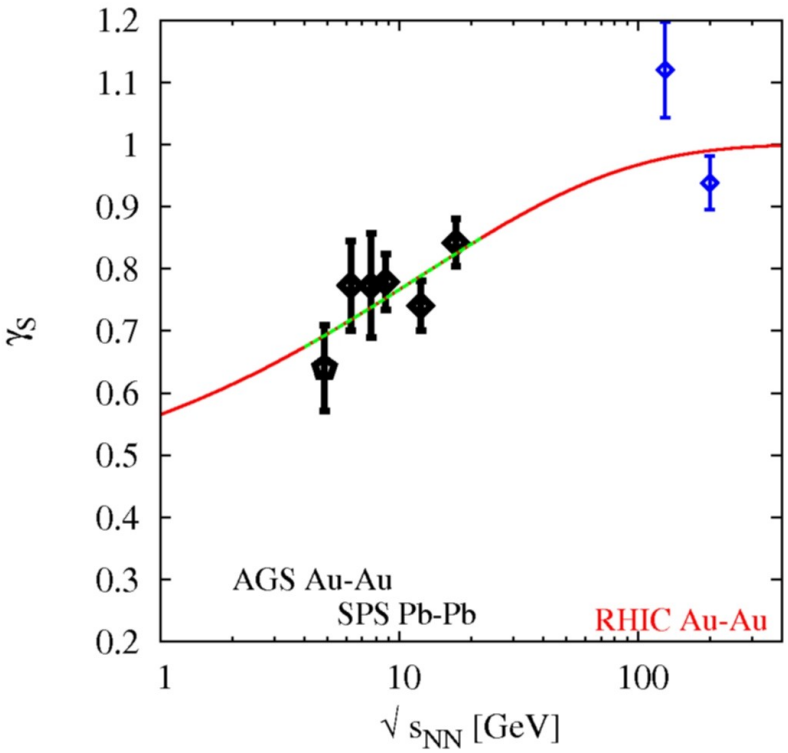

Figure 2.16: γ_S as a function of $\sqrt{s_{\mathrm{NN}}}$ [29].

could change the relative hadron abundances (this will be treated in detail in Chapter 6). Particle multiplicities in the final state have two contributions: the thermal production and the feed-down from heavier particles decaying to lighter hadrons:

$$< N_i > (T, \mu_B, V) =< N_i >^{th} (T, \mu_B, V) + \sum_j \Gamma_{j\to i} < N_j >^{th} (T, \mu_B, V) \tag{2.8}$$

where $\Gamma_{j\to i}$ is the branching ratio for the $j \to i$ decay. The hadron states with the related set of decay channels are implemented in the model according to the PDG compilation [2].

The parameters T_{ch}, μ_B and V are extracted from a fit to the measured integrated yields. The fit is based on a χ^2 minimization procedure:

$$\chi^2 = \sum_i \frac{(N_i^{\text{measured}} - N_i^{\text{model}})^2}{\sigma_i^2} \tag{2.9}$$

It is possible to fit particle ratios instead of yields, in this case the volume V cancels out in the fit leaving only T_{ch} and μ_B as free parameters[3].

The statistical hadronisation model has proved to be very successful in describing the measured multiplicities in nucleus-nucleus interactions over a broad range of energy. The results from previous experiments have been shown in Sec. 2.2.2. The inclusion of the LHC results gives a broader overview of the thermal picture of hadron production: it is the main subject of Chapter 6.

It has been shown [31] that hadron production shows a thermal behaviour also in small systems, such as p–p or e^+– e^- collisions. Calculations for e^+– e^- have to be carried out in the full microcanonical ensemble, including conservation of energy-momentum, angular momentum, parity, isospin, and all relevant charges, including a strangeness suppression parameter $\gamma_S \approx 0.7$. The T_{ch} and γ_S extracted from e^+– e^- collisions are essentially the same obtained with the analysis of inclusive hadronic multiplicities in high energy p–p collisions. This favours the idea that hadronisation is a process occurring at a critical energy density and it uniformly populates the available phase space.

2.4 Hydrodynamics

In the case of high-energy heavy-ion collisions, the fluid under study is a complex system which undergo a phase transition. The corresponding model can be represented as a train:

[3]It is important to stress that this is a perfectly legitimate procedure ONLY if in the ratios all the correlated errors are taken carefully into account [30].

Initial conditions

↓ are the input for the $t_{eq} \approx 0.6$ fm/c

Hydrodynamic evolution of the QGP

↓ which turns at the hadronisation to $t_{ch} \approx 10$ fm/c

Hydrodynamic evolution of a hadron gas

↓ up to the $t_{kin} \approx 15$ fm/c

Kinetic freeze − out

↓ which is the input for the

Particle transport to the detector

In this section the different "wagons" of the hydrodynamic description of heavy-ion collisions are described in detail.

2.4.1 Initial conditions

The incoming nuclei are Lorentz contracted such that the two nuclei pass through each other in a time t_{coll} that is a small faction of fm/c. This collision creates a large energy deposition in a small volume which materialises in thousands of partons which strongly interact. If enough interactions occur, the system may reach a state of local thermodynamic equilibrium. Initial conditions are defined at the thermalisation time t_0. Data from elliptic flow at RHIC energy suggest a very short thermalisation time (in the order of 0.6 fm/c at RHIC energy). Before this moment the system is in a pre-equilibrium stage, in which secondary particles are created and strong interactions lead (rapidly) to thermalisation. Initial condition are mainly calculated using two different approaches:

- The first is based on the model of wounded nucleons with the Glauber geometry [32]. The idea is that nucleus-nucleus collision can be considered as a superposition of binary nucleon-nucleon collisions. The positions of the initial partons are determined according to the nuclear overlapping density within the Glauber geometry using the Woods-Saxon profile.

- An alternative approach is represented by the Colour Glass Condensate (CGC) [33]. The idea is that strong interactions at extremely high energies form a dense condensate of gluons. It is coloured because gluons carry *colour* charge; it behaves like a *glass* which is disordered and is a liquid on long time scales but seems to be a solid on short time scales; is *condensate* because the gluon density is very high. A

general feature of CGC is that initial conditions calculated in such way give larger initial eccentricity than the Glauber-type ones.

A complete set of initial conditions involves the initial energy and baryon density and the three components of the fluid velocity [34]: these represent the starting point for the hydrodynamic evolution of the system.

2.4.2 Hydrodynamic Evolution

Initial conditions provide the input for the hydrodynamic evolution of the system at the thermalisation time t_{eq}. The system is assumed to be in local thermodynamic equilibrium: pressure and temperature vary so slowly that for any point one can assume thermodynamic equilibrium in some neighbourhood about that point. The dynamic of the system is described by the energy-momentum tensor $T^{\mu\nu}$, which for a relativistic fluid can be expressed as:

$$T^{\mu\nu} = (\epsilon + P)u^{\mu}u^{\nu} - Pg^{\mu\nu} \tag{2.10}$$

where:

- ϵ is the energy density $\epsilon \equiv U/V$,
- P is the thermodynamic kinetic pressure $P = \frac{1}{V}\sum_{\vec{p}} p_x v_x e^{-\frac{E_{\vec{p}}+\mu}{T}}$,
- u^{μ} is the 4-velocity,
- $g^{\mu\nu} \equiv \mathrm{diag}(1, -1, -1, -1)$ is the Minkovski metric tensor.

In the energy-momentum tensor:

- T^{00} is the energy density,
- T^{0j} is the j^{th} momentum density component,
- T^{i0} is the energy flux along axis i,
- T^{ij} is the j^{th} momentum flux along axis i.

The conservation equations of energy and momentum in the case of a relativistic inviscid hydrodynamic fluid can be written as:

$$\partial_{\mu} T^{\mu\nu} = 0. \tag{2.11}$$

The hydrodynamic equations of motion can be obtained starting from the conservation laws of energy-momentum (Eq. 2.11) and baryon number:

$$\partial_\mu j_B^\mu = 0 \tag{2.12}$$

where j_B^μ is the baryon number current $j_B^\mu = n_B u^\mu$.

The number of variables is 6 in total: 3 component of the 4-velocity (given the fact that the 4-velocity is a Lorentz scalar $u^\mu u_\mu = 1$), the energy density ϵ, the pressure P and the baryon density n_B. The conservation laws 2.11 and 2.12 give 5 partial differential equations. The system must be closed by the equation of state, which, in the case of hot nuclear matter, comes from QCD.

Inclusion of viscosity

The equations discussed in Sec. 2.4.2 refer to ideal (i.e. inviscid) fluids. The comparison between hydrodynamic and experimental data from elliptic and triangular flow suggests that the average value of the shear viscosity to entropy ratio η/s is small [6, 34] (≈ 0.16 but it depends on the initial conditions). It is interesting to note that this value is not far from the Kovtun-Son-Starinets KSS "conjectured" lower limit. Based on the correspondence with black-hole physics, a universal lower bound on the viscosity to entropy ratio, which might hold for all field theories, has been proposed [34]:

$$\frac{\eta}{s} > \frac{\hbar}{4\pi} \tag{2.13}$$

The energy-momentum tensor 2.10 is modified by the viscosity as:

$$T^{\mu\nu} = (\epsilon + P)u^\mu u^\nu - P g^{\mu\nu} + \pi^{\mu\nu} + \Pi\Delta^{\mu\nu} \tag{2.14}$$

where $\pi^{\mu\nu}$ and $\Pi^{\mu\nu}$ are the stress corrections for shear and bulk viscosity respectively (for a complete treatment of this subject please refer to [35]). A sketch of the effects of shear viscosity in the hydrodynamic evolution of the fireball is reported in Figure 2.17 [36]. The effect of viscosity is to blur the system and reduce the elliptic flow.

2.4.3 Equation of state

The equation of state is the missing piece in order to close the system of equations given by Eq. 2.11 and 2.12. The equation of state $P(\epsilon, n_B)$ can be extracted from lattice QCD calculations: it matches a hadron resonance gas below T_C to an ideal gas of massless

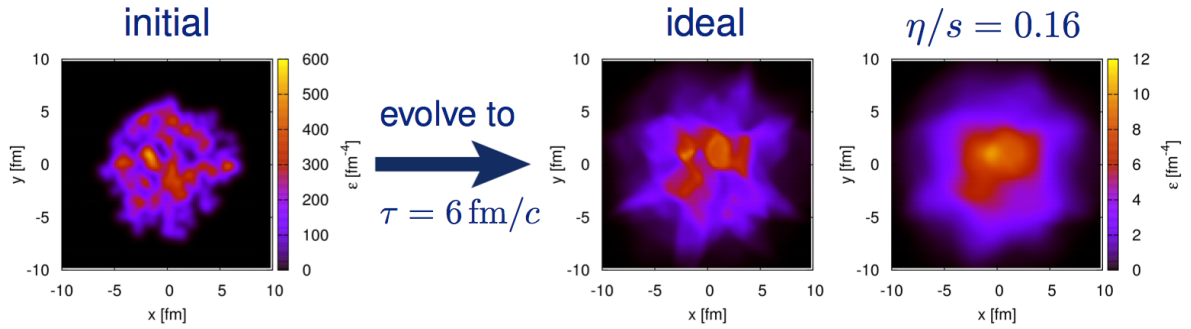

Figure 2.17: The effects of shear viscosity in the hydrodynamic evolution of the fireball [36].

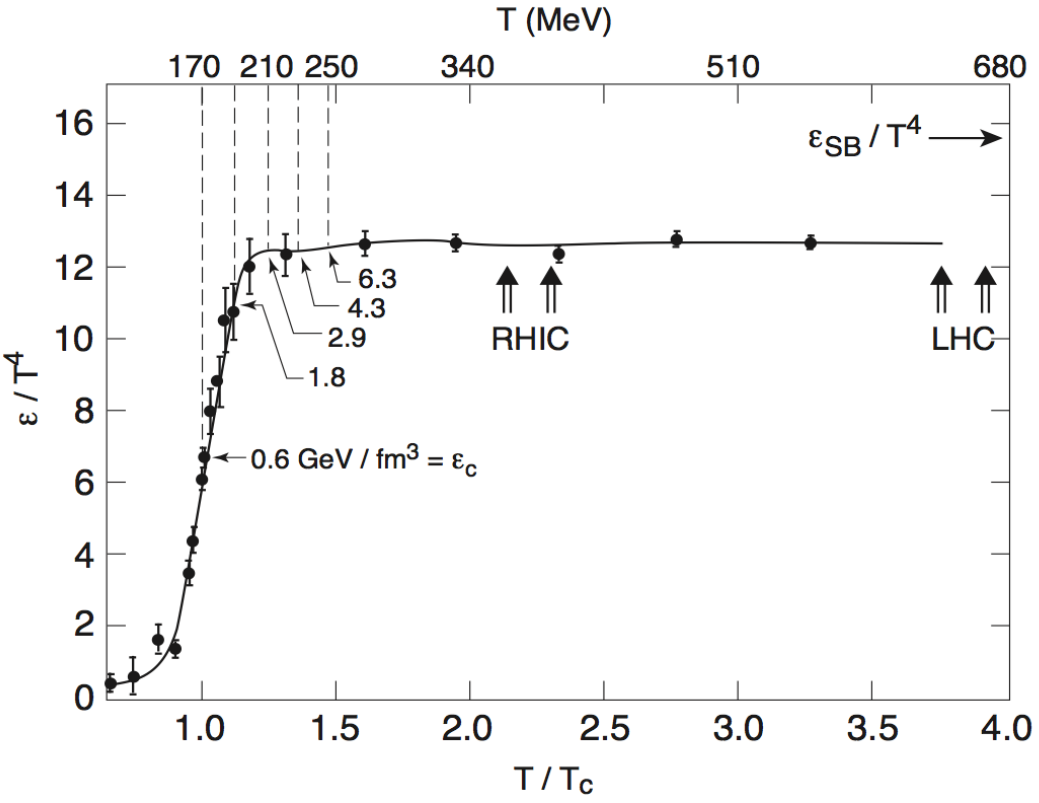

Figure 2.18: Energy density in units of T^4 for QCD with three light dynamical quark flavours. The curve was calculated for three light quark flavours of mass $m_q/T = 0.4$ [8].

quarks and gluons above T_C. The energy density in units of T^4 is reported as a function of T/T_C ($T_C = 173$ MeV) in Figure 2.18[4]. The deconfinement of massive hadrons in almost massless quarks and gluons at T_C is reflected in a sharp increase of the energy density: this reflects the increase of massless degrees of freedom of the system. The Stefan-Boltzmann limit (calculated using the degrees of freedom of hot QCD matter in the Standard Model) is represented by the arrow in the upper-right of the figure. The energy density of the QGP remains $\sim 20\%$ lower than the Stefan-Boltzmann limit. The effect of the hadronisation is the dramatic drop of this ratio occurring at T_C. According to these calculations, the critical energy density for deconfinement is $\epsilon_C \approx 0.6$ - 0.7 GeV/fm^3. The expected initial energy densities at RHIC and LHC are well above this threshold.

It is important to stress that this increase of the number of degrees of freedom at T_C is not an external ingredient of the theory but it is natural in Quantum Chromodynamics. The QCD equation of state allows to close the system given by Eq. 2.11 and 2.12 and makes it possible to solve the equations of motion of the system. The system evolves hydrodynamically and cools down, undergoes the phase transition and reaches the kinetic freeze-out temperature T_{kin}.

2.4.4 Kinetic freeze-out

When the system reaches the kinetic freeze-out temperature T_{kin} the elastic interactions are no longer able to keep the system in equilibrium. The assumption of local thermal equilibrium, necessary to describe the system in terms of hydrodynamics, ceases to be applicable. This decoupling can be implemented in two different ways:

- truncating the hydrodynamic phase abruptly with the Cooper-Frye algorithm,
- switching from hydrodynamics to a hadronic cascade.

Cooper-Frye freeze-out

The description of the transition from hydrodynamic fluid to free particles which reach the detector is usually done using the Cooper-Frye freeze-out picture [37]. In this picture it is assumed that the momentum distribution of the final state particles is essentially the momentum distribution within the fluid, towards the end of the hydrodynamical expansion, and that the fluid consists of independent particles (ideal gas). Fluid is instantaneously converted into free particles at T_{kin} on a three-dimensional hypersurface

[4]This is the results of lattice QCD calculations [8].

$\Sigma(x)$ in the 4-dimensional space-time. The invariant momentum distribution for particle species i can be calculated as:

$$E\frac{dN_i}{d^3p} = \frac{dN_i}{dy\ p_{\mathrm{T}}\ dp_{\mathrm{T}}\ d\phi_p} = \frac{dN_i}{dy\ m_{\mathrm{T}}\ dm_{\mathrm{T}}\ d\phi_p} = \frac{1}{2\pi^3}\int_{\Sigma} p\ d^3\sigma_\mu(x) f_i(x,p) \tag{2.15}$$

where $f_i(x,p)$ is the Lorentz covariant local equilibrium distribution for specie i [34]. This is the Cooper-Frye formula [37]. To compute the measured momentum spectrum one have to shrink the surface Σ to the "surface of last scattering" or "freezeout surface" Σ_{fo}. Particles are then transported to the detector by free-streaming. The multiplicities of each hadronic species after hadronisation is taken from thermal model (Sec. 2.3).

Hadronic cascade

The kinetic freeze-out temperature T_{kin} is estimated[5] to be much lower than the hadronisation temperature ($T_{ch} \approx 170$ MeV). This means that after hadronisation particles keep rescattering for quite a while. Hadronic cascade models can be used to simulate these rescatterings, using everything that is known about hadron masses and cross sections from the Particle Data Tables [2]. After the chemical freeze-out particles are fed to the hadronic cascade model which transport them to the detector. One example is the UrQMD [38] model, in which different resonant processes such as $\pi + N \rightarrow \Delta \rightarrow \pi + N$, $\pi + \pi \rightarrow \rho \rightarrow \pi + \pi, \pi + K \rightarrow K^* \rightarrow \pi + K$ are implemented. Almost all of these resonances have the tendency to decay into the same hadrons from which they were created. The total measured yield is therefore not strongly modified by these processes. However these processes are able to re-equilibrate the hadron momentum distributions to the falling temperature: the hadronic cascade modify the p_{T} shape of the spectrum, as shown in Sec. 5.1.1. More important is the contribution of baryon-antibaryon annihilation during the rescattering stage (e.g. $p + \bar{p} \rightarrow$ several pions) which could significantly modify the final multiplicities of baryon and corresponding antibaryon [39]. The effect of the hadronic cascade is presented in detail in Chapter 6.

Hydrodynamic models are able to reproduce a large number of features of heavy-ion collisions (e.g. particle p_{T} spectra, radial flow, elliptic flow, HBT correlations ...). Hydrodynamics has proved to be very successful in describing soft probes up to RHIC energies. The extrapolation of hydrodynamic models from RHIC to LHC energy has

[5] T_{kin} is estimated from a fit to the particle spectra using hydrodynamics-inspired models (i.e. blast wave). It is described in detail in Sec. 5.1.1

provided predictions consistent with the measurements at the LHC. The results on the radial and elliptic flow at the LHC point to a hydrodynamic behaviour in Pb–Pb collisions at $\sqrt{s_{\mathrm{NN}}} = 2.76$ TeV. The study of the particle p_{T} distribution in terms of hydrodynamics is the main subject of Chapter 5.

3

A Large Ion Collider Experiment - ALICE

The main features of the Large Hadron Collider (LHC) and the ALICE (A Large Ion Collider Experiment) experiment are reported in this Chapter. The offline data processing framework used in ALICE, which includes data simulation and reconstruction, is described.

3.1 The Large Hadron Collider - LHC

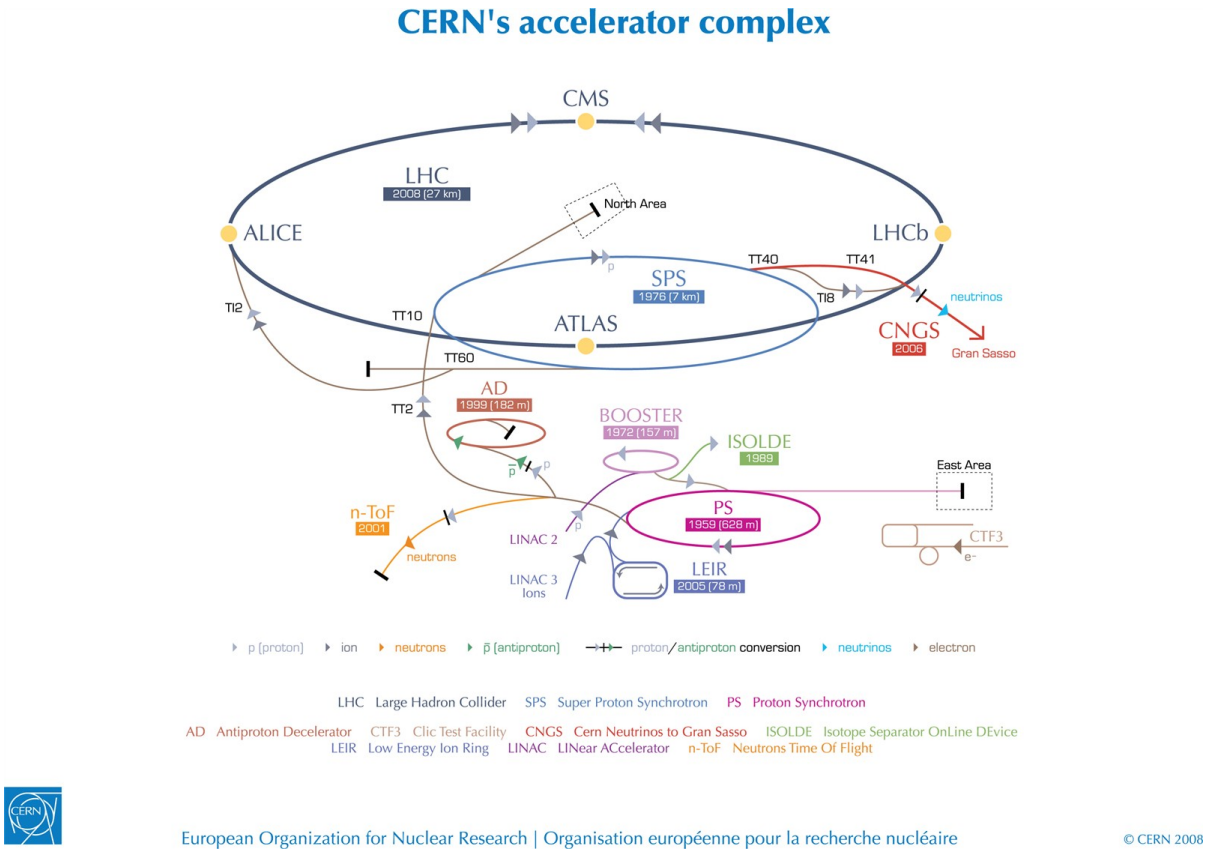

Figure 3.1: The CERN's Accelerator Complex

The Large Hadron Collider (LHC) is the last ring of a complex chain of accelerators built by the European Organisation for Nuclear Research (CERN) [40]. The accelerator complex at CERN is depicted in Figure 3.1. The LHC was built from 1998 to 2009 with the aim of testing the predictions of different theories of particle and high-energy physics. The first p–p collision at the LHC is dated November 23^{rd}, 2009. The LHC lies in a tunnel 27 kilometres in circumference, as deep as 175 metres. The LHC has been designed to collide beams of either protons or nuclei. The nominal energy for p–p collision is $\sqrt{s_{\rm NN}} = 14$ TeV and it is expected to be achieved on late 2014. In terms of luminosity the LHC performance has been outstanding since November 2009. The LHC delivered luminosity, as measured by the ATLAS experiment, is reported in Figure 3.2 [41]. In 2010 the integrated luminosity delivered by the LHC was $\sim 48\ pb^{-1}$ for p–p collisions at $\sqrt{s_{\rm NN}} = 7$ TeV and $\sim 10\ \mu b^{-1}$ for Pb–Pb collisions at $\sqrt{s_{\rm NN}} = 2.76$ TeV. In 2011 the beam energy was the same as in 2010 for both p–p and Pb–Pb. The performance of the

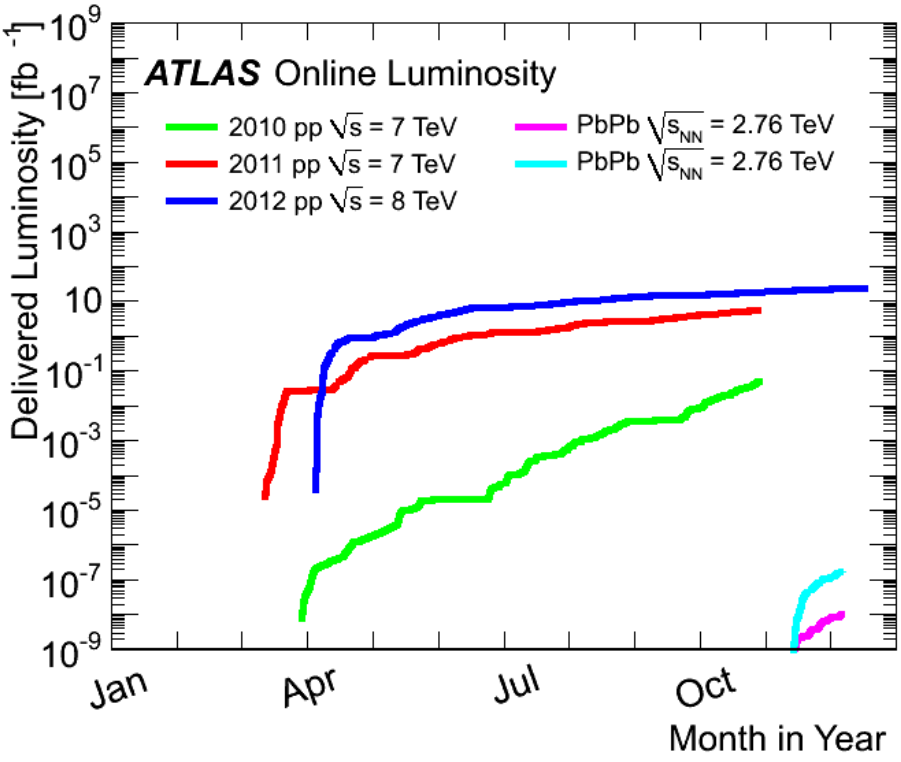

Figure 3.2: Luminosity delivered by the LHC measured by the ATLAS experiment [41].

LHC improved in terms of luminosity with $\sim 5.6\ fb^{-1}$ for p–p collisions and $\sim 143\ \mu b^{-1}$ for Pb–Pb collisions. The 2012 run was even better: the centre-of-mass energy for p–p collisions was brought to 8 TeV and the integrated luminosity (up to October 2012) was $\sim 16.8\ fb^{-1}$. In addition to this LHC provided a p–p run at $\sqrt{s_{\mathrm{NN}}} = 900$ GeV on November 2009, a p–p run at $\sqrt{s_{\mathrm{NN}}} = 2.76$ TeV (the same energy as Pb–Pb) on March 2011 and a pilot p–Pb run at $\sqrt{s_{\mathrm{NN}}} = 5.02$ TeV on September 2012. The p–Pb run is expected before the first long shutdown (LS1) on February 2013.

The p–p program at the LHC is expected to cast new light upon some of the fundamental open questions in physics, in particular regarding the electroweak symmetry breaking, supersymmetry and CP violation. LHC experiments were able to cope with the increasing luminosity delivered by the LHC. One example of the remarkable performance of the LHC is the Higgs search. The observation of a resonance with a mass near 125 GeV was presented for the first time at CERN on July 2012. Only the high luminosity and good quality of the p–p collisions provided by the accelerators have made possible this important observation [42].

The heavy-ion program is devoted to the study of the nature and properties of the

QGP, believed to have existed in the early universe (Sec. 1). The LHC is expected to extend the results obtained by previous experiments at CERN's Super Proton Synchrotron (SPS) and Brookhaven National Laboratory's Relativistic Heavy Ion Collider (RHIC). The heavy-ion program is mainly carried out by the ALICE experiment, which is the only heavy-ion devoted experiment at the LHC. ATLAS and CMS also have a heavy-ion study program.

3.2 A Large Ion Collider Experiment - ALICE

ALICE is the only heavy-ion devoted experiment. It aims at studying the role of chiral symmetry in the generation of hadrons using heavy-ion collisions to attain high-energy densities over large volumes and long time scales. The aim is to gain insight into the physics of parton densities close to phase-space saturation, and their collective dynamical evolution towards hadronisation in a dense nuclear environment. In this way, one also expects to gain further insight into the structure of the QCD phase diagram and the properties of the QGP phase.

3.2.1 Experimental apparatus

The main experimental challenge for a heavy-ion experiment is to cope with the high multiplicity of nucleus-nucleus collisions. The ALICE detectors were designed to cope with multiplicities up to 8000 charged particles per rapidity unit, a value which ensures a comfortable safety margin. The detector acceptance must be sufficiently large to enable the study of the different QGP signatures, presented in Chapter 2. This implies tracking several thousand particles in every event. The tracking system has been designed driven by safe and robust track finding, according to the challenging requirements of the heavy-ion program. The momentum cutoff should be as low as possible. For this reason in addition to the "global" tracking algorithm a dedicated tracking algorithm which uses only the reconstructed clusters in the innermost detector has been developed (Sec. 4.2). Particle identification over a broad p_{T} range is one of the strengths of the ALICE experiment. The forward muon spectrometer is designed to measure the heavy-quark resonances spectrum. Trigger must provide a fast signal to the slower detectors, and be able to reject beam-gas interactions. This is achieved by a set of segmented scintillator counters placed on both sides of the interaction point at large rapidities. The ALICE experiment is depicted in Figure 3.3. A detailed description of the detectors and their performance can be

found in [43–45]. Detectors in the central barrel are embedded in a 0.5 T magnetic field provided by the solenoid magnet previously used in the L3 experiment of the Large Electron-Positron (LEP) collider. A large warm dipole magnet with resistive coils and a horizontal field perpendicular to the beam axis is used for the muon spectrometer. The field integral in the forward direction is 3 Tm.

Central detectors

- **Inner tracking System - ITS.** The ITS is used to localise the primary vertex with a resolution better than 100 μm; to reconstruct the secondary vertices from the decays of hyperons, D and B mesons; to track and identify particles with momentum below 200 MeV/c (Chapter 4); to improve the momentum and angle resolution for particles reconstructed by the Time Projection Chamber (TPC) and to reconstruct particles traversing dead regions of the TPC. It is described in detail in Section 4.1

- **Time Projection Chamber - TPC.** The TPC is the main tracking detector in the central barrel. It provides charged particle momentum measurements with good two-track separation, particle identification, and vertex determination. The pseudorapidity coverage of tracks with full radial track length is $|\eta| < 0.9$. The detector is made of a large cylindrical field cage, filled with 90 m^3 of $Ne/CO_2/N_2$ (90/10/5), in which the primary electrons are transported over a distance of up to 2.5 m on either side of the central electrode to the end plates. Electrons are detected by multi-wire proportional chambers at each end-plate. The position resolution for the inner/outer radii is 1100/800 μm in the transverse plane and 1250/1100 μm along the beam axis. The charge collected at the end plate is proportional to the energy loss of particles in the gas mixture. The corresponding dE/dx resolution is 5% for isolated tracks and 6.8 % in a high-occupancy environment dN/dy = 8000. The dE/dx measurement in the ALICE TPC is reported in Figure 3.4. The TPC allows the identification of hadrons and nuclei over a wide p_{T} range. The relativistic rise at high (> 4 GeV/c) of the dE/dx can also be used to identify π, K and p at high p_{T}.

- **Time Of Flight detector - TOF.** The TOF detector consists of a large area array of Multi-gap Resistive-Plate Chambers (MRPC). It is used for PID in the intermediate momentum range, below about 3 GeV/c for pions and kaons, up to 5 GeV/c for protons. The pseudorapidity coverage is $|\eta| < 0.9$. The TOF has a

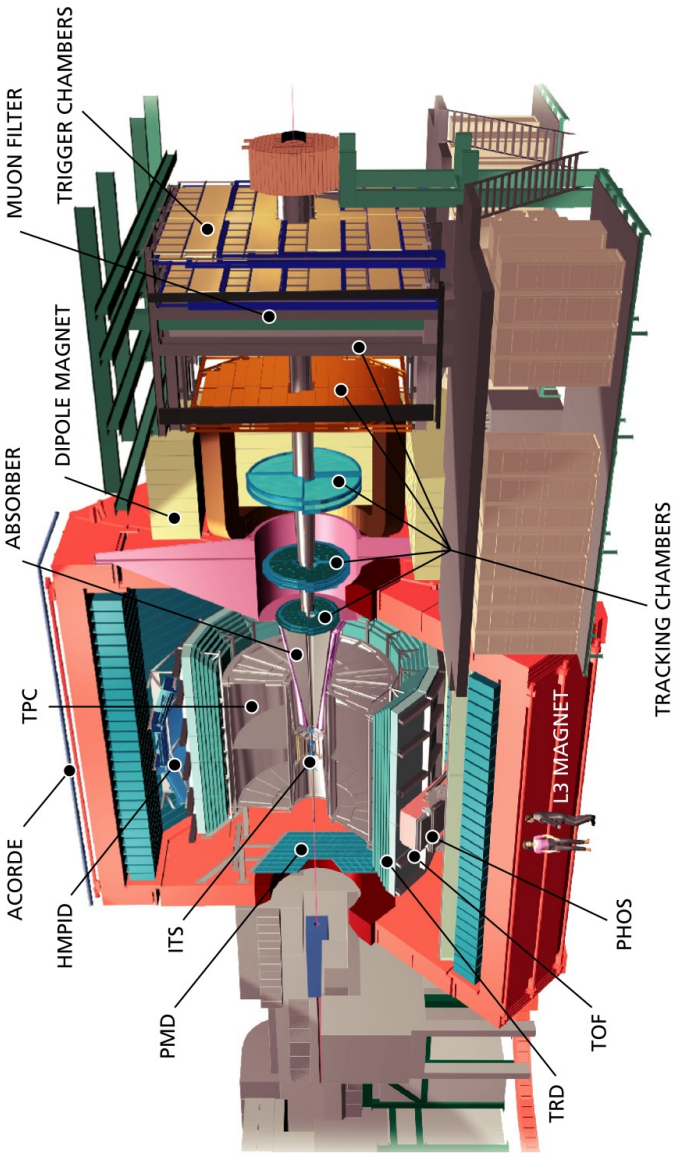

Figure 3.3: A Large Ion Collider Experiment - ALICE

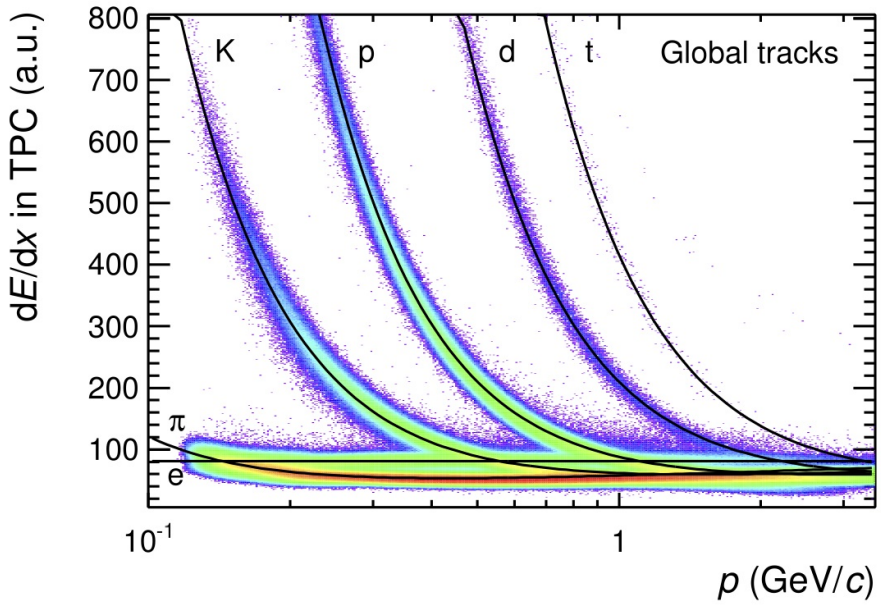

Figure 3.4: $\mathrm{d}E/\mathrm{d}x$ measurement in the ALICE TPC.

modular structure corresponding to 18 sectors in ϕ and to 5 segments in z direction. The whole device is inscribed in a cylindrical shell with an internal radius of 370 cm and an external one of 399 cm. The whole device thickness corresponds to 30% of a radiation length. The $\beta - p$ TOF performance plot for the 2011 Pb–Pb run is reported in Figure 3.5.

– **Transition Radiation detector - TRD.** The main purpose of the TRD is to provide electron identification in the central barrel for momenta above 1 GeV/c. It consists of 540 individual readout detector modules. It is positioned at $2.9 < r < 3.68$ m and the nominal pseudorapidity coverage is $|\eta| < 0.84$. During the data taking in 2010 (used in this work) the TRD was not fully installed. The completion of the TRD installation is expected for the LHC Long Shutdown 1 (2013 - 2014).

– **High-Momentum Particle IDentification detector - HMPID.** The aim of the HMPID is to enhance the PID capability of the ITS, TPC and TOF at high p_{T}. The HMPID was designed as a single-arm array with an acceptance of 5% of the central barrel phase space. It is based on proximity-focusing Ring Imaging Cherenkov (RICH) counters and composed of seven modules. The HMPID covers the η, ϕ range $|\eta| < 0.6$ and $1.2° < \phi < 58.8°$.

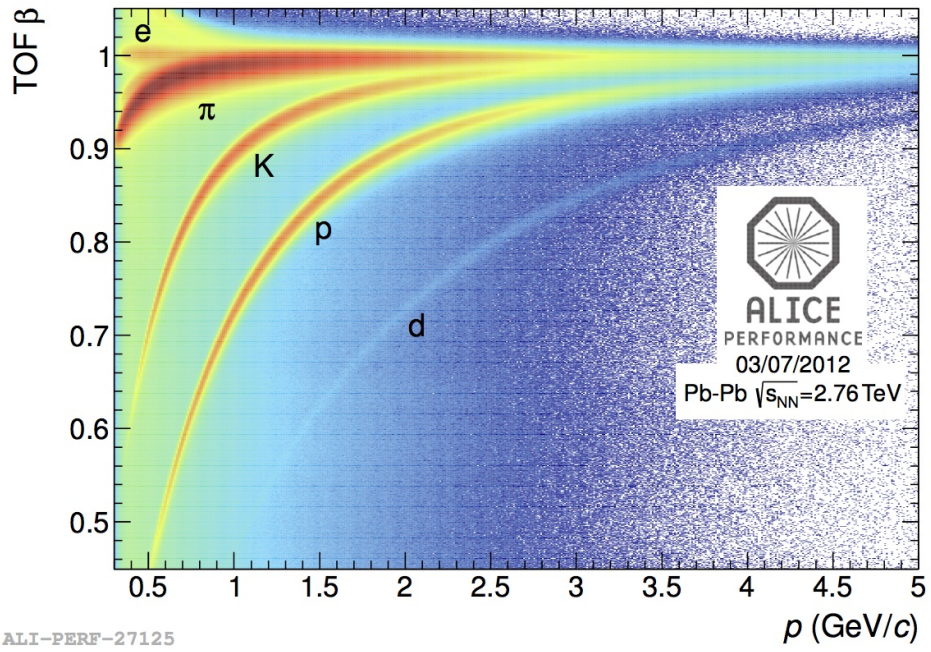

Figure 3.5: TOF $\beta - p$ performance plot in the 2011 Pb–Pb run.

– **PHOton Spectrometer - PHOS.** The PHOS allows the measurement of direct photon and the study of jet quenching through the measurement of high p_{T} π^0 and γ-jet correlations. It is a high-resolution electromagnetic spectrometer covering a limited acceptance domain at central rapidity ($|\eta| < 0.12$ and $220° < \phi < 320°$).

– **ElectroMagnetic Calorimeter - EMCal.** The study of jet quenching is further substained by the EMCal. It covers $|\eta| \leq 0.7$ and $\Delta\phi = 107°$, and is positioned approximately opposite in azimuth to the PHOS.

– **ALICE COsmic Ray DEtector - ACORDE.** ACORDE is the ALICE cosmic ray detector. It is an array of plastic scintillator counters placed on the upper surface of the L3 magnet. It consists of an array of scintillator counters covering $|\eta| \leq 1.4$ and $-60° < \phi < 60°$.

The PID performance of the central barrel detectors is reported in Figure 3.6. The separation power between π-K (K-p) is reported for each detector in the upper left (right) panel of the figure. The p_{T} ranges in which the separation is $> 2\ \sigma$ are reported in the bottom panels.

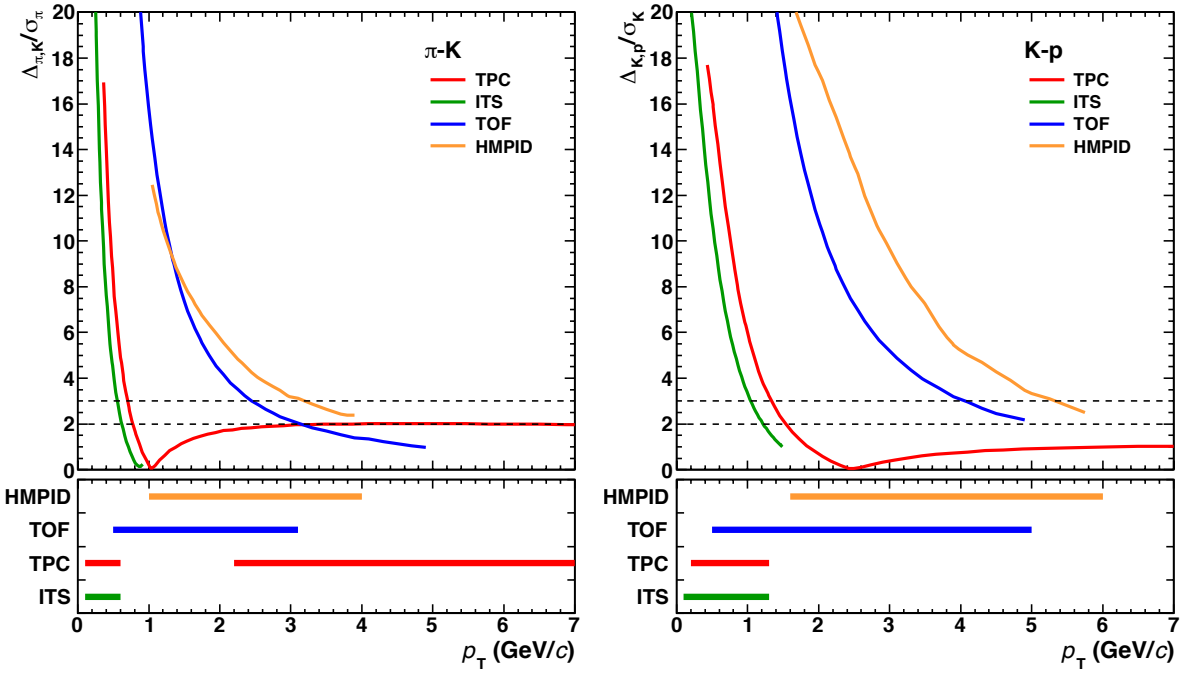

Figure 3.6: Upper left (right) panel: separation power between π-K (K-p). The p_{T} ranges in which the separation is $> 2\ \sigma$ are reported in the bottom panels.

Muon spectrometer

Muon detection is performed in the pseudorapidity region $4.0 < \ \eta \ < 2.5$ by the muon spectrometer. It allows the measurement of the complete spectrum of heavy-quark vector-mesons resonances, as well as the ϕ meson, through their $\mu^+\mu^-$ decay channel. The spectrometer consists of the following components: a passive front absorber to absorb hadrons and photons from the interaction vertex; a high-granularity tracking system of 10 detection planes; a large dipole magnet; a passive muon-filter wall, followed by four planes of trigger chambers; an inner beam shield to protect the chambers from primary and secondary particles produced at large rapidities.

The front absorber, whose length is 4.13 m (10 λ_{int}, 60 X_0), is located inside the solenoid magnet. The fiducial volume of the absorber is made predominantly out of carbon and concrete to limit small-angle scattering and energy loss by traversing muons.

Tracking is performed using cathode pad chambers. The tracking chambers were designed to achieve a spatial resolution of about 100 μm. They are arranged in five stations: two are placed before, one inside and two after the dipole magnet.

The trigger system consists of four Resistive Plate Chamber RPC planes arranged in two stations, one metre apart from each other, placed behind the muon filter.

Forward detectors

- **Zero Degree Calorimeter - ZDC.** ZDC consists of two sets of hadronic ZDCs are located at 116 m on either side of the Interaction Point (IP). In addition, two small electromagnetic calorimeters (ZEM) are placed at about 7 m from the IP, on both sides of the LHC beam pipe, opposite to the muon arm. Spectator nucleons can be measured by the ZDC. It can be also used as a position-sensitive detector, which can give an estimate of the reaction plane in nuclear collisions.

- **Photon Multiplicity Detector - PMD.** The measurement of photon multiplicity gives important information in terms of limiting fragmentation, order of phase transition, the equation of state of matter and the formation of disoriented chiral condensates. The PMD consists of a large array of gas proportional counters in a honeycomb cellular structure. It covers the pseudorapidity range $2.3 < \eta < 3.7$.

- **Forward Multiplicity Detector - FMD.** The FMD provides charged particle multiplicity information in the pseudorapidity range $-3.4 < \eta < -1.7$ and $1.7 < \eta < 5.0$. It is composed of three rings of silicon strips sensors placed at 320, 75.2 and -62.8 cm from the IP respectively.

- **VZERO detector - VZERO.** The V0 detector is a small angle detector consisting of two arrays of scintillator counters, called V0A and V0C, which are installed on either side of the ALICE interaction point. V0A detector is located 340 cm from the vertex on the side opposite to the muon spectrometer whereas V0C is fixed to the front face of the hadronic absorber, 90 cm from the vertex. They cover the pseudo-rapidity ranges $2.8 < \eta < 5.1$ (V0A) and $-3.7 < \eta < -1.7$ (V0C) and are segmented into 32 individual counters each distributed in four rings.

  The VZERO is used for different purposes.

  - It provides minimum-bias triggers for the central barrel detectors.
  - The centrality of the collisions can be estimated via the multiplicity recorded in the event. It is evaluated from a Glauber fit to the distribution of the summed amplitudes in the VZERO scintillator tiles (Figure 3.7).
  - It is used to reject background events.
  - As described in Section 5.2 it can be used to calculate the flow vector $\vec{Q}_2$ on an event-by-event basis.

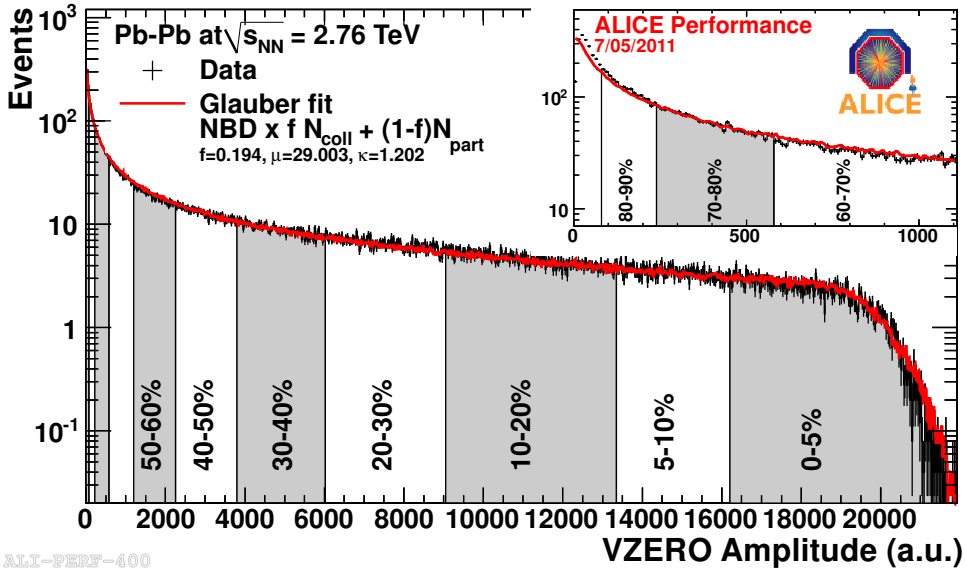

Figure 3.7: Distribution of the summed amplitudes in the VZERO scintillator tiles (histogram); inset shows the low amplitude part of the distribution. The curve shows the result of the Glauber model fit to the measurement. The vertical lines separate the centrality classes.

– **T0 detector - T0.** The T0 detector is used to generate a start time (T0) for the TOF detector, to measure the vertex position (with a precision ± 1.5 cm) for each interaction and to provide a L0 trigger when the position is within the preset values. The detector consists of two arrays of Cherenkov counters placed at -72.7 cm and 375 cm from the nominal interaction point. The corresponding pseudorapidity range is -3.28 < η < -2.97 and 4.61 < η < 4.92.

3.2.2 ALICE offline framework

The ALICE Offline Project started developing the software framework in 1998 [46]. The ALICE computing framework is used to:

– simulate the primary pp and heavy-ion interactions and the resulting detector response,

– reconstruct and analyse the data coming from simulated and real interactions.

The AliRoot framework is based on Object-Oriented technology and depends on the ROOT framework [47]. ROOT is written in C++ and offers integrated I/O with class schema evolution, an efficient hierarchical object store with a complete set of object

containers, a C++ interpreter allowing one to use C++ as scripting language. The data processing framework is shown schematically depicted in Figure 3.8.

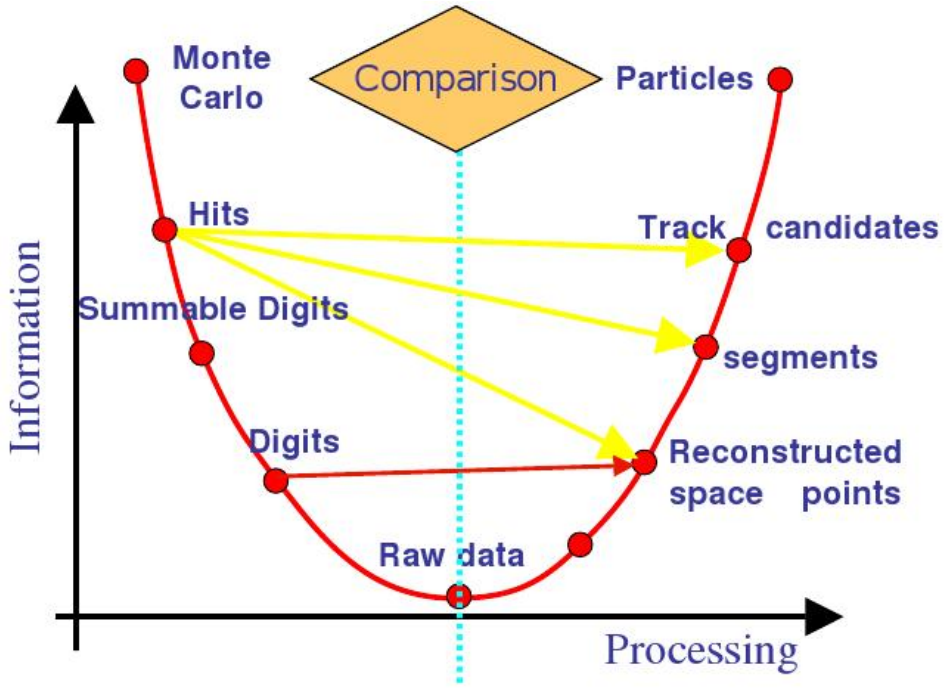

Figure 3.8: Data processing framework.

Simulation

The whole simulation process, represented by the left part of the parabolic path in Figure 3.8, includes the following steps:

- **Event generation of final-state particles.** An event generator produces a set of particles with their momenta, origin point and identity. This set of particles, where one maintains the production history (in form of mother-daughter relationship and production vertex), forms the kinematic tree. The collision is simulated by a physics generator code like PYTHIA [48], HIJING [49] or a parameterisation (with the class `AliGenParam`) of the kinematical variables. Final state particles are fed to the transport program.

- **Particle transport.** Particles emerging from the interaction of the beam particles are transported through the detector material, simulating their interaction with it, and the energy deposition that generates the detector response (*hits*). Hits contain

also information ("track labels") about the particles that have generated them. The main models used to transport generated particles through the detector are GEANT [50] and FLUKA [51].

– **Signal generation and detector response.** During this phase the detector response is generated from the energy deposition of the particles traversing it. This is the ideal detector response, before the conversion to digital signal and the formatting of the front-end electronics is applied. The detector response is proportional to the particle energy loss. There is one main exception, namely the calorimeter (PHOS and EMCAL) hits, where a hit is the energy deposition in the whole detecting element volume. This happens because inside these detectors the particle is completely stopped.

– **Digitisation.** The detector response is digitised and formatted according to the output of the front-end electronics and the data acquisition system. The results should resemble closely the real data that is produced by the detector. Furthermore in some detectors digits are used for comparison with a given threshold, for example in TOF and ITS pixel layers. These are in fact "digital" detector in the sense that they are requested only for an on-off response, depending on the threshold overcoming. There are two types of digits: *summable digits*, where low thresholds are used, in order to preserve the possibility to add signals from other particles (event merging), and *digits*, where real thresholds are used, and the result is similar to what one would get in the real data taking. In some sense the *summable digits* are precursors of the *digits*. The noise simulation is activated when *digits* are produced. There are two differences between the *digits* and the *raw* data format produced by the detector: firstly, the information about the Monte Carlo particle generating the *digit* is kept, and secondly, the *raw* data are stored in binary format (like the detector data) while the *digits* are stored in ROOT classes. Two conversion chains are provided in AliRoot: *hits* $\rightarrow$ *summable digits* $\rightarrow$ *digits*, and *hits* $\rightarrow$ *digits*. Summable digits are used for the so called "event merging", where a signal event is embedded in a signal-free underlying event. This technique is widely used in heavy-ion physics and allows to reuse the underlying events with substantial economy of computing resources. Optionally it is possible to perform the conversion *digits* $\rightarrow$ *raw data*, which is used to estimate the expected data size, to evaluate the high level trigger algorithms, and to carry on the so called computing data challenges. The `AliSimulation` class provides a simple user interface to the simulation framework.

Reconstruction

Most of the ALICE detectors are tracking detectors. Each charged particle going through them leaves a number of discrete signals that measure the position of the points in space where it has passed. The task of the reconstruction algorithms is to assign these space points to tracks and to reconstruct their kinematics. This operation is called *track finding*. In ALICE it is required a good track-finding efficiency for tracks down to $p_{\mathrm{T}} = 100$ MeV/c even at the highest track density. Given this situation, most of the development is done for Pb–Pb central events, since lower multiplicities are considered an easier problem once the high-multiplicity ones can be handled. However, the opposite may be true for some quantities, such as the main vertex position, where a high track multiplicity will help to reduce the statistical error. Track reconstruction is represented by the right part of the parabolic path in Figure 3.8. The reconstruction steps are:

- **Raw data.** This is a digitised signal (ADC count) obtained by a sensitive pad of a detector at a certain time.

- **Rec Points.** Reconstructed space points: this is the measurement of the position where a particle crossed the sensitive element of a detector (often, this is done by calculating the centre of gravity of the "cluster", which is a group of contiguous cells with signals above applied threshold).

- **Tracks.** Reconstructed tracks: this is a set of five parameters (the curvature, two angles with respect to the coordinate axes, two positions) of the trajectory of particles together with the corresponding covariance matrix estimated at a given point in space and the information of the detector in which reconstruction occurred.

This procedure is used for both real and simulated data. The input to the reconstruction framework are digits in ROOT `TTree` format or raw data. First a local reconstruction of clusters/rec points is performed in each detector. The vertex position is firstly estimated using rec points in the SPD. Tracks are reconstructed, particle types are identified and the production vertex is calculated using tracks. The output of the reconstruction is the Event Summary Data (ESD), which is an array of AliESDtracks, an AliRoot class object. The `AliReconstruction` class provides a simple user interface to the reconstruction framework. The size of the ESD is about one order of magnitude lower than the corresponding raw data. The analysis tasks produce Analysis Object Data (AOD) specific to a given set of physics objectives.

Distributed computing and the Grid

The amount of computing resources necessary to store and process the data generated by the experiment is huge. To cope with this request a distributed computing is necessary. The way it is implemented is depicted in Figure 3.9. It is based on a hierarchy of centres

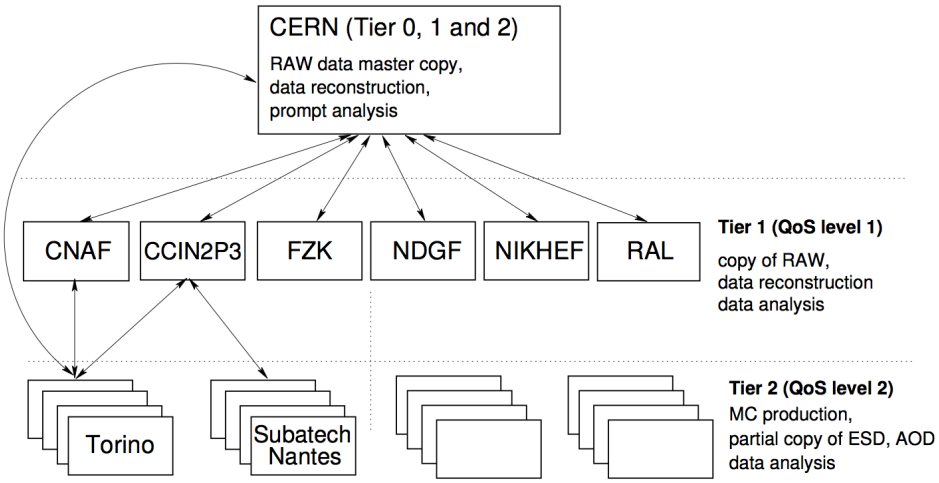

Figure 3.9: Schematic view of the ALICE offline computing tasks in the framework of the tiered model [46].

called Tiers, where Tier 0 is CERN, Tier 1s are the major computing centres which provide a safe data storage, likely in the form of a mass storage system, Tier 2s are smaller regional computing centres. The basic principle underlying the ALICE computing model is that every physicist should have equal access to the data and the computing resources necessary for its processing and analysis. The AliEn (ALIce Environment) framework [52] has been developed with the aim of offering to the ALICE user community a transparent access to computing resources distributed worldwide through a single interface.

3.2.3 The ALICE Collaboration

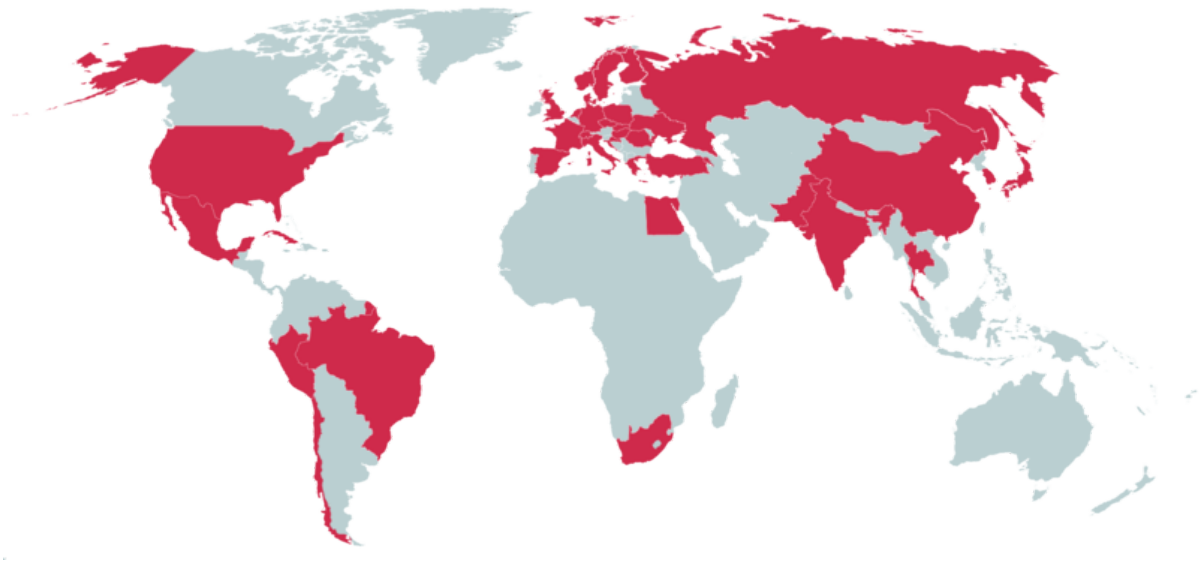

36 Countries - **132** Institutes - **1200** Members

4

Particle Identification in the ALICE ITS

In this Chapter a comprehensive overview of the Particle IDentification (PID) in the ALICE Inner Tracking System (ITS) is reported. It includes a description of:

- **The ITS detector** (Sec. 4.1). The features of the detector are reported in detail, focusing mainly on PID and tracking. Part of my Ph.D. activity was devoted to the calibration and maintenance of the SDD detector.
- **The ITS tracking algorithm** (Sec. 4.2). The procedure used to reconstruct tracks in the ITS is described, together with its performance.
- **The PID signal in the ITS** (Sec. 4.3). The PID calibration of the SDD detector is reported. The procedure used to parameterise the expected energy loss for different particles and the measured $\mathrm{d}E/\mathrm{d}x$ resolution are presented.
- **The PID analysis** (Sec. 4.4). All the steps needed to measure the p_{T} distributions of identified primary particles are reported in detail. The analysis is described in the specific case of the ITS but it can be easily generalised to other detectors. The comparison with other analyses is reported both for p–p and Pb–Pb collisions.

4.1 The ALICE Inner Tracking System (ITS)

The ALICE Inner Tracking System (ITS), depicted in Figure 4.1, is the central barrel detector closest to the beam axis. It is composed of six cylindrical layers of silicon detectors. The two innermost layers are equipped with pixel detectors (SPD), followed by two

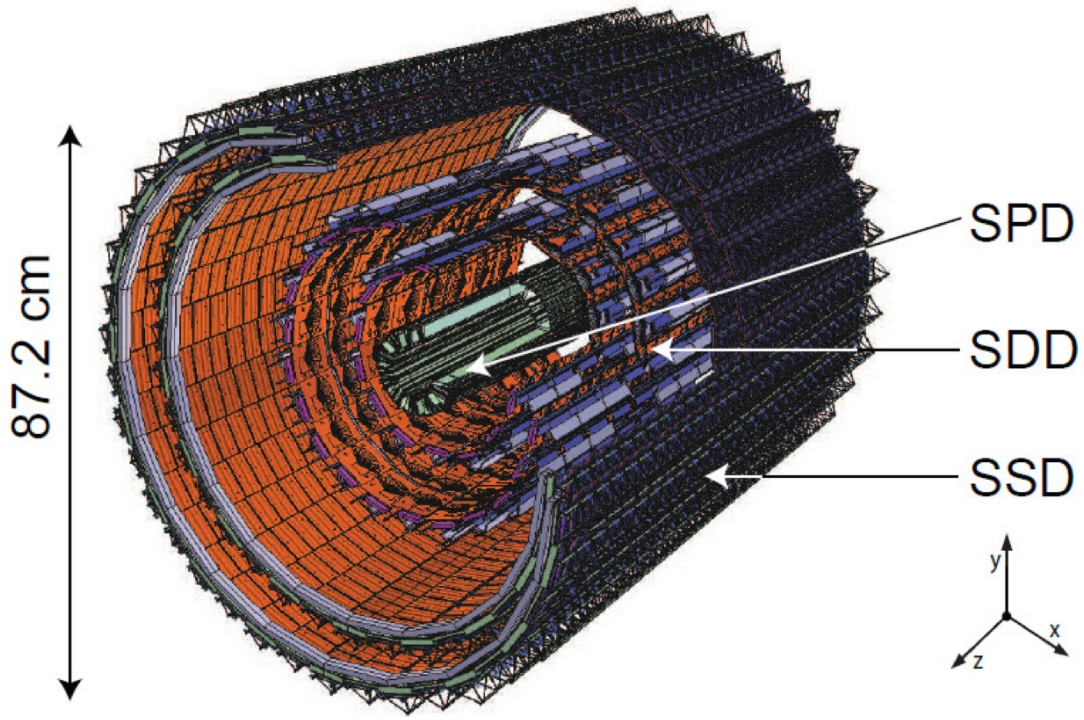

Figure 4.1: The ALICE Inner Tracking System (ITS)

layers of drift detectors (SDD) and two layers of double-sided strip detectors (SSD). The four layers equipped with SDD and SSD also provide a measurement of the specific energy loss $\mathrm{d}E/\mathrm{d}x$. The ITS is also used as a standalone tracker to reconstruct charged particles that are deflected or decay before reaching the Time Projection Chamber (TPC), and to recover tracks crossing dead regions of the TPC. The ITS has been designed to keep good tracking efficiency in a high multiplicity environment, as that produced in Pb–Pb collisions at the nominal LHC energy where some models predicted up to 8000 charged particles per rapidity unit at the time of the ALICE design. The ITS performance is crucial to provide high spatial resolution (better than 100 μm) on the primary vertex of the collision, on the secondary vertices (like those from heavy flavor decays) and on the track impact parameter. Moreover the ITS allows the improvement of the momentum resolution of the TPC. To reduce multiple scattering effects, the volumes and the effective thickness of the ITS detectors and services (cabling and cooling) have been kept as small

as possible. The total amount of radiation length for the full ITS is less than 8% X/X_0 for particles at $\eta = 0$. The percentage of radiation length as a function of the radius is shown in Figure 4.2. The layer dimensions along the beam axis, reported in Table 4.1, allow to

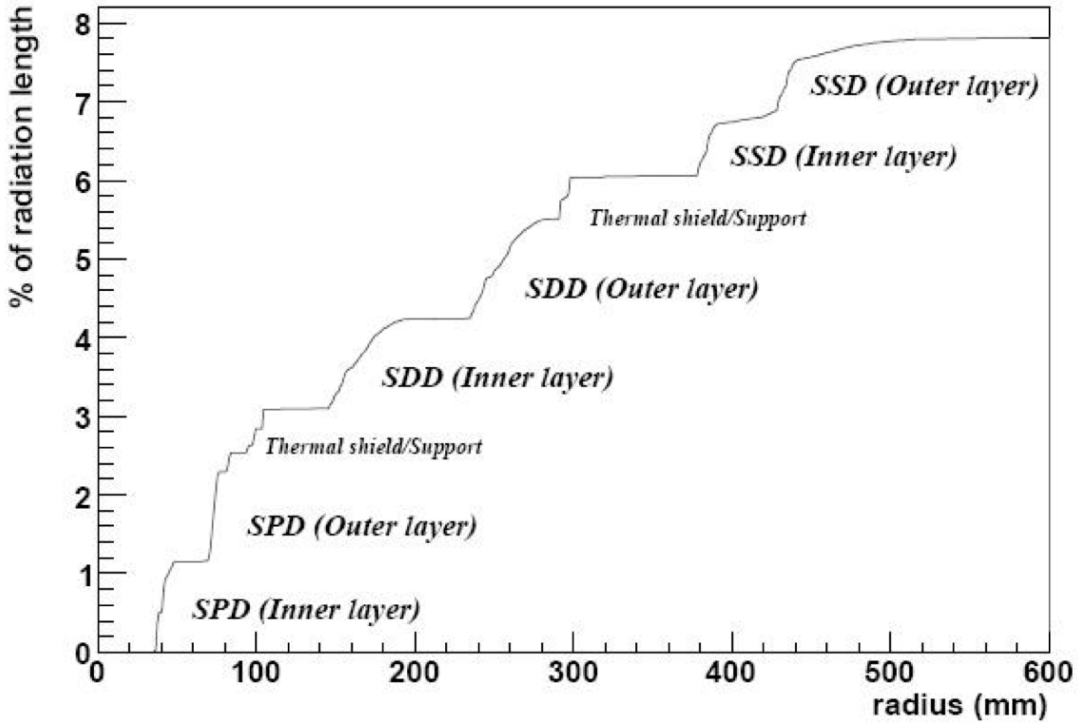

Figure 4.2: Material budget in the ALICE Inner Tracking System (ITS).

cover a pseudo-rapidity range of $|\eta| < 0.9$ for all vertices located within the length of the interaction diamond.

4.1.1 Silicon Pixel Detector (SPD)

The Silicon Pixel Detector (SPD), depicted in Figure 4.3, is the innermost detector of the ALICE experiment. It consists of two cylindrical layers of hybrid silicon pixel detectors located at radii of 3.9 cm and 7.6 cm respectively. The SPD is required to have low material budget, high spatial precision, high double-track resolution and capability to work (with low occupancy) in the high multiplicity environment of the most central Pb–Pb collisions. The two layers cover the pseudo-rapidity ranges $|\eta| \leq 2$ (inner layer) and $|\eta| \leq 1.4$ (outer layer) respectively, for particles originating at the centre of the detector. The SPD also provides a prompt trigger signal, called fast-OR, which can contribute to the experimental L0 trigger decision [53]. The total thickness of the SPD amounts to about

Layer	Type	r (cm)	± z (cm)	Active Area (m^2)
1	Pixels	3.9	14.1	0.07
2	Pixels	7.6	14.1	0.14
3	Drift	15.0	22.2	0.42
4	Drift	23.9	29.7	0.89
5	Strips	37.8	43.1	2.09
6	Strips	42.8	48.9	2.68

Table 4.1: The ALICE Inner Tracking System (ITS) layer dimensions.

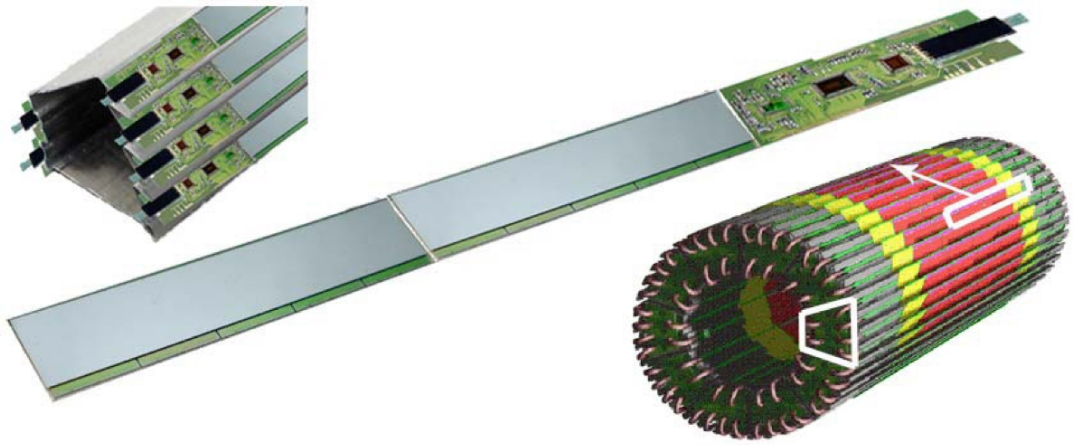

Figure 4.3: The ALICE Silicon Pixel Detector (SPD) layout (bottom right image), and two details.

2.3 % of a radiation length including the sensitive volumes, the electronics, services and supports. The SPD detector provides a binary information for each pixel. The half-stave (HS) is the independent modular unit of the pixel detector. The full detector is composed of 120 HS. The size of a single pixel cell is 50 μm in the rϕ direction and 425 μm in the z direction. Each front-end chip has 8192 channels of pixels arranged in a matrix of 32 columns and 256 rows. The SPD contains 1200 readout chips and about 10^7 pixels. The spatial resolution of the SPD is determined by the cell size, by the track angle with respect to the cell orientation and by the detector thresholds applied in the readout. The SPD can achieve a resolution of 12 μm in the transverse plane and 100 μm along the beam axis.

4.1.2 Silicon Drift Detector (SDD)

The Silicon Drift Detectors (SDDs) were proposed in the early eighties by Gatti and Rehak [54], but they have still a moderate employment in physics experiments. The basic idea is to use the time necessary to electrons produced by ionization of crossing particles to drift to the collecting anodes, as shown in Figure 4.4. An adequate electrostatic field

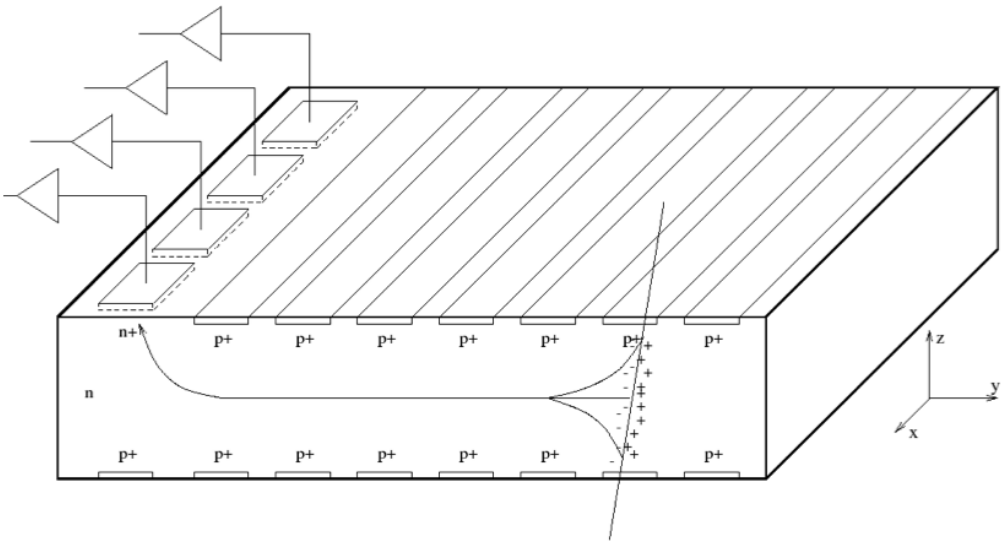

Figure 4.4: Operating principle of a Silicon Drift Detector.

has to be applied in order to generate the drift field. The advantage of this detector is the high 2D resolution with limited number of read-out channels and the low material budget. The high-granularity and the good multi-track capability make the SDDs adapt to the high multiplicity environment of heavy-ion collisions at the LHC.

The ALICE SDD detector

The SDD detectors equip the two intermediate layers of the ALICE ITS. The ALICE SDD modules are produced from 300 μm thick silicon wafers characterised by a good doping homogeneity (5%) and high resistivity (3 kΩcm). The SDD operational module, depicted in Figure 4.5, has a sensitive area of 7.017 $\times$ 7.526 cm^2, corresponding to 88% of the total detector area. The central cathode divides the active area in two independent drift regions. Each drift region has 256 collection anodes with 294 μm pitch and 291 p$^+$ cathode strips with 120 μm pitch (on both sides of the detector). The drift field is obtained by gradually scaling down the high voltage HV applied from the central cathode towards the anodes. This is performed by the voltage divider located on the detector sides,

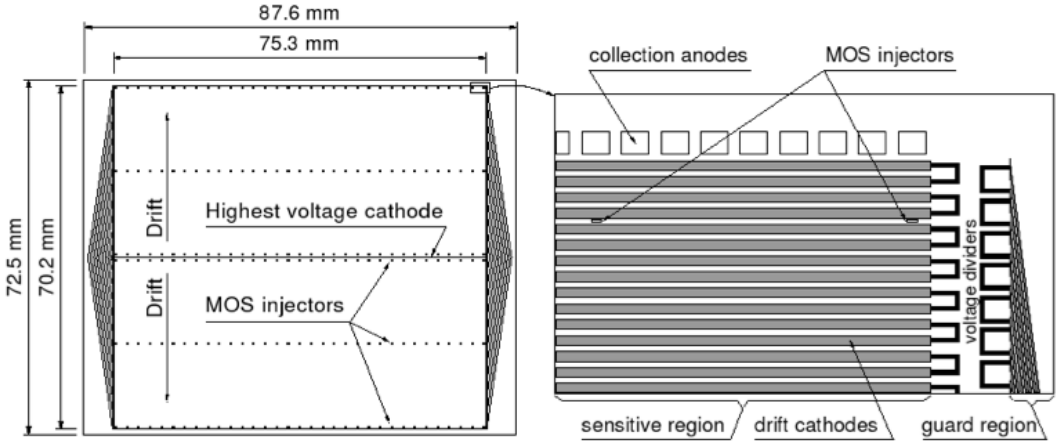

Figure 4.5: The ALICE SDD module.

see Fig. 4.5. An external medium voltage MV is applied at the other side of the voltage divider, close to the anodes, in order to ensure the sensor depletion in the collection region. The drift speed is sensitive to the temperature: three rows of MOS injectors are placed at 3.225, 17.625 and 34.425 mm from the anodes in order to measure the drift speed. The SDD modules are mounted on linear structures called ladders. There are 14 (22) ladders in the inner (outer) layer with 6 (8) modules each, resulting in 260 modules in total. The maximum drift time is ~ 5.5 μs, the read-out time is ~ 1023 μs. The SDD detector can achieve a spatial resolution of 35 μm along the drift direction and 25 μm on the anode coordinate. The ALICE experiment is able to guarantee a good stability of the running conditions, as can be observed in Figure 4.6 where the drift speed measurement from the MOS injectors is reported for the 2011 Pb–Pb run for four selected modules. The dotted lines represent 1 ‰ variation with respect to the mean. The detector is calibrated each time the LHC provides stable beams with collisions, in order to take into account the (small) variation of the experimental running conditions.

The SDD is not only a tracking detector but it is also used to identify particles. The charge collected at the anodes is proportional to the particle energy loss in the silicon. The offline calibration of the $\mathrm{d}E/\mathrm{d}x$ signal includes the correction for charge diffusion along the drift coordinate and the conversion from ADC to KeV. It is described in detail in Sec. 4.3.

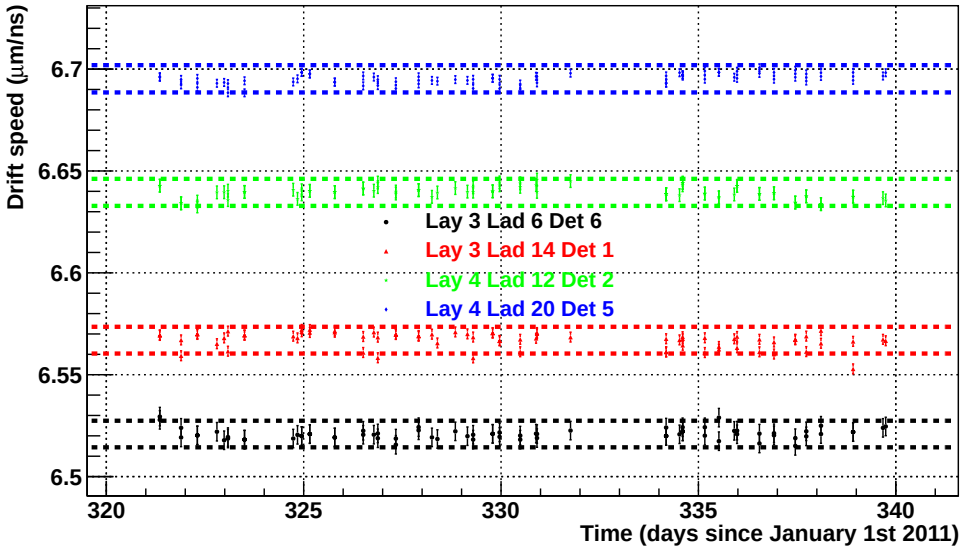

Figure 4.6: Drift speed as measured from the MOS injectors during the 2011 Pb–Pb run.

4.1.3 Silicon Strip Detector (SSD)

Being the closest ITS detector to the TPC, the SSD layers are crucial for the matching of tracks from the TPC to the ITS. The SSD detector provides a two dimensional measurement of the track position and $\mathrm{d}E/\mathrm{d}x$ information for particle identification. Its operating principle is based on the collection on each strip side of the electron/hole pairs created by a charged particle crossing the detector. The basic building block of the ALICE SSD is a module composed of one double-sided strip detector (Figure 4.7). In total 768 strips are implanted on each side of the sensor. Each strip is 40 mm long and has a pitch of 95 μm. Strips are almost parallel to the beam axis in order to minimise "ghost" clusters and provide the best resolution in the transverse plane ($\sim$ 20 μm on the rϕ coordinate and $\sim$ 800 μm along the beam direction). The two layers of the SSD contain a total of 1698 modules.

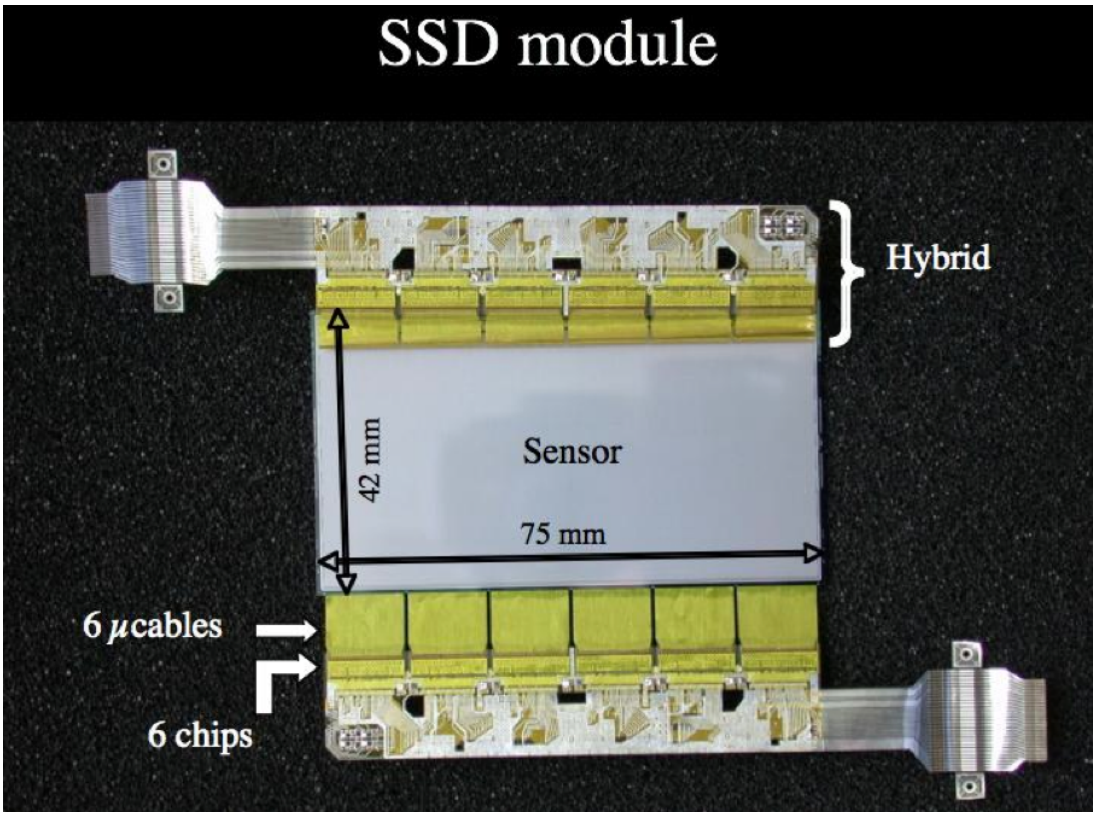

Figure 4.7: The ALICE SSD module.

4.2 Tracking in the ITS

4.2.1 ITS standalone tracking

The tracking algorithm

The event reconstruction in the central barrel is performed using the tracking detectors (ITS, TPC and TRD), as described in Sec. 3.2.2. The ITS allows to improve the momentum and angle resolution for tracks reconstructed in the TPC and prolonged to the ITS (Figures 4.15, 4.16).

In addition to this, the ITS can be used as a standalone tracker with a dedicated tracking algorithm [55]. In this way it is possible to reconstruct low momentum particles that decay before reaching the TPC but also high momentum particles that pass through the dead zones of the TPC or decay between the ITS and the TPC. The interaction vertex is firstly estimated using reconstructed points in the SPD layers. The ITS standalone tracking algorithm is divided in two main parts:

– **Track finding.** The track seeding starts from the inner SPD layer and goes toward the external SSD layer. Search windows are defined by two quantities:

$$\lambda = \arctan\left[\frac{(z - z_V)}{\sqrt{(x - x_V)^2 + (y - y_V)^2}}\right] \tag{4.1}$$

$$\phi = \arctan\left[\frac{y - y_V}{x - x_V}\right] \tag{4.2}$$

where x_V, y_V and z_V are the coordinates of the primary vertex reconstructed with the SPD. For each pair of points belonging to the same (λ, ϕ) window the track curvature is estimated using the vertex information. The expected position on the next layer is calculated and points are searched in a given ($\Delta\lambda$, $\Delta\phi$) window. If the point on a given layer is missing (because of a dead region or detector inefficiency) the seeding is prolonged to the following layer. At least 3 associated points are requested to form a candidate track. The track finding procedure is iterated increasing progressively the size of the window in order to reconstruct low p_{T} tracks which are significantly bent in the magnetic field and deflected by multiple scattering.

– **Track fitting.** The track fit is done with the Kalman filter method also used in the global track (TPC+ITS) reconstruction [45]. If a track candidate has more than two associated points on the same layer the fit is performed using all the possible

combinations and the one associated with the lowest χ^2 is chosen. The track is then fitted through the associated points outward and then inward from the outer associated point to the primary vertex.

It is possible to distinguish two different sets of tracks reconstructed only with the ITS:

- **ITS standalone tracks.** The ITS standalone tracking algorithm runs after the reconstruction of global tracks (TPC+ITS). Only ITS clusters that are not attached to a global track are used in the reconstruction. This sample contains only tracks not reconstructed by the TPC, such as particles not reaching the TPC or crossing the dead regions of the TPC. It is not a "complete" set of tracks but it is "complementary" to the ITS-TPC track sample.
- **ITS Pure standalone tracks.** The ITS standalone tracking algorithm runs using all the reconstructed ITS clusters of the event. This sample contains all the particles in the event. It represents a crucial cross-check for the global track reconstruction since it is completely independent, as it were "another experiment".

Performance in Pb-Pb

The ITS standalone tracking efficiency can be estimated from the Monte Carlo simulation as

$$\epsilon = \frac{\text{Tracks reconstructed by the ITS standalone algorithm}}{\text{Particles generated within the ITS acceptance}}^{1} \tag{4.3}$$

The ITS standalone tracking efficiency as a function of p_{T} is shown in Figure 4.8 for the different particle species for Pb–Pb collisions. Fake tracks are removed using Monte Carlo information, no specific track cuts are applied in this definition of efficiency. The ITS standalone tracking allows the reconstruction of particles with low transverse momentum (down to $p_{\mathrm{T}} = 70$ MeV/c for pions). The tracking efficiency depends strongly on the centrality (i.e. on the occupancy of the detector). This is mainly due to the high combinatorial background and the limited number of points available for reconstruction in the ITS. The contamination from fake tracks can be estimated on the Monte Carlo simulated data. On the real data it is not possible to tag fake tracks, for this reason it is important to find a cut able to reduce the contamination from fake tracks. A detailed Monte Carlo study has been performed[2].

[1] The denumerator includes primary particles which decay or are absorbed before reaching the detector.

[2] For this study ITS standalone tracks are requested to have at least 1 reconstructed point in the SPD and 3 points in the SDD+SSD. These are the cuts used in the analysis (Sec. 4.4.2)

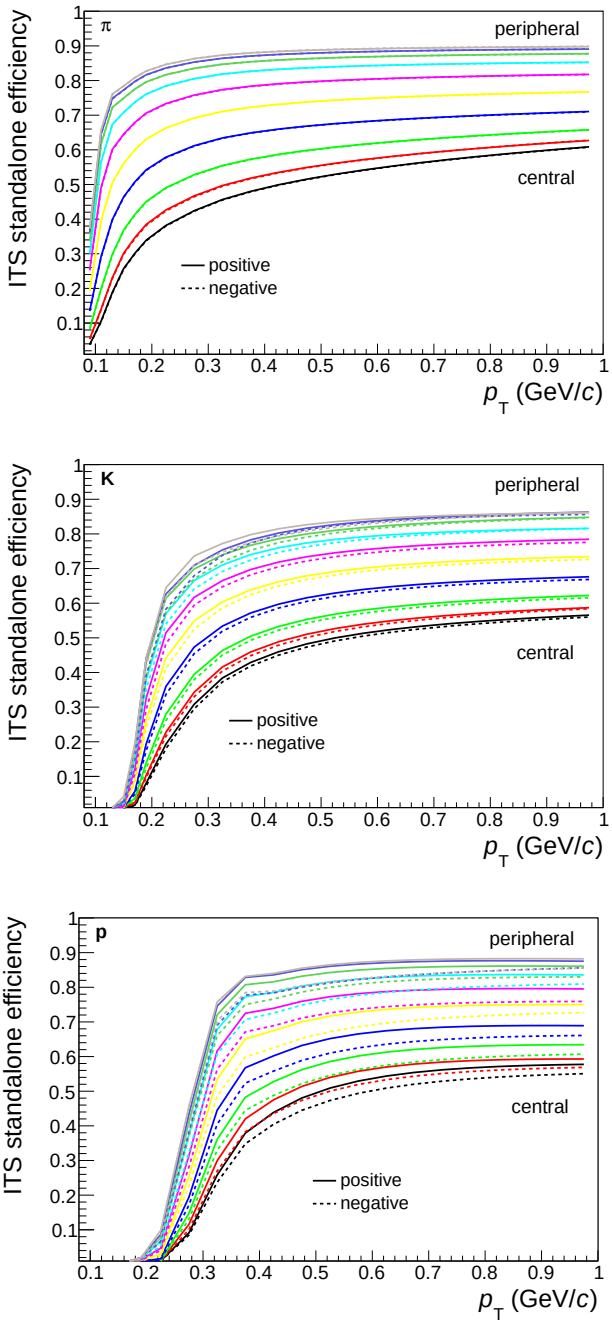

Figure 4.8: ITS standalone tracking efficiency. Top to bottom: pions, kaons, protons. Dashed Curves: negative particles, continuous curves: positive particles. The different curves for the same particles represent different centrality bins. Fake tracks are removed using Monte Carlo information, no specific track cuts are applied in this definition of efficiency.

The $\chi^2/N_{clusters}$ distribution is reported in Figure 4.9 for "good" ITS Pure standalone tracks (i.e. tracks reconstructed using clusters associated with only one Monte Carlo particle), "fake" tracks (i.e. tracks reconstructed with one or more wrongly associated clusters) and the sum of the two samples in simulated central Pb–Pb collisions. The

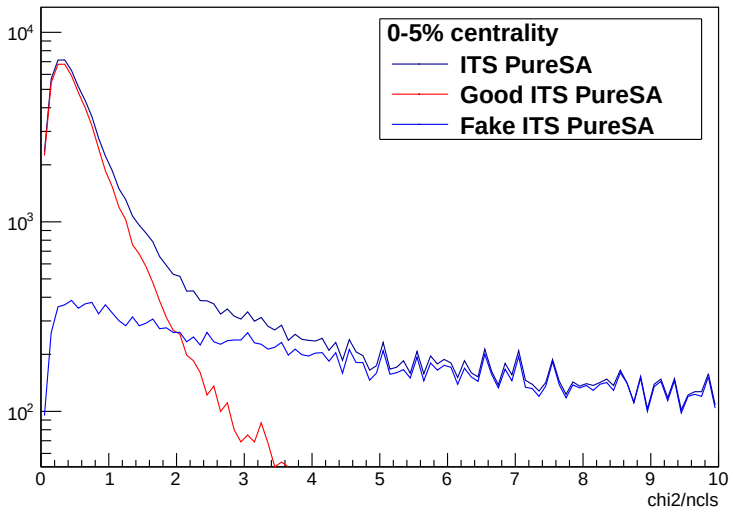

Figure 4.9: $\chi^2/N_{cluster}$ distribution for "good" ITS Pure standalone tracks (i.e. tracks reconstructed using clusters associated with only one Monte Carlo particle), "fake" tracks (i.e. tracks reconstructed with one or more wrongly associated clusters) and the sum of the two samples in simulated central Pb–Pb collisions.

$\chi^2/N_{clusters}$ distribution for fake tracks is significantly wider than for good tracks. A cut on the $\chi^2/N_{clusters}$ value allows the reduction of the contamination from fake tracks on the real data. The effect of this cut is reported in the upper panel of Figure 4.10. The contamination from fake tracks increases with the centrality of the collision. A cut on $\chi^2/N_{cluster} < 2.5$ allows one to significantly reduce the contamination from fakes (from $\sim$ 42% to $\sim$ 13% in the most central bin). The $< N_{clusters} >$ attached to a reconstructed track is reported in the central panel. It is smaller for fake tracks than for good ITS Pure standalone tracks. The $< \chi^2/N_{clusters} >$ is reported in the bottom panel. As already observed in Figure 4.9 fake tracks have a significantly wider $\chi^2/N_{cluster}$ distribution. Contamination from fake tracks is mostly relevant at low p_{T}, as shown in Figure 4.11. By cutting on the lowest accepted p_{T} value it is also possible to reduce the contamination from fake tracks[3]. The tuning of the cuts has to be done according to the

[3]This is not used in the spectra analysis since ITS PID is used to extend the low p_{T} reach of the TPC.

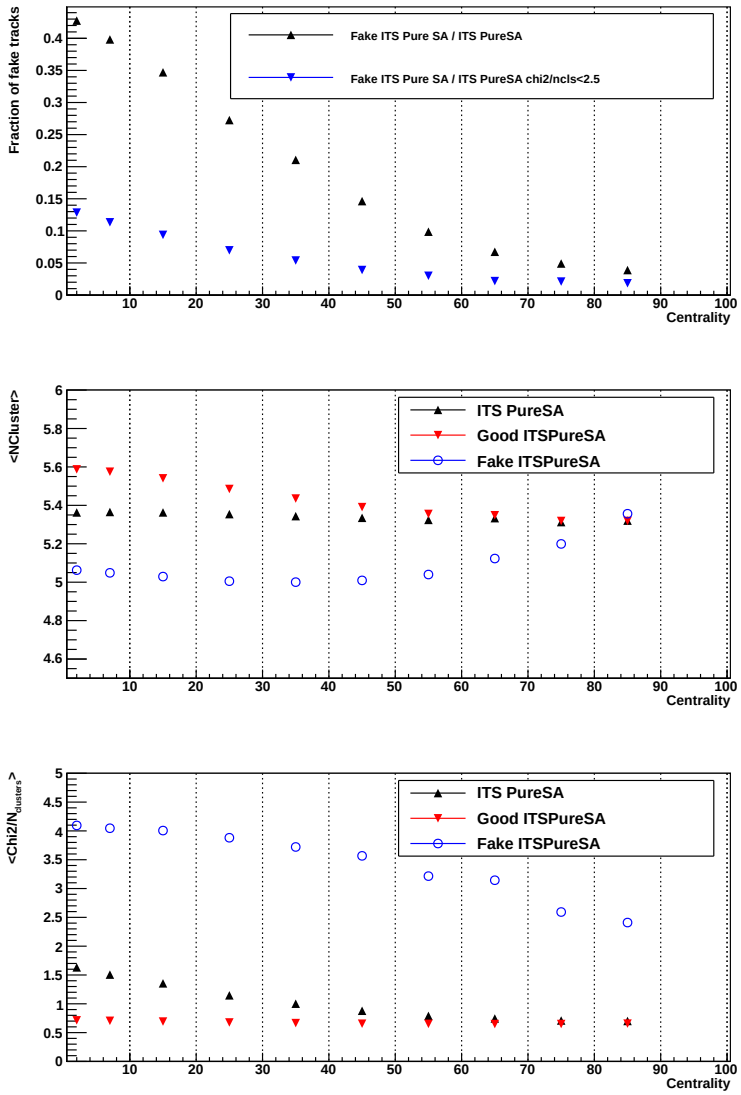

Figure 4.10: Fraction of fakes, $< N_{clusters} >$ and $< \chi^2/N_{clusters} >$ for "good" ITS Pure standalone tracks (i.e. tracks reconstructed using cluster associated with only one Monte Carlo particle), "fake" tracks (i.e. tracks reconstructed with one or more wrongly associated clusters) and the sum of the two samples as a function of centrality in simulated Pb–Pb collisions.

needs of the analysis. For the specific case of the spectra analysis, track cuts are reported in Sec. 4.4.2.

It is very important that the centrality dependence observed in Monte Carlo simulations (Fig. 4.8) reflects the real centrality dependence of the tracking efficiency. Two different data-driven approaches are used in order to investigate the agreement between

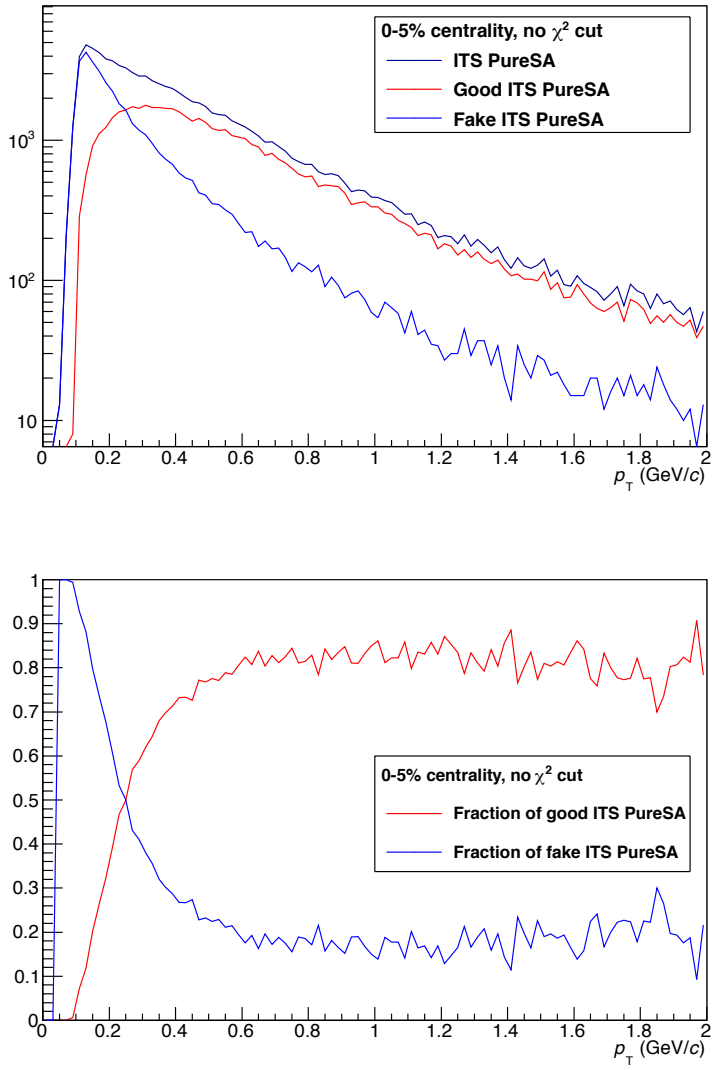

Figure 4.11: p_{T} distribution for "good" ITS Pure standalone tracks (i.e. tracks reconstructed using clusters associated with only one Monte Carlo particle), "fake" tracks (i.e. tracks reconstructed with one or more wrongly associated clusters) and the sum of the two samples in simulated central Pb–Pb collisions. The fraction of good and fake tracks is reported in the bottom panel.

data and Monte Carlo:

– **Track Count.** The ratio

$$\mathrm{r}_{\text{Track Count}} = \frac{\text{ITS Pure standalone tracks}}{\text{Global tracks} \ + \ \text{ITS standalone tracks}} \tag{4.4}$$

has been studied separately on data and Monte Carlo in various p_{T} intervals in

the range 0 - 1 GeV/c. The discrepancy between real and simulated data can be estimated looking at the ratio data/Monte Carlo. The ratio $r_{\text{Track Count}}$ is shown for different centrality bins in the top left (right) panel of Figure 4.12 for data (Monte Carlo). The data/Monte Carlo ratio is reported in the bottom plot. A discrepancy of ~ 10 % at low p_{T} between data and Monte Carlo is observed in the most central bin. Data and Monte Carlo become closer with decreasing centrality.

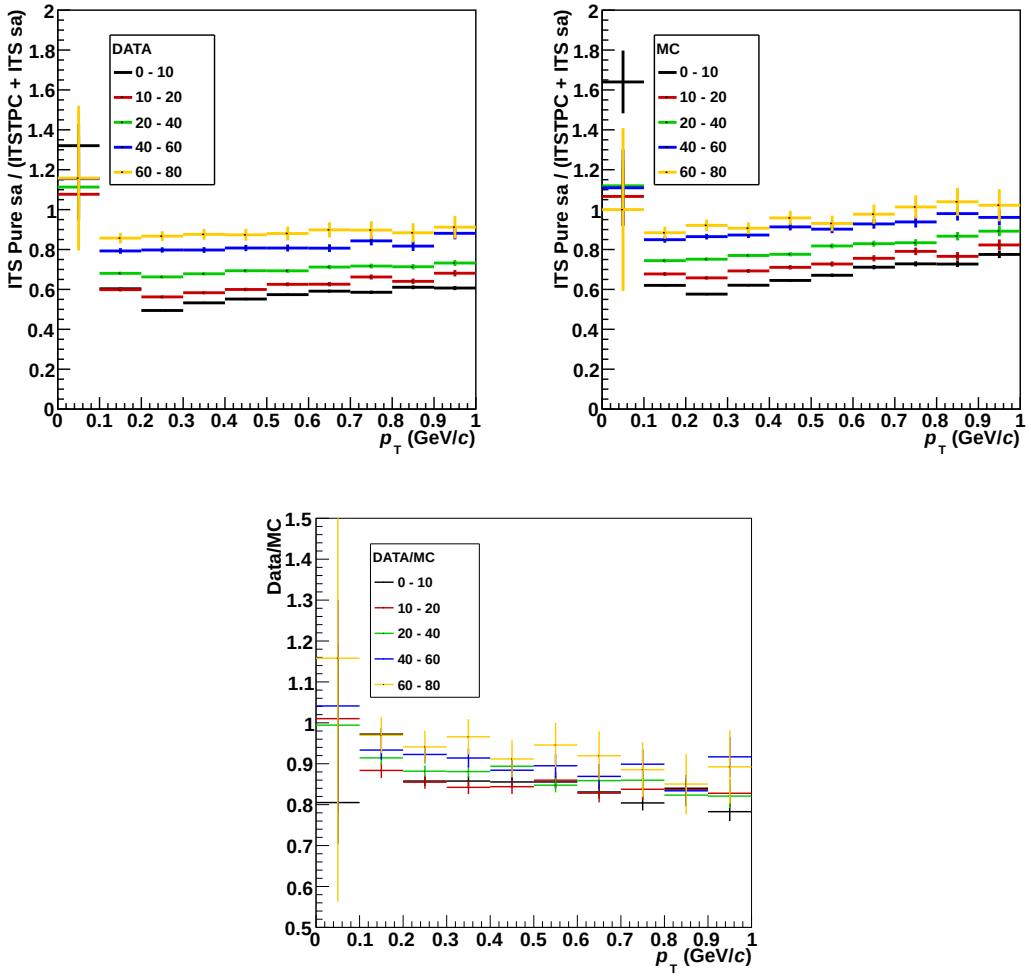

Figure 4.12: Top left (right): $r_{\text{Track Count}}$ (Eq. 4.4) for different centrality bins for data (Monte Carlo). Bottom: data/Monte Carlo ratio.

– **Track Matching.** For each global track a matching ITS Pure standalone track is searched in the window:

$$\Delta p_{\text{T}} < 0.1 \times p_{\text{T}}(\text{global track}), \quad \Delta\eta < 0.03, \quad \Delta\phi < 0.03 \tag{4.5}$$

and the fraction of matched tracks is studied as a function of p_{T}. This is shown for different centrality bins in the top left (right) panel of Figure 4.13 for data (Monte Carlo). The data/Monte Carlo ratio is reported in the bottom plot. A discrepancy

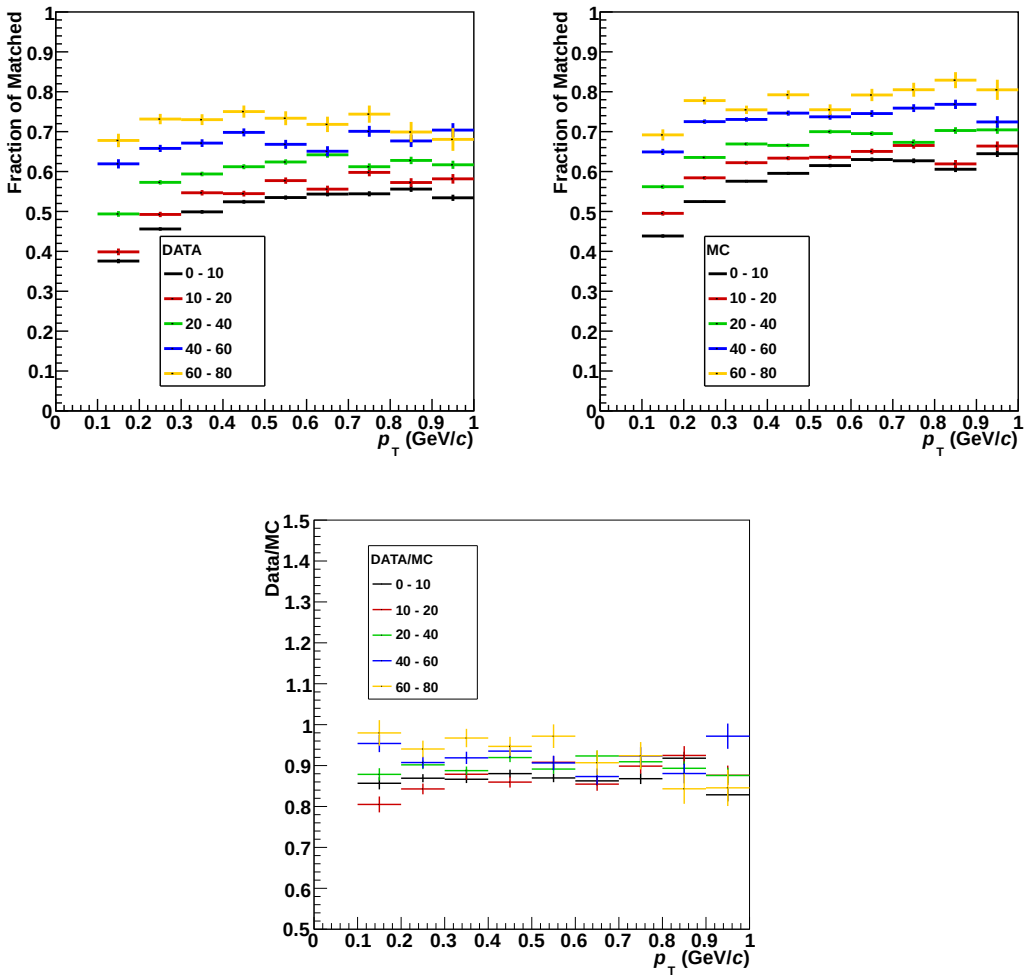

Figure 4.13: Top left (right): fraction of matched tracks for different centrality bins for data (Monte Carlo). Bottom: data/Monte Carlo ratio.

of $\sim$ 12 % between data and Monte Carlo is observed in the most central bin. The agreement between data and Monte Carlo gets better with decreasing centrality.

Both the data-driven approaches suggest a discrepancy of $\approx$ 10 % between data and Monte Carlo in central Pb–Pb collisions. The agreement between data and Monte Carlo improves with decreasing centrality. This has to be considered in the systematic error estimation for measurements using tracks reconstructed with the ITS standalone algorithm.

The impact parameter is defined as the distance of closest approach between the trajectory of a particle and the interaction vertex. The resolution on the transverse component of the impact parameter ($d0_{r\phi}$) for ITS standalone tracking is shown in Figure 4.14 for π, K and p in data and Monte Carlo. The resolution is estimated from a Gaussian fit to the π, K and p distribution of the transverse component of the impact parameter. The impact parameter resolution is determined by two main contributions:

– a momentum-independent contribution due to the spatial resolution of the detectors,

– a momentum-dependent contribution due to multiple scattering.

Since multiple scattering angle depends on $1/\beta$, for low momenta, where this is the main contribution to the impact parameter resolution, the resolution itself depends on the particle type, being worse for heavier particles. The resolution in the data is well reproduced in the Monte Carlo simulation. The resolution on $d0_{r\phi}$ and $d0_z$[4] for ITS standalone tracks

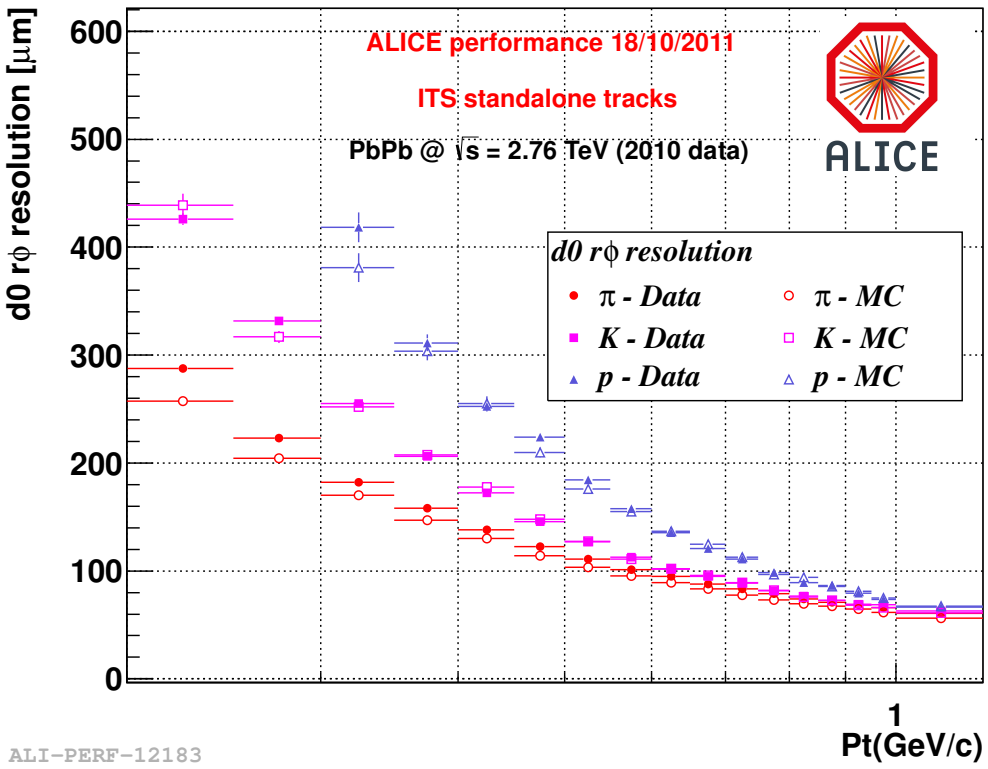

Figure 4.14: Impact parameter resolution in the transverse plane ($d0_{r\phi}$) for ITS standalone tracks for π, K and p in data and Monte Carlo.

[4]The (r, ϕ) plane corresponds to the (x, y) plane. z is the beam direction.

and global tracks are compared in Figure 4.15 as a function of p_{T} for unidentified charged hadrons. The two tracking algorithms provide a similar resolution in the transverse plane:

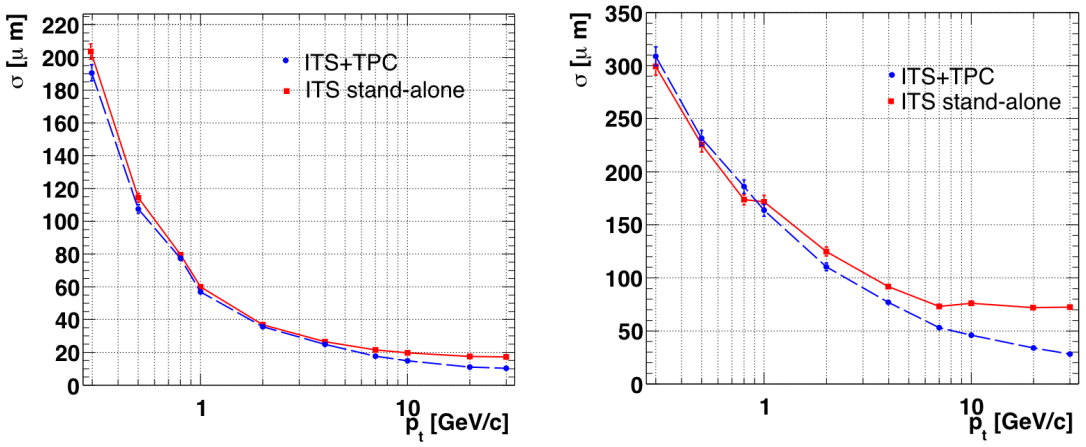

Figure 4.15: Impact parameter resolution in the transverse plane (left) and along the beam direction (right) for ITS standalone tracks and global tracks as a function of p_{T} [55].

this is due to the fact that the resolution is mainly given by the high precision points of the SPD. Along the beam direction a clear worsening of the resolution for ITS standalone tracking can be observed. In the ITS only the SDD provides a high precision measurement of the z coordinate, while for global tracking the larger level-of-arm of the TPC results in a better resolution at high p_{T}.

The p_{T} resolution for ITS standalone tracks and global tracks is reported in Figure 4.16 as a function of p_{T}. The p_{T} resolution for ITS standalone tracks results to be much worse with respect to that of global tracks. At low p_{T} the resolution is $\sim 5\%$ for ITS standalone tracks and $\sim 0.6\%$ for global tracks. This is mainly due to the smaller level-of-arm and the limited number of points in the case of the ITS standalone tracking.

4.3 PID signal

The identification of electrons, π, K and p in the ITS is performed using the $\mathrm{d}E/\mathrm{d}x$ information in the 4 layers of SDD and SSD. The offline PID calibration of the SDD has been one of the activity I carried out during my Ph.D. work and it is described in detail.

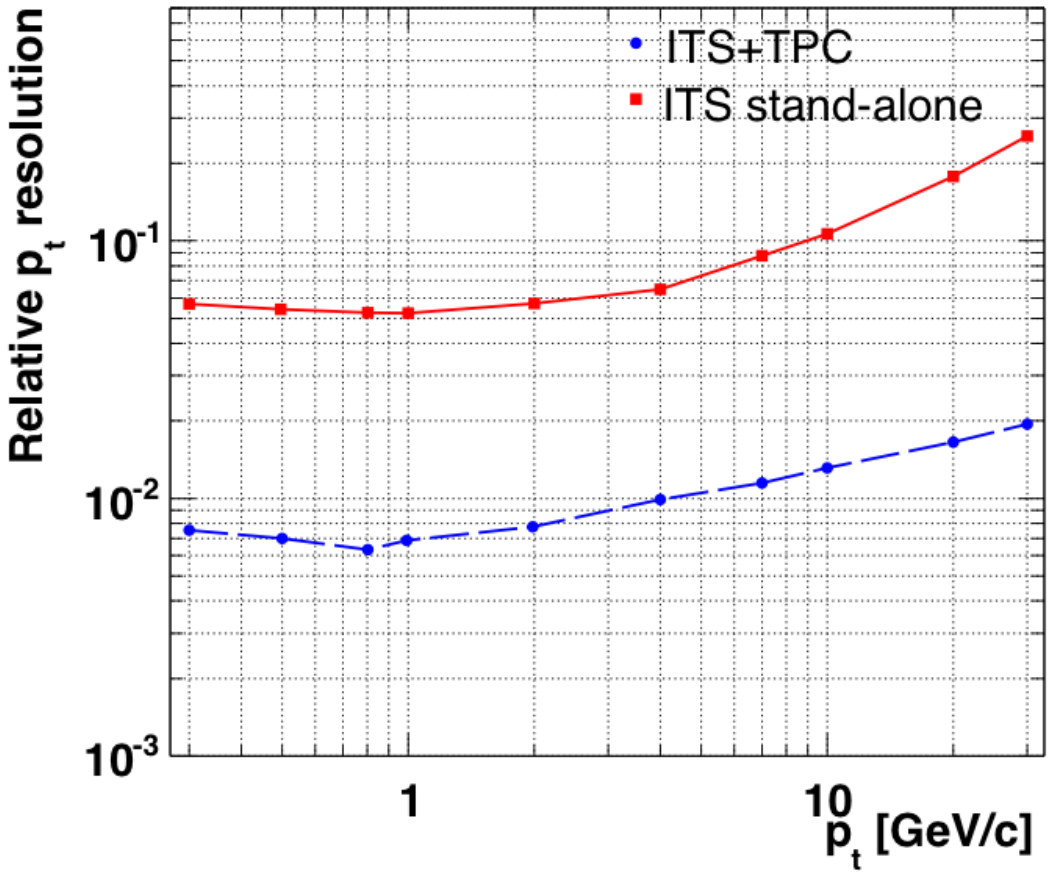

Figure 4.16: p_{T} resolution for ITS standalone tracks and global tracks (ITS-TPC) as a function of p_{T} [55].

4.3.1 Offline PID calibration of the SDD

The charge collected at the anodes of the SDD module is proportional to the energy loss of particles in the sensors. When a trigger signal is received, the detector signal is digitised by the PASCAL chip [56]. The second stage is handled by the AMBRA chip [57], which performs the pedestal equalisation and the data compression. The last step is handled by the CARLOS chip [58], which performs the zero suppression and sends the data to the CARLOSrx board via optical fibre. The read-out chain returns a digitised signal. During the tracking the signal collected in the SDD modules is corrected, during the final fit inward, in order to take into account the effect of the inclination of the track with respect to the module. The offline calibration of the detector response is performed in two steps:

– **Correction for diffusion.** The $\mathrm{d}E/\mathrm{d}x$ signal is corrected in order to take into account the signal loss due to charge diffusion in the drift region. When a particle crosses the detector far from the anodes the charge diffuses much more with respect to a particle crossing the detector in the region near to the collecting anodes. Due to the zero suppression algorithm, this diffusion effect can also give rise to a dependence of the reconstructed cluster charge on the drift distance. The longer the drift time, the larger the charge diffusion and consequently the larger the fraction of charge in the electron-cloud tails which is more easily cut by the zero suppression. This correction is done in three steps:

  1. The $\mathrm{d}E/\mathrm{d}x$ distribution of clusters reconstructed in the SDD is extracted in different drift time slices. For each drift time bin the distribution is fitted with a Landau+Gaussian function. The Landau function describes the energy loss of particles in the material, while the Gaussian term takes into account the detector resolution.

  2. The Most Probable Value (MPV) extracted from the Landau+Gaussian fit is plotted as a function of the drift time and it is fitted with a straight line.

  3. The slope m[5] extracted from the linear fit to the MPV distribution as a function of the drift time is used to correct the charge signal according to the drift time value associated to the cluster.

[5] As explained above the longer the drift time, the larger the charge diffusion. For this reason the slope m is < 0.

– **ADC to KeV conversion.** After the first step the ADC signal corrected for diffusion is converted in KeV. Since the ITS PID combines the information from SDD and SSD it is important to have the same reference value for the Minimum Ionising Particle (MIP) energy loss. This value is 84 KeV in the 300 μm silicon bulk of SDD and SSD.

The dE/dx distribution, corrected using the procedure described above, is reported in Figure 4.17 as a function of the drift time for a typical module. The MPV extracted from

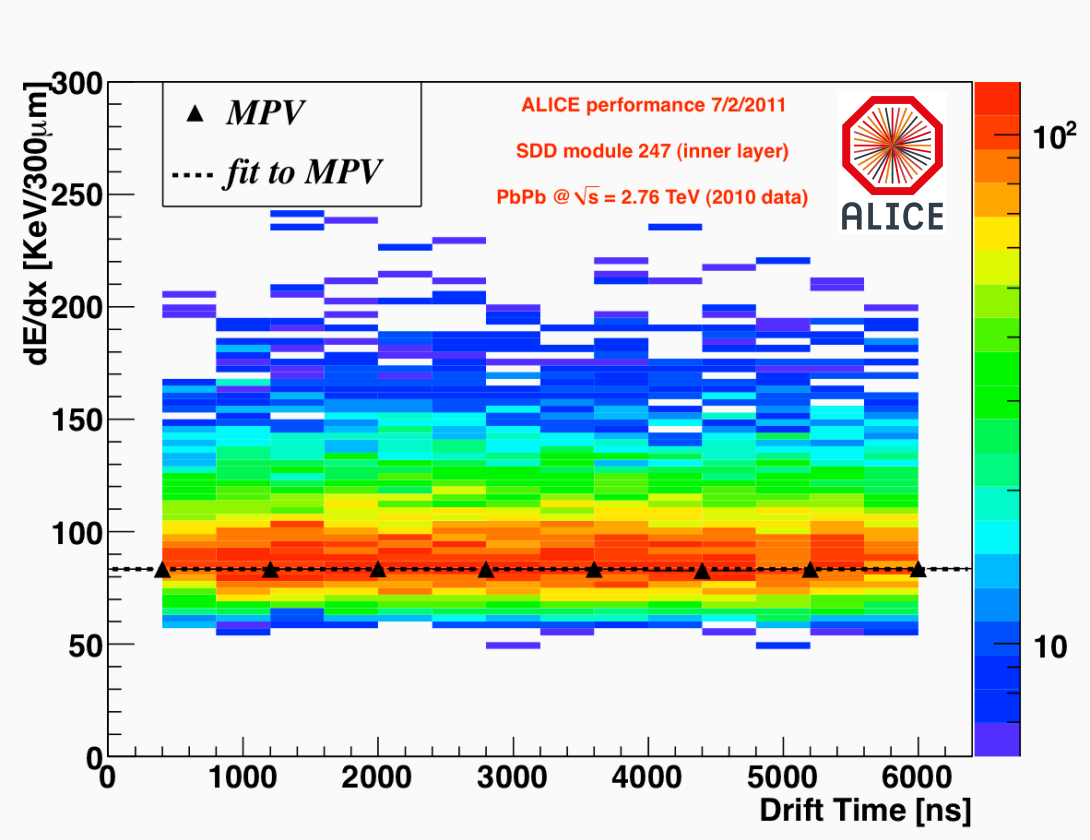

Figure 4.17: dE/dx distribution after correction as a function of the drift time for a typical SDD module. The MPV extracted from Landau+Gaussian fit in different drift time slices is reported on top of the distribution. The MPV distribution as a function of the drift time is fitted with a straight line (dotted line).

Landau+Gaussian fit in different drift time slices is reported on top of the distribution. The MPV distribution as a function of the drift time is fitted with a straight line (dotted line). From the fit it is possible to appreciate that, after the correction procedure described above, the MPV is constant as a function of the drift time.

Two examples of Landau+Gaussian fit to the dE/dx distribution (after correction) are reported in Figure 4.18 for small ($<$ 1200 ns) and large ($>$ 4400 ns) drift times. The two distributions are normalised to the number of entries. The dE/dx distributions nicely agree after the corrections described above.

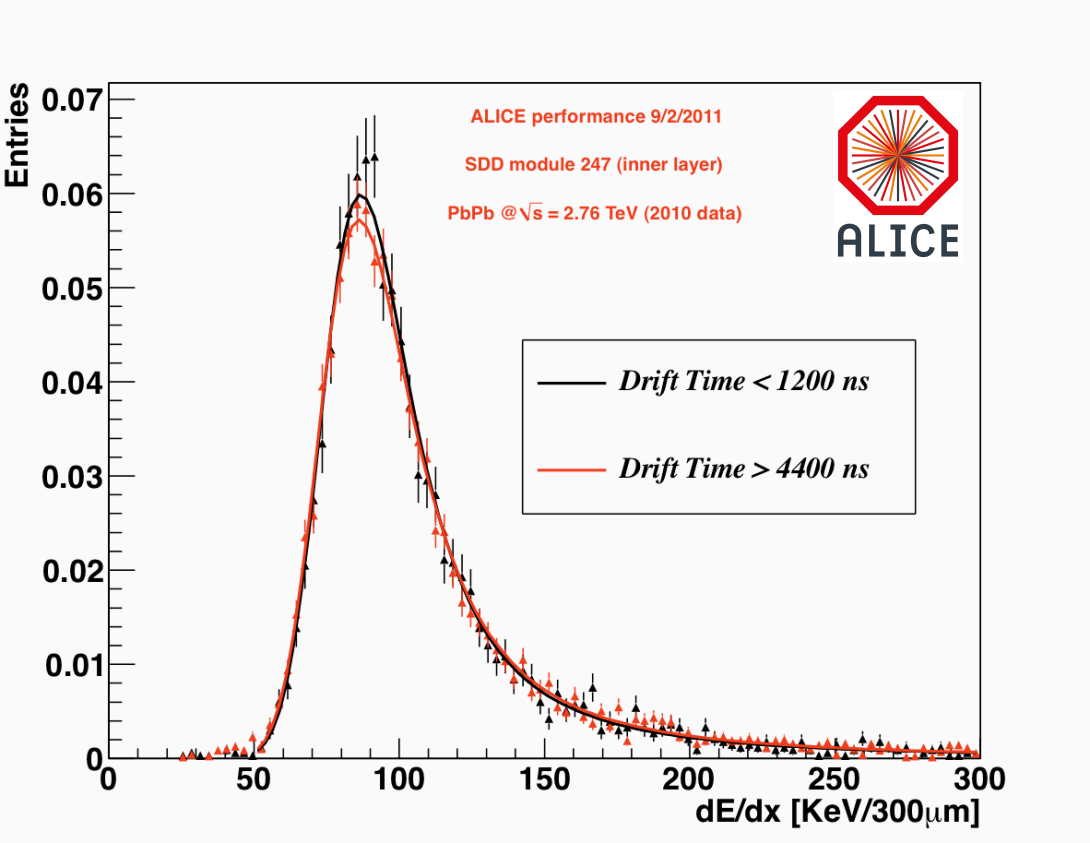

Figure 4.18: Fit to the dE/dx distribution (after correction) for small ($<$ 1200 ns) and large ($>$ 4400 ns) drift time for a typical SDD module.

For a detailed description of the SSD dE/dx calibration please refer to [59].

4.3.2 Energy loss parameterisation

For each track, dE/dx value is calculated using a truncated mean of the single measurements in SDD and SSD layers: the average of the lowest two points in case four points are measured, or a weighted average of the lowest (weight 1) and the second lowest point (weight 1/2), in case only three points are measured. The truncated mean is expected to reduce the Landau tails of the dE/dx distribution. Even with this truncated mean approach, the small number of samples results in residual non-gaussian tails which need to be taken into account in the analysis.

The most probable energy loss in the ITS detector as a function of $\beta\gamma$ deviates from a Bethe-Bloch function for small $\beta\gamma$. This is mainly due to resolution effects for large energy deposits and momentum bias at low $\beta\gamma$. The expected energy loss is calculated using the PHOBOS [60] parameterisation of the Bethe-Bloch function, complemented by a polynomial fit at low $\beta\gamma$:

$$\begin{aligned} &\mathrm{d}E/\mathrm{d}x = E_0\beta^{-1}(b + 2\ln\gamma - \beta^2) \qquad (\beta\gamma > 0.7) \\ &E_0 \text{ and } b \text{ are free parameters} \\ &\mathrm{d}E/\mathrm{d}x = p_0 + p_1/\beta\gamma + p_2/(\beta\gamma)^2 + p_3/(\beta\gamma)^3 \qquad (\beta\gamma \leq 0.7) \\ &p_0,\ p_1,\ p_2 \text{ and } p_3 \text{ are free parameters} \end{aligned} \tag{4.6}$$

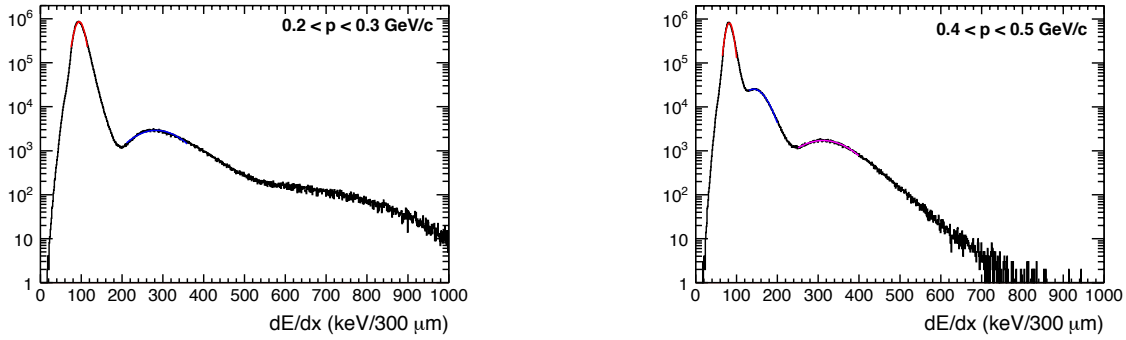

Figure 4.19: Fit of the $\mathrm{d}E/\mathrm{d}x$ distributions in the momentum bins $0.2 < p < 0.3$ GeV/c (left) and $0.4 < p < 0.5$ GeV/c (right). It should be noted that in the left plot the p peak is not visible, because protons in this momentum range cannot be reconstructed with the ALICE detector, due to multiple scattering and absorption.

The tuning of the expected energy loss is done in two steps:

– The $\mathrm{d}E/\mathrm{d}x$ distribution is plotted for different momentum slices in the region where pions, kaons and protons are clearly separated and the corresponding peaks are fitted with three Gaussian functions (Fig. 4.19).

– The extracted $\mathrm{d}E/\mathrm{d}x$ mean values are plotted as a function of $\beta\gamma$. In the considered momentum range for all practical purposes $\mathrm{d}E/\mathrm{d}x$ in the material is a function of $\beta\gamma$ alone [2]. The parameters of the Bethe-Bloch parameterisation in Eq. 4.6 are extracted from a fit to this distribution. Discontinuities seen correspond to the transition from π to K and from K to p in the $\beta\gamma$ distribution. This is mainly due to the fact that when the track is fitted, the π mass is assumed for each track.

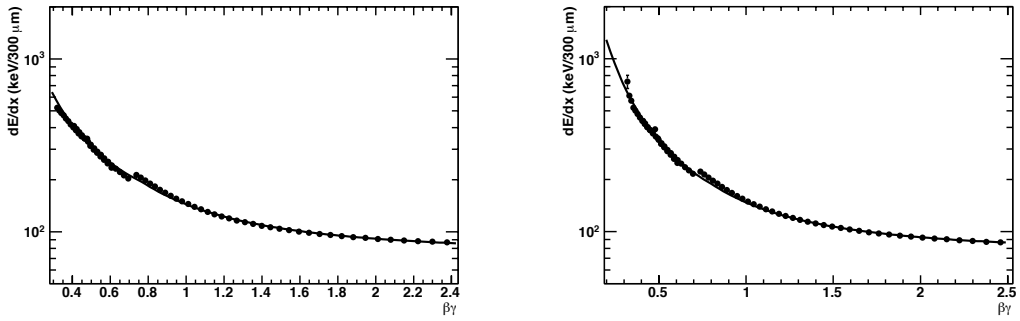

Figure 4.20: Fit to the distribution of the mean $\mathrm{d}E/\mathrm{d}x$ as a function of $\beta\gamma$ for data (left) and Monte Carlo (right). Discontinuities seen correspond to the transition from π to K and from K to p in the $\beta\gamma$ distribution. This is mainly due to the fact that when the track is fitted, the π mass is assumed for each track. This effect is taken into account in the systematic error estimation by varying the energy loss parameterization within errors.

The resulting expected energy loss distribution is shown for the pion, kaon and proton mass hypothesis in Figure 4.21 on top of the measured $\mathrm{d}E/\mathrm{d}x$.

Below $p \sim 200$ MeV/c it is possible to separate electrons from pions in the ITS. The Bethe-Bloch parameterisation described above does not scale simply with the mass for electrons, given the different nature of energy loss. For this reason a dedicated tuning of the PHOBOS Bethe-Bloch parameterisation is needed. The tuning of the detector response for electrons is done in an analogous way as for π, K and p. The dotted line on Fig. 4.21 represents the expected energy loss of electrons in the ITS.

The same procedure is repeated for the Monte Carlo sample in order to extract the Bethe-Bloch parameterisation for simulated data. The parameterisations of the expected energy loss in data and Monte Carlo are compared in Figure 4.22. The two parameterisations differ by few percent.

4.3.3 Energy loss resolution

The relative energy loss $\mathrm{d}E/\mathrm{d}x$ resolution, shown in Figure 4.23, depends on the number of SDD+SSD clusters attached to the track and does not show any significant trend with the moment of the track. The resolution is independent from the colliding system. It is evaluated by fitting the π peak in the $\mathrm{d}E/\mathrm{d}x$ distribution in different slices of p_{T} with a Gaussian function. The small number of $\mathrm{d}E/\mathrm{d}x$ measurements in the ITS

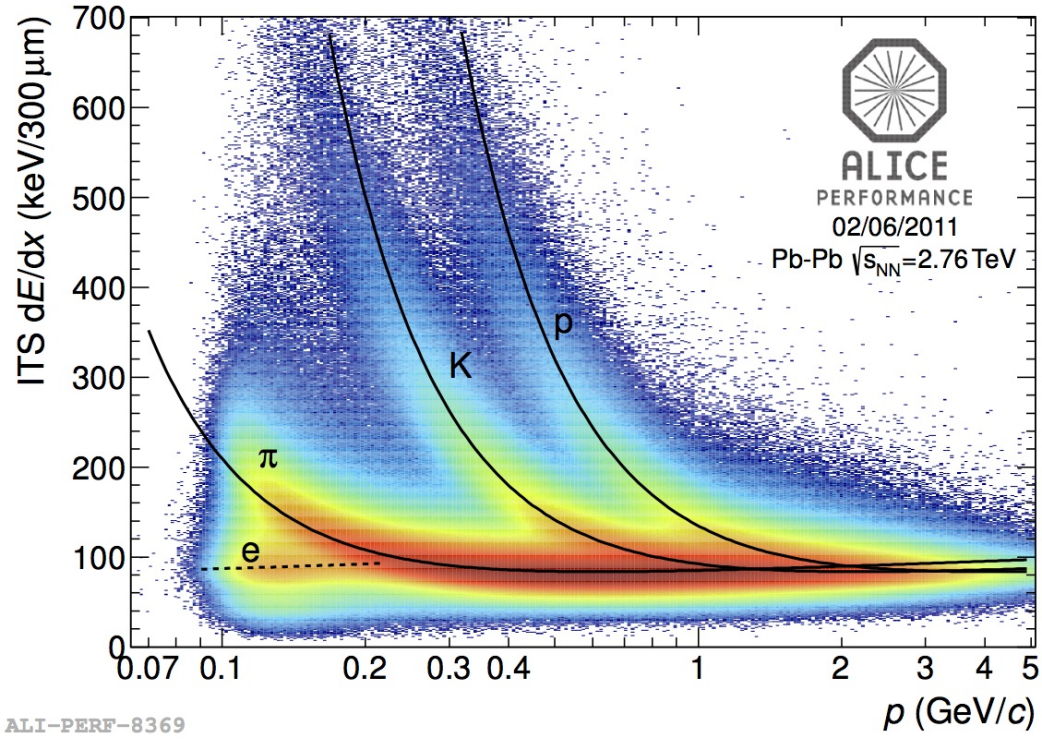

Figure 4.21: $\mathrm{d}E/\mathrm{d}x$ distribution as a function of track momentum p, with the tuned Bethe-Bloch parameterisation for data.

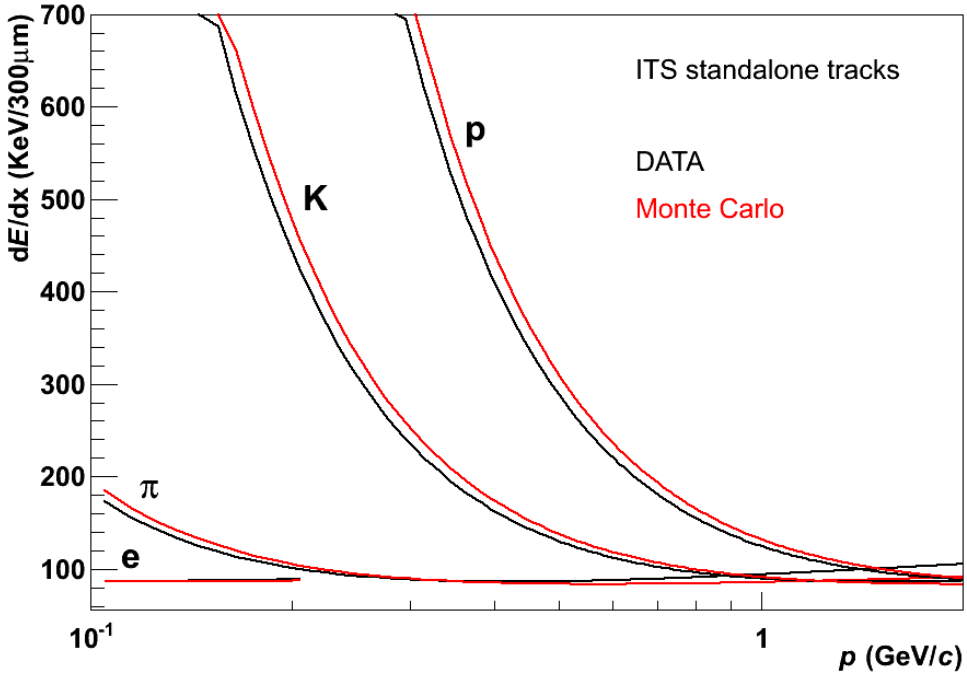

Figure 4.22: Expected $\mathrm{d}E/\mathrm{d}x$ as a function of track momentum p in data and Monte Carlo for ITS standalone tracks.

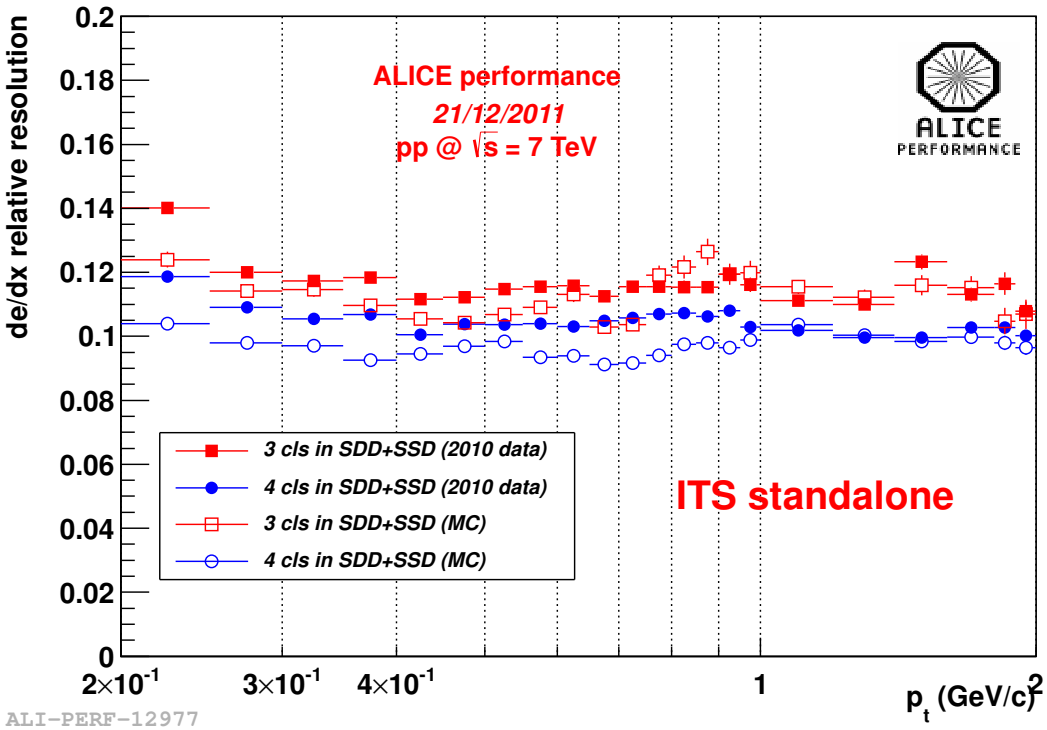

Figure 4.23: $\mathrm{d}E/\mathrm{d}x$ relative resolution for ITS standalone tracks as a function of transverse momentum p_{T} for data and Monte Carlo.

results in a residual Landau tail when the truncated mean approach is adopted. For this reason a narrow fit range around the peak is used. A good agreement between data and Monte Carlo is found. It is very important to have a precise and reliable measurement of the $\mathrm{d}E/\mathrm{d}x$ resolution, calculated for data and Monte Carlo independently, in order to use for particle identification the distance measured in number of sigma ($n\sigma$) between the measured $\mathrm{d}E/\mathrm{d}x$ and expected $\mathrm{d}E/\mathrm{d}x$ for a given particle specie.

4.4 PID analysis

In this section the steps needed to obtain the corrected spectra for identified charged primary hadrons are described in detail. The analysis is reported for ITS standalone tracks but it can be easily generalised to different track samples or PID detectors. The starting point for each analysis is the track reconstruction, described in Section 4.2 for the ITS.

The roadmap to build fully corrected spectra for identified π, K, p can be summarized as follow:

1. Event selection and normalisation, Sec. 4.4.1.
2. Track selection, Sec. 4.4.2.
3. Raw yield extraction, Sec. 4.4.3.
4. Efficiency correction with Monte Carlo simulation, Sec. 4.4.4.
5. Subtraction of secondary particles, Sec. 4.4.5.

4.4.1 Event selection and normalisation

The purpose of the event selection is to tag hadronic interactions with the highest possible efficiency, while rejecting the machine-induced and physical backgrounds.

Online trigger selection

The online minimum bias trigger evolved during the 2010 Pb–Pb run to accommodate the increasing luminosity. The trigger logic requires a combination of the following conditions:

– At least 2 chips hit in the outer layer of the SPD,

– A signal in the VZERO, A side,

– A signal in the VZERO, C side.

According to the period, the trigger implemented one of following requirements:

– 2 out of 3 of the above conditions,

– "AND" of the VZERO signal on the A and C side,

– 3 out of 3 of the above conditions.

In addition to these conditions the signals in the beam pick-up counters (BPTX) is requested. In practice, this trigger was implemented online as a combination of different trigger classes, for more information see the trigger coordination web page [61]. Control empty triggers were also collected with the same trigger logic, in coincidence with only one beam crossing the ALICE interaction point (from either the A or the C side) or with no beam at all ("empty"). No events were observed in the present sample for the empty triggers, meaning that the noise from the triggering detectors is negligible.

Offline selection

– **Machine-induced background (MIB).** The machine-induced background (MIB) is caused by beam ions interacting with the residual gas in the beam pipe (beam-gas) or by ions in the halo of the beam interacting with mechanical structures in the machine. These events can be rejected making use of the timing information of the VZERO or the ZDCs. Only the neutron ZDCs are used in this analysis, due to their higher efficiency. MIB events caused by one of the beam, happen upstream of the VZERO on that side and thus produce an "early" signal as compared to the time corresponding to a collision in the nominal interaction point. This is illustrated in Fig. 4.24(a). The time difference between the ZDC signal on either side, corresponding to the vertex position of the event, is also a powerful cut to reject the MIB in Pb–Pb collisions. The MIB contamination amounts to about 25%. The second source of background is due to parasitic collisions from debunched ions. The radio-frequency (RF) structure of the LHC is such that there are 10 RF "buckets" within a 25 ns bunch, spaced by 2.5 ns. These events are rejected using the correlation between the sum and the difference of times measured in the ZDC[6],

[6]The sum of times changes because the start time is always referred to the nominal time for a good collision.

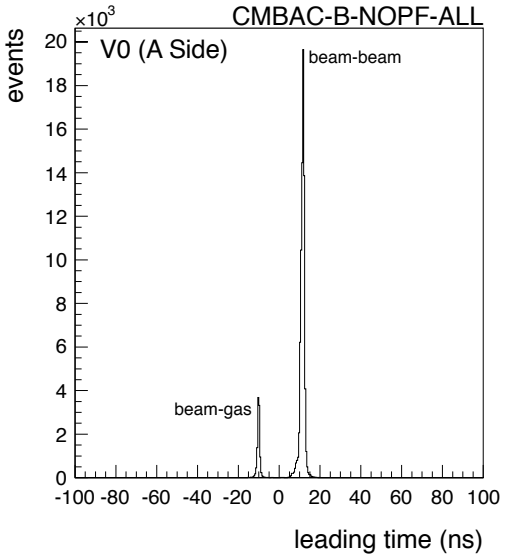

(a) Time distribution of the VZERO signals on the A side. The peaks corresponding to beam-beam and to beam-gas events are clearly visible (Pb–Pb)

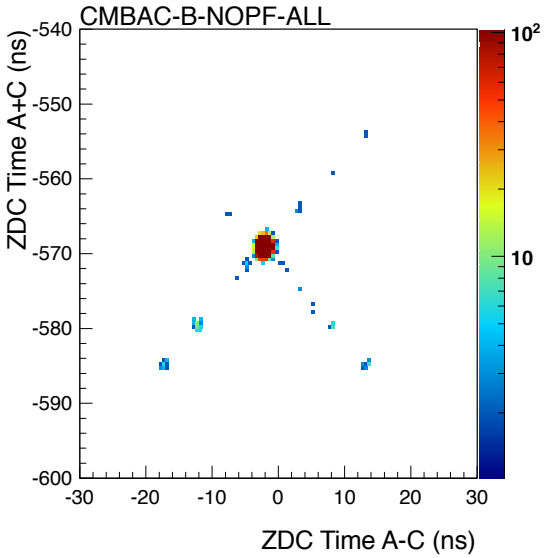

(b) Correlation between the sum and the difference of times recorded by the neutron ZDCs on either side (Pb–Pb). The big cluster in the middle corresponds to collisions between ions in the nominal RF bucket on both sides, while the small clusters along the diagonals (spaced by 2.5 ns in the time difference) correspond to collisions in which at least one of the ions is displaced by one or more RF buckets.

Figure 4.24: Machine-induced backgrounds.

as shown in Fig. 4.24(b).

– **Physical background.** The main physical background is given by the strong EM fields generated by the heavy-ions moving at relativistic velocity, leading to huge cross-sections ($\mathcal{O}$(kbarn)) [62] for QED processes. This needs to be rejected in heavy-ion collisions to isolate hadronic interactions. Those events can be classified into several processes:

  – QED pairs: lepton pairs are produced via QED processes.

  – Nuclear dissociation: one (single) or both (mutual) nuclei break up as a consequence of the EM interaction.

  – Photo-production: one photon from the EM field of one of the nuclei interacts with the other nucleus, possibly fluctuating to a vector meson. Can be single or double.

  All those processes are characterised by production of soft particles and low multiplicity at mid-rapidity. Some of them are asymmetric (e.g single photo-production or single EM dissociation).

  In the event selection, an energy deposit above 500 GeV in both neutron ZDC calorimeters is required, which rejects the asymmetric contributions to the EM background. The symmetric ones still survive, but they are negligible in the 90% most central events, as demonstrated by the study of dedicated simulation of the EM background [62], by data-driven checks based on the comparison of the measured distribution of SPD clusters, V0 amplitude or tracks with different selections and by the comparison to the Glauber fits [7].

Normalization

The experimental data are first of all normalised to the number of events passing the event selection criteria. In Pb–Pb collisions, for the centrality selection considered in this work, the vertexing and event selections are 100% efficient, so that the number of events after selection corresponds to the total number of collisions in the corresponding centrality interval. The centrality of the collision can be estimated using the signal in the VZERO detector or the reconstructed multiplicity in the central barrel. The measured signal distributions are fitted with a Glauber model [7].

Cut	Value	Effect
N_{cls} in SPD	≥ 1	Improve the DCA_{xy} resolution and reduce contamination from secondary and fake tracks.
N_{cls} in SDD+SSD	≥ 3	Reduce the Landau tail in the $\mathrm{d}E/\mathrm{d}x$ distribution calculated as the truncated mean in SDD+SSD.
χ^2/N_{cls}	≤ 2.5	Reduce contamination from fake tracks and select high quality tracks.
DCA_{xy}	$\leq 7\sigma$	Reduce contamination from secondary tracks. The resolution on the transverse component of the impact parameter as a function of p_{T} is reported in Figure 4.15.

Table 4.2: Track cuts applied in the ITS standalone PID analysis

4.4.2 Track selection

After the reconstruction of the event the track sample that is intended to be used in the analysis is selected applying different track cuts. Track cuts have to be tuned according to the purpose of each analysis. There are several reasons why track cuts are needed:

- to reduce contamination from secondary particle (e.g. cut on the distance of closest approach to the vertex),
- to improve the resolution on a given quantity (e.g. cut on N_{cls} in a given detector),
- to reduce the contamination from fake tracks (e.g. cut on the χ^2 associated to the track).

The track cuts applied in the case of the spectra analysis with ITS standalone tracks are reported in Table 4.2.

4.4.3 Raw yield extraction

The transverse momentum p_{T} distributions of π, K and p can be extracted using different analysis techniques which can be distinguished in two main categories:

– **Unfolding.** The raw yield is extracted from a multi-component fit of the $\mathrm{d}E/\mathrm{d}x$ distribution. The advantage is that in this way it is possible to estimate the contamination from wrongly identified particles using the data (unfolding procedure). This approach enables the particle identification also in the region were the contamination is not negligible. The extracted yield depends on the fit parameters and in general the fit procedure has to be carefully tuned on the data and the Monte Carlo separately.

– **Track-by-track PID.** The identity (π, K or p) is assigned on a track-by-track basis. This methods are simple and powerful but one has to keep the contamination from mis-identified particles under control. Contamination has to be evaluated and kept under control using Monte Carlo simulations or, if possible, selecting a pure sample of particles in the data.

In the ITS 4 different analysis methods are implemented. The last one, the $n\sigma$ method, is described in more detail since it was used for the first analysis of Pb–Pb data.

Gaussian unfolding

This approach was used for the first analysis of 900 GeV p–p data [63]. It consists in an unfolding method in which a set of Gaussian functions is used to fit the measured $\mathrm{d}E/\mathrm{d}x$ distribution in each p_{T} interval [64,65]. The distribution of the difference between the measured and the expected energy deposition for the tracks is fitted with 3 Gaussians (for π, K, p) and eventually a fourth Gaussian for electrons at low p_{T}. The expected energy loss depends on the measured track momentum and the assumed mass for the particle. The procedure is repeated three times for the entire set of tracks in the selected rapidity region, assuming the pion, kaon and proton mass.

TFractionFitter unfolding

This method is an extension of the Gaussian fit approach. It consists in an unfolding method in which instead of the Gaussian function the Monte Carlo templates for different particle species are used to fit the $\mathrm{d}E/\mathrm{d}x$ signal distribution. The fit is based on the ROOT TFractionFitter class [66], which allows to fit the measured $\mathrm{d}E/\mathrm{d}x$ distribution with Monte Carlo templates for electrons, π, K and p. In this way it is possible to include in the fit the residual non-Gaussian tails of the $\mathrm{d}E/\mathrm{d}x$ distribution.

Landau+Gaussian PID

It is a track-by-track method in which, instead of the truncated mean, the probability extracted from the $\mathrm{d}E/\mathrm{d}x$ information in each ITS layer is combined in order to assign the identity to the track. This requires a reliable parameterisation of the response function for each ITS layer both for data and Monte Carlo. The response is calculated by fitting the $\mathrm{d}E/\mathrm{d}x$ distribution with a convolution of a Landau (related with the energy deposit of particles) and a Gaussian (related with the detector resolution).

nσ PID

The results reported in Sec. 5 and Sec. 6 are obtained using this PID method. In this track-by-track PID approach, the $n\sigma$ separation between the truncated mean $\mathrm{d}E/\mathrm{d}x$ and the expected $\mathrm{d}E/\mathrm{d}x$ for a given particle specie is used. The $n\sigma$ separation in the i mass hypothesis is defined as:

$$n\sigma_i = \frac{\mathrm{d}E/\mathrm{d}x_{measured} - \mathrm{d}E/\mathrm{d}x_{i,expected}}{\sigma_{\mathrm{d}E/\mathrm{d}x_{measured}}} \tag{4.7}$$

The $n\sigma$ separation as a function of the track momentum assuming the kaon mass is reported in Figure 4.25. Usually the $n\sigma$ PID is implemented with an explicit cut on the maximum value of σ accepted. Assuming a perfectly Gaussian response the $n\sigma$ distribution of particle i in the i mass hypothesis is a Gaussian centred in zero with $\sigma = 1$. The way it is implemented in this work is different: a particle is assigned the identity of the closest theoretical curve without any explicit cut on its distance from the curve based on the number of σ. Only a lower bound for pions is defined at two times the experimental σ in order to reduce the contamination from electrons at low p_{T}. The mean distance between the p and the deuteron $\mathrm{d}E/\mathrm{d}x$ defines the upper bound for protons. The $\mathrm{d}E/\mathrm{d}x$ distribution, together with the Bethe-Bloch parameterisation and the bands used for the particle identification (dotted lines) are reported in Figure 4.26. The contamination from wrongly identified particles, which is negligible in the momentum range where the $\mathrm{d}E/\mathrm{d}x$ of the various species are well separated, is corrected using the Monte Carlo simulation, reweighted for the experimentally measured particle ratios. This analysis can be used in the region where the contamination is < 10 %. In terms of p_{T} ranges this means identification of π, K and p up to 0.6 GeV/c, 0.5 GeV/$c$and 0.6 GeV/c respectively. The advantage of this method consists in the asymmetric bands around the Bethe-Bloch parameterisation which are used for the identification, reflecting the asymmetric nature of the energy loss.

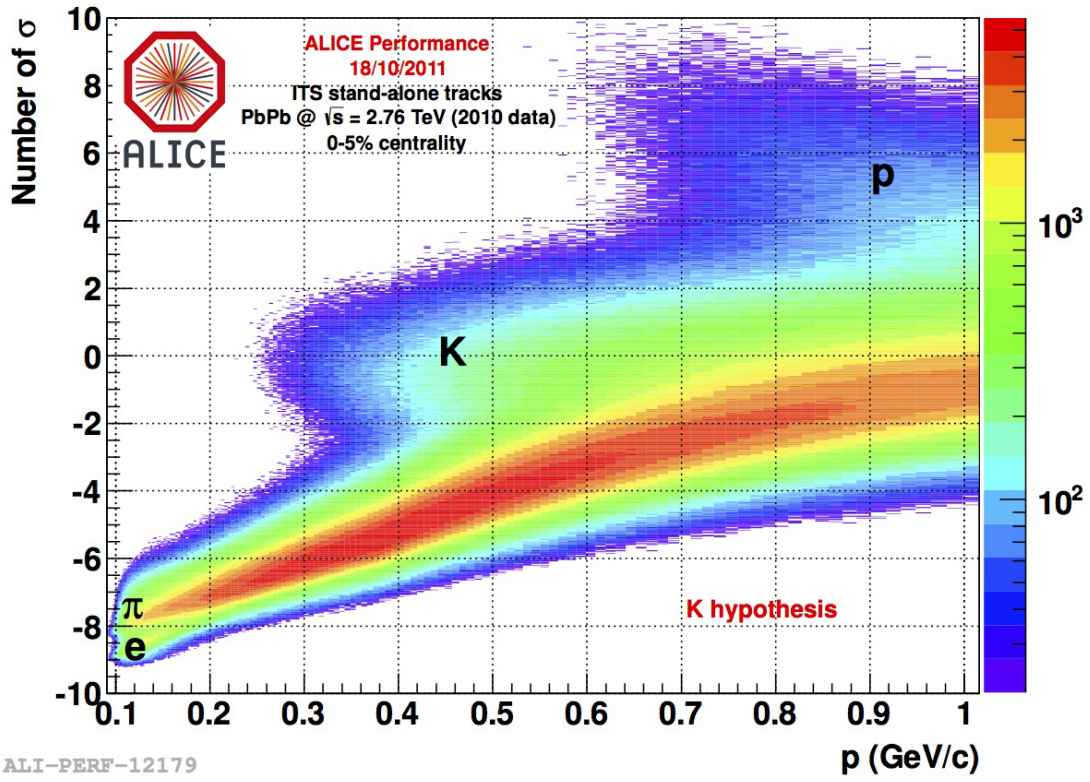

Figure 4.25: $n\sigma$ separation (Eq. 4.7) as a function of track momentum for ITS standalone tracks assuming the kaon mass.

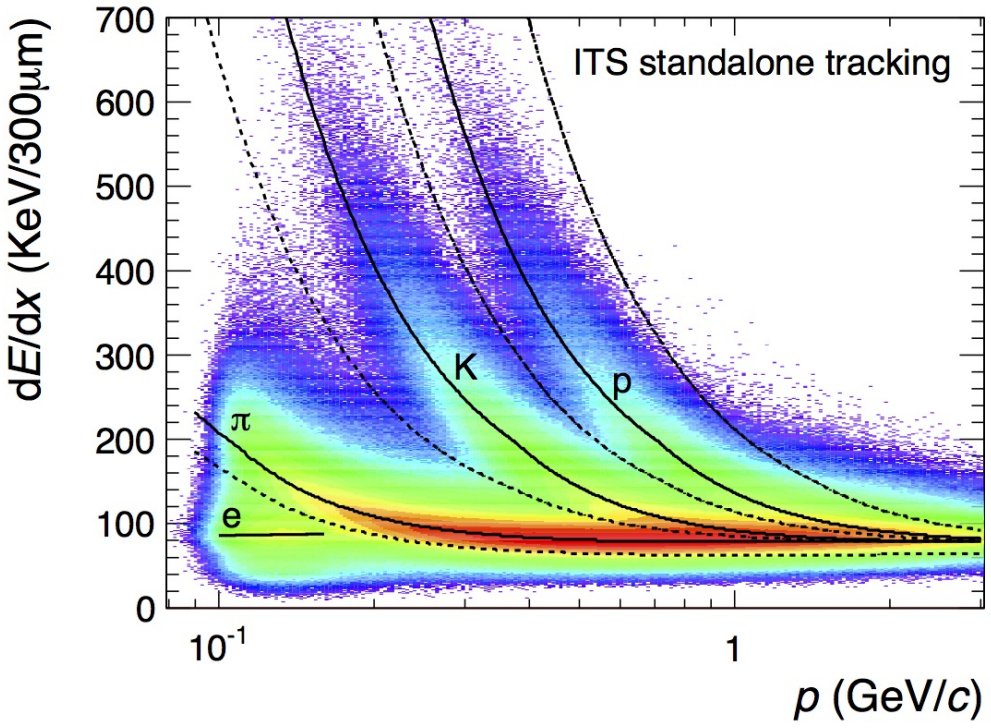

Figure 4.26: dE/dx distribution for ITS standalone tracks. The Bethe-Bloch parameterisation and the bands used for the particle identification (dotted lines) are also reported.

In addition it is less sensitive to the details of the tuning of the Bethe-Bloch and to the estimated $\mathrm{d}E/\mathrm{d}x$ resolution.

4.4.4 Efficiency correction with Monte Carlo simulation

Monte Carlo simulation is needed in order to correct the raw data. The various Monte Carlo correction steps are discussed in the following sections.

Tracking efficiency and contamination from other species

The basic correction factor is computed dividing the number of tracks reconstructed with a $\mathrm{d}E/\mathrm{d}x$ closer to the expected value of the Bethe-Bloch function for particle specie i (regardless of the true identity of the particle) by the total number of generated primary particles of specie i.

$$\frac{dN_{primary,RAW}/dp_{\mathrm{T}}dy_i}{dN_{primary,GENERATED}/dp_{\mathrm{T}}dy_i} \tag{4.8}$$

It should be noted that in the numerator of Eq. 4.8 the particle identity is assigned using the same PID method used on the data, without using the true Monte Carlo particle identity. Primary particles are selected using the Monte Carlo truth. The denumerator represents the spectrum of generated primary particles in the selected rapidity interval. Monte Carlo simulations are known to reproduce the measured particle ratios with an accuracy of $\sim 10\%$. The differences between data and Monte Carlo are estimated in the following way. While filling the correction factor, if the particle is of specie j (as identified from the Monte Carlo truth), it is rescaled by the double ratio $(j/i)_{\mathrm{DATA}}/(j/i)_{\mathrm{MC}}$, to account for the different particle abundances in the data and Monte Carlo. The maximum discrepancy between data and Monte Carlo on particle ratios is $\sim 10\%$ and the analysis is stopped when the contamination becomes $> 10\%$: this means that the correction is smaller than 1%. In practical terms it was decided to add this contribution to the systematic uncertainty without applying this correction. The correction factor of Eq. 4.8 includes also the tracking efficiency correction reported in Figure 4.8.

Interactions with the material, transport code correction

The transport code used in all the productions considered in this work is Geant 3.11. It is well known that the cross-section for interactions of negative particles with material in Geant 3 are larger than in nature, leading to an over-correction when the efficiency is computed. The Fluka Monte Carlo is known to have a description of cross section closer

to reality (as illustrated in Fig. 4.27 [67]). A correction factor based on the comparison between Geant 3 and Fluka was developed in the context of the antibaryon/baryon ratio analysis [67]. An additional cross-check has been done using Geant 4 [68] Monte Carlo

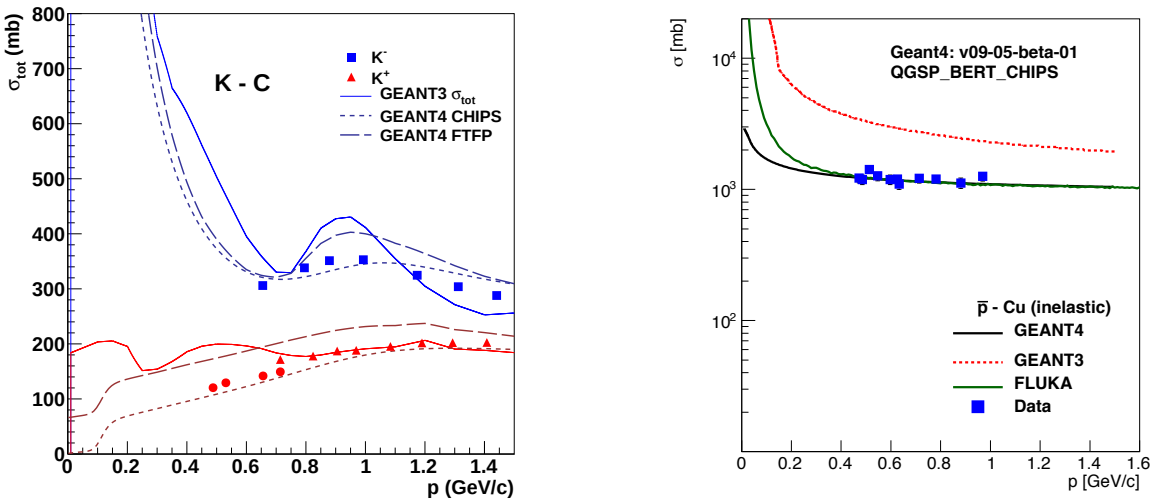

Figure 4.27: Comparison of K-C (left) and $\bar{\text{p}}$-Cu (right) cross sections, transport codes compared to data.

simulation. These corrections are shown in Fig. 4.28 as a function of transverse momentum p_{T} for ITS standalone tracks. The correction calculated using Fluka is used to correct the data. As suggested by Fig. 4.28 Geant 4 and Fluka agree within ~ 2 %. This contribution has been added to the systematic uncertainty.

4.4.5 Subtraction of secondary particles

The fraction of secondary particles has been estimated using a data driven approach based on the impact parameter of reconstructed tracks. It has already been measured by the ALICE experiment that the strangeness is not well reproduced in the Monte Carlo [69]. This method allows the estimation of the feed-down and secondary corrections on the data themselves, using only the Monte Carlo DCA_{xy} distribution of primaries, secondaries from weak decay and material (which are expected to be well reproduced in the simulated data). The measured distribution of the distance of closest approach of tracks to the primary vertex in the transverse plane (DCA_{xy}) has been fitted with Monte Carlo templates. These templates were obtained for primary particles, secondaries from weak decay and secondaries from material separately. The contamination of pions and kaons is much

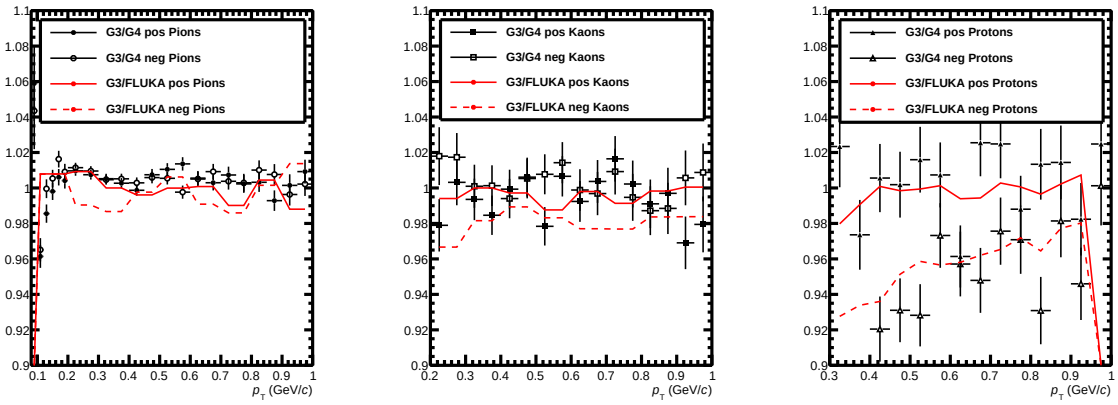

Figure 4.28: Geant3/Fluka and Geant3/Geant4 corrections as a function of transverse momentum p_{T} for ITS standalone tracks.

smaller than the one for protons (and anti-protons), given the large amount of Λ decaying to protons. For π and K a MC-only correction is used, leading to a small systematic error. In the case of anti-protons, the contamination of secondaries from material is negligible so that only the first two templates are used.

An example of the DCA$_{xy}$ fit to protons is shown in Figure 4.29 for a typical p_{T} interval. The fit is performed using the ROOT TFractionFitter class [66]. The contribution of secondary protons is relevant at low p_{T} where it goes up to $\sim 30\%$ of the measured yield.

4.4.6 Validation of the analysis

The combination of different detectors which use different particle identification techniques allows the identification of π, K and p over a broad p_{T} range in ALICE. Different analyses have been used in the ALICE experiment:

- **ITSsa:** ITS standalone analysis. It has been described in detail in previous sections. This approach allows the extension of the low p_{T} reach of the other analyses.

- **ITS-TPC:** global tracks are considered and the ITS is used for PID, with an unfolding method.

- **TPC-TOF:** global tracks are used and either TOF or TPC are used for the identification, using a $n\sigma$ method.

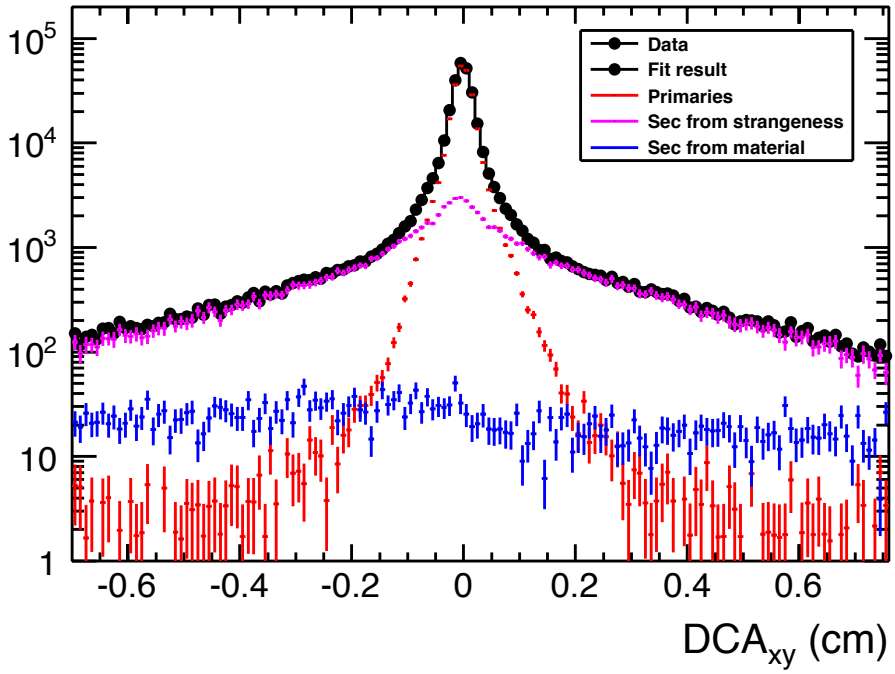

Figure 4.29: Fit to the data distribution of the distance of closest approach to the primary vertex in the transverse plane (DCA_{xy}) for protons in the bin $0.50 < p_T < 0.55$ MeV/c.

– **TOF:** global tracks are used and the TOF for the identification, using a Gaussian unfolding method.

– **HMPID:** global tracks are used and the HMPID for the identification, using a Gaussian unfolding method.

The momentum ranges covered by the considered analyses are shown in Table 4.3.

Analysis	π range GeV/c	K range GeV/c	p range GeV/c
ITSsa	0.1-0.6	0.2-0.5	0.30-0.6
ITS-TPC	0.2-0.55	0.25-0.5	0.4-0.85
TPC-TOF	0.3-1.5	0.3-1.3	0.5 -2.4
TOF	0.5-3	0.5 -3	0.5-3
HMPID	1-3	1-3	1.5-5

Table 4.3: p_{T} ranges (GeV/c) covered by the different analyses.

These analyses differ in the track sample, the PID signal used for the identification and the raw yield extraction approach. The systematic error associated with each analysis is largely independent: the comparison of these results is an important cross-check to validate the PID procedure and the Monte Carlo corrections.

Comparison in p–p

The low-multiplicity environment of p–p collisions is the ideal place to compare and validate the analyses (especially in the case of the ITS standalone, where a strong dependence of the tracking efficiency as a function of centrality is observed in Pb–Pb, Fig. 4.8). The comparison among the analyses is reported in Figure 4.30 for p–p collisions at $\sqrt{s_{\mathrm{NN}}}$ = 7 TeV. Only statistical error is reported on the plot. The agreement between the analyses is at the level of 5 %. The agreement is well below the systematic uncertainty of the measurement, that is $\sim$ 6%, $\sim$8%, $\sim$10% for π, K and p respectively.

Comparison in Pb–Pb

Only the ITS standalone, TPC-TOF and TOF analyses are used in Pb–Pb. The comparison, reported in Figure 4.31 for central (0-5%) Pb–Pb collisions at $\sqrt{s_{\mathrm{NN}}}$ = 2.76 TeV shows a nice agreement among different analyses.

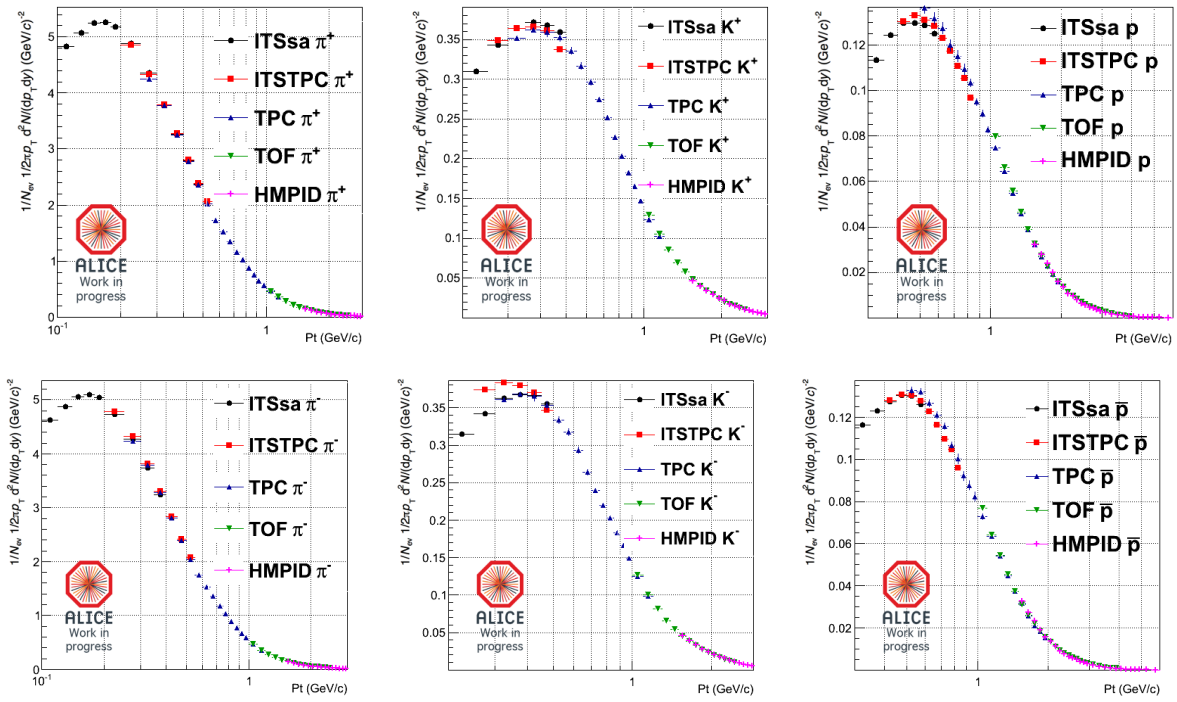

Figure 4.30: Comparison between different analyses in p–p collisions at $\sqrt{s_{\rm NN}} = 7$ TeV. Only statistical uncertainty plotted.

The techniques described in this Chapter are used to extract the $p_{\rm T}$ spectra of identified particles (Chapter 5) and the integrated yields at mid-rapidity (Chapter 6).

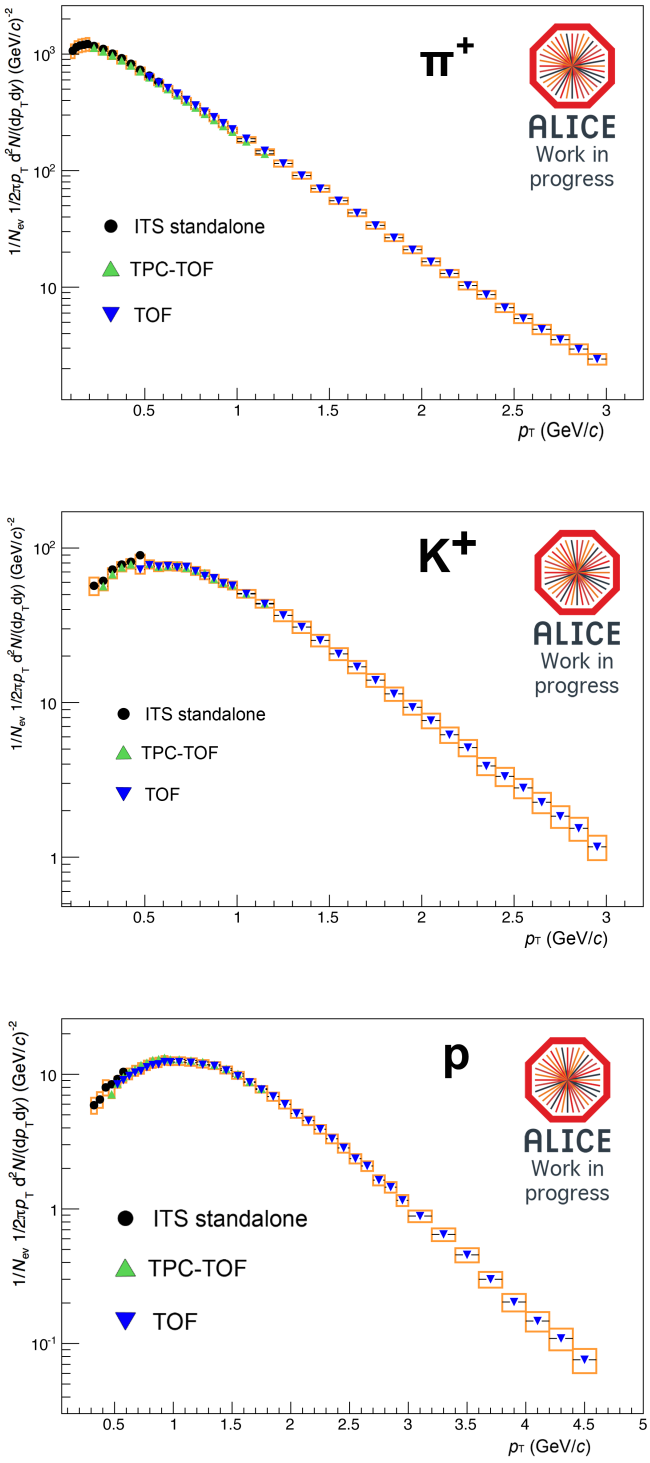

Figure 4.31: Comparison between different analyses in central (0-5%) Pb–Pb collisions at $\sqrt{s_{\rm NN}}$ 2.76 TeV. Statistical end systematic uncertainties plotted. Only positive particles are reported since the positive to negative ratio is close to unity for all the particle species in the considered $p_{\rm T}$ range (Fig. 5.4).

5

p_T distribution of primary identified π, K, p

In this Chapter a general overview of the hadron production as a function of transverse momentum p_T in Pb–Pb collisions at $\sqrt{s_{NN}} = 2.76$ TeV is reported. It includes:

- **Transverse momentum distribution of identified primary particles** (Sec. 5.1). The measurement of the p_T distributions of primary π, K, p is described for central Pb–Pb collisions in Sec. 5.1.1 and in different centrality bins in Sec. 5.1.2. The results are discussed in terms of the hydrodynamic picture and compared with previous experiments at lower energies.

- **Transverse momentum spectra as a function of the event-by-event flow** (Sec. 5.2). As for the centrality selection, events can be selected looking at the initial geometry of the system. The "Event Shape Engineering - ESE" is described and the identified particle raw spectra are measured in events selected according to the ESE.

5.1 $\mathbf{p_T}$ distribution of identified primary $\boldsymbol{\pi}$, K, p in Pb–Pb collisions at $\boldsymbol{\sqrt{s_{NN}} = 2.76}$ TeV

The $p_{\rm T}$ distribution of hadrons contains the information about the collective expansion of the fireball (radial flow) and the temperature of kinetic freeze-out (T_{kin}). In this section the results from Pb–Pb collisions at $\sqrt{s_{\rm NN}} = 2.76$ TeV are presented. Particle spectra are obtained from three different analyses, described in Sec. 4.4.6:

1. ITS standalone
2. TPC-TOF
3. TOF

The combination of different detectors and PID techniques is crucial to have good PID and tracking performance over a broad $p_{\rm T}$ range. The $p_{\rm T}$ ranges used by each analysis are summarised in Table 4.3.

The great strength of this measurement is that each analysis is mostly independent, resulting in largely independent systematic errors. The statistical error is negligible if compared with the systematic one. The systematic uncertainties associated with the measurement are summarised in Table 5.1.

The error related with the subtraction of secondary particles was estimated for all the analyses by:

- varying the range of the DCA$_{xy}$ fit (Sec. 4.4.5),
- varying the composition of the Monte Carlo templates used in the DCA$_{xy}$ fit,
- using different track selections (for instance using TPC-only tracks),
- applying different cuts on the distance of closest approach DCA$_{xy}$ and DCA$_z$.

The uncertainty on the energy loss correction was estimated by using a simulation with the material budget scaled by $\pm 7\%$. The contribution from hadronic interactions has been estimated, as described in Sec. 4.4.4, by comparing different transport codes (Geant 3, Geant 4, Fluka).

The systematic uncertainty for the ITS standalone analysis is dominated by the tracking efficiency, due to the high occupancy and the small number of tracking points. This was estimated from the data using global tracks as a reference, as described in Sec. 4.2.1.

effect	$\pi^{\pm}$		$\mathrm{K}^{\pm}$		p and $\overline{\mathrm{p}}$	
p_{T} range (GeV/c)	0.1	3	0.2	3	0.35	4.5
correction for secondaries	1.5%	1%	negl.		4%	1%
material budget	5%	negl.	3%	negl.	3%	negl.
hadronic interactions	2%	1%	4%	1%	6% 4%	1% ($\overline{\mathrm{p}}$) negl. (p)
p_{T} range (GeV/c)	0.1	0.5	0.2	0.5	0.35	0.65
ITS tracking (central)	10%		10%		10%	
(peripheral)	3%		3%		3%	
ITS PID	2%		4%		4.5%	
global tracking efficiency	4%		4%		4%	
TPC PID	3%		5%		1.5%	
p_{T} range (GeV/c)	0.5	3	0.5	3	0.5	4.5
TOF matching efficiency	3%		6%		3%	
TOF PID	2%	7%	3%	15%	5%	25%

Table 5.1: Main sources of systematic uncertainty. See text for details.

The contribution from other sources to systematic uncertainty is smaller, it includes the effect of the magnetic field configuration, of the track selection and of the PID cuts. The latter two contributions were estimated varying the track cuts reported in Tab. 4.2, the Bethe-Bloch parameterisation within the errors of the parameters and from the comparison with other ITS analyses (Sec. 4.4.3).

The uncertainty related to the tracking efficiency for global tracks was investigated by comparing different sets of tracks in data and Monte Carlo and by varying the quality selections. The uncertainty related to the combined TPC-TOF PID procedure was estimated by varying the PID cut between 2 and 5 σ.

Tracks reaching the TOF detector cross a significantly larger amount of material ($X/X_0 \approx 0.23$), mostly due to the TRD. Since the TRD was not fully installed in 2010,

the analysis has been repeated for regions with and without installed TRD modules. The uncertainty due to the additional material has been estimated from this comparison. The systematics related to the PID extraction in the TOF analysis were estimated by varying the fit parameters by ±10%.

Final spectra are obtained combining the results of the three analyses using the (largely independent) systematic error as weight in the overlapping regions.

The trigger configuration used to collect the data and the offline background rejection are described in Sec. 4.4.1. Centrality is estimated from the signal amplitude in the VZERO detectors [7]. This analysis has been performed using Event Summary Data - ESD [70].

5.1.1 Central (0-5%) Pb–Pb collisions

The ALICE measurement of identified particle spectra in central (0-5%) Pb–Pb collisions at $\sqrt{s_{\rm NN}} = 2.76$ TeV is represented by the empty circles in Figure 5.1 (from [71]). The $p_{\rm T}$ distributions of positive and negative particles are found to be compatible within errors (Fig. 5.4), for this reason results for summed charge states are presented. The measurement spans the $p_{\rm T}$ range from ~ 0.1 GeV/c up to ~ 4.5 GeV/c.

Spectra measured at the LHC are compared with RHIC results for Au–Au collisions at $\sqrt{s_{\rm NN}} = 200$ GeV. The spectral shape is significantly harder at the LHC with respect to RHIC.

The $\langle\beta_{\rm T}\rangle$ and T_{kin} parameters can be extracted from a simultaneous fit to the π, K and p spectra using the blast wave function [72]:

$$\frac{1}{p_{\rm T}}\frac{{\rm d}N}{{\rm d}p_{\rm T}} \propto \int_0^R r{\rm d}r\, m_{\rm T}\, {\rm I}_0\left(\frac{p_{\rm T}\sinh\rho}{T_{kin}}\right) {\rm K}_1\left(\frac{m_{\rm T}\cosh\rho}{T_{kin}}\right), \tag{5.1}$$

where the dependence on the velocity profile is described by

$$\rho = \tanh^{-1}\left(\left(\frac{r}{R}\right)^n \beta_t\right). \tag{5.2}$$

The freeze-out temperature T_{kin}, the average transverse velocity $\langle\beta_{\rm T}\rangle$ and the exponent of the velocity profile n are the free parameters in this fit. The $p_{\rm T}$ ranges used in the fit are 0.5-1 GeV/c, 0.2-1.5 GeV/c, 0.3-3 GeV/c for π, K and p respectively. Data are well described by the blast wave function with $\langle\beta_{\rm T}\rangle = 0.65 \pm 0.02$ and $T_{kin} = 96 \pm 10$ MeV. It should be noted that T_{kin} is sensitive to the pion fit range (due to large contribution

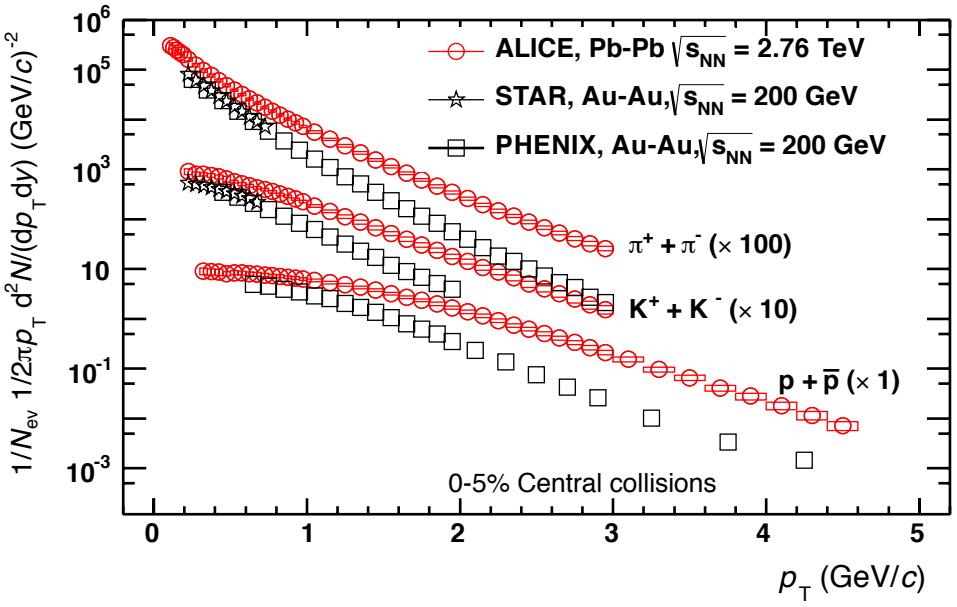

Figure 5.1: Transverse momentum distributions of the sum of positive and negative particles (box: systematic errors; statistical errors smaller than the symbol for most data points) compared to RHIC data (from [71]).

from resonances) while $\langle\beta_{\mathrm{T}}\rangle$ does not strongly depend on the p_{T} range used in the fit. A similar fit to central Au–Au collisions at $\sqrt{s_{\mathrm{NN}}} = 200$ GeV was performed in [73] and [74]: the $\langle\beta_{\mathrm{T}}\rangle$ is $\sim 10\%$ larger at the LHC with respect to RHIC and T_{kin} is compatible within errors.

The ALICE data are compared to different hydrodynamic models in Figure 5.2. In general the model parameters have been tuned to reproduce RHIC data and extrapolated at the LHC energy. At low p_{T}, below 1.5 GeV/c, a viscous hydrodynamic model (VISH2+1 [75]) describes quite well the π and K spectra, but it misses the protons, both in shape and absolute yield. This discrepancy can be due to the lack of an explicit description of the hadronic phase in the model. This is supported by the comparison with the HKM [76] model, in which the hadronic phase of the fireball evolution is described with the UrQMD [38] model (hadronic cascade model). The third model is the Krakòw model [35], which introduces non-equilibrium corrections due to viscosity at the transition from the hydrodynamic description to particles, which change the effective T_{ch}, leading to a good agreement with the data. The last model reported is an event-by-event 3-D viscous hydrodynamic model (MUSIC [77]), coupled with UrQMD. The agreement with the data is good (the disagreement with protons at high p_{T} can be explained in terms of the

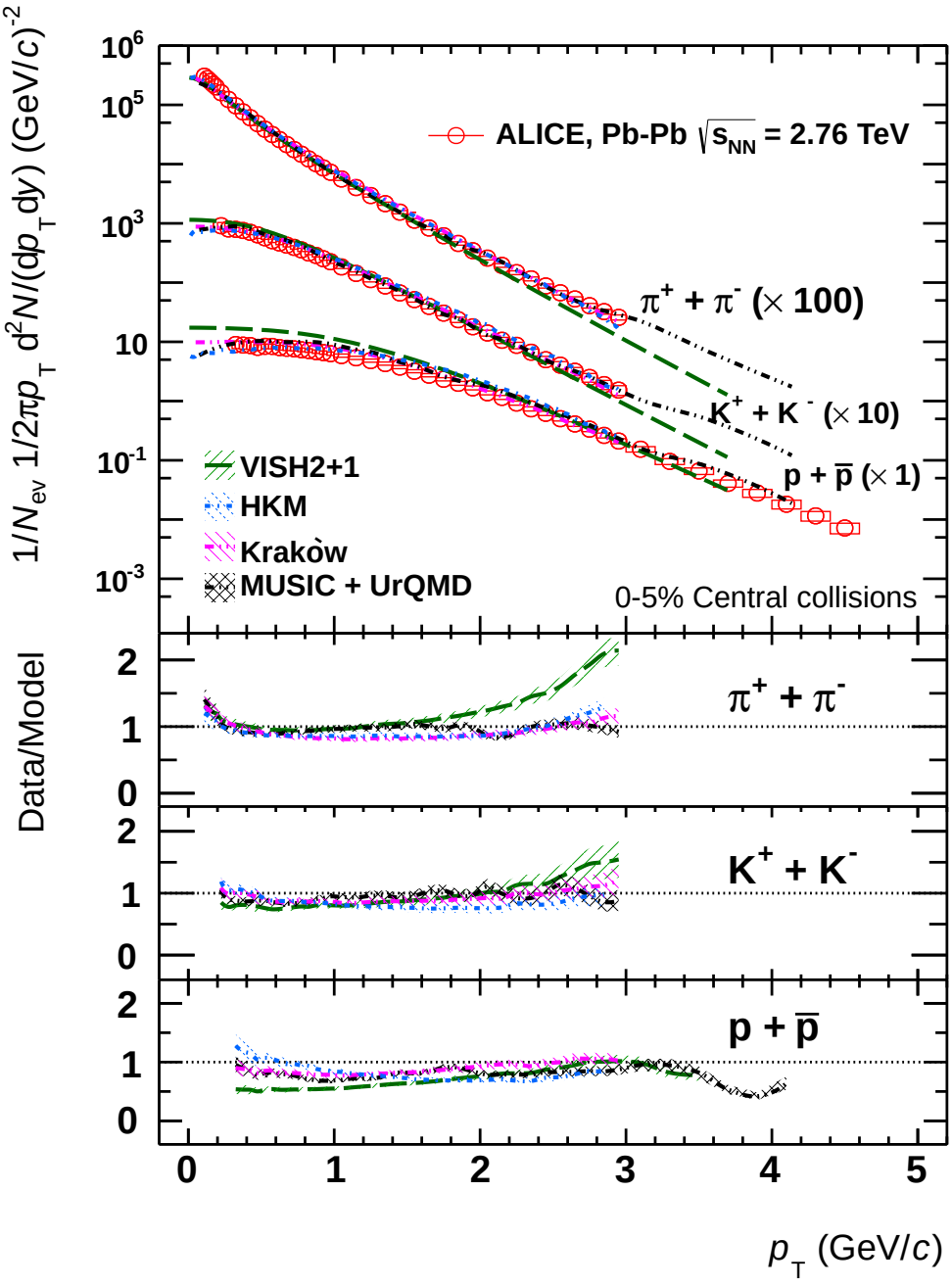

Figure 5.2: Transverse momentum distributions of the sum of positive and negative particles (box: systematic errors; statistical errors smaller than the symbol for most data points) compared to hydrodynamic models (from [71]).

contribution from jets and mini-jets which is not included in the model).

From these comparisons one can conclude that particle $p_{\rm T}$ spectra in central (0-5%) Pb–Pb collisions at $\sqrt{s_{\rm NN}}$ = 2.76 TeV at the LHC show an hydrodynamic behaviour. Models including a refined description of the late fireball evolution are able to nicely reproduce the data.

5.1.2 $\mathbf{p_T}$ distributions as a function of centrality

The measurement presented in Sec. 5.1.1 has been extended to different centrality classes to study the hadron $p_{\rm T}$ distribution as a function of centrality. The ALICE measurement of identified particle spectra for different centrality classes in Pb–Pb collisions at $\sqrt{s_{\rm NN}}$ = 2.76 TeV is reported in Figure 5.3.

The distributions of positive and negative particles are compatible within errors over the whole measured $p_{\rm T}$ range, as expected at LHC energies and seen in the ratio of negative to positive $p_{\rm T}$ spectra shown in Figure 5.4. The negative to positive ratio as a function of $\mathrm{d}N_{\rm ch}/\mathrm{d}\eta$ is reported in Figure 5.5 for LHC and RHIC. The ratios of the negative to positive values are compatible with unity for all centralities at the LHC. The $\bar{\rm p}$/p ratio, in particular, confirms the expectation of a vanishingly small baryon transport to mid-rapidity at the LHC. This is not the case at RHIC energy, where the $\bar{\rm p}$/p ratio was found to be about 0.8 for central Au–Au collisions at $\sqrt{s_{\rm NN}}$ = 200 GeV.

The shape of the spectra shown in Fig. 5.3 evolves with the centrality of the collision: spectra get harder with increasing centrality, this is more evident for protons. This modification is due to the stronger radial flow in central Pb–Pb collisions. In central collisions the $p_{\rm T}$ shape is mainly exponential at high $p_{\rm T}$. In more peripheral collisions, the onset of the pQCD power-law tail, typical of p–p collisions [63], starts to be visible.

In order to study the observed shape modification with centrality the local inverse slope T_{loc} of spectra, as a function of $p_{\rm T}$ is reported in Figure 5.6. It is evaluated from a fit using five bins in the proximity of each $p_{\rm T}$ bin with the function:

$$\frac{1}{p_{\rm T}}\frac{\mathrm{d}N}{\mathrm{d}p_{\rm T}} \propto e^{-p_{\rm T}/T_{loc}} \tag{5.3}$$

As expected K and p spectra are harder (less steep) at low $p_{\rm T}$. The evolution of T_{loc} with $p_{\rm T}$ is more pronounced for more central events and becomes smaller with increasing $p_{\rm T}$. Above $p_{\rm T} \sim 1$ GeV/c for K and $p_{\rm T} \sim 2$ GeV/c for p, the slope does not change with $p_{\rm T}$ for central and semi-central collisions, consistent with an exponential shape, as already observed in Fig. 5.3. On the other hand in peripheral collisions T_{loc} increases

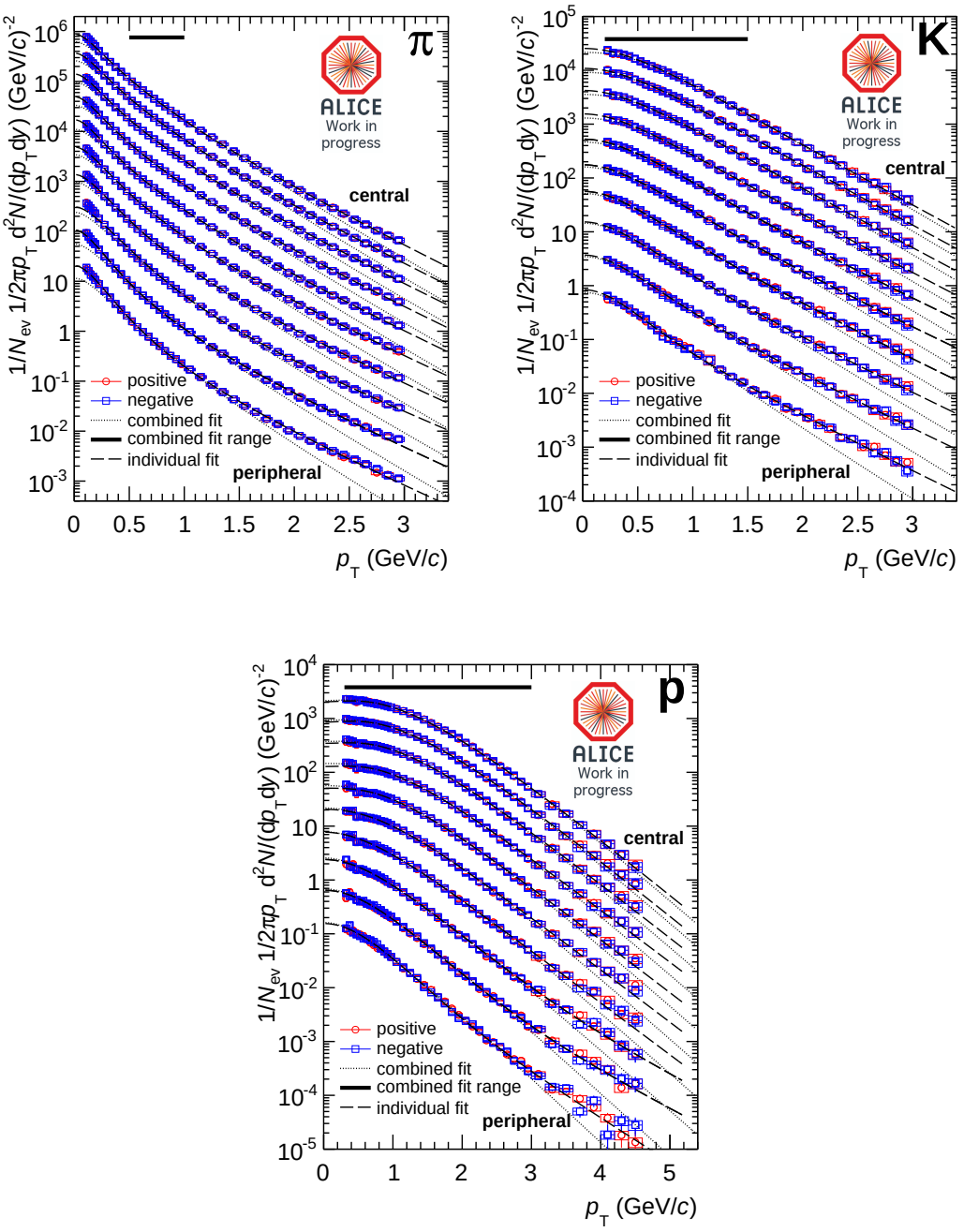

Figure 5.3: Transverse momentum distribution of π, K, and p as a function of centrality, for positive (circles) and negative (squares) particles (from [78]). Top to bottom: central to peripheral; spectra scaled by factors 2^n. Continuous curves: blast wave fits to individual particles; dashed curves: combined blast wave fits (see text for details). Statistical (error bars) and systematic (boxes) errors plotted. An additional normalisation uncertainty (Table 6.1.1) has to be added in quadrature.

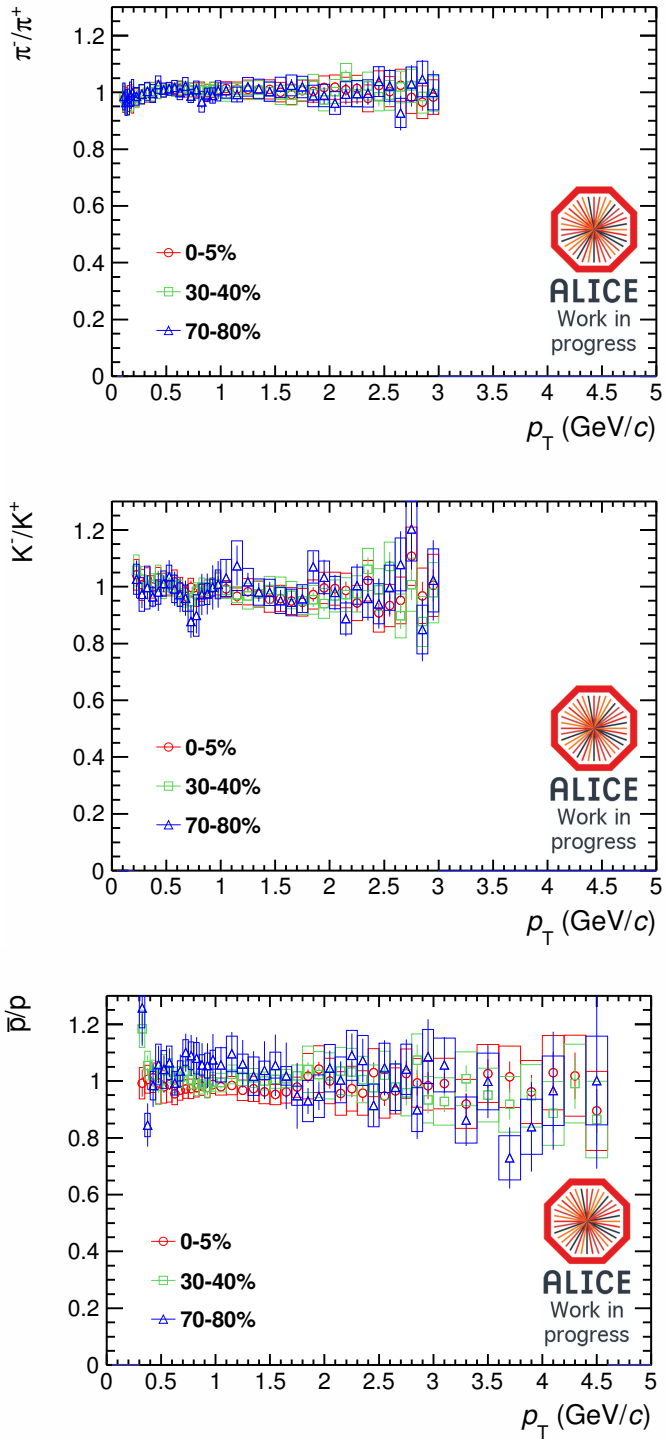

Figure 5.4: Ratio of negative to positive particles as a function of p_T for different centrality classes (from [78]).

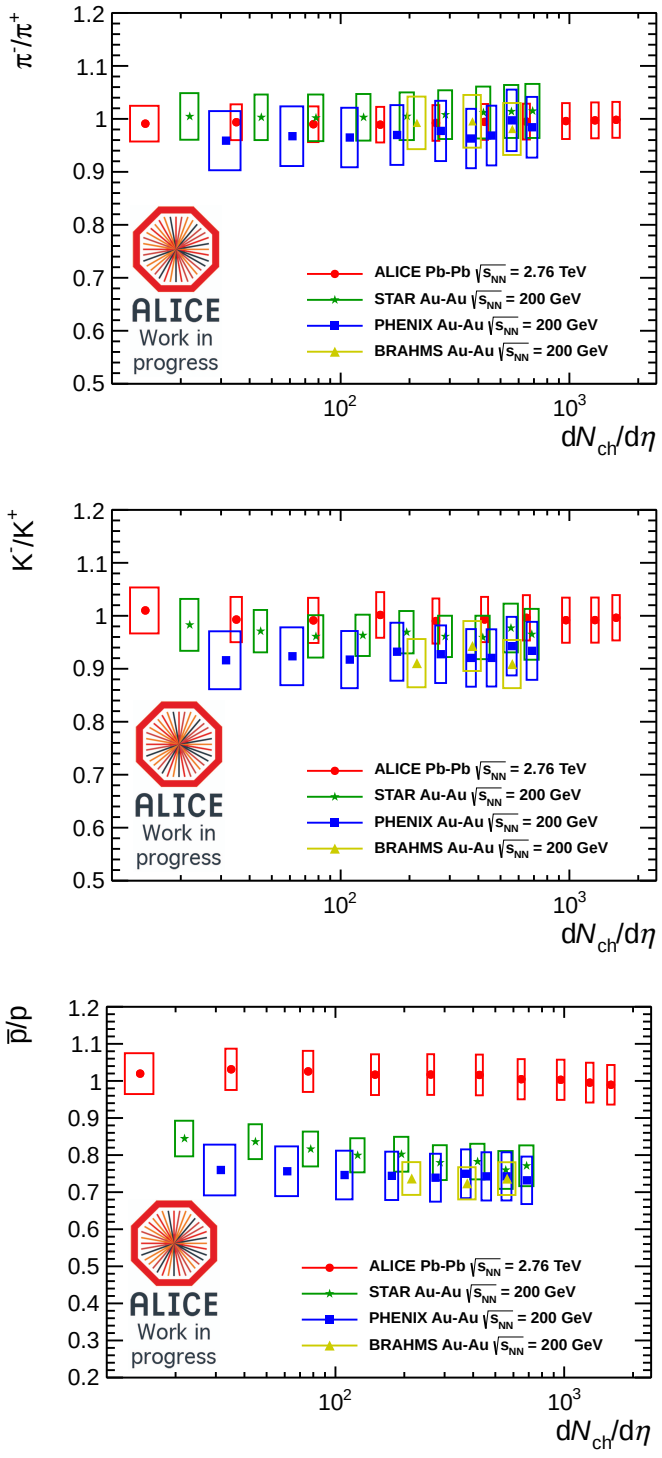

Figure 5.5: Ratio of negative to positive particles as a function of $\mathrm{d}N_{\mathrm{ch}}/\mathrm{d}\eta$ at the LHC and at RHIC (from [78]).

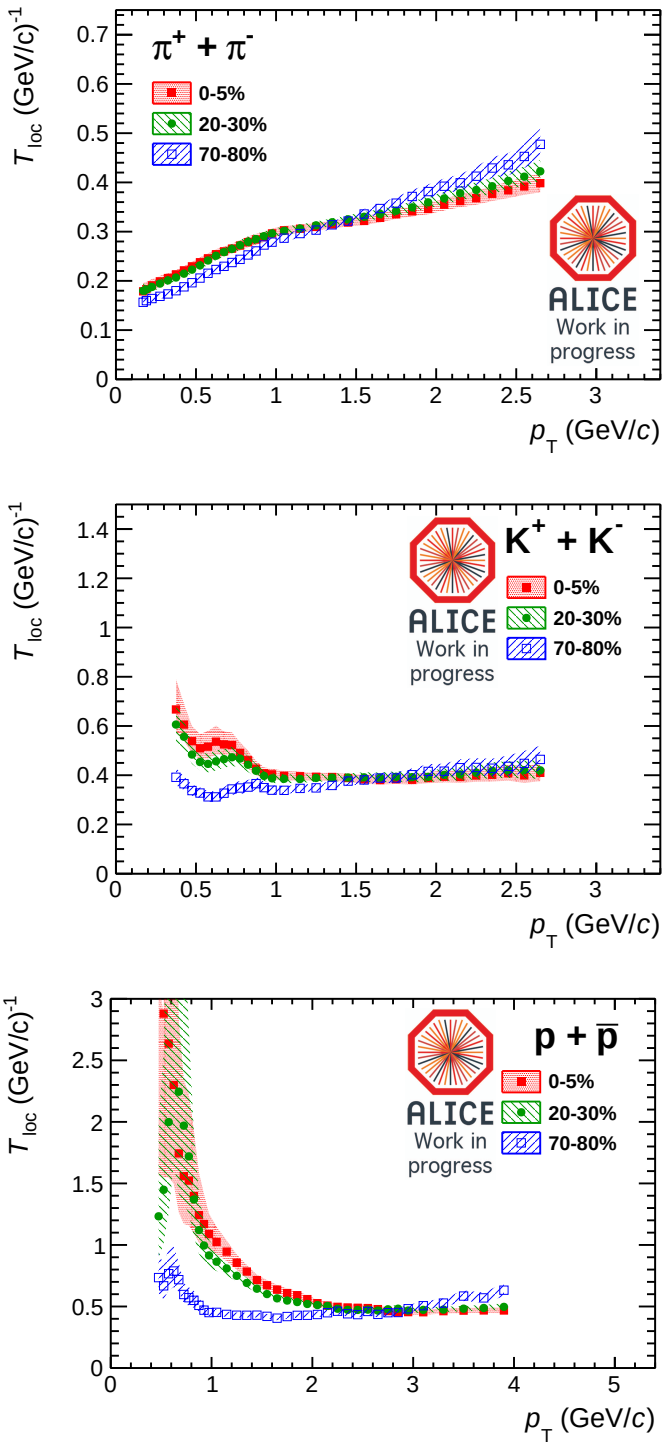

Figure 5.6: Local slopes of the transverse momentum distributions of π, K, and p (summed charges) as a function of centrality (from [78]).

slightly at the highest $p_{\rm T}$, indicating that the onset of a power-law behaviour starts to be visible. Pions show a completely different behaviour. At low $p_{\rm T}$, T_{loc} increases with $p_{\rm T}$, the opposite trend observed for kaons and protons. This steepening of the spectra is due to the large contribution of resonance decays to the pion spectrum [72]. Above $p_{\rm T} \simeq 1$ GeV/c, T_{loc} keeps increasing, but at a lower rate and in a less pronounced way for central collisions. The π spectra are not purely exponential, but the power-law rise is much more suppressed in central collisions as compared to peripheral ones. The centrality dependence of the spectral shapes shown in Fig. 5.3 and Fig. 5.6 can be interpreted in terms of hydrodynamics. A flattening of the spectra, more pronounced at low $p_{\rm T}$ and for heavier particles is expected in the hydrodynamic models (as a consequence of the blue-shift induced by the collective expansion). The change of the local slope, especially in the proton spectra, thus suggests a progressively stronger radial flow.

In order to evaluate the average transverse momentum $\langle p_{\rm T} \rangle$, the hadron spectra are fitted individually with a blast wave function [72] (Eq. 5.1). This function is found to describe very well all particle species over the whole measured $p_{\rm T}$ range, as shown in Figure 6.1. It should be noted that from an individual fit to a single particle no physical meaning can be attached to the blast wave parameters, due to the strong correlations between them. The individual blast wave fit is represented by the full lines in Figure 5.3.

The mean transverse momentum $\langle p_{\rm T} \rangle$ as a function of $\mathrm{d}N_{\rm ch}/\mathrm{d}\eta$, compared to previous results at RHIC is shown in Figure 5.7. The systematic uncertainty was estimated using different fit functions (Boltzmann, $m_{\rm T}$ exponential, $p_{\rm T}$ exponential, Tsallis-Levy, Fermi-Dirac, Bose-Einstein) and changing the fit range for those functions not giving a satisfactory fit result over the measured $p_{\rm T}$ range. The uncertainty due to the extrapolation amounts to 2%, 2%, 3% (peripheral) and 2%, 3.5%, 3.5% (central) for π, K, p respectively. The $\langle p_{\rm T} \rangle$:

- increases with centrality (large radial flow in central collisions),
- is higher than that observed at lower energies for comparable charged particle density (radial flow increases with energy).

The $\langle p_{\rm T} \rangle$ measured in different centrality classes is reported in Table 5.2.

The freeze-out parameters T_{kin} and $\langle \beta_{\rm T} \rangle$ can be evaluated from a combined fit to the measured spectra using the blast wave function (eq. 5.1). The combined fits are represented by the dashed lines in Fig. 5.3. A similar fit to Au–Au collisions at $\sqrt{s_{\rm NN}} =$

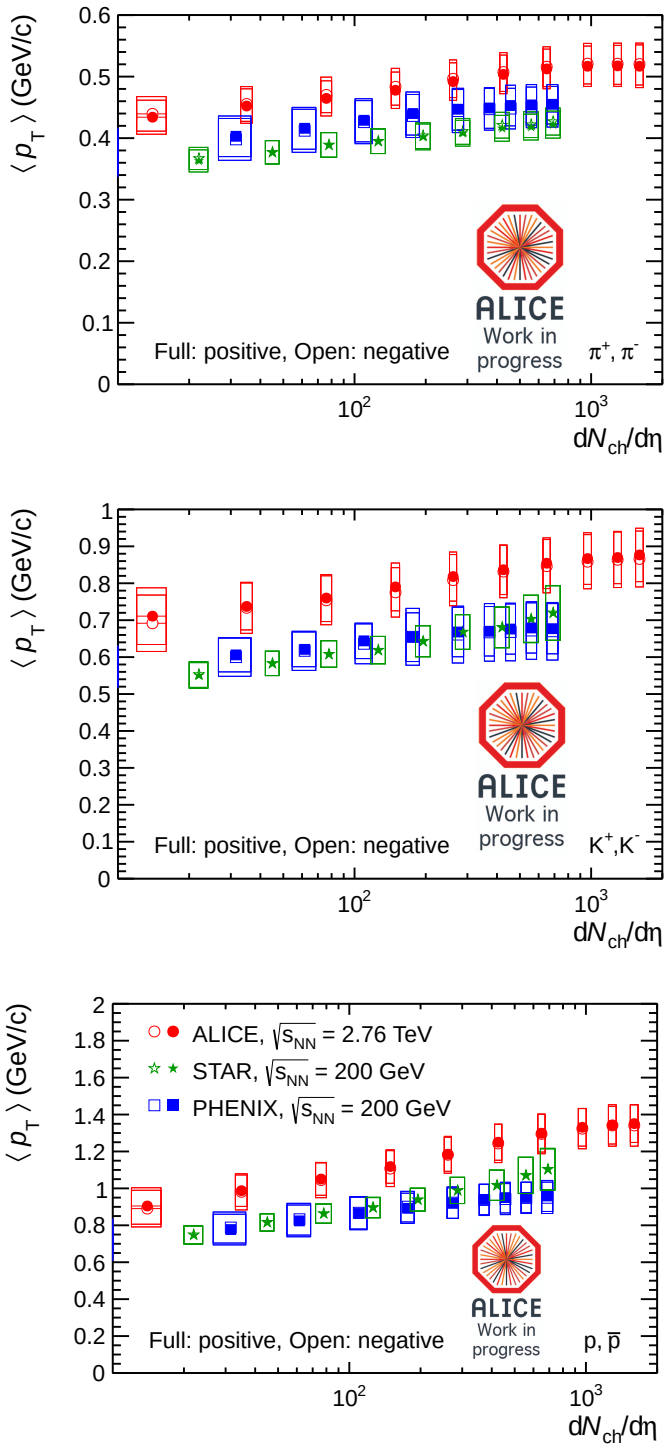

Figure 5.7: Mean transverse momentum $\langle p_{\mathrm{T}} \rangle$ as a function of $\mathrm{d}N_{\mathrm{ch}}/\mathrm{d}\eta$ compared to RHIC results at $\sqrt{s_{\mathrm{NN}}} = 200$ GeV (from [78]).

Centrality	π^+	π^-	K^+	K^-	p	$\overline{\mathrm{p}}$
0–5%	$0.52 \pm 0.0004 \pm 0.03$	$0.52 \pm 0.0004 \pm 0.03$	$0.88 \pm 0.002 \pm 0.07$	$0.87 \pm 0.003 \pm 0.08$	$1.35 \pm 0.004 \pm 0.10$	$1.34 \pm 0.005 \pm 0.11$
5–10%	$0.52 \pm 0.0005 \pm 0.03$	$0.52 \pm 0.0005 \pm 0.03$	$0.87 \pm 0.002 \pm 0.07$	$0.86 \pm 0.003 \pm 0.08$	$1.34 \pm 0.004 \pm 0.10$	$1.34 \pm 0.005 \pm 0.11$
10–20%	$0.52 \pm 0.0004 \pm 0.03$	$0.52 \pm 0.0004 \pm 0.03$	$0.87 \pm 0.002 \pm 0.07$	$0.86 \pm 0.002 \pm 0.07$	$1.33 \pm 0.003 \pm 0.10$	$1.32 \pm 0.004 \pm 0.11$
20–30%	$0.51 \pm 0.0004 \pm 0.03$	$0.52 \pm 0.0004 \pm 0.03$	$0.85 \pm 0.002 \pm 0.07$	$0.85 \pm 0.002 \pm 0.07$	$1.30 \pm 0.003 \pm 0.10$	$1.30 \pm 0.004 \pm 0.11$
30–40%	$0.50 \pm 0.0005 \pm 0.03$	$0.51 \pm 0.0005 \pm 0.03$	$0.84 \pm 0.002 \pm 0.07$	$0.83 \pm 0.003 \pm 0.07$	$1.25 \pm 0.004 \pm 0.10$	$1.24 \pm 0.005 \pm 0.10$
40–50%	$0.49 \pm 0.0005 \pm 0.03$	$0.50 \pm 0.0005 \pm 0.03$	$0.82 \pm 0.003 \pm 0.07$	$0.81 \pm 0.003 \pm 0.07$	$1.18 \pm 0.004 \pm 0.09$	$1.18 \pm 0.006 \pm 0.10$
50–60%	$0.48 \pm 0.0007 \pm 0.03$	$0.48 \pm 0.0007 \pm 0.03$	$0.79 \pm 0.004 \pm 0.06$	$0.78 \pm 0.004 \pm 0.07$	$1.12 \pm 0.005 \pm 0.09$	$1.11 \pm 0.007 \pm 0.10$
60–70%	$0.46 \pm 0.0008 \pm 0.03$	$0.47 \pm 0.0008 \pm 0.03$	$0.76 \pm 0.004 \pm 0.06$	$0.75 \pm 0.005 \pm 0.07$	$1.05 \pm 0.006 \pm 0.09$	$1.05 \pm 0.008 \pm 0.10$
70–80%	$0.45 \pm 0.0009 \pm 0.03$	$0.46 \pm 0.0009 \pm 0.03$	$0.74 \pm 0.005 \pm 0.06$	$0.73 \pm 0.006 \pm 0.07$	$0.99 \pm 0.007 \pm 0.09$	$0.98 \pm 0.009 \pm 0.10$
80–90%	$0.43 \pm 0.0013 \pm 0.03$	$0.44 \pm 0.0013 \pm 0.03$	$0.71 \pm 0.007 \pm 0.08$	$0.69 \pm 0.008 \pm 0.08$	$0.90 \pm 0.009 \pm 0.10$	$0.89 \pm 0.012 \pm 0.10$

Table 5.2: $\langle p_{\mathrm{T}} \rangle$ as a function of centrality (GeV/c), statistical errors and systematic errors including extrapolation uncertainty (from [78] - Work in progress).

200 GeV was performed in [73] and [74]. The $p_{\rm T}$ ranges used in the fit are 0.5-1 GeV/c, 0.2-1.5 GeV/c, 0.3-3 GeV/c for π, K and p respectively. The ratio of the measured spectra to the combined fits is shown in Figure 5.8. If the behaviour of the spectra would be purely hydrodynamic over the full considered $p_{\rm T}$ range, one would expect the parameters determined by a fit in a limited $p_{\rm T}$ range to be able to predict the full shape. This is what is observed in the most central bin for protons and kaons. The same is not true for the more peripheral bins, and the $p_{\rm T}$ threshold at which the function deviates from the data decreases with centrality, indicating the limit of applicability of the hydrodynamic picture. The discrepancy observed for pions at low $p_{\rm T}$ is due to the large contribution from resonances to the pion spectrum. The resulting values of the fit parameters (T_{kin} and $\langle\beta_{\rm T}\rangle$) are shown in Figure 5.9 and compared with RHIC results. The uncertainty contours include the effect of the bin-by-bin systematic uncertainty. The dashed error bars represents the full systematic uncertainty, including besides the bin-to-bin systematic uncertainties, the effect of the variation of the lower fit bound for pions (to test the effect of resonance feed-down), the sensitivity to different particle species (i.e. excluding pions or Kaons or protons) and to the individual analyses. It should be noted that T_{kin} is sensitive to the pion fit range (due to large contribution from resonances) while $\langle\beta_{\rm T}\rangle$ does not strongly depend on the $p_{\rm T}$ range used in the fit. These fits by no means replace a full hydro calculation: their usefulness lie in the ability to compare with a few, simple, parameters the measurements of different experiments. In order to test the stability of this result, the fit was repeated in the ranges (for π, K, p respectively):

- high $p_{\rm T}$ range: 1-2 GeV/c, 0.5-1.5 GeV/c, 1-3 GeV/c,
- low $p_{\rm T}$ range: 0.3-0.7 GeV/c, 0.2-1 GeV/c, 0.3-1.5 GeV/c.

The results are shown in Figure 5.10 compared to the default ones. As it can be observed, while the value of $\langle\beta_{\rm T}\rangle$ is relatively stable, especially for the most central bins, the value of T_{kin} is strongly affected by the fit range, with differences of the order of 20 MeV also for the most central events. For most peripheral events, also $\langle\beta_{\rm T}\rangle$ shows some instability, albeit the uncertainty on this parameter increases significantly when the fit range for the protons is reduced.

Particle spectra in 20-30% and 70-80% are compared with the available hydrodynamic models and previous RHIC results for Au–Au collisions at $\sqrt{s_{\rm NN}} = 200$ GeV in Figure 5.11 and Figure 5.12. Models are described in Section 5.1.1. As already discussed when commenting Figure 5.2, the change in shape with respect to RHIC is evident. A general

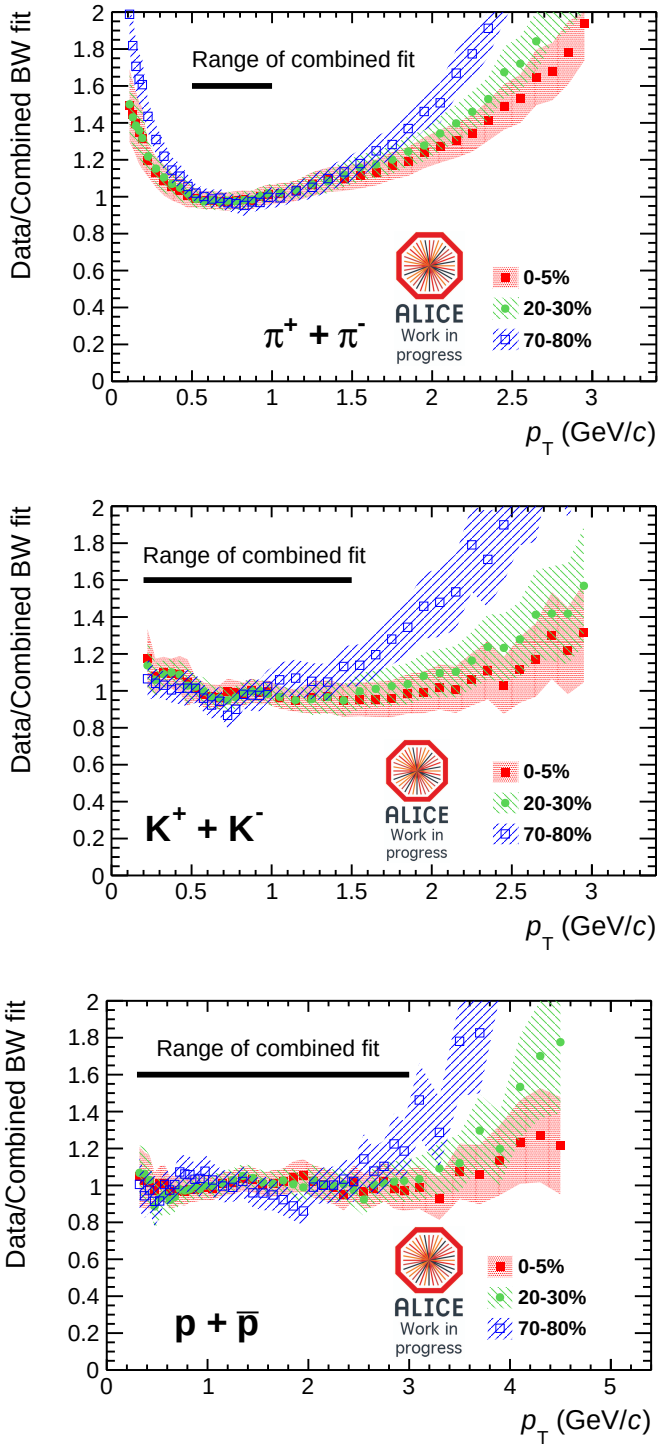

Figure 5.8: Ratio of the measured spectra to the combined blast-wave fit for 3 different centrality classes (from [78]).

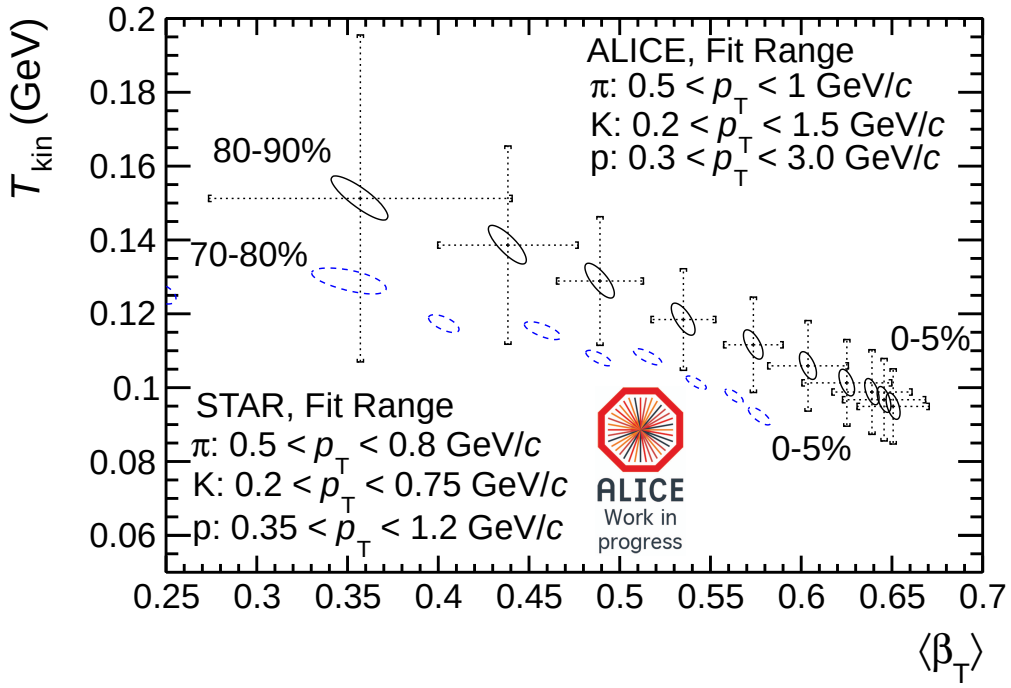

Figure 5.9: T_{kin} and $\langle\beta_{\mathrm{T}}\rangle$ from blast wave fits in different centrality classes, compared to similar fits at RHIC energies (from [78]). The uncertainty contours include the effect of the bin-by-bin systematic uncertainty, the dashed error bars represents the full systematic uncertainty (see text for details), the STAR contours include only statistical uncertainties.

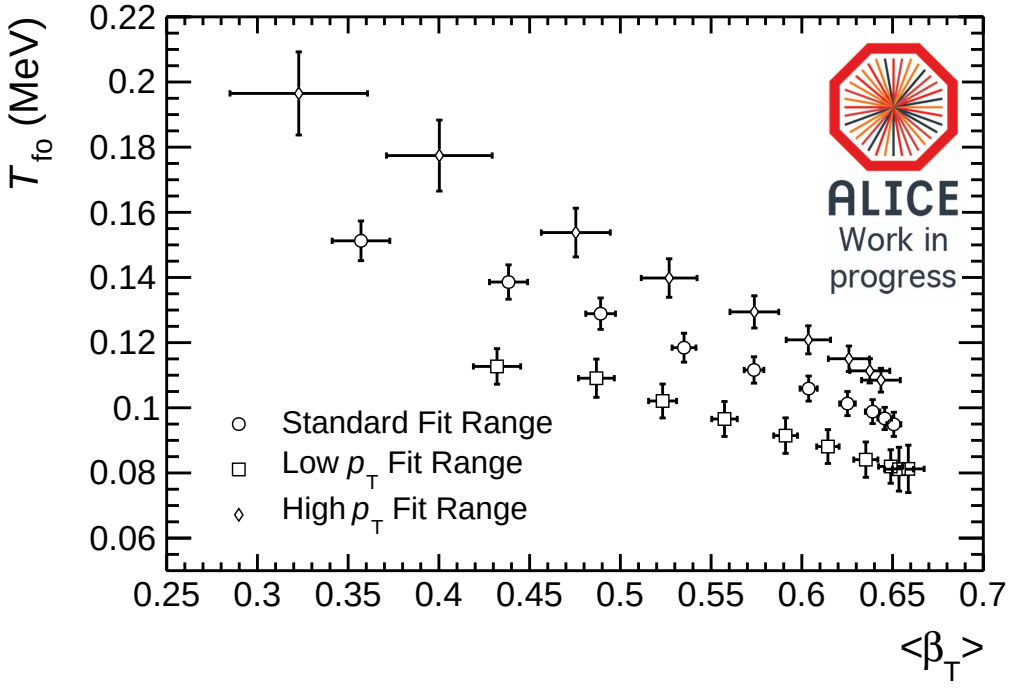

Figure 5.10: Comparison of fit results for different fit ranges; the error bars include only the effect of the bin-by-bin systematics (from [78]).

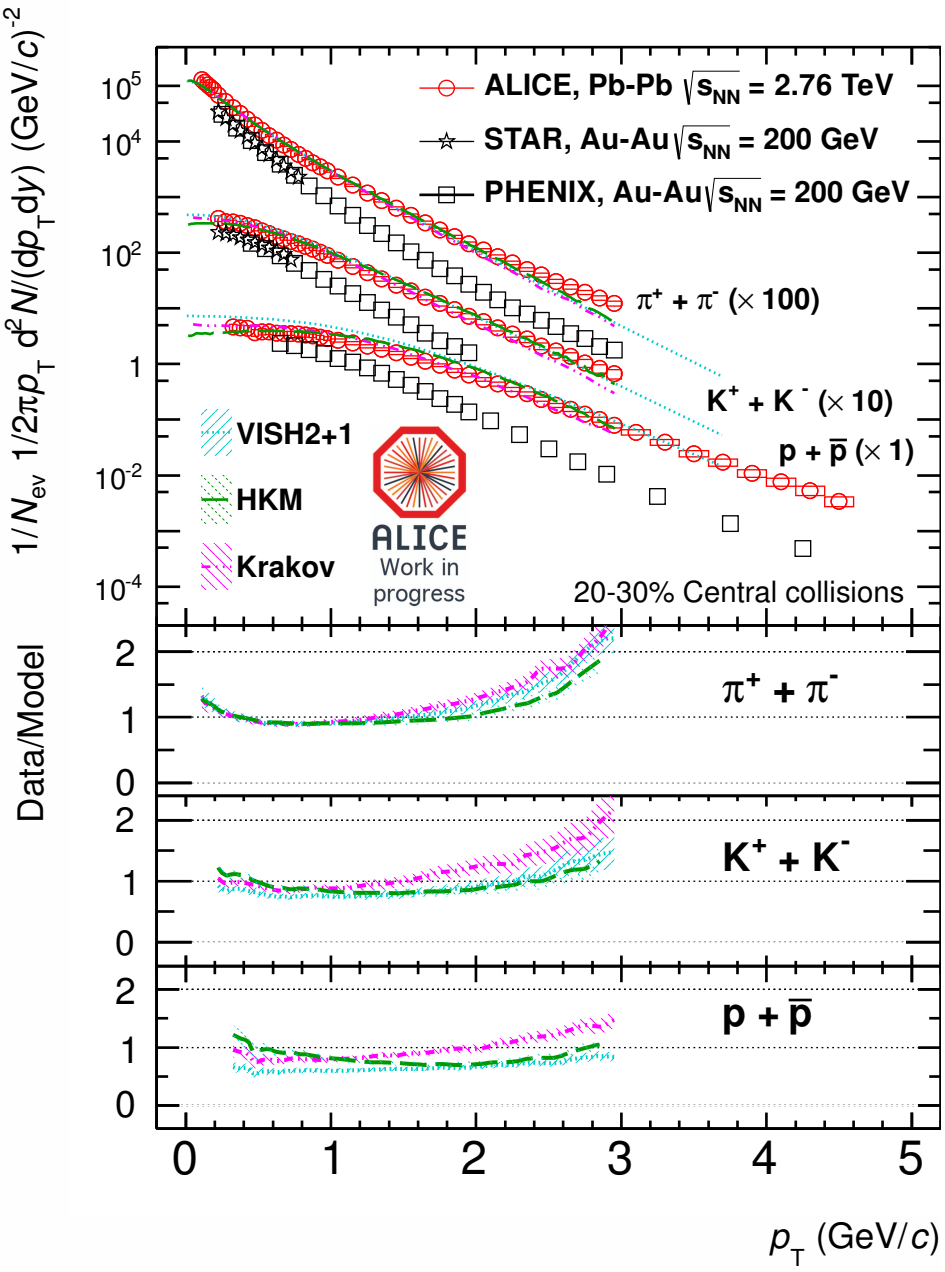

Figure 5.11: Spectra of particles (sum of positive and negative) in the centrality class 20-30% compared to hydrodynamic models and previous RHIC results for Au–Au collisions at $\sqrt{s_{\rm NN}}$ = 200 GeV (from [78]). Statistical (bars) and systematic (boxes) errors are plotted.

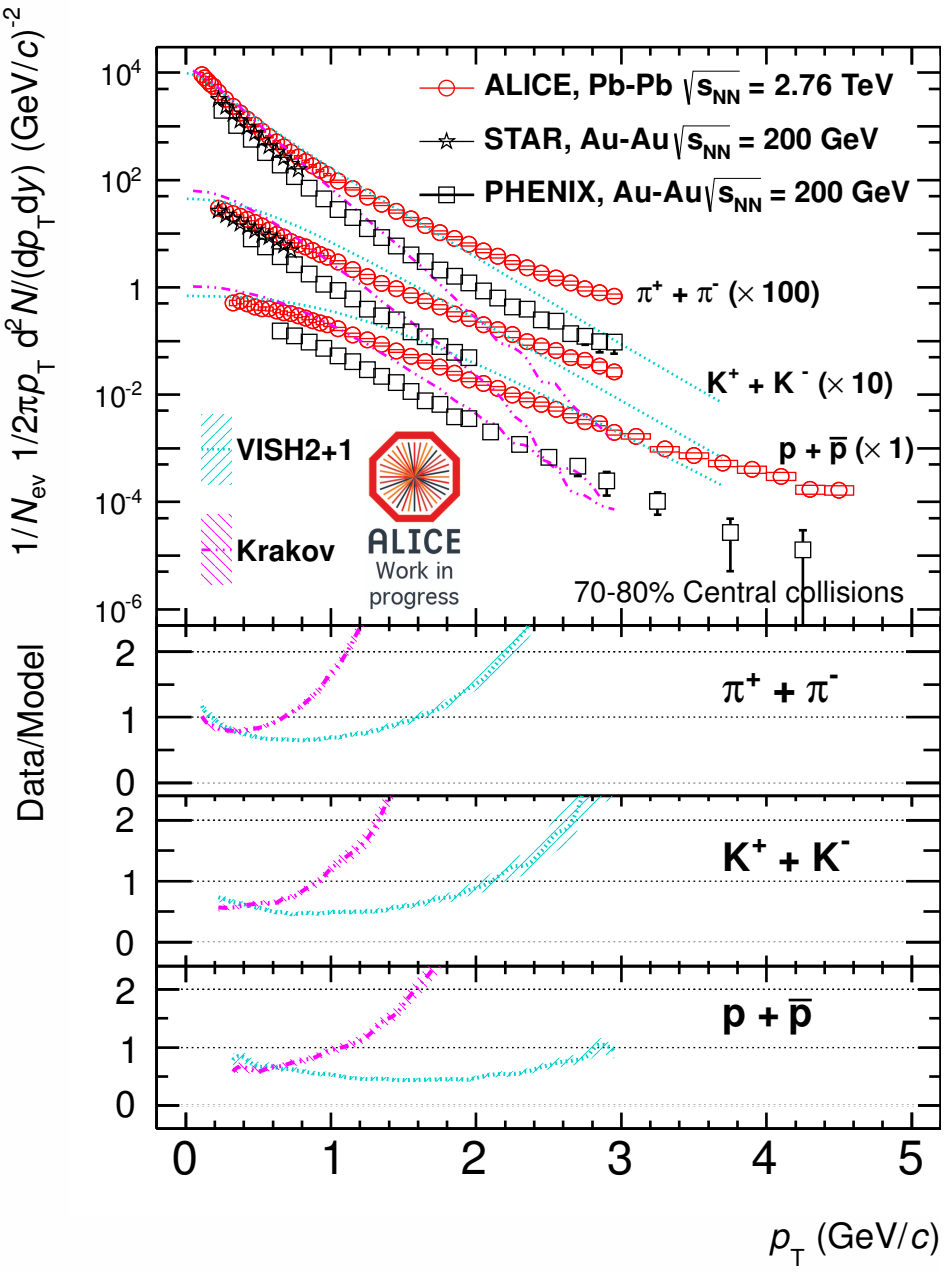

Figure 5.12: Spectra of particles (sum of positive and negative) in the centrality class 70-80% compared to hydrodynamic models and previous RHIC results for Au–Au collisions at $\sqrt{s_{\rm NN}}$ = 200 GeV (from [78]). Statistical (bars) and systematic (boxes) errors are plotted.

feature of all the models is that, going to more peripheral events, the theoretical curves start to deviate from the measured data at high p_{T} (Fig. 5.11 and Fig. 5.12). In Sec. 5.1.1 it was shown that in central (0-5%) Pb–Pb collisions data suggest an hydrodynamic behaviour at the LHC. When going to more peripheral events an increasing discrepancy between hydrodynamic models and measured spectra starts to appear. This could indicate the onset of a non-thermal (hard) component, which in more peripheral collisions is not dominated by the flow-boosted thermal component [79].

5.2 $\mathbf{p_T}$ distributions as a function of the event-by-event flow

As explained in Sec. 2.2.2 collective flow is an unavoidable consequence of the Quark Gluon Plasma formation. The hadron p_{T} distributions in Pb–Pb collisions show a strong radial flow given by the pressure gradient between the thermal pressure of the fireball and the surrounding vacuum. Together with radial flow, anisotropic flow is a sign of multiple interactions between constituents, eventually leading to thermalisation. This behaviour is interpreted in terms of hydrodynamics. Some of the fundamental properties of the matter created in nucleus-nucleus collisions (such as the sound velocity, the shear viscosity and the spatial eccentricity) can be constrained by the elliptic flow measurement.

5.2.1 Event Shape Engineering - ESE

The integrated elliptic flow at the LHC was found to be $\sim 30\%$ larger with respect to RHIC value [24]. If one looks at the elliptic flow on an event-by-event basis this increase can be much larger. This is due to the fact that for a given centrality the eccentricity of the distribution of participant nucleons (related with the specific initial geometry) fluctuates [80]. The eccentricity distribution in Monte Carlo Glauber model versus the impact parameter, b, in Au–Au collisions is reported in Figure 5.13 (from [80]). The eccentricity is defined as

$$\epsilon = \frac{\sum_i y_i'^2 - \sum_i x_i'^2}{\sum_i y_i'^2 + \sum_i x_i'^2} \tag{5.4}$$

where $x_i^{'}$ and $y_i^{'}$ are the coordinates of the constituents in the plane perpendicular to the beam and $x^{'}$ is in the reaction plane [80]. It is an estimate of the initial *spatial* anisotropy of the system, that is expected to give rise to the *momentum* anisotropy of final state particles, that is quantified by the elliptic flow measurement.

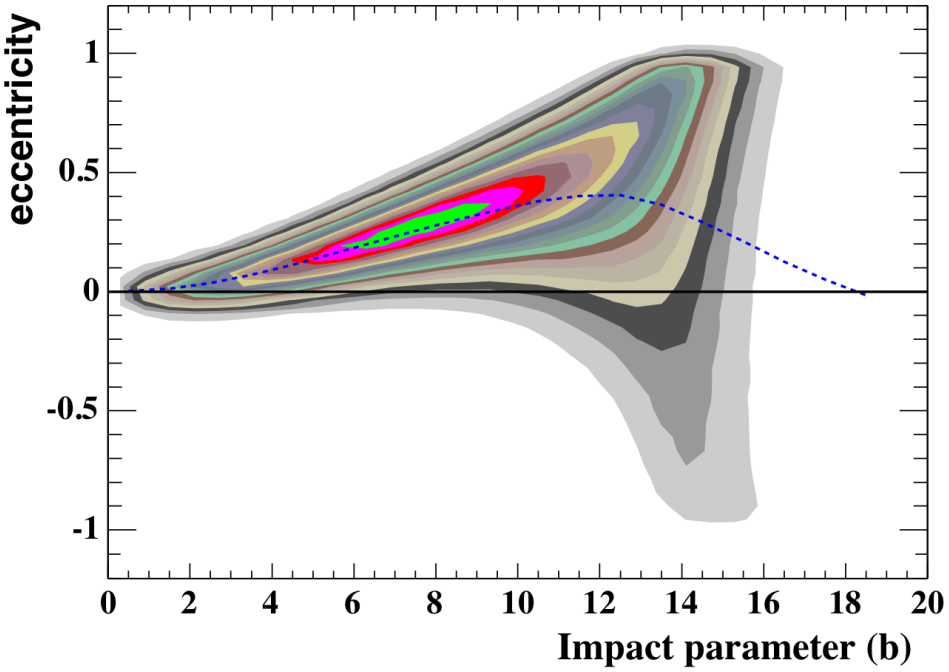

Figure 5.13: Contour plot of the calculated eccentricity in Monte Carlo Glauber model versus the impact parameter, b, in Au+Au collisions (from [80]). The mean value of the eccentricity is represented by the dashed curve.

The way to experimentally select events based on the geometry of the overlapping region (so called "Event Shape Engineering" - ESE) was presented for the first time in [81] and [82]. One way to do this is using the VZERO detector to calculate the flow vector $\vec{Q}_2$, a 2D vector with components:

$$Q_{2,x} = \sum_i w_i \cos(2\phi_i), \qquad Q_{2,y} = \sum_i w_i \sin(2\phi_i) \tag{5.5}$$

where the sum i runs over all the azimuthal sectors of the VZERO detector, w_i is the i signal amplitude and ϕ_i is azimuthal angle of the centre of sector i. The module of the $\vec{Q}_2$ vector is normalized to the multiplicity M in the VZERO:

$$q_2 = \frac{|Q_2|}{\sqrt{M}}. \tag{5.6}$$

The probability of having a given value of q_2 is reported in Figure 5.14 for the 30-40% centrality class (upper panel). The bottom panel shows the cumulative probability distribution. From the latter distribution it is possible to tune the event selection. The cuts have been tuned to select the 10% highest (lowest) q_2 events. In order to reduce the correlation between the centrality and the q_2 selection, tracks reconstructed in the central barrel are used to estimate the centrality [7]. In this way it is possible to have a large pseudo-rapidity gap between the region at mid-rapidity where the centrality and the spectra are measured and the forward rapidity used to measure q_2, as reported in Figure 5.15. The ESE allows the selection of events with different value of the elliptic flow, with negligible non-flow contributions. This is shown in Figure 5.16 in which the measured v_2 value is reported as a function of transverse momentum p_{T} for the unbiased sample and for events selected according to the ESE.

5.2.2 Potential biases

The q_2 selection could introduce two different types of bias. A detailed study of these effects is needed in order to be sure that the final observed effect is not a trivial consequence of the event selection:

Multiplicity bias

In [24] it is possible to see that in the selected centrality class (30-40%) the v_2 distribution is not flat but rather decreases from peripheral to central events, as also reported in Figure 5.17. Figure 5.18 shows the unidentified charged hadron ($All_{Charged}$) distribu-

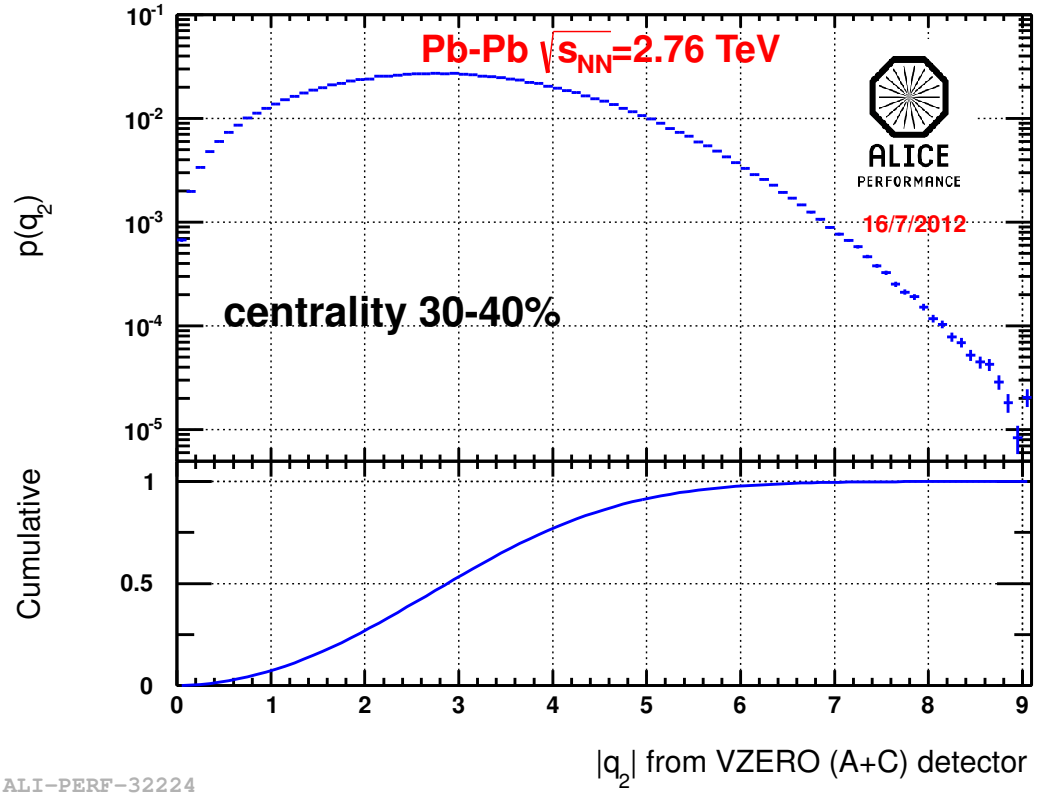

Figure 5.14: Probability of having a given value of q_2 (upper panel) for the 30-40% centrality class. Cumulative probability distribution (bottom panel).

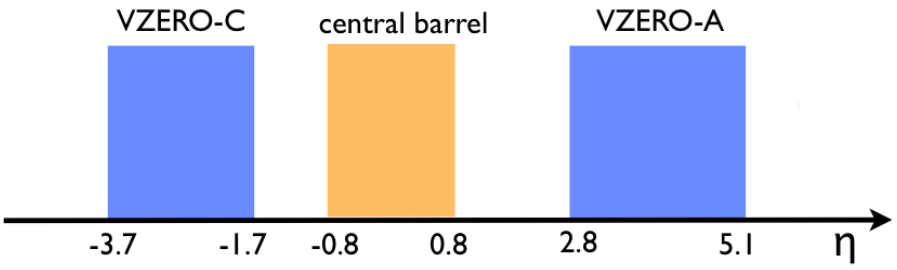

Figure 5.15: Pseudo-rapidity gap between the region at mid-rapidity where the spectra and centrality are measured and the forward rapidity regions where the flow vector q_2 is calculated.

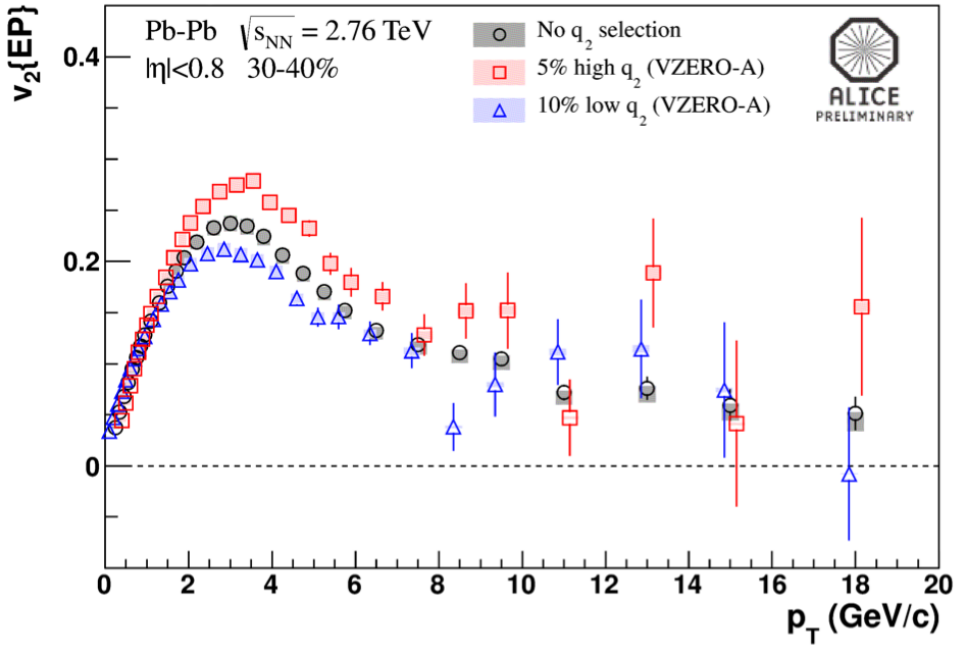

Figure 5.16: Measured v_2 value is reported as a function of transverse momentum p_T for the unbiased sample and for events selected according to the ESE (from [82]).

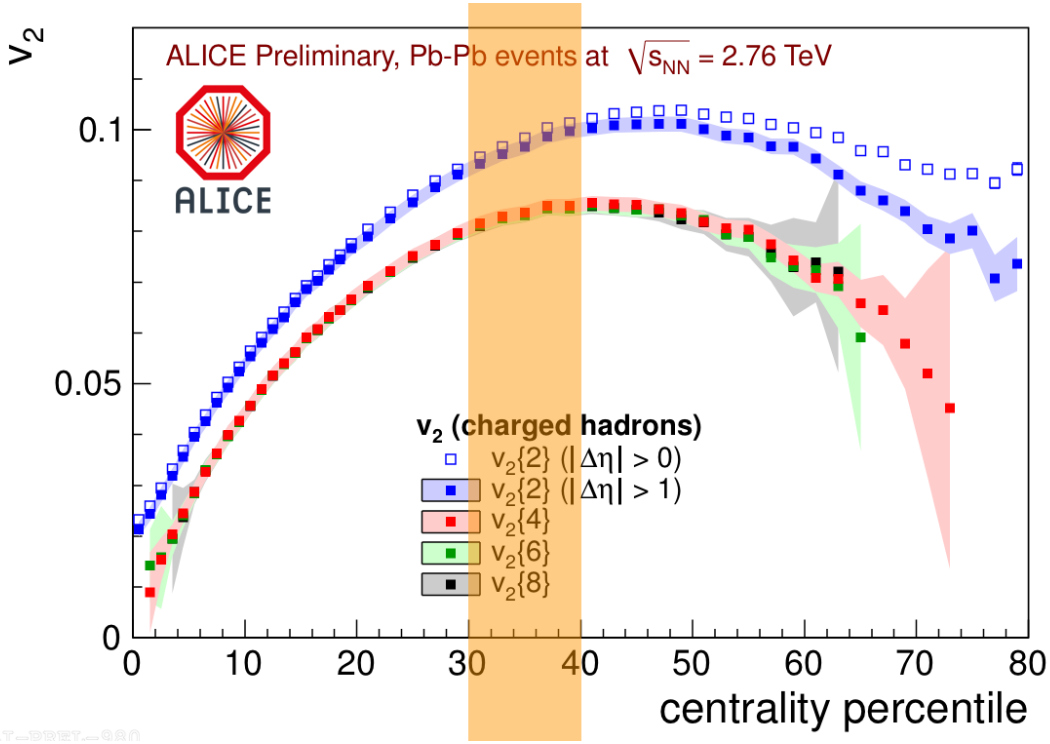

Figure 5.17: v_2 distribution (from [24]). The centrality class used in this analysis is highlighted.

tion for the small-q_2 and the large-q_2 sample, normalised to the number of entries. The large-q_2 sample distribution seems to be a bit shifted towards small multiplicities. This is expected: elliptic flow increases with decreasing centrality (Fig. 5.17). When selecting events with large value of q_2 we bias the sample (inside the selected centrality bin) towards smaller multiplicity (i.e. more peripheral events). In order to estimate its size two

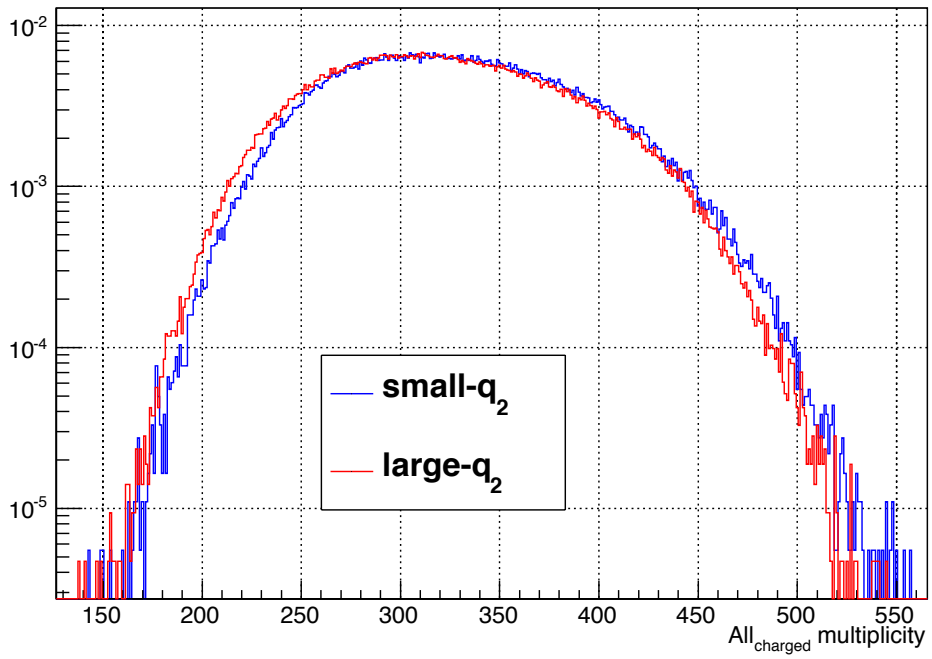

Figure 5.18: $All_{Charged}$ distribution for the small-q_2 and the large-q_2 samples, normalised to the number of entries.

different checks have been performed:

- The analysis has been repeated with a cut in multiplicity. In order to get rid of the edges of the distributions where the discrepancy between the two samples is observed, only the range [260,400] for $All_{Charged}$ has been used in the analysis and the final result is found to be in good agreement with the default analysis.

- Two different classes with large overlap are considered: [30-40%] and [31-41%], without any selection on q_2. The ratio [31-41%]/[30-40%] is reported in Figure 5.19 for $All_{Charged}$ and all the particles species as a function of p_T. As expected, a small shift of the order of 1% is observed.

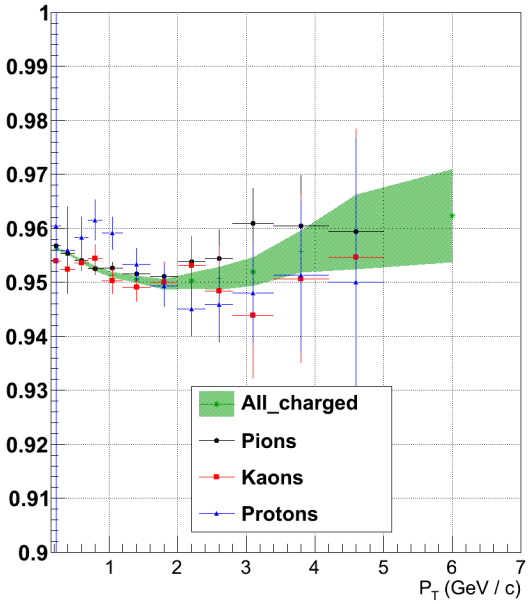

Figure 5.19: Ratio [31-41%]/[30-40%] for the p_T distribution of $All_{Charged}$ and of the various particle species

In order to get rid of this bias, the centrality bin 30-40% has been split in 10 bins 1% wide and the spectra for the small q_2 and large q_2 samples are obtained as the sum of the spectra in each single bin. A similar procedure is used in the flow analysis for similar purposes. In this way the $All_{Charged}$ distribution in the large-q_2 and in the unbiased sample is similar, as demonstrated by the flat ratio in Figure 5.20 (bottom-right plot). From Figure 5.20 it is possible to conclude that using this "splitting" procedure it is possible to get rid of the multiplicity bias. The final result for the 30-40% centrality class is obtained using this procedure to obtain the 30-40% bin. In addition to this a cut on $All_{Charged}$ [260,400] is applied for the final result, to further reduce the shift in multiplicity. The effect of the multiplicity shift is therefore negligible.

Jet contribution

Jets can contribute to the azimuthal anisotropy of the event giving rise to a contribution to the elliptic flow not due to collective motion (non-flow contribution). In order to estimate the contamination from jets, the uncorrected transverse momentum $p_{T,jet}$ distribution of reconstructed jets has been studied in the small q_2 and large q_2 samples. A simplifies jet cone algorithm is used. The transverse momentum density ρ is defined as:

$$\rho = \frac{p_{T,\text{total}}}{\text{total acceptance}} \tag{5.7}$$

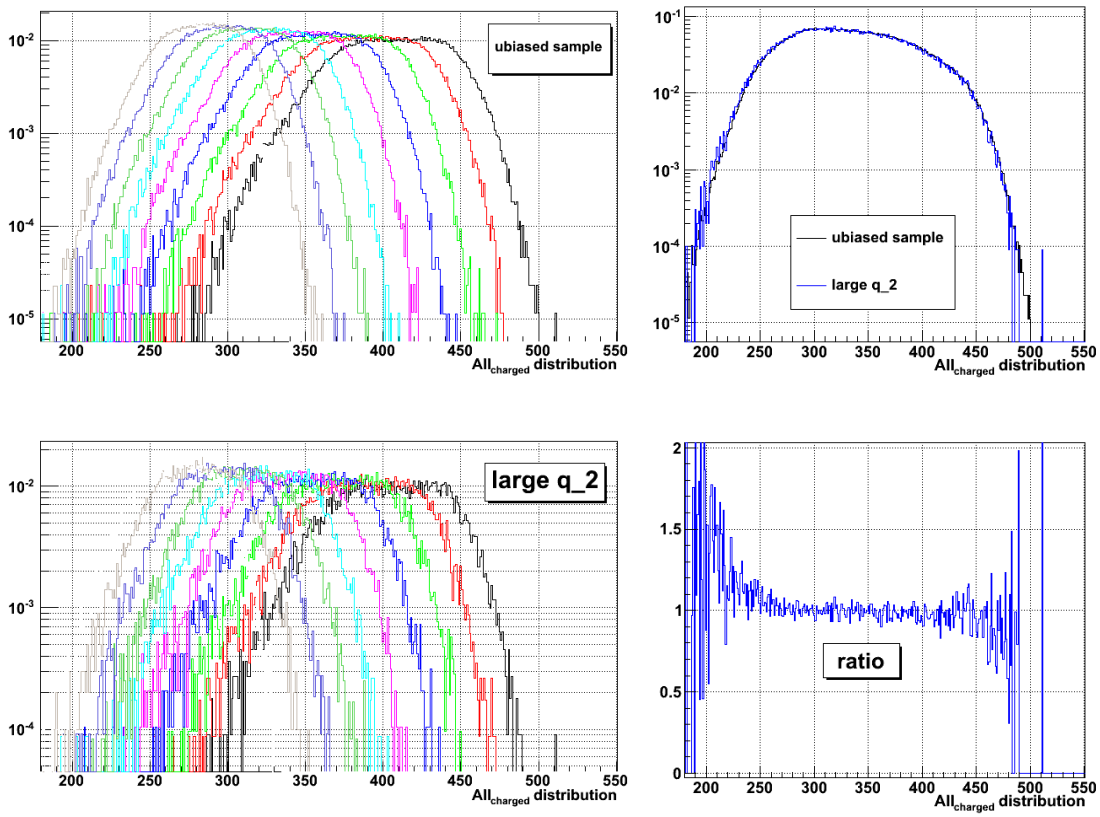

Figure 5.20: Centrality class 30-40% has been split in 10 1% wide intervals and the spectra are obtained as the sum of spectra in single bins. The $All_{Charged}$ distribution is reported here for single intervals and their sum. In the bottom-right plot the ratio between the unbiased sample and the large-q_2 is reported.

where $p_{\mathrm{T,total}}$ is the sum of all the p_{T} of tracks in our acceptance ($2\pi(\phi) \times 1.6(\eta)$). A seed particle is defined as a particle in the event with $p_{\mathrm{T}} > 5$ GeV/c. Every particle with $p_{\mathrm{T}} > 5$ GeV/c is considered as a seed particle. An (η, ϕ) cone of radius R = 0.3 is defined around the seed particle. The p_{T} inside the cone ($p_{\mathrm{T,sum}}$) is calculated by summing the transverse momenta of particles with distance from the seed particle $d = \sqrt{\Delta_\eta + \Delta_\phi}$ smaller than R. The sum of the transverse momenta inside the cone $p_{\mathrm{T,sum}}$ is corrected for the background: the p_{T} of the jet (the cone is not a proper jet but it can be considered a good approximation of it at high enough p_{T}) is defined as:

$$p_{\mathrm{T,jet}} = p_{\mathrm{T,sum}} - \rho * \mathrm{area} \tag{5.8}$$

where area = $2\pi \times \mathrm{R}^2$. This method can be applied only at high enough p_{T} ($p_{\mathrm{T}} \gtrsim 20$ GeV/c): at low p_{T} several effects such as background fluctuations or random jet reconstruction are not taken into account in this raw jet measurement. The $p_{\mathrm{T,jet}}$ distribution of identified jets is reported in Figure 5.21 for the unbiased, small-q_2 and large-q_2 samples. The bottom plot shows the ratio between small-q_2 and large-q_2. This ratio is flat above $p_{\mathrm{T}} = 20$ GeV/c and it is compatible with unity. This is an hint that the non-flow contribution in the two samples is similar, as also demonstrated in [82]. The same check has been repeated with a p_{T} cut of 10 GeV/c for the seed particle and selecting only one seed particle per event.

These checks, together with the studies presented in [81] and [82], suggest that the Event Shape Engineering is a powerful tool to select events with different value of elliptic flow. In the selected samples the non flow contributions are negligible. It should be noted indeed that there is a large pseudo-rapidity gap between the region at mid-rapidity where the spectra are measured and the forward rapidity regions where the flow vector is calculated, as schematised in Figure 5.15.

5.2.3 Track selection and PID strategy

The analysis has been performed using Analysis Object Datasets AOD [70,83][1]. Global tracks are used in the analysis (i.e. tracks reconstructed using all the tracking detectors in the central barrel). Track candidates in the TPC are required to have hits in at least 120 (out of a maximum of 159) pad-rows and χ^2 per point of the momentum fit smaller than

[1]The data sample consists of the runs of LHC10h-pass2 period marked as "good" in the Run Condition Table (RCT) [84]. The standard AOD 086 production is used.

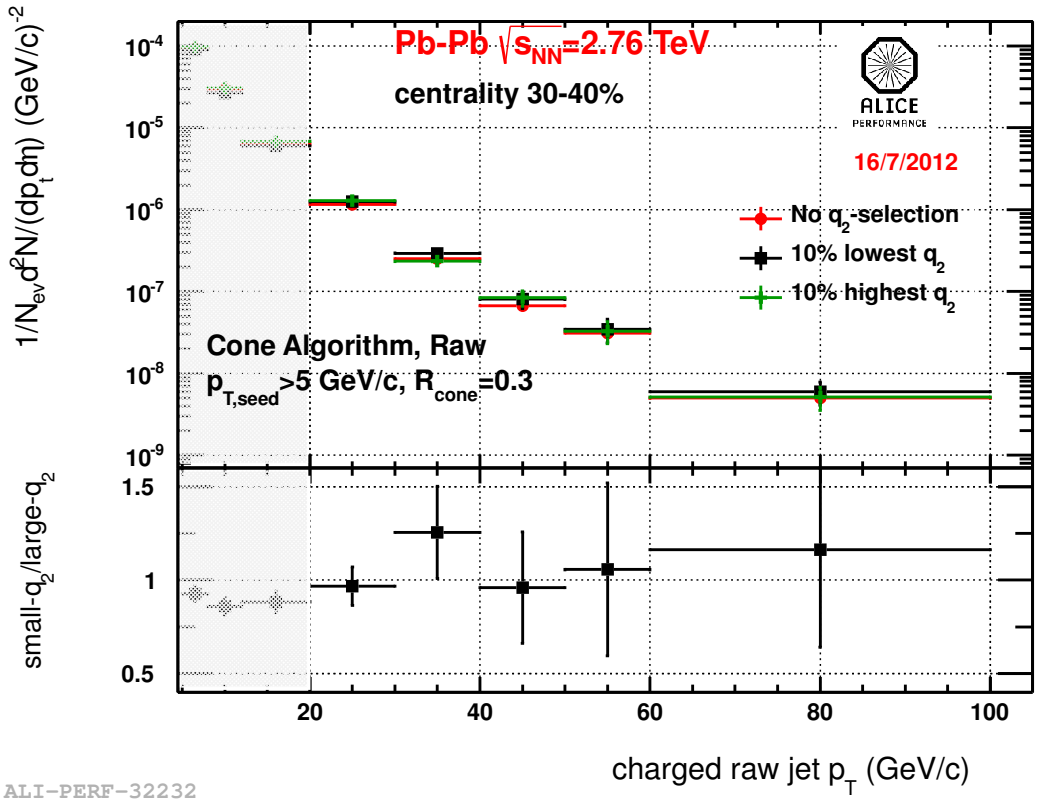

Figure 5.21: $p_{T,jet}$ distribution of jets for the unbiased, small-q_2, and large-q_2 samples. In the bottom plot the ratio between small-q_2 and large-q_2 is reported.

4. Such tracks are projected to the ITS and used in the analysis if at least 2 matching hits (out of a maximum of 6) in the ITS, including at least one in the SPD, are found. In addition, the χ^2 per point of the momentum fit in the ITS must be smaller than 36. Finally, tracks are rejected from the sample if their distance of closest approach to the reconstructed vertex is larger than 2 cm in the longitudinal direction (DCA_z) or 7 times the resolution in the transverse plane (DCA_{xy}) [10].

Particle Identification (PID) is done using an $n\sigma$ cut: for tracks with $p_{\rm T} < 0.6$ GeV/c only the information from particle energy loss in the TPC is used. For $p_{\rm T} > 0.6$ GeV/c tracks are requested to have a signal in the TOF and both the signals from TPC and TOF are used. The combined $n\sigma$ is calculated as the squared sum of the two measurements:

$$n\sigma_{\rm combined} = \sqrt{\frac{n\sigma^2_{\rm TPC} + n\sigma^2_{\rm TOF}}{2}} \tag{5.9}$$

The $n\sigma$ separation for data in the kaon mass hypothesis is reported in Figure 5.22. Rows represent (from the top): $n\sigma$ separation in the TPC, in the TOF and the combined $n\sigma$ (squared sum of the separation in the TPC and TOF, Eq. 5.9). This plot is analogous to the one of Fig. 4.25 for the case of the ITS.

5.2.4 Monte Carlo studies

In order to estimate the dependence of the efficiency (for both PID and tracking) on the q_2 event selection, a study on AMPT (A Multi-Phase Transport model for relativistic heavy ion collisions) [85] Monte Carlo production has been done. The aim of this study is to see if the Monte Carlo efficiency depends on the local occupancy that can be larger in high elliptic flow events.

The correction factor for the unbiased, small-q_2, and large-q_2 samples are reported in Figure 5.23 (upper panel). For $p_{\rm T} > 0.6$ GeV/c tracks are requested to have a signal in the TOF: this is reflected in the step at $p_{\rm T} = 0.6$ GeV/c. In the bottom panel the ratio $\frac{\mathrm{small-q_2(large-q_2)}}{\mathrm{unbiased}}$ is reported. From the ratios in Fig. 5.23 it is possible to conclude that the Monte Carlo correction factor is not dependent on the q_2 selection applied (as it is also expected looking at the centrality dependence of the efficiency in [78]). It should be noted that for this analysis global tracks are selected. The tracking efficiency for global tracks does not depend on the multiplicity of the event, thanks to the large number of points available for reconstruction in the TPC. The ratio has been fitted with a straight line and the discrepancy from unity is taken as systematic error. The contribution is $\sim$ 1%. The fact that the efficiency does not depend on the q_2 selection applied allows one

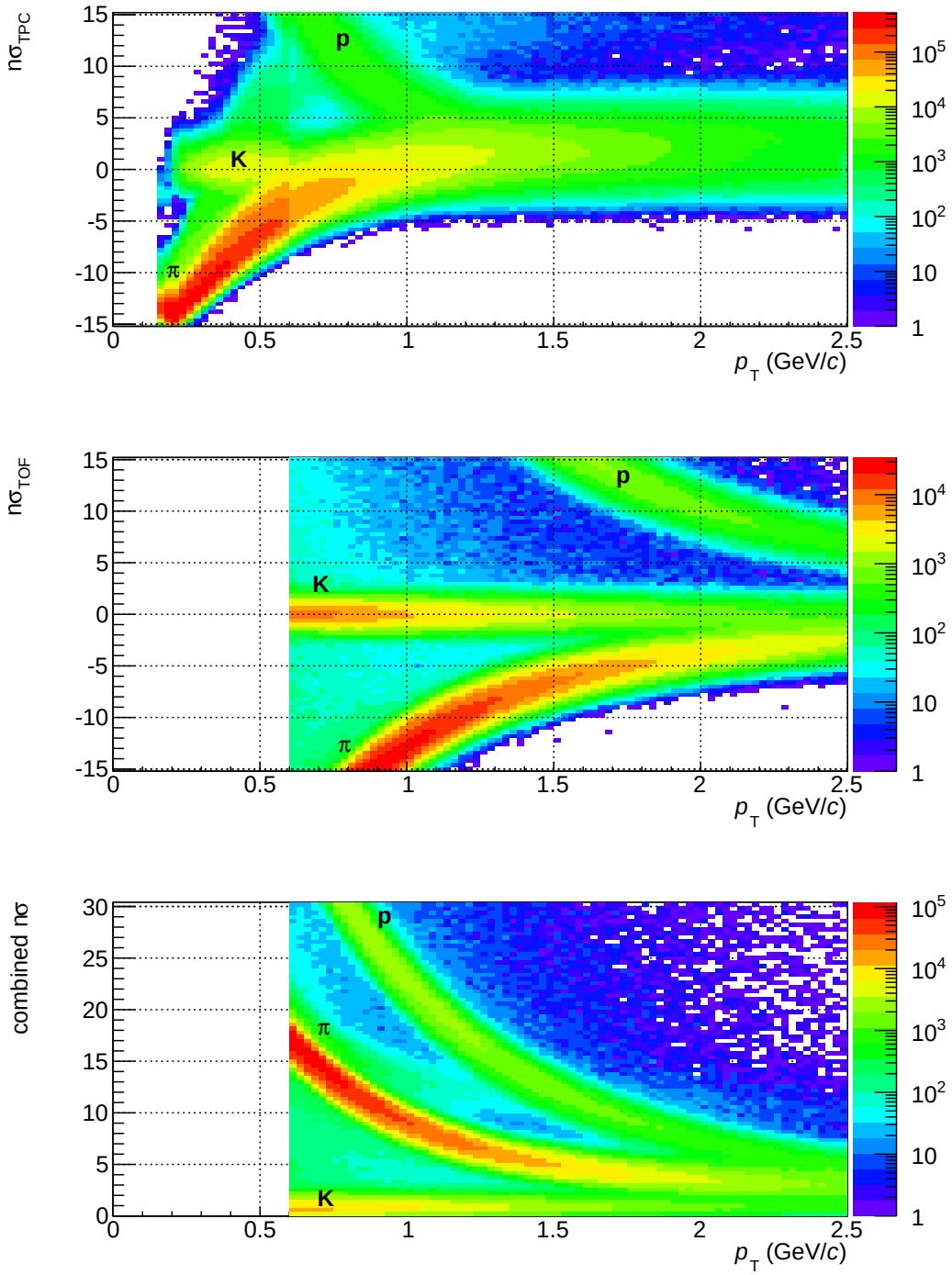

Figure 5.22: $n\sigma$ separation for data in the kaon mass hypothesis. Rows represent (from the top): $n\sigma$ separation in the TPC, in the TOF, and the combined $n\sigma$ (squared sum of the separation in the TPC and TOF, Eq. 5.9)

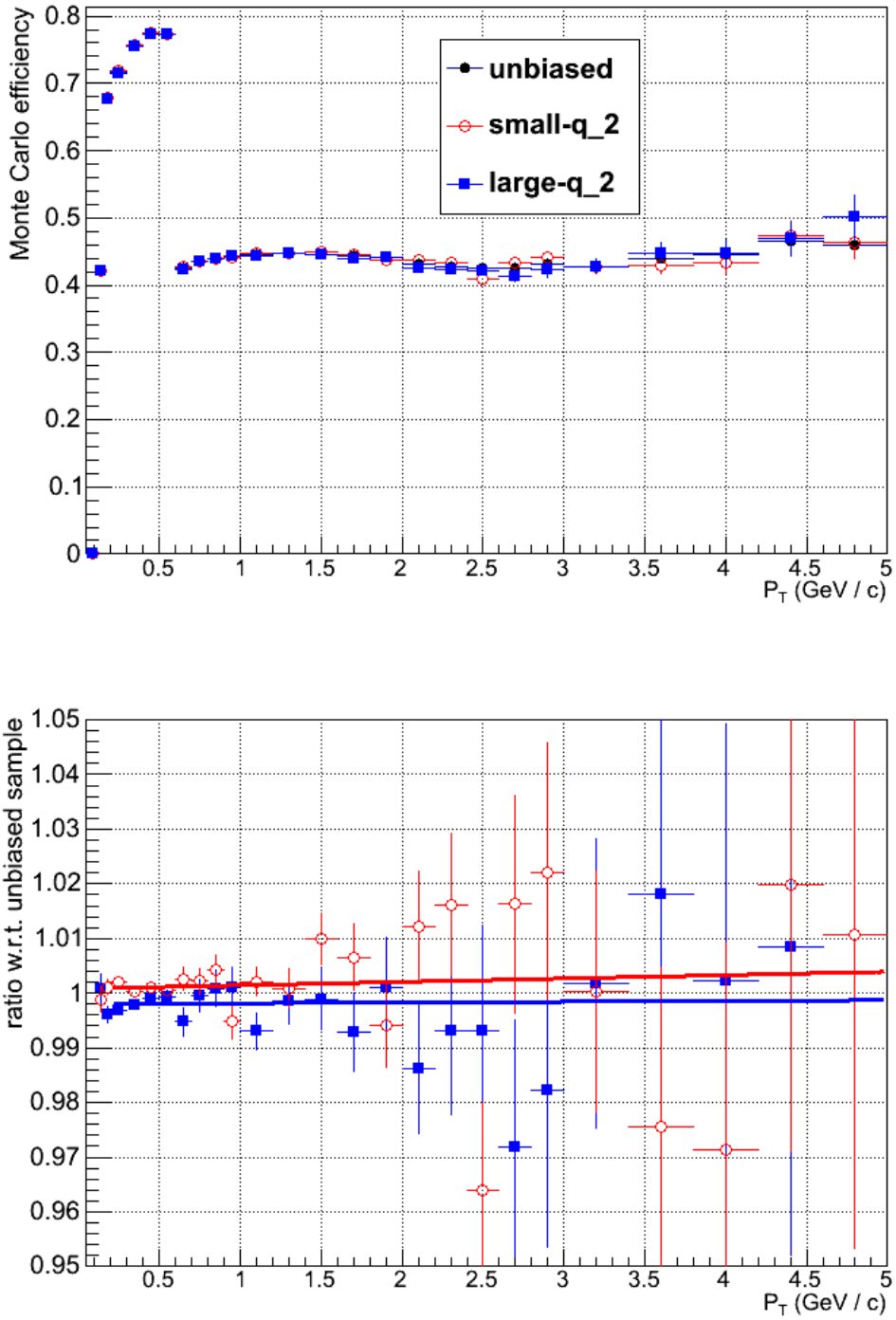

Figure 5.23: Correction factor for the unbiased, small-q_2 and large-q_2 samples (upper panel). In the bottom panel the ratio $\frac{\text{small}-q_2(\text{large}-q_2)}{\text{unbiased}}$ is reported. The lines represent a linear fit to the ratios and it used to estimate the systematic uncertinty.

to estimate the spectrum modification as a function of q_2 only looking at raw yields (only statistical error from data). This is what is done in the following.

5.2.5 p_T distributions of π, K, p in events selected according to the ESE

In order to estimate the modification of the p_T spectrum in events selected according to the ESE the ratio:

$$r = \frac{10\% \text{ highest } q_2}{\text{unbiased sample}} \tag{5.10}$$

has been studied as a function of p_T for the $All_{Charged}$ sample and for identified π, K and p. The same is done for the 10% lowest q_2 events. As shown in Section 5.2.4, the Monte Carlo efficiency does not depend on the q_2 selection applied: for this reason the ratio described above is obtained using raw p_T distributions (not corrected for efficiency). The ratio r is reported in Figure 5.24 for the large-q_2 (top) sample and for the small-q_2 sample (bottom).

A modification of the p_T shape is observed when events are selected according to the ESE. In the large-q_2 sample the p_T distribution looks harder than the unbiased one below $p_T = 3$ GeV/c. The modification vanishes at high p_T (only $All_{Charged}$ are measured above 3 GeV/c) where the hydrodynamic picture is no longer applicable. In the same transverse momentum range the spectrum in the small-q_2 sample looks softer than the unbiased one below $p_T = 3$ GeV/c. Both the ratios measured in Figure 5.24 are compatible with unity at high p_T ($p_T \gtrsim 6$ GeV/c). This, together with the checks on the potential biases discussed in Sec. 5.2.2, is a hint that this effect seems to be due to soft processes rather than hard processes (such as jet contribution). A mass ordering seems to be present in the transverse momentum range $p_T \lesssim 3$ GeV/c. This is more evident in Figure 5.25 where the ratio between the large-q_2 and the small-q_2 is reported. It should be noted that this is the same behaviour obtained by studying the elliptic flow v_2 in events selected according to the ESE [82].

A more detailed study (including comparison with models and hydrodynamic fit of particle spectra) would tell more about the observed correlation between v_2 and radial flow.

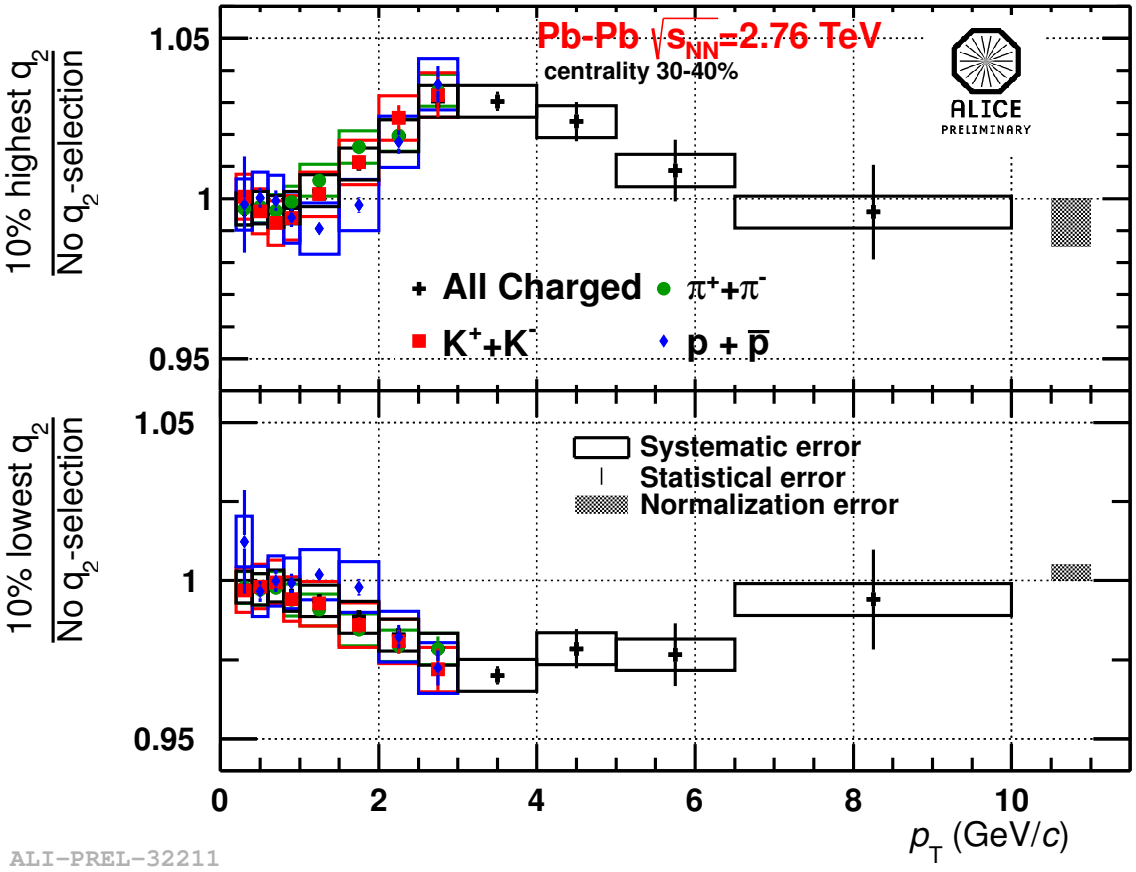

Figure 5.24: Ratio r (Eq. 5.10) of the p_T distributions for the large-q_2 (top) sample and for the small-q_2 sample (bottom).

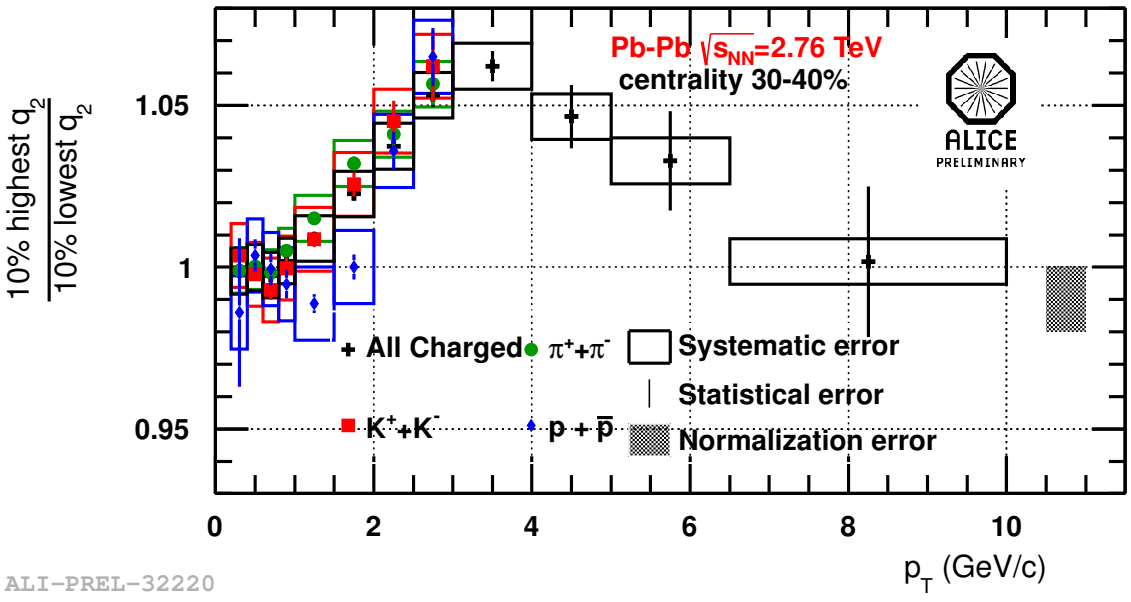

Figure 5.25: Ratio r between the p_{T} distributions in the large-q_2 sample and in the small-q_2 sample.

6

Thermal production of hadrons in Pb–Pb collisions

In this Chapter the measured $p_{\rm T}$ integrated hadron yields at mid-rapidity $\mathrm{d}N/\mathrm{d}y$ are described in terms of the thermal (or statistical hadronisation) model. In particular:

- **Light flavour hadrons yields** (Sec. 6.1). The extrapolation to zero $p_{\rm T}$ of the spectra is described in detail. $p_{\rm T}$ integrated π, K, p yields are compared with predictions from calculations based on thermal models.

- **Thermal analysis of particle yields** (Sec. 6.2). Strange and multi-strange hadrons are included in the thermal analysis. Yields of different particles are compared with thermal model prediction. The freeze-out parameters are extracted from a fit to integrated yields at mid-rapidity. The observed deviations from the thermal behaviour are discussed and the most recent scenario conjectures are described.

The thermal or statistical hadronisation model, described in detail in Sec. 2, has been used so far to describe the hadron production in heavy-ion collisions. It has been found to be very successful in describing the hadron abundances over a broad range of energies (from AGS energies up to RHIC energies). The energy increase between the higher RHIC energy ($\sqrt{s_{\rm NN}} = 200$ GeV) and the $\sqrt{s_{\rm NN}} = 2.76$ TeV provided by the LHC is more than one order of magnitude. One of the main questions concerning the hadron production at the LHC is if the hadron abundances would show a thermal behaviour. As discussed in Sec. 2 hadron yields show a thermal behaviour also in small systems such as p–p or e^{+}– e^{-} collisions [31]. The free parameters of the model (the chemical freeze-out temperature T_{ch}, the baryochemical potential μ_B and the volume V) can be extracted from a fit to the measured integrated yields.

6.1 Integrated π, K, p yields

6.1.1 Extrapolation of the p_T distribution

The extrapolation to zero p_T is performed using an individual blast wave (Eq. 5.1) fit to the particle p_T distribution. As already discussed in Sec. 5.1.2 no physics meaning can be addressed to the individual blast wave fit. The blast wave function is found to nicely describe the data over the measured p_T range. The ratio between the measured p_T distribution and the individual blast wave fit is reported in Figure 6.1 for the summed charge states in different centrality classes. Thanks to the good PID and tracking performance at low p_T of the ALICE experiment, the fraction of extrapolated yield is small: about 7%, 6%, 4% for π, K, p respectively. The measured distributions are mainly extrapolated at low p_T, the contribution from the high p_T part of the extrapolation is much smaller compared to low p_T. The systematic uncertainty on the extrapolation does not depend on centrality. It amounts to 2.5%, 3%, 3% for π, K, p respectively. As for the systematic error on the $\langle p_T \rangle$ it has been evaluated using different fit functions (Boltzmann, m_T exponential, p_T exponential, Tsallis-Levy, Fermi-Dirac, Bose-Einstein) and restricting the fit range to low p_T for those functions not giving a satisfactory fit result over the measured p_T range. The extracted integrated yields at mid-rapidity $\mathrm{d}N/\mathrm{d}y$ are reported in Table 6.1.1.

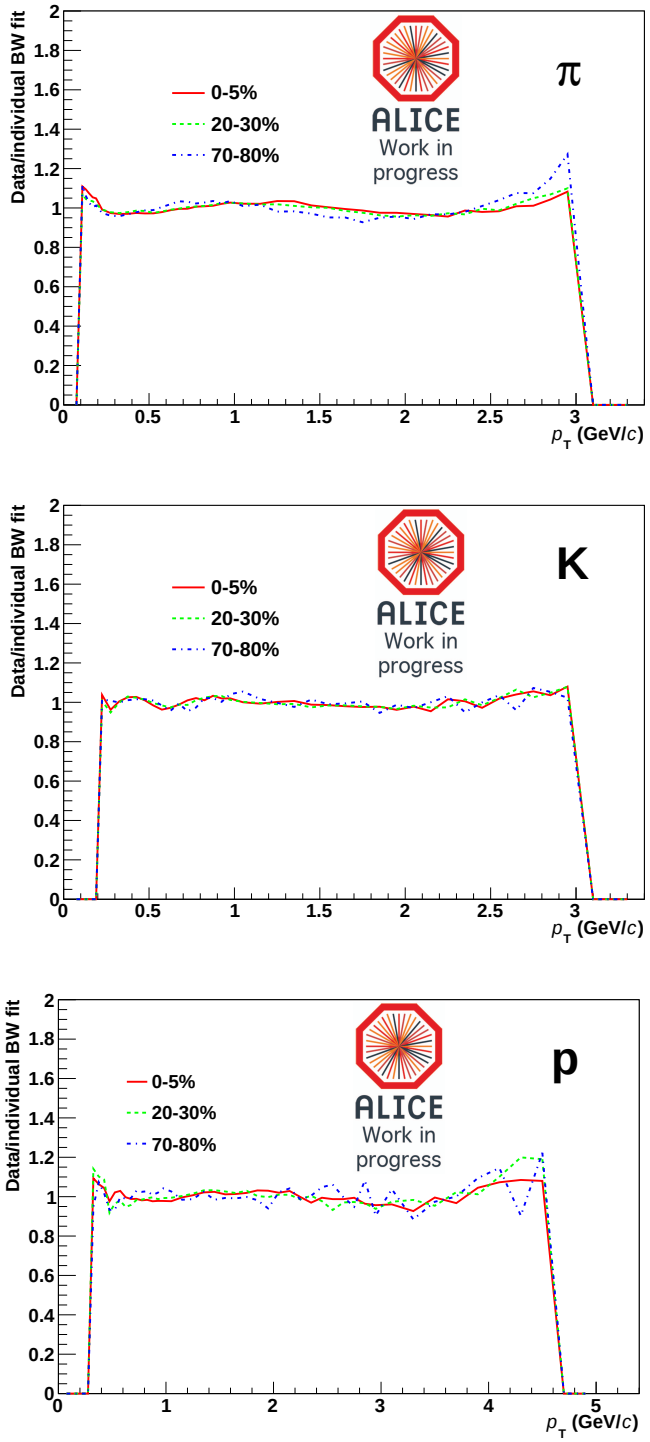

Figure 6.1: Ratio of the measured p_{T} distributions to the individual blast-wave fit.

Centrality	$dN_{ch}/d\eta$	π^+	π^-	K^+	K^-	p	$\bar{p}$	Norm. Uncert.
0–5%	1601 ± 60	$733 \pm 0.5 \pm 54$	$732 \pm 0.5 \pm 52$	$109 \pm 0.3 \pm 9$	$109 \pm 0.3 \pm 9$	$34 \pm 0.1 \pm 3$	$33 \pm 0.1 \pm 3$	0.5%
5–10%	1294 ± 49	$606 \pm 0.5 \pm 42$	$604 \pm 0.4 \pm 42$	$91 \pm 0.2 \pm 7$	$90 \pm 0.3 \pm 8$	$28 \pm 0.1 \pm 2$	$28 \pm 0.1 \pm 2$	0.5%
10–20%	966 ± 37	$455 \pm 0.3 \pm 31$	$453 \pm 0.3 \pm 31$	$68 \pm 0.1 \pm 5$	$68 \pm 0.2 \pm 6$	$21.0 \pm 0.04 \pm 1.7$	$21.1 \pm 0.05 \pm 1.8$	0.7%
20–30%	649 ± 23	$307 \pm 0.2 \pm 20$	$306 \pm 0.2 \pm 20$	$46 \pm 0.1 \pm 4$	$46 \pm 0.1 \pm 4$	$14.4 \pm 0.03 \pm 1.2$	$14.5 \pm 0.04 \pm 1.2$	1%
30–40%	426 ± 15	$201 \pm 0.1 \pm 13$	$200 \pm 0.1 \pm 13$	$30 \pm 0.1 \pm 2$	$30 \pm 0.1 \pm 2$	$9.6 \pm 0.03 \pm 0.8$	$9.7 \pm 0.03 \pm 0.8$	2%
40–50%	261 ± 9	$124 \pm 0.1 \pm 8$	$123 \pm 0.1 \pm 8$	$18.3 \pm 0.06 \pm 1.4$	$18.1 \pm 0.07 \pm 1.5$	$6.1 \pm 0.02 \pm 0.5$	$6.2 \pm 0.03 \pm 0.5$	2.4%
50–60%	149 ± 6	$71 \pm 0.1 \pm 5$	$71 \pm 0.1 \pm 4$	$10.2 \pm 0.04 \pm 0.8$	$10.2 \pm 0.05 \pm 0.8$	$3.6 \pm 0.01 \pm 0.3$	$3.7 \pm 0.02 \pm 0.3$	3.5%
60–70%	76 ± 4	$37 \pm 0.1 \pm 2$	$37 \pm 0.1 \pm 2$	$5.1 \pm 0.03 \pm 0.4$	$5.1 \pm 0.03 \pm 0.4$	$1.9 \pm 0.01 \pm 0.2$	$2.0 \pm 0.01 \pm 0.2$	5%
70–80%	35 ± 2	$17.1 \pm 0.03 \pm 1.1$	$17.0 \pm 0.03 \pm 1.1$	$2.3 \pm 0.02 \pm 0.2$	$2.3 \pm 0.02 \pm 0.2$	$0.90 \pm 0.006 \pm 0.08$	$0.93 \pm 0.008 \pm 0.09$	6.7%
80–90%	13.4 +1.6 -1.2	$6.7 \pm 0.02 \pm 0.4$	$6.7 \pm 0.02 \pm 0.4$	$0.87 \pm 0.010 \pm 0.08$	$0.80 \pm 0.011 \pm 0.09$	$0.37 \pm 0.004 \pm 0.04$	$0.37 \pm 0.005 \pm 0.04$	+12% -8.5%

Table 6.1: Charged particle multiplicity density [7] (total errors) and mid-rapidity particle yields $\frac{dN_i}{dy}\big|_{|y|<0.5}$ (statistical errors and systematic errors including extrapolation uncertainty) (from [78] - Work in progress). The last column indicate the additional normalisation uncertainty coming from the centrality definition.

6.1.2 Integrated π, K, p yields in central (0-5% Pb–Pb collisions)

Particle ratios in the most central (0-5%) centrality bin are reported in Figure 6.2 and compared with the results from RHIC experiments [74, 86, 87] at $\sqrt{s_{\rm NN}}$ = 200 GeV and predictions from thermal models [20, 21]. The systematic error on particle ratios has

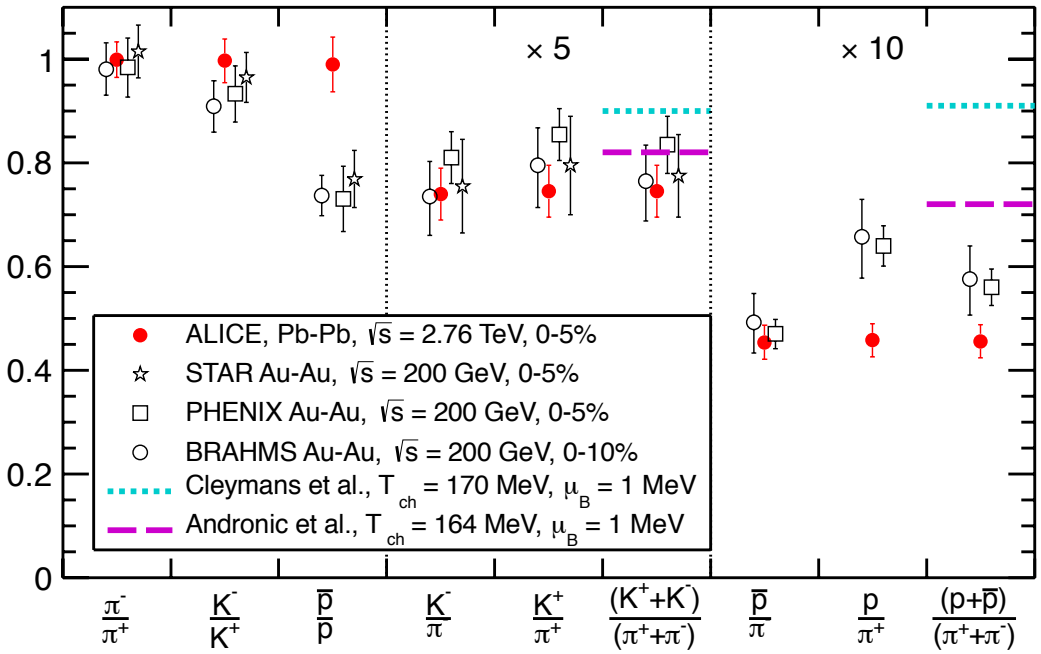

Figure 6.2: Mid-rapidity particle ratios, compared to RHIC results [74, 86, 87] and predictions from thermal models [20, 21] for central Pb-Pb collisions at the LHC (combined statistical and systematic errors) (from [71]).

been calculated on the measured ratio itself, without propagating the error from single yields. In this way all the correlated sources of uncertainty have been considered and cancelled in the ratios. The statistical error is negligible if compared to the systematic one. As already shown in Fig. 5.4 and 5.5 the antiparticle to particle ratio is close to unity for all the species. For this reason the model predictions have been obtained using the value μ_B = 1 MeV. This value is much lower than the one estimated at the SPS or at RHIC. As shown in Fig. 2.8 the T_{ch} is constant above few tens of GeV in $\sqrt{s_{\rm NN}}$ (SPS energies). The model predictions were hence calculated using the T_{ch} value extracted from fits to RHIC data. In order to minimise the effect of the μ_B difference between LHC and RHIC the ratio $\mathrm{K}/\pi = (\mathrm{K}^+ + \mathrm{K}^-)/(\pi^+ + \pi^-)$ and $\mathrm{p}/\pi = (\mathrm{p} + \bar{\mathrm{p}})/(\pi^+ + \pi^-)$ are also

reported. The ratio $K/\pi = 0.149 \pm 0.010$ is close to the value measured at RHIC and is found to be in agreement with thermal model expectations. This is not the case for the $p/\pi = 0.046 \pm 0.003$, where a significant reduction is observed with respect to RHIC (p/π ratio is $\sim$ a factor 1.2 lower at the LHC). Thermal models over-predict the p/π ratio significantly, being the measured value a factor ~ 1.5 lower than the expectation. The two models shown in Fig. 6.2 differ mainly in the hadron mass spectrum implementation, but both were able to reproduce RHIC data.

Thermal models proved to be very successful in describing particle ratios over a broad energy range: such a large deviation of the most abundant baryon is therefore unexpected. The small statistical and systematic uncertainties and the precise procedure of secondary subtraction in the ALICE proton measurement show that the discrepancy with the thermal model is significative. It should be noted that a discrepancy of $\sim 20\%$ on the p/π ratio between thermal model and data was observed at RHIC. This was not considered significant because of the large model uncertainties and the experimental error due to secondary subtraction. Interaction in the hadronic phase, such as baryon-antibaryon annihilation could change significantly the relative particle abundances [88,89], as suggested also by the HKM [76] model which predicts the p/π to be 0.52, in agreement with the measured value. An alternative picture suggests the possible presence of bound states also in the equilibrated component of the QGP phase [90, 91], which would result in a flavour/baryon number dependence of T_{ch}. A more complete study of the hadron production, with the inclusion of strange and multi-strange hadrons in the thermal analysis would cast new light upon this issue. It is presented in the following Sections.

6.2 Thermal analysis of hadron production at the LHC

In this section the integrated production of hadrons (including identified π, K and p but also other hadronic states carrying strange quarks) is studied in terms of the thermal model. Measured particle ratios are compared with results from previous RHIC experiments and expectations from thermal models. The integrated yields at mid-rapidity dN/dy are fitted using the thermal model in order to extract the T_{ch} and μ_B.

6.2.1 Strange and multi-strange particle measurement in ALICE

A complete study of the hadron composition in term of the thermal model can be achieved with the inclusion of strange and multi-strange particles in the statistical hadronisation picture. A detailed description of the analysis techniques used to measure strange and multi-strange hadrons results to be out of scope for this work. The main features of each analysis is reported in the following, for the details please see the references.

- Λ(uds), [92]. The Λ is the most abundant strange baryon. The reconstruction is based on the decay topology of V0 particles. Because of the high combinatorial background different cuts are needed in Pb–Pb to select signal candidates. These include a cut on the DCA between the tracks that form the V0, DCA_{xy} of the daughter tracks with respect to the primary vertex, the cosine on the V0 pointing angle and the radial boundaries of the fiducial volume. Candidate Λs are also required to have a good PID signal in the TPC for the daughter proton. The signal is extracted from the resulting invariant-mass distributions. The feed down correction amounts to $\sim$ 19 % and is estimated from the ALICE Ξ measurement, using the Monte Carlo to estimate the phase space distribution of the decay products.

- Ξ(dss) and Ω(sss), [93]. Multi-strange baryon reconstruction is based on the cascade decay topology. Firstly, a V0 candidate is selected (using similar cuts as for the Λ). The cascade reconstruction is performed applying different cuts, such as on the DCA_{xy} of the V0 (and the daughter π or K) to the primary vertex, the cosine of the pointing angle and the fiducial region. PID, invariant mass and decay length cuts are also applied in order to reduce the combinatorial background in Pb–Pb. The signal is extracted from an invariant mass fit. Feed down contribution is found to be negligible.

- $\phi(\mathrm{s\bar{s}})$ [94]. The ϕ meson yield is extracted from a fit to the K^+K^- invariant mass distribution. The combinatorial background is estimated from like-sign kaon pairs and using an event-mixing approach. The mean lifetime of the ϕ meson is 45 fm/c, comparable with the lifetime of the fireball, makes this particle sensible to the properties of the medium trough re-scattering and re-generation effects [95].

- $\mathrm{K}^*(892)^0(\mathrm{d\bar{s}})$ [96]. The $K^*(892)^0$ resonance is of particular interest because it has a small lifetime (4 fm/c) compared to the one of the fireball. As for the ϕ meson

the study of the $K^*(892)^0$ allows to study the system trough re-scattering and re-generation effects. The hadronic decay channel $K^0 \rightarrow \pi^- K^+$ (B.R. $\sim$ 66 %) is reconstructed. A 2σ cut in the TPC is applied to identify pions and kaons. As for the ϕ meson reconstruction the invariant mass distribution of unlike-sign kaon and pion pairs is fitted in order to extract the signal. The combinatorial background is estimated from like-sign distribution and event mixing.

The most recent results on strange hadron production can be found in [95].

6.2.2 Yield relative to pions in central (0-20%) Pb–Pb collisions

The ratio of particle yields to pions has been used so far to study the chemical composition of the system and compare different energy regimes. The yields relative to pions in central (0-20%)[1] Pb–Pb collisions are reported in Figure 6.3. Yields at the LHC are compared with previous measurements at RHIC [74, 86, 87]. It should be noted that all the ALICE measurements are corrected for feed-down, this is not the case for RHIC. For consistency the feed down correction for the RHIC experiments has been calculated, based on the thermal model. For STAR a feed-down correction of -36% has been applied to protons and -39% to anti-protons. For PHENIX a -10% correction has been applied to the π yields. Most of the ratios are compatible within error. This is not the case for the p/π and Λ/π ratios, where the discrepancy between the two energy regimes is significant. It should be noted that no significant variation of these ratios was predicted by the thermal model, as already explained in Sec. 6.1.2.

6.2.3 Comparison to thermal model extrapolation from lower energies

Measured yields are compared with predictions from the thermal model [20], assuming (as already explained in Sec. 6.1.2):

- $\mu_B = 1$ MeV, since the antiparticle to particle ratio is close to unity at the LHC, Fig. 5.4, 5.5 and 6.2.

[1] When available the the measurement in 0-20% has been used, for some particles the bin 0-20% is obtained from measurements in narrower centrality intervals (e.g. π, K and p are measured in 0-5%, 5-10% and 10-20%), considering that the centrality percentile is calculated as the fraction of the total cross-section.

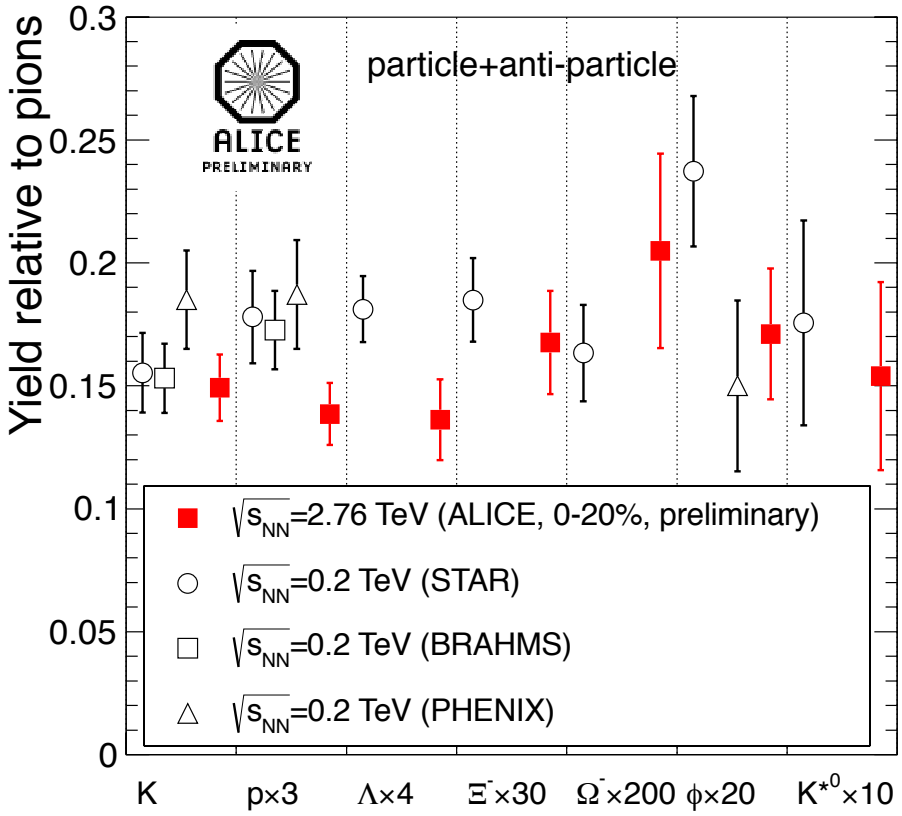

Figure 6.3: Yields relative to pions at RHIC [74, 86, 87] and LHC (from [97]).

– $T_{ch} = 164$ MeV extracted from the fit to RHIC data and assuming T_{ch} to be constant above SPS energies (Fig. 2.8)

The comparison is reported in Figure 6.4. As already observed in Fig. 6.2 the K/π ratio

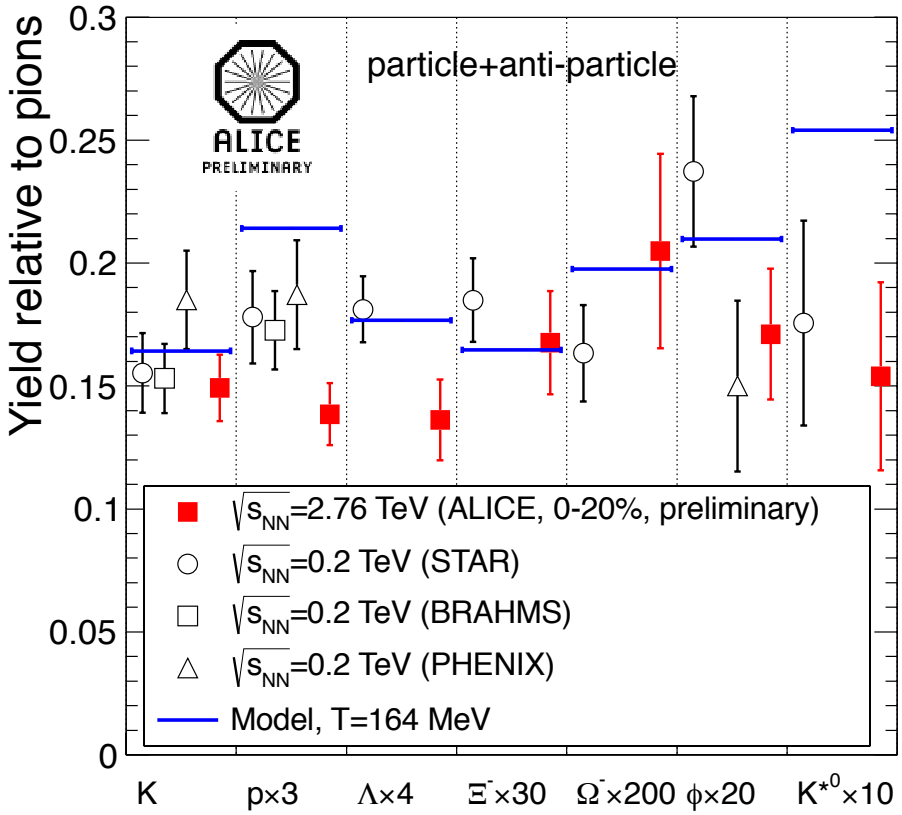

Figure 6.4: Yields relative to pions at RHIC [74, 86, 87] and LHC (from [97]). Prediction from thermal model [20] assuming $\mu_B = 1$ MeV and $T_{ch} = 164$ MeV is also reported.

is close to the thermal expectation while the p/π ratio shows a significant discrepancy. The latter is also the case for the Λ/π ratio, being lower than the expectation. Ratios involving multi-strange baryons show a good agreement with the model expectation. It should be noted that the same multi-strange ratios are basically unchanged when going from RHIC to LHC. The ϕ/π and K^{*0}/π ratios are lower than the expectations, but the uncertainty on the model prediction is large for these particles given their small lifetime which can lead to re-scattering and re-generation [95] effects.

The general picture seems to suggest some unexpected deviations from the pure thermal behaviour that was observed at lower energies. Strange mesons and multi-strange baryons are close to the thermal model expectation, while the two most abundant baryons,

p and Λ, are significantly lower than the expectation. Two of the possible scenarios advocated to explain this discrepancy have already been introduced in Sec. 6.1.2.

6.2.4 Thermal model fit to p_{T} integrated yields in central (0-20%) Pb–Pb collisions.

In order to extract the T_{ch} from the data a fit to p_{T} integrated yields at mid-rapidity, $\mathrm{d}N/\mathrm{d}y$, has been performed. Fits to hadron yields have been carried out by many groups for almost 15 years by now. The fit is based on a χ^2 procedure, from which it is possible to extract the best values of T_{ch}, μ_B and V. Frequently in literature the thermal fit to integrated particle ratios instead of yields can be found, allowing the cancellation of the parameter V in the ratio, thus using only two free parameters μ_B and T_{ch}. It is important to stress that this is a perfectly legitimate procedure ONLY if in the ratios all the correlated uncertainties are taken properly into account [30]. In the case of this work it is not possible to carefully estimate all the correlated uncertainties, since results from different analyses are combined. For this reason the fit is performed on the p_{T} integrated yields instead of ratios. Due to their short lifetime, comparable with the lifetime of the fireball, ϕ and K^{*0} could have modifications due to interactions of their decay products in the medium, hence they are not included in the fit.

The fit is reported in Figure 6.5 [98]. μ_B has been fixed at 1 MeV in the fit, given the vanishing baryon density at LHC energy. The freeze-out temperature T_{ch} obtained from the fit ($T_{ch} = 152$ MeV) is much lower than the one expected assuming T_{ch} constant above SPS energies ($T_{ch} \sim 164$ MeV) (Fig. 2.8). It should be noted that the fit quality is not perfect, as indicated by the $\chi^2/N_{d.f.} = 39.6/9$ value. The thermal fit fails the description of strange and multi-strange baryons. The fit parameters T_{ch} and V are anti-correlated, as shown in Figure 6.6, were the χ^2 distribution is reported in the (T_{ch},V) plane. This distribution exhibits local minima in addition to the minimum selected as the fit result. An error of $\pm$ 3 MeV has been assigned to the T_{ch} extraction.

The result of the thermal fit seems to indicate that at the LHC a pure thermal model is not able to reproduce both light and multi-strange hadron yields with a common set of freeze-out parameters.

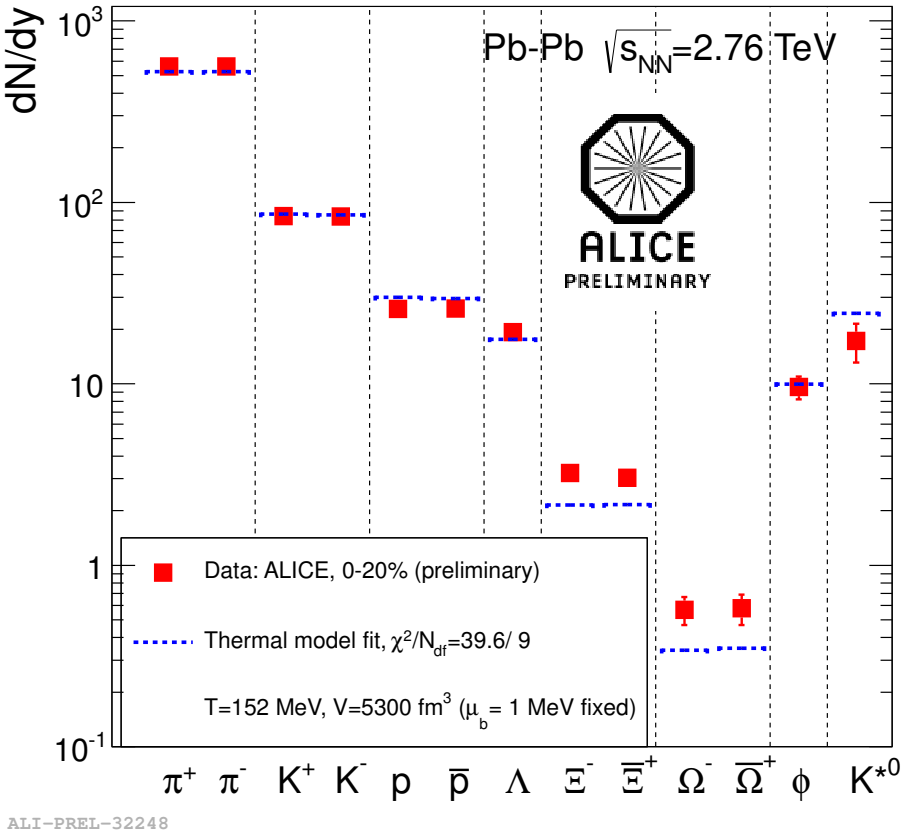

Figure 6.5: Thermal fit [20] to integrated hadron yields at mid-rapidity $\mathrm{d}N/\mathrm{d}y$ (from [97]). ϕ and K^{*0} are not included in the fit.

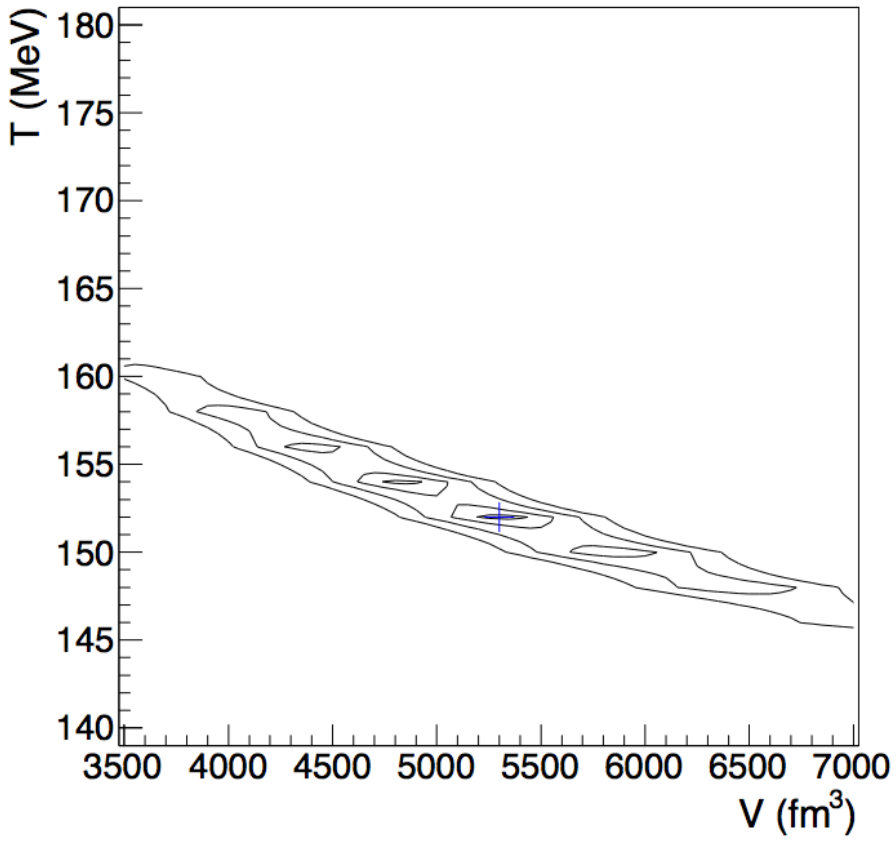

Figure 6.6: χ^2 contour in the T-V plane for the thermal fit [20] to integrated hadron yields at mid-rapidity $\mathrm{d}N/\mathrm{d}y$ (from [98]). ϕ and K^{*0} are not included in the fit.

6.2.5 Current understanding of thermal behaviour of hadron production.

Particle yields relative to pions can be compared with thermal model expectation using $T_{ch} = 152$ MeV extracted from the fit to hadron yields. This is reported in Figure 6.7 where all the results described in this Chapter are summarised. Figure 6.7 can be considered a

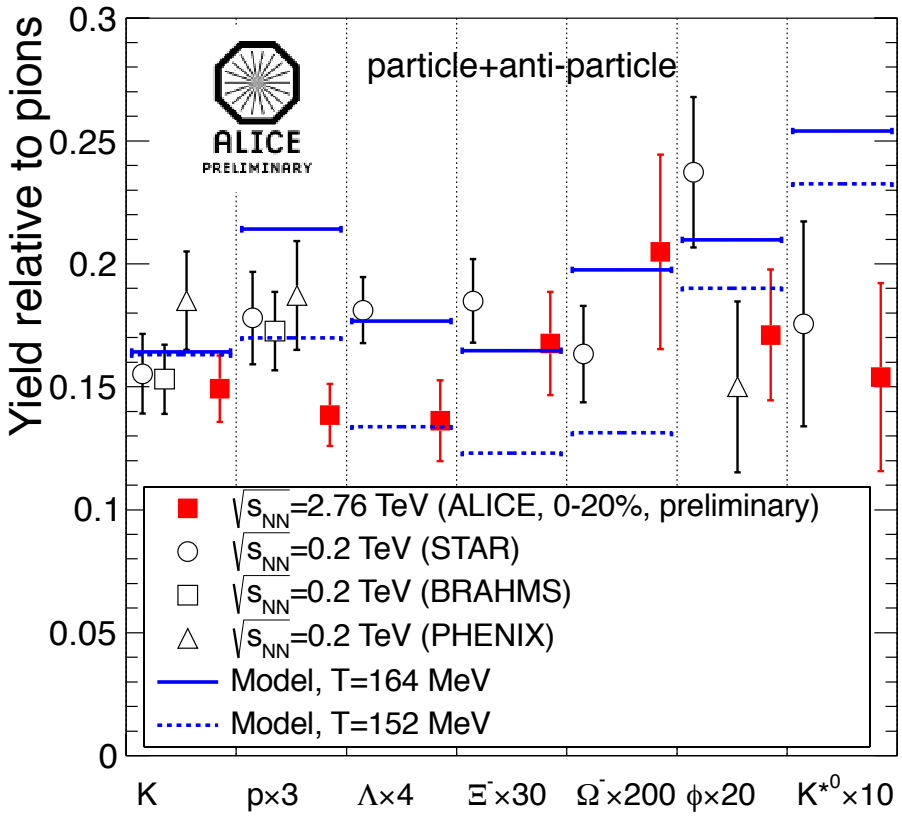

Figure 6.7: Yields relative to pions at RHIC [74, 86, 87] and LHC (from [97]). Predictions from thermal model [20] assuming $\mu_B = 1$ MeV and $T_{ch} = 164$ MeV (from lower energies extrapolation) and $T_{ch} = 152$ MeV (from thermal fit to hadron yields [98]) are reported.

summary of the current understanding of the thermal behaviour of the hadron production in the new energy regime. Some considerations follow.

– **Only looking at the data**. The only significant modification of the particle ratios when moving from RHIC to LHC is observed in the p/π and Λ/π ratios. All the other particle ratios are almost unchanged. It is interesting to note that this is a suppression of the most two abundant baryons, while a similar suppression is not

observed in the meson sector nor for multi-strange baryons. This means that at the LHC energy some abundance-changing physics process (most likely negligible at lower energies) starts being important for lighter baryons.

– **What we were expecting**. If some yet-to-be-understood process modifies the relative hadron abundances, the same model that was able to reproduce the hadrons yields at lower energies should not work at the LHC. This is what it is possible to conclude from the comparison with the model prediction with $T_{ch} = 164$ MeV. The same ratios that are different from RHIC, p/π and Λ/π, are quite far from the model expectation.

– **What we extracted from the data**. The value of $T_{ch} = 152$ MeV obtained from thermal fit to integrated yields at mid-rapidity, $\mathrm{d}N/\mathrm{d}y$, is much lower than what was expected considering a saturation of the freeze-out temperature (164 MeV) for $\sqrt{s_{\mathrm{NN}}}$ larger than few tens of GeV. The model prediction with $T_{ch} = 152$ MeV is closer (but still incompatible) to the p/π ratio and get the Λ/π ratio. Using this temperature multi-strange hadrons are significantly underestimated. It should be noted that the K/π ratio is not sensitive to the variation of T_{ch}: the prediction is basically unchanged at the two different temperatures considered. It should be also noted that the small error on the proton yield tends to reduce the temperature in the fit.

In summary, the experimental data show a change in the p/π and Λ/π ratios with respect to RHIC. A pure statistical hadronisation model [20] could not describe all the different hadron yields with a common set of freeze-out parameters. This is an important result in the heavy-ion field. It means that the thermal production of hadrons has to be reconsidered in a critical manner. A non comprehensive list of the proposed alternative scenarios is reported in the following.

Interactions in the hadronic phase

In this scenario the deviation of the p and Λ yields from thermal model expectations is due to final state interactions of hadrons after the chemical freeze-out. In particular the large cross section channel for baryon-antibaryon annihilation could selectively modify the usual thermal ratios. This is usually implemented using the UrQMD [38] model, which describes the final hadron-resonance cascade. The description of the fireball hence includes hadronic interactions after chemical freeze-out, which are neglected in the case

of free hadron stream. At lower energies these interactions could be too weak to modify significantly the particle ratios. This scenario has been studied by different groups [88,89, 99]. As an example a plot from [99] is reported in Figure 6.8, where the effect of the final UrQMD cascade stage is reported. UrQMD cascade expansion stage is attached to the Cooper-Frye output, as an "afterburner". The effect can be quantified by the modification factor $M = N(Hydro + Aft)/N(Hydro)$ between hadron multiplicities at the end of the cascade and hadron multiplicities directly after the hydrodynamic stage. At SPS energies ($\sqrt{s_{\rm NN}}$ = 7.6 GeV, 8.7 GeV and 17.3 GeV) the bulk of hadron is relatively unaffected by the hadronic cascade stage. Antibaryon yields ($\bar{\rm p}$, $\bar{\Lambda}$ and $\bar{\Xi}$) are strongly modified by the hadronic cascade, being their multiplicities suppressed by 25% up to 50% after the hadronic cascade. Both Ω and $\bar{\Omega}$ show signal of possible dynamical regeneration [89]. At the LHC energy the vanishing baryochemical potential μ_B results in an equal suppression of baryon and corresponding antibaryon. The effect of the hadronic cascade appears to be restricted to p and Ξ. Regeneration effects can significantly modify the Λ and Ω yields [89]. The data presented in this Chapter have been used in [99] to extrapolate the freeze-out parameters in Figure 6.9. The fit is performed using the standard Statistical Hadronisation Model (SHM) and using modification factors from UrQMD (from Figure 6.8) applied in the statistical model fit. The standard SHM fit (top panel) yields to similar results to what is shown in this work (Figure 6.5): T_{ch} = 156 ± 5 MeV lower than expectations and not satisfactory $\chi^2/N_{d.f.}$. The inclusion of UrQMD correction factors in the fit (lower panel) yields to a T_{ch} value (T_{ch} = 166 ± 3 MeV) compatible with RHIC energies and expectation from lattice QCD calculations [99], with an improved $\chi^2/N_{d.f.}$ value. This scenario is further supported by the comparison with models reported in Sec. 5.1.1, where it was shown that hydrodynamic models including a description of hadronic final state interactions [76,77] are able to reproduce the measured $p_{\rm T}$ spectra of π, K and p. It should be noted that a description of hadronic phase interactions, including baryon-antibaryon annihilation, is needed also to explain the two-pion Bose-Einstein correlations [100].

Non equilibrium corrections given by the viscosity

This scenario is described in [35]. It has been found that shear viscosity is needed in model predictions to describe the elliptic flow measurement. As described in Sec. 2.4.2 the average value of the shear viscosity to entropy ratio η/s, estimated from the elliptic and the triangular flow measurements, is small [6, 34]. The v_2 coefficient can therefore be used to determine the shear viscosity in this model. The inclusion of bulk viscosity in the hadronic

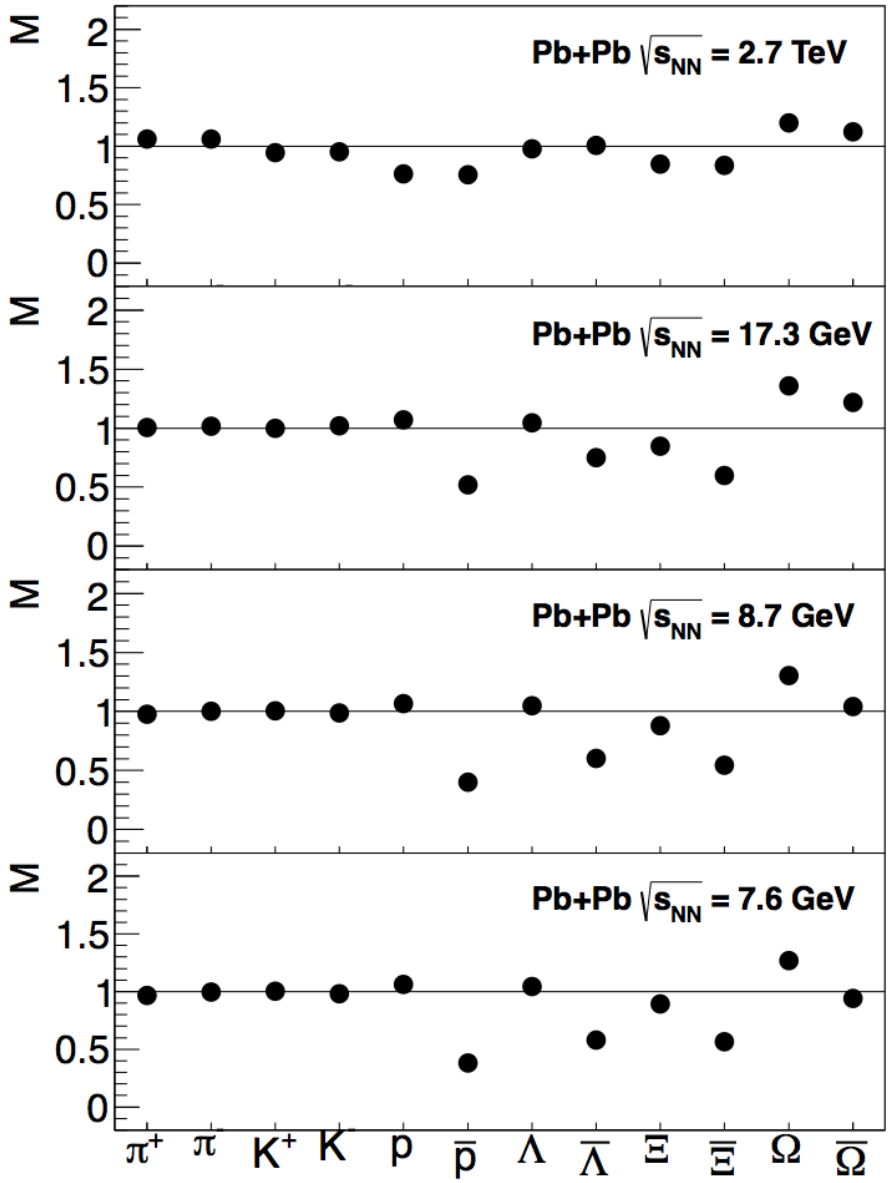

Figure 6.8: Modification factor $M = N(Hydro + Aft)/N(Hydro)$ between hadron multiplicities at the end of the cascade and hadron multiplicities directly after the hydrodynamic stage at different energies (from [99]).

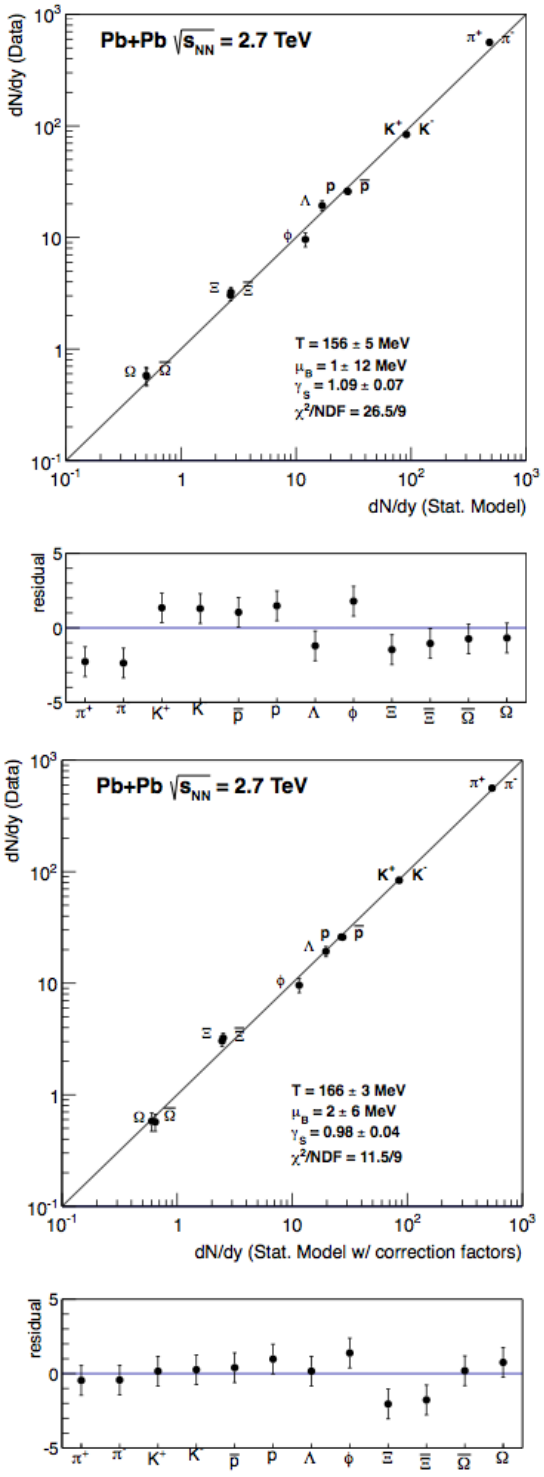

Figure 6.9: Statistical model fits to preliminary ALICE data for 20% central Pb-Pb collisions at $\sqrt{s_{\rm NN}} = 2.76$ TeV and to the same data but with modification factors from UrQMD applied in the statistical model fits (from [99]).

phase reduces the effective freeze-out temperature T_{ch}, improving the agreement between the model and the measured p_{T} distributions of π, K and p and the Hanbury Brown-Twiss (HBT) correlation [100] radii. Both shear and bulk viscosity are not constant in this calculation: one expects significant dissipation and effective viscosity in the hadronic cascade stage. This leads to viscous corrections to the equilibrium momentum distribution f_0:

$$f = f_0 + \delta f_{0,shear} + \delta f_{0,bulk} \tag{6.1}$$

which lower the effective T_{ch} for different particles. The agreement with the data is good, as shown in Figure 5.2 (Krakòw model).

Non-equilibrium statistical hadronisation model

In some models the non-equilibrium strangeness effect is quantified by introducing the phase space occupancy parameter γ_S (described in Sec. 2.3). The same factor can be introduced for light flavours with the inclusion of γ_q ($q = u, d$). This allows to consider full chemical non-equilibrium statistical hadronisation model [101]. This situation arise when the source of hadrons disintegrates faster than the time necessary to re-equilibrate the yield of light quarks. This approach was shown to successfully describe the measured integrated hadron yields at the LHC [102] with a common set of freeze-out parameters. The freeze-out temperature T_{ch} extracted from non-equilibrium thermal fit to integrated hadron yields decreases when considering more central collisions ($\sim$ 135 MeV in central collisions and $\sim$ 145 MeV in the most peripheral centrality class). This can be interpreted as due to a more violent transverse fireball expansion leading to a greater and faster cooling of the system. This would also explain the systematic decrease of the freeze-out temperature between LHC and RHIC.

Hadronic bound states above the QCD transition temperature

This alternative scenario is described in [90, 91]. The improvements in lattice QCD calculations (using the physical pion mass and lattice spacings approaching the continuum) have revealed that quasi-particles or colour-neutral bound states could be possible up to $2 \times T_{ch}$. Since the transition from equilibrated QGP to hadron gas has found to be a crossover [103], it is likely that, in the temperature regime between 1-2 T_{ch}, quark and gluon quasi-particles and pre-hadronic bound states can coexist. For these colour-neutral bound states inside a coloured medium the interaction cross section will

be strongly reduced (colour transparency). In this model the possible presence of colour-neutral (pre)-hadronic states in the equilibrated component of the QGP phase [90, 91] would result in a flavour/baryon number dependence of T_{ch}.

Identified hadron results at the LHC cast a new light upon the hydrodynamic and thermal behaviour of the hadron production in heavy-ion collisions. The p-A run expected at the LHC at the beginning of 2013, together with the continuously improving experimental precision and the more accurate description from the theory, will provide an important piece in the heavy-ion puzzle.

Bibliography

[1] J. Letessier and J. Rafelski. Hadrons and Quark-Gluon Plasma. *Cambridge University Press*, 2002.

[2] J. Beringer et al. (Particle Data Group). Review of particle physics. *Phys. Rev. D 86, 010001*, 2012.

[3] K. G. Wilson. Confinement of quarks. *Phys. Rev. D 10, 2445–2459*, 1974.

[4] N. Cabibbo and G.Parisi. Exponential hadronic spectrum and quark liberation. *Phys.Lett. B 59, 67*, 1975.

[5] R. Rapp, T. Schaefer, E.V. Shuryak and M. Velkovsky. Diquark Bose Condensates in High Density Matter and Instantons. *Phys.Rev.Lett. 81, 53-56*, 1998.

[6] R. Snelling. Elliptic Flow: A Brief Review. *New J.Phys.13:055008*, 2011.

[7] ALICE Collaboration. Centrality Dependence of the Charged-Particle Multiplicity Density at Midrapidity in Pb-Pb Collisions at $\sqrt{s_{NN}} = 2.76$ TeV. *Phys. Rev. Lett.*, 106:032301, Jan 2011.

[8] U. W. Heinz. Concepts of Heavy-Ion Physics. *arXiv:hep-ph/0407360*, 2004.

[9] ALICE Collaboration. Transverse Momentum Distribution and Nuclear Modification Factor of Charged Particles in p-Pb Collisions at $\sqrt{s_{NN}} = 5.02$ TeV. *arXiv:1210.4520v1*, 2012.

[10] ALICE Collaboration. Centrality Dependence of Charged Particle Production at Large Transverse Momentum in Pb–Pb Collisions at $\sqrt{s_{\rm NN}}$ = 2.76 TeV. *arXiv:1208.2711v1 [hep-ex]*, 2012.

[11] ATLAS Collaboration. Jet size dependence of single jet suppression in lead-lead collisions at $\sqrt{s_{NN}}$ = 2.76 TeV with the ATLAS detector at the LHC. *arXiv:1208.1967v1 [hep-ex]*, 2012.

[12] ATLAS Collaboration. Observation of a Centrality-Dependent Dijet Asymmetry in Lead-Lead Collisions at $\sqrt{s_{NN}}$= 2.76 TeV with the ATLAS Detector at the LHC. *Phys.Rev.Lett.105:252303*, 2010.

[13] CMS Collaboration. Measurement of isolated photon production in p–p and Pb–Pb collisions at $\sqrt{s_{NN}}$ = 2.76 TeV. *arXiv:1201.3093v1 [nucl-ex]*, 2012.

[14] P.V. Ruuskanen. Photons and lepton pairs: The deep probes of quark-gluon plasma. *NATO ASI Series B: Physics Vol. 303 - 593*, 1993.

[15] B. Sahlmueller. Photons at PHENIX. *arXiv:0904.4764v2 [nucl-ex]*, 2010.

[16] ALICE Collaboration. Suppression of high transverse momentum prompt D mesons in central Pb–Pb collisions at $\sqrt{s_{NN}}$=2.76 TeV. *JHEP 9, 112*, 2012.

[17] ALICE Collaboration. J/ψ Suppression at Forward Rapidity in Pb–Pb Collisions at $\sqrt{s_{NN}}$ = 2.76 TeV. *Phys. Rev. Lett. 109, 072301*, 2012.

[18] CMS Collaboration. Suppression of non-prompt J/ψ, prompt J/ψ, and Υ (1S) in PbPb collisions at $\sqrt{s_{NN}}$=2.76 TeV. *arXiv:1201.5069 [nucl-ex]*, 2012.

[19] A. Andronic, P. Braun-Munzinger and J. Stachel. Hadron production in central nucleus-nucleus collisions at chemical freeze-out. *Nucl.Phys.A772:167-199*, 2006.

[20] A. Andronic, P. Braun-Munzinger, and J. Stachel. Thermal hadron production in relativistic nuclear collisions: the hadron mass spectrum, the horn, and the QCD phase transition. *Phys.Lett.B678:516*, 12 2009.

[21] J. Cleymans and K. Redlich. Unified Description of Freeze-Out Parameters in Relativistic Heavy Ion Collisions. *Phys.Rev.Lett. 81 5284-5286*, 1998.

[22] Nu Xu. Explore the QCD Phase Diagram. *International School of Nuclear Physics, 30th Course, Erice-Sicily*, 2008.

[23] A. R. Timmins. Overview of Strangeness Production at the STAR Experiment. *J.Phys.G36:064006*, 2009.

[24] ALICE Collaboration. Elliptic flow of charged particles in Pb-Pb collisions at 2.76 TeV. *Phys.Rev.Lett. 105.252302*, 2010.

[25] ALICE Collaboration. Two-pion Bose-Einstein correlations in central PbPb collisions at $\sqrt{s_{NN}} = 2.76$ TeV. *Phys.Lett.B 696 (4): 328-337*, 2011.

[26] E. Fermi. High Energy Nuclear Events. *Prog. Theor. Phys. Vol. 5 No. 4, 570-583*, 1950.

[27] R. Hagedorn. Statistical thermodynamics of strong interactions at high-energies. *Nuovo Cim.Suppl.3:147-186*, 1965.

[28] F. Becattini. An introduction to the Statistical Hadronization Model. *arXiv:0901.3643v1 [hep-ph]*, 2009.

[29] F. Becattini. Strangeness production in relativistic heavy ion collisions. *QGP school, Torino, March 2011.*

[30] F. Becattini. Remark on statistical model fits to particle ratios in relativistic heavy ion collisions. *arXiv:0707.4154v2 [nucl-th]*, 2007.

[31] L. Ferroni and F. Becattini. Statistical hadronization with exclusive channels in $e^+ - e$ annihilation. *arXiv:1109.5185v1 [hep-ph]*, 2011.

[32] M. Rybczyn ski and W. Broniowski. Wounded nucleon model with realistic nucleon-nucleon collision profile and observables in relativistic heavy-ion collisions. *Phys.Rev.C84:064913*, 2011.

[33] L. McLerran. The Color Glass Condensate and Small x Physics: 4 Lectures. *Lect.Notes Phys.583:291-334*, 2002.

[34] J. Y. Ollitrault. Relativistic hydrodynamics for heavy-ion collisions. *Eur.J.Phys.29:275-302*, 2008.

[35] Piotr Bozek. Flow and interferometry in 3+1 dimensional viscous hydrodynamics. *Phys. Rev. C 85, 034901*, 10 2012.

[36] B. Schenke. Initial state fluctuations and higher harmonic flow in heavy-ion collisions. *Quark Matter 2012 proceedings*, 2012.

[37] F. Cooper and G. Frye. Single-particle distribution in the hydrodynamic and statistical thermodynamic models of multiparticle production. *Phys. Rev. D 10, 186–189*, 1974.

[38] C. Spieles S.A. Bass C. Ernst S. Soff L. Bravina M. Belkacem H. Weber H. Stöcker M. Bleicher, E. Zabrodin and W. Greiner. Relativistic Hadron-Hadron Collisions in the Ultra-Relativistic Quantum Molecular Dynamics Model (UrQMD). *J.Phys.G25:1859-1896*, 1999.

[39] Y. Pan and S. Pratt. Baryon Annihilation in Heavy Ion Collisions. *arXiv:1210.1577v1 [nucl-th]*, 2012.

[40] CERN. The Large Hadron Collider, `http://public.web.cern.ch/public/en/LHC/LHC-en.html`.

[41] ATLAS Collaboration. Luminosity Public Results, `https://twiki.cern.ch/twiki/bin/view/AtlasPublic/LuminosityPublicResults`.

[42] Public results on Higgs search. `https://twiki.cern.ch/twiki/bin/view/AtlasPublic/HiggsPublicResults` and `http://cms.web.cern.ch/org/cms-higgs-results`.

[43] ALICE Collaboration. The ALICE experiment at the CERN LHC. *JINST 3 S08002*, 2008.

[44] ALICE Collaboration. ALICE: Physics Performance Report, Volume I. *J. Phys. G: Nucl. Part. Phys. 30 1517*, 2004.

[45] ALICE Collaboration. ALICE: Physics Performance Report, volume II. *J.Phys.G32 1295-2040*, 2006.

[46] ALICE Collaboration. ALICE computing : Technical Design Report. *CERN-LHCC-2005-018*, 2005.

[47] ROOT Project homepage, `http://root.cern.ch/drupal/`.

[48] PYTHIA online manual, `http://home.thep.lu.se/~torbjorn/pythia81html/Welcome.html`.

[49] HIJING Documentation, `http://www-nsdth.lbl.gov/~xnwang/hijing/`.

[50] GEANT - Detector Description and Simulation Tool, `http://wwwasd.web.cern.ch/wwwasd/geant/`.

[51] FLUKA project homepage, `http://www.fluka.org/fluka.php`.

[52] AliEn - ALICE Environment, `http://alien2.cern.ch`.

[53] R. Santoro et al. The ALICE Silicon Pixel Detector: readiness for the first proton beam. *J. Instrum. 4 P03023*, 2009.

[54] E. Gatti and P. Rehak. Semiconductor drift chamber - an application of a novel charge transport scheme. *Nucl. Instrum. Meth.A225:608-614*, 1984.

[55] E. Crescio, A. Dainese, M. Masera and F. Prino. Performance of the ITS stand-alone tracker in pp collisions. *ALICE-INT 2009-046*, 2009.

[56] A. Rivetti et al. The front-end system of the silicon drift detectors of ALICE. *Nucl. Instrum. Meth., A541:267–273*, 2005.

[57] G. Mazza, P. De Remigis and K. Kloukinas. AMBRA: A multi-event buffer- ing and readout ASIC for the silicon drift detectors of the ALICE experiment. *IEEE Trans. Nucl. Sci., 55:2414–2419*, 2008.

[58] S. Antinori, D. Falchieri, A. Gabrielli and E. Gandolfi. Implementation of a bidimensional compressor for a high- energy physics experiment. *IEEE Trans. Nucl. Sci., 51:2941–2946*, 2004.

[59] M. Chojnacki. Measurement of pions, kaons and protons with the ALICE detector in pp collisions at the LHC. *Ph.D. thesis, Utrecht University*, 2012.

[60] PHOBOS Collaboration. Identified hadron transverse momentum spectra in Au+Au collisions at $\sqrt{s_{NN}} = 62.4$ GeV. *Phys.Rev.C75, 024910*, 2007.

[61] ALICE Collaboration. Trigger twiki, `https://twiki.cern.ch/twiki/bin/viewauth/ALICE/TriggerCoordination`.

[62] O. Djuvsland and J. Nystrand. Single and Double Photonuclear Excitations in Pb–Pb Collisions at $\sqrt{s_{NN}} = 2.76$ TeV at the CERN Large Hadron Collider. *Phys.Rev.C83, 041901*, 2011.

[63] ALICE Collaboration. Production of pions, kaons and protons in *pp* collisions at $\sqrt{s} = 900$ GeV with ALICE at the LHC. *Eur.Phys.J.*, C71:1655, 2011.

[64] E. Biolcati. Distribution of hadrons identified with the Inner Tracking System of the ALICE experiment for p–p data. *Ph.D. thesis, Turin University*, 2011.

[65] M. Siciliano. Transverse Momentum Distribution with ITS Standalone Tracking with Particle Identification. *Ph.D. thesis, Turin University*, 2012.

[66] R. Barlow and C. Beeston. Fitting using finite Monte Carlo samples. *Comp. Phys. Comm. 77 219-228*, 1993.

[67] P. Christakoglou and M. Oldenburg. Estimation of the Systematic Uncertainties in $\bar{\text{p}}$-p Measurements. *ALICE-INT-2008-010*, 2008.

[68] Geant4 - a simulation toolkit, `http://geant4.cern.ch`.

[69] ALICE Collaboration. Multi-strange baryon production in pp collisions at with ALICE. *Physics Letters B712, 309 - 318*, 2012.

[70] ALICE Collaboration. The AliRoot Offline bible, `http://aliceinfo.cern.ch/Offline/sites/aliweb.cern.ch.Offline/files/uploads/OfflineBible.pdf`.

[71] ALICE Collaboration. Pion, Kaon, and Proton Production in Central Pb–Pb Collisions at $\sqrt{s_{NN}} = 2.76$ TeV. *arXiv:1208.1974 [hep-ex]*, 08 2012.

[72] E. Schnedermann, J. Sollfrank and U.W. Heinz. Thermal phenomenology of hadrons from 200-A/GeV S+S collisions. *Phys.Rev.C48, 2462-2475*, 1993.

[73] STAR Collaboration. Experimental and Theoretical Challenges in the Search for the Quark Gluon Plasma: The STAR Collaboration's Critical Assessment of the Evidence from RHIC Collisions. *Nucl.Phys.A757:102-183*, 2005.

[74] STAR Collaboration. Systematic Measurements of Identified Particle Spectra in pp, d+Au and Au+Au Collisions from STAR. *Phys.Rev.C79:034909*, 08 2008.

[75] Chun Shen, Ulrich W. Heinz, Pasi Huovinen, and Huichao Song. Radial and elliptic flow in Pb+Pb collisions at the Large Hadron Collider from viscous hydrodynamic. *arXiv:1105.3226 [nucl-th]*, 05 2011.

[76] Y. M. Sinyukov I. A. Karpenko and K. Werner. Uniform description of bulk observables in the hydrokinetic model of A+A collisions at RHIC and LHC. *arXiv:1204.5351 [nucl-th]*, 04 2012.

[77] S. Jeon. E-by-E MUSIC Afterburner. *Quark Matter 2012 proceedings*, 2012.

[78] ALICE Collaboration. Centrality dependence of π, K, p Production in Pb–Pb Collisions at $\sqrt{s_{NN}} = 2.76$ TeV. *In print*, 2013.

[79] P. Bozek and I. Wyskiel-Piekarska. Particle spectra in Pb-Pb collisions at 2.76 TeV. *arXiv:1203.6513v2 [nucl-th]*, 2012.

[80] M. Miller and R. Snellings. Eccentricity fluctuations and its possible effect on elliptic flow measurements. *arXiv:nucl-ex/0312008*, 2003.

[81] S. Voloshin for the ALICE Collaboration. Results on flow from ALICE. *Quark Matter 2012 proceedings*, 2012.

[82] A. F. Dobrin for the ALICE Collaboration. Event shape engineering with ALICE. *Quark Matter 2012 proceedings*, 2012.

[83] ALICE Collaboration. Analysis Object Data (AOD), `http://aliweb.cern.ch/Offline/Activities/Analysis/aod.html`.

[84] ALICE Collaboration. Run Condition Table (RCT), `http://alimonitor.cern.ch/configuration/`.

[85] L. Zi-Wei, K. Che Ming, L. Bao-An, Z. Bin and P. Subrata. A Multi-Phase Transport Model for Relativistic Heavy Ion Collisions. *Phys.Rev.C72:064901*, 2005.

[86] PHENIX Collaboration. Identified Charged Particle Spectra and Yields in Au+Au Collisions at $\sqrt{s_{NN}} = 200$ GeV. *Phys.Rev.C69:034909*, 2004.

[87] BRAHMS Collaboration. Centrality Dependent Particle Production at $y = 0$ and $y \sim 1$ in Au+Au Collisions at $\sqrt{s_{NN}}$=200GeV. *Phys.Rev.C72:014908*, 2005.

[88] Francesco Becattini, Marcus Bleicher, Thorsten Kollegger, Michael Mitrovski, Tim Schuster, and Reinhard Stock. Hadronization and Hadronic Freeze-Out in Relativistic Nuclear Collisions. *arXiv:1201.6349 [nucl-th]*, 01 2012.

[89] Jan Steinheimer, Jörg Aichelin, and Marcus Bleicher. Non-thermal p/π ratio at LHC as a consequence of hadronic final state interactions. *arXiv:1203.5302 [nucl-th]*, 03 2012.

[90] C. Ratti, R. Bellwied, M. Cristoforetti and M. Barbaro. Are there hadronic bound states above the QCD transition temperature? *Phys. Rev. D85, 014004*, 2012.

[91] R. Bellwied. Hadron formation in the deconfined matter at RHIC and LHC. *arXiv:1205.3625 [hep-ph]*, 2012.

[92] L. S. Barnby, I. Belikov, D. Dobrigkeit Chinellato, L. D. Hanratty, P. Kalinak, M. Putis, S. Schuchmann. Measurement of K^0_S and Λ spectra and yields in Pb–Pb collisions at $\sqrt{s_{NN}} = 2.76$ TeV with the ALICE experiment. *ALICE-ANA-229*, 2012.

[93] D. Colella, D. Elia and M. Nicassio. Measurement of multi-strange baryons in Pb-Pb collisions at $\sqrt{s_{NN}} = 2.76$ TeV. *ALICE-ANA-116*, 2012.

[94] A.G. Knospe. Yield of phi mesons at low p_{T} in Pb-Pb collisions at $\sqrt{s_{NN}} = 2.76$ TeV (2010 data). *ALICE-ANA-300*, 2012.

[95] S. Singha for the ALICE Collaboration. Strange hadrons and resonances in Pb-Pb collisions at $\sqrt{s_{NN}} = 2.76$ TeV with ALICE experiment at LHC. *Quark Matter 2012 proceedings*, 2012.

[96] S. Singha. K^{*0} resonance production in Pb-Pb collisions at $\sqrt{s_{NN}} = 2.76$ TeV. *ALICE-ANA-211*, 2012.

[97] L. Milano for the ALICE Collaboration. Identified charged hadron production in Pb-Pb collisions at the LHC with the ALICE Experiment. *Quark Matter 2012 proceedings*, 2012.

[98] A. Andronic. A thermal fit of ALICE hadron yields. *ALICE-ANA-421*, 2012.

[99] F. Becattini, M. Bleicher, T. Kollegger, T. Schuster, J. Steinheimer and R. Stock. Hadron Formation in Relativistic Nuclear Collisions and the QCD Phase Diagram. *arXiv:1212.2431 [nucl-th]*, 2012.

[100] M. S. Szymanski for the ALICE Collaboration. Meson and baryon femtoscopy in heavy-ion collisions at ALICE. *Quark Matter 2012 proceedings*, 2012.

[101] J. Letessier and J. Rafelski. Chemical non-equilibrium and deconfinement in 200 A GeV Sulphur induced reactions. *Phys.Rev. C59 947-954*, 1999.

[102] J. Rafelski. Hadron production in Pb-Pb collisions at LHC, CERN Heavy Ion Forum - `http://indico.cern.ch/conferenceDisplay.py?confId=216559`. 2012.

[103] E. Laermann and O. Philipsen. The Status of Lattice QCD at Finite Temperature. *Ann.Rev.Nucl.Part.Sci. 53 163-198*, 2003.